ISSN 2738-0971
eISSN 2738-1013

Bulletin of Natural Sciences Research

Vol. 15, Nº 1, 2025.

BULLETIN OF NATURAL SCIENCES RESEARCH

Published by
Faculty of Sciences and Mathematics, University of Priština in Kosovska Mitrovica
Republic of Serbia

Focus and Scope

Bulletin of Natural Sciences Research is an international, peer-reviewed, open access journal, published annually, both online and in print, by the Faculty of Sciences and Mathematics, University of Priština in Kosovska Mitrovica, Republic of Serbia. The Journal publishes articles on all aspects of research in biology, chemistry, geography, geoscience, astronomy, mathematics, computer science, mechanics and physics.

Directors

Dejan M. Gurešić

Editor in Chief

Dejan M. Gurešić

Associate Editors

Ljubiša D. Kočinac; Nataša Z. Kontrec, Bojana B. Laban; Časlav M. Stefanović; Ljiljana R. Gulan; Nikola M. Milentijević; Tatjana R. Jakšić.

Editorial Board

Gordan Karaman, Montenegro; Gerhard Tarmann, Austria; Ernest Kirkby, United Kingdom; Nina Nikolić, Serbia; Predrag Jakšić, Serbia; Slavica Petović, Montenegro; Momir Paunović, Serbia; Bojan Mitić, Serbia; Stevo Najman, Serbia; Zorica Svirčev, Serbia; Ranko Simonović, Serbia; Miloš Đuran, Serbia; Radosav Palić, Serbia; Snežana Mitić, Serbia; Vukadin Leovac, Serbia; Slobodan Marković, Serbia; Milan Dimitrijević Serbia; Sylvie Sahal-Brechot, France; Milivoj Gavrilov, Serbia; Jelena Golijanin, Bosnia and Herzegovina; Dragoljub Sekulović, Serbia; Dragica Živković, Serbia; Ismail Gultepe, Canada; Stefan Panić, Serbia; Petros Bithas, Greece; Pavlou Street, Greece; Petar Spalević, Serbia; Marko Petković, Serbia; Milan Simić, Australia; Darius Andriukaitis, Lithuania; Marko Beko, Portugal; Bojan Prlinčević, Serbia; Gradimir Milovanovic, Serbia; Ljubiša Kočinac, Serbia; Ekrem Savas, Turkey; Zoran Ognjanović, Serbia; Donco Dimovski, R. Macedonia; Nikita Šekutkovski, R. Macedonia; Leonid Chubarov, Russian Federation; Žarko Pavićević, Montenegro; Miloš Arsenović, Serbia; Vishnu Narayan Mishra, India; Svetislav Savović, Serbia; Slavoljub Mijović, Montenegro; Saša Kočinac, Serbia.

Technical Secretary

Danijel B. Đošić

Editorial Office

Ive Lole Ribara 29; 38220, Kosovska Mitrovica, Serbia, e-mail: editor@bulletinnsr.com, office@bulletinnsr.com; fax: +381 28 425 397

Printed by

Sigraf, Ćrila i Metodija bb, 37000 Kruševac, tel: +38137427704, e-mail: stamparijasigraf@gmail.com

Available Online

This journal is available online. Please visit http://www.bulletinnsr.com to search and download published articles.

BULLETIN OF NATURAL SCIENCES RESEARCH

Vol. 15, N^{o} 1, 2025.

CONTENTS

BIOLOGY

CHEMISTRY

GEOGRAPHY, GEOSCIENCE AND ASTRONOMY

MATHEMATICS, COMPUTER SCIENCE AND MECHANICS

Bulletin of Natural Sciences Research
Vol. 15, No. 1, 2025, pp. 1-8.

DOI: https://doi.org/10.5937/bnsr15-57799
Original Scientific Paper

BIOACCUMULATION OF HEAVY METALS IN THE ROMAN SNAIL (*HELIX POMATIA*) IN THE AREA OF KOSOVSKA MITROVICA

ŽELJKO BULATOVIĆ[1*], TATJANA JAKŠIĆ[1], MAJA PAVLOVIĆ[1], NIKOLA BAČEVIĆ[1]

[1]Faculty of Natural Sciences and Mathematics, University of Priština in Kosovska Mitrovica, Kosovska Mitrovica, Serbia

ABSTRACT

The bioaccumulation of heavy metals in the Roman snail (*Helix pomatia Linnaeus, 1758*) was investigated in October 2024. Animals were sampled at the location "Gornje Polje," which is situated near the former "Trepča" plant. The snails were collected by hand and then transported to the laboratory. A total of 34 medium-aged snails and 36 older snails were collected. The snails were dissected, and the content of heavy metals determined in the hemolymph, hepatopancreas, kidney and shell. In addition to analyzing the heavy metal content in the snails, an analysis of the heavy metals content in the soil was performed. The soil was collected in a quantity of 1 dm³ using a shovel and transported to the laboratory. The content of seven elements was examined: Arsenic (As), Copper (Cu), Iron (Fe), Cadmium (Cd), Manganese (Mn), Lead (Pb), and Zinc (Zn). The highest level of accumulation is heavy metal observed in the hepatopancreas. Furthermore, other structures exhibit a significantly high level of accumulation. All of this suggests that snails are a highly useful tool for diagnostic purposes in environmental of heavy metal accumulation. The analysis of heavy metal content was performed at the Public Health Institute of Kosovska Mitrovica.

Keywords: Heavy metal, Hemolymph, Hepatopancreas, Shell, Kidney, Soil.

INTRODUCTION

Bioaccumulation refers to the progressive accumulation of metals in biological organisms over time relative to ambient concentrations. This process occurs when the rate of metal uptake and storage exceeds its metabolism and excretion (Markich et al., 2001).

Early studies on metal accumulation in terrestrial invertebrates highlighted their significance in ecotoxicological research. Hopkin (Hopkin, 1989) proposed that "terrestrial invertebrates are key organisms in studying the accumulation of heavy metals due to their close association with the substrate and relative immobility."

Snails are particularly suitable for ecotoxicological research as they effectively reflect changes in metal bioavailability in the environment (Dallinger, 1994).

Subsequent studies have confirmed the ability of snails to accumulate heavy metals such as copper (Cu), lead (Pb), zinc (Zn), and cadmium (Cd). Beeby and Richmond (Beeby & Richmond, 2003) demonstrated that terrestrial snails could serve as reliable bioindicators of metal pollution, findings that were further supported by (Notten et al., 2005; Jordaens et al., 2006). Snails can accumulate heavy metals in their tissues and shells. Their ability for bioaccumulation makes them highly reliable for assessing environmental conditions. (Zalewski et al., 2010; Nica et al., 2012).

Various studies, including those conducted by different authors, have significantly expanded knowledge, emphasizing atmospheric deposition as a key source of metal contamination in soils. These studies indicate that metals, which accumulate in soils through atmospheric deposition, can cause long-term negative effects in ecosystems. The process of atmospheric deposition contributes to the accumulation of these metals in the soil, thereby increasing their bioaccumulation in organisms at higher trophic levels, such as snails and other terrestrial invertebrates. Consequently, this contamination can impact soil quality, reducing its fertility and disrupting ecosystem balance. These findings underscore the importance of continuous monitoring of atmospheric metal deposition and research into its effects on biodiversity and ecological processes. (Gomot-deVaufleury, 2000; Azimi et al., 2004; Regoli & Giuliani, 2014).

The growing ecological implications of industrial metal pollution highlight serious long-term consequences for ecosystems, biodiversity, and human health. Continuous monitoring of metal concentrations is crucial for timely identification of distribution and accumulation changes. This approach aids in assessing and mitigating negative ecological impacts, while improving ecosystem adaptation. Monitoring is essential for environmental protection strategies, tracking trends, and identifying contamination sources, contributing to sustainable resource management and reduced pollution impacts. (Dixit et al., 2015).

The bioaccumulation process depends on both physicochemical and biological factors, with metal bioavailability in soil playing a critical role in their uptake and transfer through the food chain (Nica, 2012).

---

* Corresponding author: zeljko.bulatovic@pr.ac.rs

In this study, soil and snail tissue samples were analyzed for the presence of as, Fe, Mn, Cd, Cu, Ni, Pb, and Zn to assess the level of accumulation under urban conditions. The results revealed significant differences in metal content across various anatomical and morphological structures, providing insight into the bioaccumulation process. Additionally, an analysis of heavy metal concentrations in the surrounding soil was conducted to better understand their environmental distribution.

The sampling site, "Gornje Polje," in Kosovska Mitrovica, was selected due to its proximity to potential pollution sources. This study aims to determine heavy metal concentrations in both snails and soil and, based on bioaccumulation patterns, to assess the ecological status of this region.

THEORETICAL PART

The city of Kosovska Mitrovica is located in Kosovo and Metohija, in the southern part of Serbia (Figure 1). Its geographical coordinates are 42° 53′ N latitude and 20° 52′ E longitude. More precisely, the city is situated in the northern part of the Kosovo Basin, at the foot of the paleo-volcanic cone of Zvečan, at the confluence of the Sitnica River into the Ibar River, where the Ibar meanders before forming the second section of its gorge (Batoćanin Srećković et al., 2020). The urban core of the city and its wider surroundings cover an area of 316 km². Kosovska Mitrovica is surrounded by the Rogozna, Kopaonik, and Mokra Gora mountains to the north, east, and west, while the southern part of the area is bordered by the Čičavica mountain range. Two-thirds of the territory is characterized by mountainous relief, that is morphologically dominant. The average altitude of the city is 510 meters above sea level (Šukrija et al., 1979).

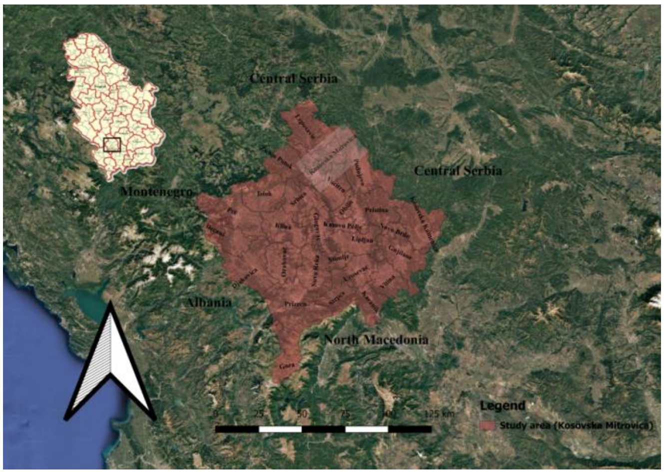

Figure 1. Physical-geographical map of Serbia and Kosovo and Metohija in Europe, with the geographical location of Kosovska Mitrovica specifically marked.

He entire territory of Kosovska Mitrovica holds a strategically significant position, particularly in terms of transit traffic, as it lies at the crossroads of routes connecting Belgrade in the north with Skopje and Thessaloniki in the south, Niš and Sofia in the east, and Podgorica and Bar in the west (Šukrija et al., 1979). The favorable geographical position and physical-geographical characteristics have facilitated the industrial development of Kosovska Mitrovica through various historical periods, from pre-Christian times to the modern era. This development has been primarily based on a highly developed mining industry, especially the extraction of silver-bearing, gold-bearing, lead, zinc, and copper ores. The "Trepča" mine in Stari Trg, along with surrounding mines, played a crucial role in the industrial development of this region (Jovanović, 2007). Following detailed research conducted in 1925, it was established that "Trepča" represents a grand-scale deposit and that its exploitation is highly profitable (Jovanović, 2008).

Sampling of the necessary indivudals of *H.pomatia* for analysis was conducted at the Gornje Polje site (Figure 2), located within the territory of Kosovska Mitrovica, in close proximity to the Ibar River (Figure 3).

Figure 2. Locality Gornje Polje.

Figure 3. Material sampling site.

The samples were collected within the following geographical coordinates: from 42° 54’ 07.6” N and 20° 51’

53.8” E to 42° 54’ 08.1” N and 20° 51’ 57.2” E. Additionally, soil sampling was conducted at the same site, with geographical coordinates of 42° 54' 10.8" N and 20° 51' 38.8" E.

This site represents an industrial waste deposit that was active from 1930 to 1965. The total amount of deposited waste, expressed in tons, is 26,344,212, while the total volume is 8,498,133 m³ (Milentijević et al., 2014).

EXPERIMENTAL

Materials and methods

At the given site, few plant species were identified, including weeds, grasses, shrubs, and small-headed plants. Additionally, human generated waste was observed in the Ibar River, along with large amounts of waste in the vicinity of the river, including remnants of wood (branches and small trees). In the immediate vicinity of the Ibar River, two major chimneys were situated, whose previous activity contributed to the contamination of the Kosovska Mitrovica area and surrounding settlements.

A soil sample measuring 10x10x10 cm (1 dm³) was collected along with vegetation. The soil was transported in a clean cardboard box to the laboratory. Geographical data of the site from which the soil was collected were labeled on the box.

The samples were collected in October 2024.

Snails of the species *H. pomatia* were manually collected using medical gloves. During collection, a high presence of snails was noticed on the surface of a shoot from the plant genus *Dipsacus* Linnaeus,1753. Most of the snails were in a state of hibernation. A smaller number of individuals were found in the vicinity of plants, in the grass, and under rocks. Empty snail shells were also observed (Figure 4).

The shell of the Roman snail is firm, spherical in shape, with a diameter ranging from 38 to 43 mm.

Figure 4. *H.pomatia c*ollected in the study area.

The color of the shell is yellow-brown, with a tendency to transition into lighter shades under the influence of sunlight. The surface of the shell is characterized by spiral lines, which are unevenly distributed and faintly visible. The shell usually contains 4.5 to 5 turns, and the opening at its apex is round. For younger individuals, the number of turns is lower.

The surface of the head and foot of this species is granular and uneven, which represents a key morphological characteristic for its identification. During hibernation, snails secrete a calcareous operculum, a firm cover that seals the shell opening, protecting them from unfavorable external factors. (Monaco Nature Encyclopedia, no date).

During collection, the air temperature ranged from 18 °C to 22 °C, and the relative humidity was on average 72%. A total of 70 snails were collected, which were then placed in plastic containers and transferred to the laboratory for further processing.

After collection, the snails were divided into two groups: medium-aged snails and older snails. A total of 34 medium-aged snails and 36 older snails were dissected. The age of the snails was determined based on the number of whorls on the shell and body mass. Snails weighing over 20 g were classified as older, with a greater number of whorls on the shell, while snails weighing less than 20 g were classified as medium-aged, with fewer whorls on the shell. The procedure was carried out in the first half of November 2024.

The procedure for isolating specific anatomical structures was performed using laboratory equipment and utensils. In separate vials, the following were isolated: 10 ml of hemolymph, 10 g of hepatopancreas, 10 g of kidneys, and 10 g of macerated shell. The material was preserved in vials. Initially, the hemolymph was isolated, followed by the shell, hepatopancreas, and finally, the kidney.

The isolation procedure: Initially, HCl was used. The shell was treated in the region of the second whorl (decalcification of the shell near the heart) using a cotton swab. Afterward, the hemolymph was sampled with a medical syringe and transferred to a vial. Immediately after this procedure, the shell was removed from the body regions with tweezers and macerated in a mortar and pestle. It was transferred to a vial and preserved for further analysis. The next procedure involved the excision of the hepatopancreas and kidneys, which were then transferred to laboratory vials using surgical scissors for precise organ dissection. (Roljic & Nikolic, 2022).

Material was distributed into eight vials and stored in the refrigerator for two days.

The analysis of heavy metal content was performed at the Public Health Institute of Kosovska Mitrovica. The material of the snails were prepared using the following method: 10 g of homogenized sample was weighed on an analytical balance, after which the sample was dried at 105°C until completely dry. Following drying, the sample was placed in a muffle furnace. The furnace temperature was gradually increased by 50°C until reaching 450°C, and the sample was left to ash overnight. The sample was then removed from the furnace and treated with concentrated 0.5 ml of HNO_3. It was evaporated to dryness on a hot plate and returned to the furnace, repeating this process until complete mineralization. Once cooled, 1 ml of concentrated HCl was added along the walls of the beaker, and the sample was transferred to a standard container via filter paper, then diluted with redistilled water to the mark.

The soil sample for analysis was prepared using aqua regia. Aqua regia was prepared the day before, consisting of 3 parts HCl and 1 part HNO_3. A 5-10 g sample was weighed, and 20 ml of aqua regia was added, leaving the sample at room temperature for 24 hours. Afterward, the sample was evaporated in a water bath at 95°C for two hours. After cooling, the sample was filtered into a standard 100 ml container and diluted with demineralized water to the mark.

The concentration of heavy metals was determined using atomic absorption spectrophotometry (AAS), with the application of flame atomization and graphite furnace techniques, depending on the specific elements being analyzed. The procedure was carried out in accordance with the guidelines provided in the Atomic Absorption Data Book (Philips Analytical).

Device model: Atomic Absorption Spectrophotometer PinAAcle 900T..

NUMERICAL RESULTS

The results of the heavy metal content analysisn in the area of Kosovska Mitrovica show a high level of heavy metals both in the soil (Figure 5) and in terrestrical snail.

Heavy metals are considered one of the major soil pollutants and contributors to soil contamination. These metals have toxic effects on soil microorganisms by altering population size, biodiversity, and the various activities of microbial communities in the soil (Ashraf and Ali, 2007). The results of the analysis show the following quantities of heavy metals: Lead (Pb) is present at a concentration of 260 mg/kg, significantly exceeding the threshold value of 85 mg/kg. The remediation capacity for Pb is 530 mg/kg of absolute dry matter.

Zinc (Zn) is present at a concentration of 686.5 mg/kg, which is far above the threshold value of 140 mg/kg. The remediation capacity for Zn is 720 mg/kg.

Iron (Fe) reaches the highest concentration at 9520 mg/kg.

Copper (Cu) is present at a concentration of 628 mg/kg, with a threshold value of 36 mg/kg, while the remediation value is 190 mg/kg.

Manganese (Mn) is present at a concentration of 737 mg/kg.

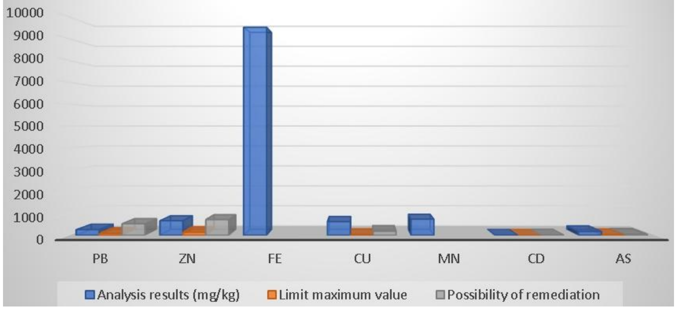

Figure 5. Heavy metal in the soil.

Cadmium (Cd) is present in the soil at a concentration of 1.59 mg/kg. The threshold value for Cd is 0.8 mg/kg, while the remediation capacity is 12 mg/kg.

Arsenic (As) is present at a concentration of 177 mg/kg, with a threshold value of 29 mg/kg, and the remediation capacity is 55 mg/kg (Figure 5).

Based on the conducted analyses, the results show that the concentrations of several heavy metals in the investigated soil significantly exceed the threshold values. The highest concentrations were recorded for iron (Fe), zinc (Zn), copper (Cu), and lead (Pb), while the concentrations of cadmium (Cd) and arsenic (As) were also above the threshold values. The concentration of lead (Pb) was 260 mg/kg, more than three times the permissible threshold value of 85 mg/kg. Zinc (Zn) was present at a concentration of 686.5 mg/kg, also high above the permissible limit of 140 mg/kg. Copper (Cu), at a concentration of 628 mg/kg, exceeded the threshold value of 36 mg/kg, and manganese (Mn), with 737 mg/kg, indicates high levels of contamination. Although the concentrations of cadmium (Cd) and arsenic (As) were above the threshold values, they were not as pronounced as the other metals.

The remediation capacities indicate that reduction of metal concentrations is possible in all cases, but values are still higher than the maximum allowable concentrations. Remediation appears particularly necessary for elements such as lead, zinc, and copper, where concentrations are several times higher than the threshold values, while cadmium and arsenic require less intensive measures.

The maximum threshold values are defined by the Regulation on Threshold Values of Pollutants, Harmful, and Hazardous Substances in Soil (Official Gazette of RS, No. 30/2018 and 64/2019).

Analysis of heavy metal content in middle-aged snails

Hemolymph is the primary circulatory fluid in mollusks, similar to blood in vertebrates, and plays a crucial role in the transport of nutrients, gases, and metals throughout the organism. Hemolymph can reflect the current exposure of snails to environmental contaminants, as "metals ingested into the organism rapidly reach the hemolymph before being distributed to target organs or excreted" (Vlahogianni et al., 2007).

The results of heavy metal content in medium-aged snails are presented in Tables 1-4, which detail the distribution of various metals in the snail's organism.

These tables contain data on the concentration of heavy metals in four different examined parameters: hemolymph, shell, kidneys, and hepatopancreas.

Table 1. Heavy metal content in the hemolymph of medium-aged snails.

Testing Parameter	Value
Arsenic (As)	0.00482 mg/kg
Copper (Cu)	10.578 mg/kg
Iron (Fe)	0.7153 mg/kg
Cadmium (Cd)	0.0012 mg/kg
Manganese (Mn)	0.1242 mg/kg
Lead (Pb)	0.0005 mg/kg
Zinc (Zn)	0.5121 mg/kg

Table 2. The content of heavy metals in the shells of medium-aged snails.

Testing Parameter	Value
Arsenic (As)	1.5641 mg/kg
Copper (Cu)	0.1695 mg/kg
Iron (Fe)	1.1248 mg/kg
Cadmium (Cd)	0.00079 mg/kg
Manganese (Mn)	0.0916 mg/kg
Lead (Pb)	0.0751 mg/kg
Zinc (Zn)	0.09184 mg/kg

Table 3. Heavy metal content in the kidney of medium-aged Snails.

Testing Parameter	Value
Arsenic (As)	0.0005 (mg/kg)
Copper (Cu)	0.3481 (mg/kg)
Iron (Fe)	0.9151 (mg/kg)
Cadmium (Cd)	0.0124 (mg/kg)
Manganese (Mn)	0.2764 (mg/kg)
Lead (Pb)	0.141 (mg/kg)
Zinc (Zn)	0.3878 (mg/kg)

Table 4. Heavy metal content in the hepatopancreas of medium-aged snail.

Testing Parameter	Value
Arsenic (As)	0.0594 (mg/kg)
Copper (Cu)	7.5241 (mg/kg)
Iron (Fe)	8.9057 (mg/kg)
Cadmium (Cd)	0.02695 (mg/kg)
Manganese (Mn)	0.8768 (mg/kg)
Lead (Pb)	1.284 (mg/kg)
Zinc (Zn)	0.79289 (mg/kg)

The snail shell primarily consists of calcium carbonate and can act as a reservoir for certain metals, particularly those that have an affinity for carbonate structures. According to studies, "snail shells can accumulate metals from the environment, serving as a long-term indicator of pollution" (Rainbow, 2002).

The kidneys play a major role in detoxifying the organism and excreting metabolic waste, including heavy metals. Research has shown that "mollusk kidneys play a key role in metal homeostasis, given their ability to accumulate and excrete toxic elements" (Dallinger et al., 1997).

The hepatopancreas is the most metabolically active organ in snails, responsible for digestion, nutrient storage, and metal detoxification. It is considered that the "hepatopancreas is the main organ for metal accumulation in snails, often showing high concentrations of heavy metals due to active removal and storage" (Regoli & Principato, 1995).

Copper (Cu) is present at the highest concentration in the hemolymph (10.578 mg/kg), reflecting its function as a respiratory pigment in the snail’s circulatory system. Elevated copper levels were also detected in the hepatopancreas (7.5241 mg/kg), indicating significant accumulation in this metabolically important organ. In contrast, copper concentrations in the shell (0.1695 mg/kg) and kidneys (0.3481 mg/kg) were much lower, suggesting these tissues are not major copper reservoirs.

Iron (Fe) reaches an exceptionally high concentration in the hepatopancreas (8.9057 mg/kg), underscoring its key role in enzymatic reactions and metabolism. High iron levels were also found in the shell (1.1248 mg/kg), while the hemolymph (0.7153 mg/kg) and kidneys (0.9151 mg/kg) contained moderate amounts.

Arsenic (As) occurs at very low concentrations in the hemolymph (0.00482 mg/kg) and kidneys (0.0005 mg/kg), with a marked increase observed in the shell (1.5641 mg/kg). The hepatopancreas contained measurable arsenic (0.0594 mg/kg), indicating possible detoxification or partial storage of this metal.

Cadmium (Cd) is generally low across all tissues, with the highest levels recorded in the hepatopancreas (0.02695 mg/kg) and kidneys (0.0124 mg/kg). These data suggest some cadmium accumulation capacity in these organs, while the shell showed extremely low values (0.00079 mg/kg).

Manganese (Mn) is most abundant in the hepatopancreas (0.8768 mg/kg), consistent with its metabolic function. Lower concentrations were recorded in the hemolymph (0.1242 mg/kg) and shell (0.0916 mg/kg), whereas the kidneys (0.2764 mg/kg) contained moderate levels.

Lead (Pb) shows notably high concentrations in the hepatopancreas (1.284 mg/kg), suggesting significant toxicity potential and bioaccumulation. Elevated levels were also found in the shell (0.0751 mg/kg) and kidneys (0.141 mg/kg), while hemolymph levels were extremely low (0.0005 mg/kg).

Zinc (Zn) is most concentrated in the hepatopancreas (0.79289 mg/kg), reflecting its important role in metabolic processes. Moderate zinc levels were measured in the hemolymph (0.5121 mg/kg), whereas the shell (0.09184 mg/kg) and kidneys (0.3878 mg/kg) showed lower concentrations.

Analysis of heavy metal content in older snails

Observed variations in metal concentrations across different organs particularly the hemolymph, shell, kidneys, and hepatopancreas may reflect both systemic distribution and organ-specific mechanisms of metal storage and excretion. These findings emphasize aging as a key factor affecting the dynamics of heavy metal bioaccumulation. Detailed data on metal content in older snails are presented in Tables 5–8.

Table 5. Heavy metal content in hemolymph of older snails.

Testing Parameter	Value
Arsenic (As)	0.00094 mg/kg
Copper (Cu)	8.088 mg/kg
Iron (Fe)	1.0198 mg/kg
Cadmium (Cd)	0.00125 mg/kg
Manganese (Mn)	0.2348 mg/kg
Lead (Pb)	0.0005 mg/kg
Zinc (Zn)	0.3799 mg/kg

Table 6. Heavy metal content in shell of older snails.

Testing Parameter	Value
Arsenic (As)	1.8964 mg/kg
Copper (Cu)	0.276 mg/kg
Iron (Fe)	0.086 mg/kg
Cadmium (Cd)	0.00016 mg/kg
Manganese (Mn)	0.0005 mg/kg
Lead (Pb)	0.01772 mg/kg
Zinc (Zn)	0.02848 mg/kg

Table 7. Heavy metal content in kidney of older snails.

Testing Parameter	Value
Arsenic (As)	0.0005 mg/kg
Copper (Cu)	3.3581 mg/kg
Iron (Fe)	4.8477 mg/kg
Cadmium (Cd)	0.0231 mg/kg
Manganese (Mn)	0.4099 mg/kg
Lead (Pb)	0.0091 mg/kg
Zinc (Zn)	0.5706 mg/kg

Table 8. Heavy metal content in hepatopancreas of older snails.

Testing Parameter	Value
Arsenic (As)	0.005 mg/kg
Copper (Cu)	9.5475 mg/kg
Iron (Fe)	9.9886 mg/kg
Cadmium (Cd)	0.0385 mg/kg
Manganese (Mn)	1.0756 mg/kg
Lead (Pb)	1.4324 mg/kg
Zinc (Zn)	0.9199 mg/kg

Copper (Cu) reaches the highest concentration in the hepatopancreas of older snails (9.5475 mg/kg), highlighting its role in the accumulation of this metal during metabolism. A moderate level of copper was recorded in the kidneys (3.3581 mg/kg), while the hemolymph contained 8.088 mg/kg and the shell showed a very low concentration (0.276 mg/kg), which contrasts with medium-aged snails, where copper levels in the shell were much lower than in other organs.

Iron (Fe) reaches an exceptionally high concentration in the hepatopancreas of older snails (9.9886 mg/kg), underscoring its key role in enzymatic reactions and metabolism. High iron levels were also found in the kidneys (4.8477 mg/kg), while the hemolymph (1.0198 mg/kg) and shell (0.086 mg/kg) contained significantly lower amounts.

Arsenic (As) occurs at very low concentrations in the hemolymph (0.00094 mg/kg) and kidneys (0.0005 mg/kg), with the highest accumulation observed in the shell (1.8964 mg/kg). The hepatopancreas contained a moderate level of arsenic (0.005 mg/kg), indicating possible detoxification or storage of this metal.

Cadmium (Cd) is present at relatively high concentrations in the hepatopancreas (0.0385 mg/kg), with lower concentrations in the kidneys (0.0231 mg/kg) and hemolymph (0.00125 mg/kg). The shell shows extremely low cadmium levels (0.00016 mg/kg), similar to the findings in medium-aged snails.

Manganese (Mn) reaches the highest concentration in the hepatopancreas (1.0756 mg/kg), reflecting its importance in enzymatic activities and metabolism. Manganese levels in the kidneys (0.4099 mg/kg) are higher than in the hemolymph (0.2348 mg/kg) and shell (0.0005 mg/kg), consistent with the metal's role in these organs.

Lead (Pb) accumulates at very high concentrations in the hepatopancreas (1.4324 mg/kg), which is higher than in medium-aged snails (1.284 mg/kg). The kidneys show lower levels (0.0091 mg/kg), while the hemolymph (0.0005 mg/kg) and shell (0.01772 mg/kg) contain much lower concentrations.

Zinc (Zn) reaches the highest concentration in the hepatopancreas (0.9199 mg/kg), indicating its role in metabolic processes. Moderate zinc levels were recorded in the kidneys (0.5706 mg/kg), while the hemolymph (0.3799 mg/kg) and shell (0.02848 mg/kg) contained lower amounts.

Comparing the results for medium-aged and older snails, significant differences in metal concentrations in various organs are observed. The hepatopancreas of older snails shows considerably higher concentrations of copper, iron, manganese, lead, and zinc, which may indicate an increased accumulation of these metals in older snails, likely due to prolonged exposure to pollution or metabolic changes occurring with age. The shell of older snails accumulates high concentrations of arsenic, suggesting long-term exposure to pollutants. Additionally, the higher concentrations of lead in the hepatopancreas and kidneys indicate potential toxic effects of this metal, especially in older snails, which may be more susceptible to toxic influences.

CONCLUSION

The study of heavy metal accumulation in terrestrial snails of the species *Helix pomatia*, as well as in soil samples from the Gornje Polje site, enabled the assessment of the ecological condition of the area, particularly in the context of industrial contamination.

Samples of medium-aged and older snails, along with soil samples from specific geographical coordinates near the Ibar River and former industrial plants, were analyzed.

The results indicate the presence of certain concentrations of heavy metals such as copper (Cu), zinc (Zn), cadmium (Cd), and lead (Pb) in the tissues of snails, particularly in: hemolymph, hepatopancreas, kidneys, and shell. These concentrations suggest significant bioaccumulation, confirming the use of terrestrial snails as indicators for ecological monitoring of heavy metal contamination. Considering the limited ability of this species to excrete metals, terrestrial snails prove to be an efficient model for assessing long-term exposure to toxic substances in urban and industrially contaminated areas.

Furthermore, the soil analysis revealed significant concentrations of the same metals, suggesting long-term contamination caused by industrial activities such as mining and metallurgy, particularly between 1930 and 1965, when the industrial landfill was active. The contamination may pose a serious risk to the ecosystem and human populations in the vicinity, as heavy metals can enter the food chain, increasing the risk of chronic poisoning.

Taking all these factors into account, the study highlights the need for continued monitoring and the implementation of strategies to reduce pollution in order to protect both ecosystems and human populations in this area. Given the high concentrations of heavy metals in both biological and abiotic samples, additional environmental protection measures are required, along with more detailed studies on the impact on the health of local communities.

REFERENCES

Ashraf, R. & Ali, T. A. 2007. Effect of heavy metals on soil microbial community and mung beans seed germination. Pakistan Journal of Botany, 39(2), pp. 629-636.

Azimi, S., Cambier, P., Lecuyer, I. & Thevenot, D. 2004. Heavy metal determination in atmospheric deposition and other fluxes in northern France Agrosystems. Water Air Soil Pollut. 157, pp. 295-313. https://doi.org/10.1023/B:WATE.0000038903.25700.5a

Beeby, A. & Richmond, L. 2003. Do the soft tissues of Helix aspersa serve as a quantitative sentinel of predicted free lead concentrations in soils? Applied Soil Ecology, 22(2), pp. 159-165.

Dallinger, R., Prosi, F., Segner, H. & Back, H. 1997. Contaminated food and uptake of heavy metals by fish: A review and proposal for further research. Oecologia, 73(1), pp. 91-98.

Dallinger, R., Berger, B., Hunziger, P. & Kgi, J. H. 1997. Metallothionein in snail Cd and Cu metabolism. Nature, 388(6639), 237.

Dallinger, R., Chabicovsky, M., Hodl, E., Prem, C., Hunziker, P. & Manzl, C. 2005. Copper in Helix pomatia (Gastropoda) is regulated by one single cell type: differently responsive metal pools in rhogocytes. American Journal of Physiology-Regulatory, Integrative and Comparative Physiology, 289(4), pp. 1185-1195.

Dixit, R., Malaviya, D., Pandiyan, K., Singh, U. B., Sahu, A., Shukla, R., Singh, B. P., Rai, J. P., Sharma, P. K., Lade, H. et al. 2015. Bioremediation of Heavy Metals from Soil and Aquatic Environment: An Overview of Principles and Criteria of Fundamental Processes. Sustainability, 7, pp. 2189-2212.

Gomot de Valfleury, A. & Pihan, F. 2000. Growing snails used as sentinels to evaluate terrestrial environment contamination by trace element. Chemosphere, 40, pp. 275-284.

Gomot de Vaufleury, A. 2000. Standardized growth toxicity testing (Cu, Zn, Pb, and pentachlorophenol) with Helix aspersa. Ecotoxicology and Environmental Safety, 46(1), pp. 41-50.

Hopkin, S. P. 1989. Ecophysiology of Metals in Terrestrial Invertebrates. Elsevier Applied Science.

Jordaens, K., De Wolf, H., Vandecasteele, B., Blust, R. & Backeljau, T. 2006. Associations between shell strength, shell morphology and heavy metals in the land snail Cepaea nemoralis (Gastropoda, Helicidae). Science of the Total Environment, 363(1–3), pp. 285-293.

Markich, S. J., Brown, P. L., Batley, G. E., Apte, S. C. & Stauber, J. L. 2001. Incorporating metal speciation and bioavailability into water quality guidelines for protecting aquatic ecosystems. Australasian Journal of Ecotoxicology, 7, pp. 109-122.

Monaco Nature Encyclopedia. (n.d.) Helix pomatia. Available at: https://www.monaconatureencyclopedia.com/helix-pomatia/?lang=en. Accessed March 15, 2025.

Nica, D. V., Bura, M., Gergen, I., Harmanescu, M. & Bordean, D. 2012. Bioaccumulative and conchological assessment of heavy metal transfer in a soil-plant-snail food chain. Chemistry Central Journal, 15, pp. 1-15.

Notten, M. J. et al., 2005. Accumulation of metals in the terrestrial snail Cepaea nemoralis. Archives of Environmental Contamination and Toxicology, 48(3), pp. 342-354.

Official Gazette of the Republic of Serbia. 2018-2019. pp. Official Gazette of RS, Nos. 30/2018 and 64/2019. Available at: https://www.pravno-informacioni-sistem.rs. Accessed March 15, 2025.

Rainbow, P. S. 2002. Trace metal concentrations in aquatic invertebrates: Why and so what? Environmental Pollution, 120(3), pp. 497-507.

Regoli, F. & Principato, G. B. 1995. Glutathione, glutathione-dependent and antioxidant enzymes in mussel, Mytilus galloprovincialis, exposed to metals under field and laboratory conditions: Implications for the use of biochemical biomarkers. Aquatic Toxicology, 31(2), pp. 143-164.

Regoli, F. & Giuliani, M. E. 2014. Oxidative pathways of chemical toxicity and oxidative stress biomarkers in marine organisms. Marine Environmental Research, 93(1), pp. 106-117.

Roljić, R. & Nikolić, V. 2022. Zoologija beskičmenjaka: praktikum sa radnom sveskom. Banja Luka: Univerzitet u Banjoj Luci, Prirodno-matematički fakultet.

Srećković-Batoćanin, D., Bačević, N., Valjarević, A. & Memović, E. 2020. Paleovolcanic Cone Zvečan – Potential Monument of Nature or Geoheritage Site. “Smederevo Ecological City” – Fourth Ecological Conference with International Participation. Smederevo, October 2020. Proceedings, pp. 89-95. ISBN 978-86-919317-3-5. Local Ecological Movement.

Šukrija, A. & Hadri, A. 1979. Kosovska Mitrovica i okolina. Priština: Institut za istoriju Kosova u Prištini.

Vlahogianni, T., Dassenakis, M., Scoullos, M. J. & Valavanidis, A. 2007. Integrated use of biomarkers (superoxide dismutase, catalase, lipid peroxidation, and acetylcholinesterase) in Mytilus galloprovincialis for assessing heavy metal pollution in coastal areas from the Saronikos Gulf of Greece. Marine Pollution Bulletin, 54(9), pp. 1361-1371.

Zalewski, M. et al., 2010. The impact of heavy metals on snail populations in polluted environments. Ecotoxicology and Environmental Safety, 73(4), pp. 287-294.

Bulletin of Natural Sciences Research
Vol. 15, No. 1, 2025, pp. 9-26.

DOI: https://doi.org/10.5937/bnsr15-55354
Original Scientific Paper

ASSESSMENT OF THE MEDICINAL PROPERTIES AND COMPONENTS OF THE BLEND OF THREE INDIGENOUS ESSENTIAL OILS (*Syzygium aromaticum*, *Monodora myristica*, AND *Xylopia aethiopica*) FROM AFRICA

SHOLA HEZEKIAH AWOJIDE[1], ABAYOMI GIDEON ADEYEMO[1*], AMINAT ADEBOLA ADEYEMO[1], ELIJAH TITILAYO BLESSING[1], ADEBANJO JACOB ANIFOWOSE[1], OMOLARA OLADIPO-OLALEKAN[1], EMMANUEL OLUWAFEMI ADENIYI[1], UMMUHANI TITILAYO ABDULAZEEZ[1]

[1]Department of Pure and Applied Chemistry, Faculty of Basic and Applied Sciences, Osun State University, Osogbo, Nigeria

ABSTRACT

The essential oils of *Syzygium aromaticum, Monodora myristica, and Xylopia aethiopica* have been used widely in Africa for medicinal purposes. This work is aimed at finding out the combined medicinal efficacy of the three essential oils. The crude EOs were extracted by the hydrodistillation method. The chemical components were determined by GC-MS analysis. The phytochemicals, antidiabetic, anti-inflammatory, and antioxidant activities were determined by standard analytical methods. The GC-MS analysis indicated eugenol (75.08%) as the major component in the EO of *S. aromaticum*, isocaryophyllene (29.36%) in the EO of *M. myristica*, isospathulenol (8.67%) in the EO of *X. aethiopica*, and eugenol (34.25%) in the blend of the EOs. The phytochemicals in all the EOs and the blend were at varying values. α-amylase and α-glucosidase inhibition showed that the EO blend with an IC_{50} value of 1250.69 µg/mL and 1080.56 µg/mL, respectively, had the highest inhibition compared with other EOs. *S. aromaticum* had the highest activity against the anti-inflammatory indicators. The least inhibitory activity for DPPH was recorded with *M. myristica* EO. *S. aromaticum* recorded the highest inhibitory efficacy against ABTS and nitric oxide assays, respectively. The blend recorded the highest inhibitory activity against lipid peroxidation, with an IC_{50} value of 827.22 µg/mL. The findings demonstrated that the crude EOs and the blend exhibited medicinal activities. However, the EO blend had higher potency.

Keywords: Essential oil, Blend, Antioxidant, Anti-inflammatory, Anti-diabetic.

INTRODUCTION

Naturally occurring substances that have a wide range of pharmacological effects can be found abundantly in plants (Samtiya et al., 2021). Products from plants are good sources of novel medications because of this attribute, as well as their exceptional chemical variety. Plant components and secondary metabolic profiles can also help with biological grouping, especially for plants that adjust morphologically to varying regions or settings (Samtiya et al., 2021).

Essential oils (EOs) are taken from the bark, leaves, roots, and stems of plants. It's also become more popular recently to employ natural or plant-based medicinal remedies. Essential oils are among the most abundant natural product families and possible sources of physiologically active compounds. They are also among the most promising and extensively studied plant secondary metabolites (Samtiya et al., 2021). When comparing to various natural medications, the percentage of essential oils used in these natural treatments is seventy percent (Yeshi et al., 2022). It has been possible to extract around 3000 essential oils thus far, most of them from the Rutaceae, Myrtaceae, Zingiberaceae, and Asteraceae families. Of these, over 300 essential oils are marketed in the culinary and perfume industries, and a value of over $15 billion is predicted by 2025 (Yeshi et al., 2022).

The naturally occurring substances included in essential oils provide them with a variety of advantageous qualities. In addition to their excellent tolerance and efficacy when tested in human and livestock trials for both the avoidance and management of ailments, such as tumours and the syndrome of obesity, essential oils and their byproducts have recently attracted interest (Ly et al., 2021). Furthermore, these naturally occurring compounds possess potent disinfectant, anti-allergic, antibacterial, anti-oxidant, and immune-stimulating qualities (Dawood et al., 2022).

Clove (*Syzygium aromaticum*) is a member of the family of Myrtaceae and has been demonstrated to have a variety of medicinal functions, such as antioxidant, anti-inflammatory, and anti-diabetic (Alghazzaly et al., 2022). Biologically active compounds abound in *S. aromaticum*, which also possesses anti-inflammatory effects and can control several medical

---

* Corresponding author: adeyemoabayomi0205@gmail.com

conditions such as drowsiness, coughing, constipation, indigestion, diarrhoea, and stomach dilation. It can also relieve the pain associated with gastrointestinal spasms and ease cramps in the uterus (Foda et al., 2022). The primary component of the extract from *Syzygium aromaticum* is eugenol, a phenolic chemical (Batiha et al., 2020). It contains a monoamine oxidation inhibitor, is neuroprotective, and has antioxidant properties (Batiha et al., 2020).

African nutmeg, or *Monodora myristica*, is a member of the Anonaceae family and is an aromatic plant that is underappreciated in Asia and Africa, yet is full of medicinal properties (Afolabi et al., 2021; Ekeanyanwu et al., 2021). It grows best in the West African evergreen forest and is native to West Africa. The flavorful powdered form of *M. myristica* seeds is used as a spice to enhance the sweetness of baked goods, stews, soups, and pastries (Irondi et al., 2023). Additionally, the powdered seed can be used to pepper soup as a stimulant to help ladies with constipation and postpartum passive uterine haemorrhage (Irondi et al., 2023). Anti-depressant, anti-inflammation, and anti-nociceptive are a few of the biological properties of *M. myristica* that have been scientifically documented (Ekeanyanwu et al., 2021).

Tall, slender, fragrant, evergreen tree of *Xylopia aethiopica* of the family of Annonaceae, can reach heights of 15 to 30 m and diameters of 60 to 70 cm (Yin et al., 2019). It is believed to originate natively in the African Savanna, especially in Senegal, Ghana, Nigeria, Cameroon, and Ethiopia, to mention a few countries (Yin et al., 2019).

X. aethiopica fruit is commonly called "Guinea pepper" or "Negro pepper," has numerous recognised applications in traditional medicine in several countries in West Africa. It has historically been employed in the treatment of numerous ailments, such as coughing, syphilis, insulin resistance, gastroenteritis, haemorrhoids, uterine fibroids, malaria, and amenorrhoea in females (Yin et al., 2019). Upon scientific examination, several of the alleged traditional applications were validated. These encompass, among other things, painkillers, anti-inflammatories, insulin-like substances, antiplasmodial, and antibacterial properties. In addition to the previously mentioned health advantages, *X. aethiopica* fruit is a well-known spice that is utilised because of its high nutritional content (Melo et al., 2021).

Despite the increased focus and encouragement, the majority of published literature on essential oils is centered on determining the therapeutic value of an individual oil (Leigh-de et al., 2021). In contrast, as the foundation of aromatic treatment is the procedure of blending various essential oils to generate an improved medicinal impact, essential oils are generally employed in numerous mixtures when used for aromatic medicine (Bunse et al., 2022). Increased antibacterial, antioxidant, anti-inflammatory and antihistaminic benefits can be achieved by blending essential oils, as the scientific evidence on aromatic treatments thoroughly indicates (Leigh-de et al., 2020). Prior research has indicated that certain manufactured and native essential oils provide medicinal properties when blended (Orchard et al., 2019).

People have endured years of suffering from a wide range of ailments and pains. One of the various methods for battling illnesses is the use of natural medicines to treat a range of ailments (Kruk et al., 2019). The trend towards natural pharmaceuticals is acquiring popularity in the wake of the launch of multiple important medications due to growing concerns about the increasing toxicities associated with primary pharmaceuticals (Akram et al., 2021). A further trend that is gaining more and more recognition is the propensity of essential oil molecules to demonstrate both synergistic and antagonistic behaviour. According to a recent investigation on cell behaviour, an oil's functionality may be influenced by the component proportions as much as by the components' identities (Cimino et al., 2021). To create an oil blend with unique benefits, there has been curiosity about blending, or mixing, different essential oils due to the potential for both synergistic and adverse effects. Future studies on the synergy, antagonistic effects, and complementary impact of essential oil blends will benefit from the present results, which will make it possible to compare the function of this mix with that of the individual essential oils and maybe other blends.

This blend of Eos is a mixture of essential oils from *S. aromaticum* bud, *M. myristica* seed, and *X. aethiopica* seed. While many of these distinct varieties of EOs and their active components are well-known to offer different medicinal benefits, we looked to investigate the effect of essential oil blends on indicators associated with diabetes, inflammatory conditions, and oxidative damage.

EXPERIMENTAL

Materials and methods

Plant Materials

African Nutmeg (*Monodora myristica*) seeds, Clove bud *(S. aromaticum*), *and* Negro pepper pod (*X. aethiopica)* were picked from an orchard at Ijebu-Ode, Ogun State, after their identification at the Department of Plant Biology, Osun State University, Osogbo, Osun State, Nigeria.

Sample Pretreatment

Extraction of Essential Oils

The powdered seeds (10 g) were extracted using the hydro-distillation process. The seed was pulverized into smaller particles to enhance its surface area, and thereafter put into a 1000 mL round-bottom flask using a funnel. Following that, 200 mL of distillate water was introduced. Subsequently, the solution was agitated using a glass stirring rod. The heating mantle was linked to an electrical outlet and activated. The water began to flow through the condensation chamber of the

Clevenger apparatus, which was then attached to a flask. The flask was thereafter put on the heating mantle. The mixture underwent heating for 5 hours, following which the resulting extract was obtained. The yield was then estimated.

GC-MS Analysis

A flame ionisation detector (FID) and an HP-5MS (30m × 0.25 mm x 0.25 μm) capillary column were fitted to an Agilent 6890N apparatus for gas chromatography and mass spectrometry analysis. An Agilent Technologies 5973N mass spectrometer was used to identify the constituents of the essential oil. The oven's thermostat was set at the beginning at 60°C for one minute, followed by a ramp of 10°C min−1 to 180°C for one minute, and a ramp of 20°C min−1 to 280°C for fifteen minutes. These were the GC configurations. At 270°C, the injector temperature was kept constant. The samples (1 µL) were split 1:10 and injected neat. Helium served as the carrier gas, flowing at a rate of 1.0 mL min1. At two scans per second, spectra were scanned from 20 to 550 m/z. Most of the substances were identified using gas chromatography via comparison of their retention indexes to those reported in the scientific literature or to real chemicals that were kept in our testing facilities. The retention indices were calculated using the same operating parameters and compared to a homologous sequence of n-alkanes (C_8–C_{24}). To confirm the identity, their mass spectra on both columns were compared to mass spectra from published works or those kept in the NIST 05 and Wiley 275 libraries. After calculating constituent proportions using GC peak areas, adjustment variables were not used (Wesołowska et al., 2019).

Preparation of the Blend

The blend was prepared by mixing equal masses of the three essential oils in a ratio of 1:1:1.

Quantitative Phytochemical Analysis

Total phenolic content (TPC)

The quantification of the phenolic content was performed with a spectrophotometer (Kim et al., 2022). The essential oil (0.1 mL) was combined with 1 mL of Phenol Folin–Ciocalteu combination, followed by the addition of 9 mL of pure distilled water. Following agitation, 10 mL of 7% Na_2CO_3 was introduced, followed by rapid dilution with fresh distilled water, generating 25 mL total volume. The entire mixture was kept at 23°C for 90 min, and the absorbance was measured at a wavelength of 750 nm. The complete experiment was done thrice to guarantee precision with the standard gallic acid. TPC was quantified as mg GAE (gallic acid equivalents)/gram dry weight extract/fraction.

Total flavonoid contents (TFC)

The spectrophotometric approach is the most straightforward and economical way to determine a plant's flavonoid content (Park et al., 2008). The reaction combination was generated in an experiment tube by the sequential mixture of 0.30 mL essential oil, 0.15 mL of $NaNO_2$ (0.5 mol/L) coupled with 0.30 M $AlCl_3 \cdot 6H_2O$ and 3.40 mL methanol (30%). The mixture was held for 5 min, after which 1 mL of 1 M NaOH was blended into it. At 506 nm wavelength, the transparency of the reaction mixture was monitored.

Total tannin content (TTC)

With a few minor adjustments, the Ejikeme et al. (2014) procedure was used to quantify the tannin content. This method involved soaking 500 mg of EO in 60 mL of distilled water. After being shaken by a machine for one hour, the sample was screened. In a volumetric flask with a capacity of 500 mL, the filtrate was adjusted to the appropriate level. 5 mL of the aforementioned filtrate was combined with 2 mL of 0.1 M $FeCl_3$ and potassium ferricyanide (0.006 M) prepared in 0.1 M HCl. Using a wavelength spectrophotometer, the intensity of absorption was measured at 200 nm with a standard gallic acid curve. The results were expressed as milligrams of gallic acid equivalents (GAE) per gram of dry plant material.

Determination of total proanthocyanin

Proanthocyanin was performed with the technique outlined by Chen et al. (2016). The combination was left to stand for 15 minutes after being blended with 0.5 mL of the 0.1 mg/mL extract solution, 3 mL of the 4% vanillin-methanol solution, and 1.5 mL of HCl. A 500 nm measurement was made of the absorbance. The final concentration of 0.1 mg/mL was used to analyze the extract samples in terms of catechin acid equivalent.

Determination of total Alkaloids

The EO (0.1 mL) was mixed with 200 mL of 10% acetic acid in ethanol. The mixture was allowed to sit for 4 minutes before being filtered. After concentrating the resulting filtrate in a water bath, NH_4OH was introduced drop by drop until the precipitation process was finished. The residue was washed using diluted NH_4OH. When it had dried, the residue was measured (Elshafie et al., 2017).

Determination of Saponin

Using the spectrophotometric approach outlined by Elshafie (2017), the saponin content was ascertained. Isobutyl alcohol, also known as but-2-ol, was poured into a beaker containing around 2 g of EO. To the mixture, 40% magnesium carbonate ($MgCO_3$) solution was added after filtration. To 1 mL of the solution, 2 mL of $FeCl_3$ solution was added, and the remaining volume was adjusted with distilled water. The absorbance was measured at 380 nm using a SpectrumLab70 spectrophotometer after this had been permitted to remain for 30 minutes to generate the colour.

Quantitative Test for Terpenoids

For 24 hours, 9 mL of ethanol and 100 mg of the extract were combined (Elshafie et al., 2017). The filtrate formed by adding 10 mL of petroleum ether was extracted using a separating funnel. After being divided into glass vials and carefully weighed, the ether extract was left to dry entirely at room temperature for 10 minutes (T_W). The total terpenoids present were then estimated:

$$T_G - T_W / T_G \times 100. \quad (1)$$

where T_G = Initial weight, T_W = Final weight.

Anti-Oxidant Analysis

DPPH radical scavenging assay

According to Kim et al. (2022), the DPPH (2,2-diphenyl-1-picrylhydrazyl) radical scavenging assay (DRSA) was used to examine the extracts' capacity to scavenge free radicals. A 0.1 mM solution of DPPH in methanol was made, and 1.6 mL of EO in methanol was combined with 2.4 mL of this solution. The mixture was kept for 30 minutes in the dark. Using spectrophotometry, the absorbance was obtained at 517 nm. The % of DPPH radical scavenging activity (%K) was determined:

$$(\%K) = \{(J_0 - J_1)/J_0\} \times 100. \quad (2)$$

J_1= absorbance of the essential oil/standard, and J_0= absorbance of the control.

ABTS radical scavenging activity

According to Schaich et al. (2015), the 2,2-azino-bis (3-ethylbenzothiazoline-6-sulphonic acid) assay was carried out. $K_2S_2O_8$ (2.45 mM) solution and ABTS solution (7 mM) were reacted in a ratio of 1:1 and left in the dark for a night to produce a dark liquid comprising ABTS radical cations. Before being used in the experiment, the thermostat was adjusted to 30°C, and the ABTS radical cation was diluted with methanol (50%) to get absorbance at 745 nm. Calculation of the % inhibition was done using:

$$\text{Inhibition effect}(\%) = [(\text{control absorbance} - \text{sample absorbance})/(\text{control asbsorbance})] \times 100. \quad (3)$$

Lipid peroxidation inhibition assay

The procedure outlined by Ayala et al. (2014) was followed to determine the lipid peroxidation inhibition assay (*LPI*). Mixtures containing 100 µL, 10 mM FeSO4, 100 µL, 0.1 mM Ascorbic acid, and 0.3 mL of EO were mixed and left for twenty minutes. The mixture was incubated at 37 °C, after which 1.5 mL of (1%) thiobarbituric acid and 1 mL of (28%) trichloroacetic acid were added. After a final 15 minutes of heating at 100 °C, the solution was left to cool at 25 °C, and absorbance was taken at 532 nm. Using the following formula, the percentage inhibition of lipid peroxidation (% *LPI*) was determined:

$$\%LPI = \frac{(\text{Control absorbance} - \text{Sample absorbance}) \times 100}{\text{Control absorbance}}. \quad (4)$$

Nitric oxide scavenging assay

The Griess reagent approach developed by Bhaskar and Balakrishnan (2009) was employed to analyse the extracts' ability to scavenge nitric oxide and their antioxidant activity. The Griess reagent was created by adding a comparable quantity of $C_6H_8N_2O_2S$ (1%) in H_3PO_4 (5%) and naphthylenediamine (0.1%) in distilled water. A batch of 10 mM $Na_2[Fe(CN)_5NO]$, prepared in saline buffered with phosphate, weighing 50–800 µg/ml, was given to each EO. Following treatment with 1 mL of Griess reagent, the mixture was left for three hours and subjected to spectrophotometric testing at 546 nm.

$$\text{Nitric oxidescavenging activity } (\%) = \\ = \frac{(CTR \text{ absorbance} - SPL \text{ absorbance}) \times 100}{\text{Control absorbance}}. \quad (5)$$

CTR= control, *SPL*= sample.

Anti-inflammatory Activity

Lipoxygenase enzyme inhibition assay

The pH borate buffer solution, stop solution, enzyme concentration, and substrate concentration were all optimised for the lipoxygenase inhibition experiment. Following optimisation, lipoxygenase activity was measured using a UV-Vis spectrophotometer device (Alzarea et al., 2021). The parameters included methanol as the solution stop, linoleic acid as the substrate of choice (900 µM), lipoxygenase (5,000 units/mL), and borate buffer (0.2 M, pH 8.5). This equation was used to determine the lipoxygenase inhibition value's inhibition percentage:

$$\%\text{Lipoxygenase inhibition} = \frac{(E-F)-(G-H) \times 100\%}{(E-F)}. \quad (6)$$

The variables *E, F, G,* and *H* in this equation represent the absorbance of the blank solution (containing the enzyme), the control blank solution (containing the enzyme but lacking the enzyme), and the standard/sample solution (containing the enzyme but lacking the enzyme).

Xanthine oxidase (XO) inhibition assay

Using a spectrophotometer, the xanthine oxidase inhibitory activity was measured as stated by Alzarea et al. (2021). The assay combination was made up of 50 µL of essential oil (1 mg/mL in phosphate buffer), 150 µL of phosphate buffer (0.066M; pH, 7.5), and 50 µL of enzyme solution (0.28U/mL). Following a three-minute pre-incubation period at room temperature (25°C), 250 µL of the substrate solution (xanthine, 0.15 M in the same buffer) was added to start the reaction. Additionally, an unaltered solution devoid of enzymes was made. At 295 nm, the response was observed for three minutes, during which time the absorbance (V_0) was noted. As a negative control, phosphate buffer was utilized (activity of the enzyme without essential oil). ibuprofen served as the positive control.

Inhibition (%) = [(V_0 ctl- V_0 spl) X 100]/ V_0 ctl.

V_0 ctl = enzyme activity in the absence of essential oil.

V_0 spl = enzyme activity when there is essential oil or ibuprofen.

Membrane Stabilizing Assay

The methodology of Oyedapo et al. (2010) was adjusted to determine the red blood cell membrane stability capability. The mixture was made of 1.0 mL of EOs, 1.0 mL of hyposaline, and 0.4 mL of 0.14 M phosphate buffer at pH 7.6. To the mixture, 0.5 mL of 2.5% (v/v) erythrocyte was included. Thirty minutes were spent incubating the reaction mixture at 56 °C, after which it was cooled and then centrifuged for ten minutes at 704 rpm. The tube containing no essential oil at all served as the control. At 560 nm, the absorbance was measured while the control lacked erythrocytes.

$$\%\text{Membrane Stability} = \frac{\{\text{abs test} - \text{abs drug control}\} \times 100}{\text{Abs drug} - \text{Abs drug control}}. (7)$$

Anti-diabetes Activity

α-Amylase inhibition assay

The assay used to assess the α-amylase inhibitory activity was modified from McCue and Shetty (2005) approach. Porcine pancreatic α-amylase solution (PPA) containing 1.3 U/mL and 200 µL of 0.02 M sodium phosphate buffer (pH 6.9; 6.7 mM NaCl) are both included in the reaction mixture. After pre-incubating the reaction medium for five minutes at 37°C, 200 µL of the 0.4% starch solution in the buffer mentioned above was added, and the mixture was incubated for ten minutes at 37°C. After adding 600 µL of $C_7H_4N_2O_7$ solution to the reaction, it was heated to boiling for seven minutes and cooled in cold water. After adding diluting with 1 mL of distilled water, the absorbance was taken at 540 nm. As a positive control, acarbose, a commercial inhibitor, was utilized at concentrations between 50 and 800 µg/mL. Instead of using a substrate, a blank buffer solution was employed. The control tube with total enzyme activity was the one containing the enzyme solution without any essential oil or aspartame. This equation was used to determine the percentage of inhibition of α-amylase:

$$\text{Inhibition of } \alpha - \text{amylase activity}(\%) = ((AD - AE)/AD) \times 100. (8)$$

Here, *AE* represents the tested sample's absorbance, and *AD* (100% enzyme activity) represents the absorbance of the control (acarbose or essential oil).

α-glucosidase inhibitory assay

A modified version of Tao et al. (2013) approach was used to test inhibitory activity on α-glucosidase. 200 µL of a crude rat intestinal α-glucosidase enzyme solution (adjusted to 0.2 U/mL as initial concentration in phosphate buffer 67 mM, pH 6.8) was combined with 200 µL of the sample, which included solutions of essential oil (50-800 µg/mL) or acarbose (50-800 µg/mL), a positive control. Additionally, 1 mL of phosphate buffer was added. After pre-incubating the mixture for 10 minutes at 37°C, 300 µL of p-nitrophenyl-α-D-glucopyranoside solution (10 mM) was included, and the mixture was kept for 40 minutes at 37°C. In addition, 3 mL of sodium carbonate Na_2CO_3 (100 mM) was added to the mixture, and the reaction was brought to an end. The released p-nitrophenol's absorbance was determined at 405 nm. Substrate was replaced with buffer solution as a blank. The control tube with total enzyme activity was the one containing the enzyme solution without any essential oil or aspartame.

Inhibition of *α*-glucosidase activity (%) = ((*AD*-*AE*)/*AD*) *100

In this instance, *AE* = absorbance (sample), *AD* = absorbance of the control (100% enzyme activity) (essential oil or acarbose).

Statistical Analysis

The result was presented as the mean of three readings. The data obtained were subjected to Analysis of variance (ANOVA). The values were significantly different when $P<0.05$.

NUMERICAL RESULTS

Yield

S. aromaticum, M. myristica, and *X. aethiopica* essential oils were extracted with a yield of 11.34%, 2.74% and 1.44% respectively.

GC-MS Analysis

The analysis of the EO of *S. aromaticum* through GC-MS is shown in Table 1. Twenty-nine compounds were observed from the essential oil of *S. aromaticum,* of which the major components are eugenol (75.08%) and caryophyllene Oxide (4.83%). The GC-MS analysis of *M. myristica* obtained in Table 2. revealed the major constituents to be isocaryophyllene (29.36%), germacrene D-4-ol (20.31%), germacrene D (9.72%), and oplopanone (6.681%). Thirty-one compounds were obtained from the analysis of *X. aethiopica* essential oil, and the main compounds were isospathulenol (8.67%), chavibetol (6.99%), β-elemene (6.76%), and calamenene (5.23%) as revealed in Table 3. The GC-MS result of the blend of essential oils is obtained in Table 4, which revealed the main components as eugenol (34.25%) and chavibetol (16.57%). This showed a decrease in the value of eugenol in the blend compared to what was obtainable in *S. aromaticum,* but an increase in the value of chavibetol in the blend compared to what was found in the *X. aethiopica*.

Table 1. Components from GC-MS Analysis of *S. aromaticum*.

Name of Compounds	% Composition	Retention Time
Eugenol	75.08	3.408
Caryophyllene Oxide	4.83	4.947
Vanillin	2.30	3.946
Trans-Anethole	1.79	9.902
Homoranillyl Alcohol	1.67	5.857
Vanilla Ethyl ether	1.51	11.419
Sinapaleolehyde	1.45	5.817
1,3-Thiazolidin-4-ones-	1.44	11.213
Garyophyilene	0.94	5.336
Beta-caryophyllene Oxide	1.24	5.410
Pulegone	0.74	5.073
1-(2-(2-(tert-Butyl)phenoxyl)ethyl)-1-3-dihydro-2H-benzo[d]imidazole-2-thione	0.51	11.304
2-[3-hydroxy-4-methoxyphenyl)]-hydrazine-boxamide	0.46	5.748
α-Acoreno	0.41	6.618
Nor Camphorone	0.31	4.054
Tricyclo[4.1.0.0(3,7)] heptanes	0.27	11.476
2-methoxy-4-(2-propenyl) phenol	0.26	3.534
Benzoyl benzonate	0.24	5.960
4-hydroxy quinoline	0.22	5.697
Epianastrophin	0.22	6.229
Barpisoflavone A, 3Me derivatives	0.21	10.938
(1R,7S,E)-7-Isopropyl-4-, 10-dimethylenecyclodec-5-enol	0.20	6.068
Indole	0.15	5.021
Phenyl 4-methoxy benzoyl ether	0.15	11.636
Thiazolidin-4-one,3-(2-furfury)-5-(2,3-dihydro-2-oxo-3-indoly)-2-Thioxo	0.13	11.522

Table 2. Components from GC-MS analysis of *M. myristica*.

Name of Compounds	% Composition	Retention Time
Isocaryophyllene	29.36	3.677
Germacrene D-4-ol	20.31	4.729
Germacrene D	9.71	4.077
Oplopanone	6.68	5.782
Farnesoic acid	4.66	6.297
Camphor	3.19	3.516
Valerenol	2.89	5.971
Cuparene	2.42	5.073
Eugenol	2.16	3.242
2-methyladamantane	2.15	3.459
Farnesol	2.13	4.174
Farnesol	2.08	4.317
Isospathulenol	1.81	6.223
Muurola-4 (14),5-diene, cis-	2.51	5.565
2-caren-4-ol	1.53	3.711
Isoniazid pyruvate	1.48	14.119
n-Hexadecanoic acid	1.45	7.087
Geraniol	1.14	7.121
2-pentadecanone	1.12	5.645
Docosatetraenoic acid	1.11	8.540
Geranic acid or Chrysanthemic acid	1.10	3.745
Alpha-cadinene T1n3	1.05	4.289
2-(Propoxycarbonyl)benzoic acid	0.94	10.011

Table 3. Components from GC-MS analysis of the *X. aethiopica*.

Name of Compounds	% Composition	Retention Time
Isospathulenol	8.67	5.147
Chavibetol	6.99	5.010
β-Elemene	6.76	3.488
Calamenene	5.23	4.615
Muurolol	4.62	5.296
Germacrena D	4.53	4.106
Caryophyllene oxide	4.34	4.809
γ-Curcumene	3.86	6.566
Oxepine, 2,7-dimethyl-	3.72	6.354
Aromadendrene	3.07	6.435
Spathulenol	2.98	4.787
16.beta, H-kauran-16-ol	2.85	8.575
α-Farnesene	2.81	7.533
Cic-2-,alpha,-Bisabolene epoxide	2.64	5.691
2,6,10,14,18-Pentamethyl-2,6,10,14,18-eicosapentaene	2.62	7.402
Alloaromadendrene epoxide	2.61	5.828
α-CadineneT1n3	4.07	4.060
3-Oxatricyclo[5.1.0.0^{2,4}]octane, 4,6,6-trimethyl-2-[(1E)-3-methyl-1,3-butadien-1-yl	2.54	6.721
(4*Z*,8*E*)-*N*-(3-chlorophenyl)bicyclo[10.1.0]trideca-4,8-diene-13-carboxamide	2.31	6.188
Aromandendrene	2.21	5.239
FenchoneT1n3	2.21	6.835
Isoaromadrene epoxide	2.07	5.925
Caryophyllene	1.94	3.671
Salvial-4(14)-en-1-one	1.78	4.867
Humulene	1.64	3.900
Cadinol	1.52	5.193
Icosa-9, 11-diyne	1.47	6.892

Table 4. Components from GC-MS analysis of the Blend.

Name of Compounds	% Composition	Retention Time
Eugenol	34.25	3.345
Chavibetol	16.57	4.489
Germacrene D	4.62	4.112
δ-Cadinene	3.60	4.489
Caryophyllene	2.70	3.700
[1,1^1-Bipheny1]-2,2^1-diol,3,3^1-dimethoxy-5,5^1-di-2-propenyl-	2.45	10.726
.tau.Muurolol	2.36	5.256
4,8*a*-dimethyl-6-prop-1-en-2-yl-2,3,5,6,7,8-hexahydro-1*H*-naphthalen-2-ol	2.92	6.309
Anethole	2.21	9.885
2-Isopropyl-5-methyl-9-methylene[4.4.0]dec-1-ene	2.19	5.170
Di(2-ethylhexyl)phthalate	1.61	10.017
α-CadineneT1n3	1.56	4.318
α-Gurjunene	1.40	5.096
[4E,8E,13E]-1-(2-Hydroxyethyl)-1,5,9-trimethyl cyclotetra decatriene.	1.00	7.367
Kaur-16-en-18-al,(4.alpha)-	0.97	8.684
M-Camphorene	0.89	7.505
Sabinene hydrate, trans-	0.89	3.591

Phytochemical Analysis

The findings of the quantitative analysis of the phytochemical characteristics of crude essential oils and their blend are displayed in Table 5. All of the extracted crude essential oils of *S. aromaticum*, *M. myristica*, *X. aethiopica*, and the blend contained phenolic content. *S. aromaticum* had the highest phenolic value of 182.46 mg GAE/g, while *M. myristica* had the lowest phenolic content of 144.01 mg GAE/g. The blend had higher phenolic and flavonoid content than *M. myristica* EO. *X. aethiopica* had the highest flavonoid value of 43.48 mg CE/g, whereas *M. myristica* had the lowest flavonoid content of 24.34 mg CE/g. Tannin content of 17.41 mg GAE/g was highest in *S. aromaticum,* and it was the only EO with higher tannin than the blend, while the least tannin was found in *M. myristica* (9.85 mg GAE/g). The value of Proanthocyanin ranged between 8.15 to 9.91 mg CE/g, where *S. aromaticum* recorded the highest value, but the lowest in the blend. *M. myristica* had the highest alkaloid content of 8.70 mg/g, but *S. aromaticum* essential oil had the lowest alkaloid content of 6.30 mg/g; the blend recorded a higher alkaloid content than *S. aromaticum* and *X. aethiopica*. Saponin was highest in *M. myristica* (3.30 mg/g) and least in the blend (1.70 mg/g). The highest terpenoid was recorded in *X. aethiopica* with a value of 20.00 mg/g, while the lowest value was recorded in the essential oil of *M. myristica* (16.30 mg/g).

Table 5. Quantitative Phytochemical Components of the Essential Oils and the Blend.

Essential Oil	*Syzygium aromaticum*	*Monodora myristica*	*Xylopia aethiopica*	Blend
Phytochemicals				
Phenolic content (mg GAE/g Extract)	182.46 ± 1.23^{d}	144.01 ± 1.37^{a}	175.68 ± 2.21^{c}	161.02 ± 2.30^{b}
Flavonoid (mg CE/g Extract)	39.03 ± 0.72^{c}	24.34 ± 0.52^{a}	43.48 ± 0.35^{d}	30.02 ± 0.32^{b}
Tannin (mg GAE/g Extract)	17.41 ± 0.33^{d}	9.85 ± 0.42^{a}	11.32 ± 0.37^{b}	14.97 ± 0.35^{c}
Proanthocyanin (mg CE/g Extract)	9.91 ± 0.57^{c}	8.45 ± 0.18^{bc}	9.89 ± 0.36^{c}	8.15 ± 0.41^{a}
Alkaloid (mg/g)	6.30 ± 0.11^{a}	8.70 ± 0.07^{d}	6.70 ± 0.14^{b}	8.00 ± 0.37^{c}
Saponin (mg/g)	2.70 ± 0.01^{c}	3.30 ± 0.02^{d}	2.30 ± 0.01^{b}	1.70 ± 0.03^{a}
Terpenoid (mg/g)	18.70 ± 0.58^{b}	16.30 ± 0.23^{a}	20.00 ± 0.27^{c}	17.00 ± 0.32^{a}

*Values here are the mean ± standard deviation. Means with different letters in a row are significantly different at $p < 0.05$.

Antioxidant Activities

DPPH

The percentage inhibitory activities of the crude essential oils, blend, and the standards (gallic acid and ascorbic acid) against DPPH were recorded in Table 6. The least percentage inhibitory activity with a concentration of 100 µg/mL was 7.73% observed in the crude essential oil of *M. myristica*, while the highest inhibitory activity value at 1600 µg/mL was recorded in the crude essential oil of *X. aethiopica* (71.75%). It was also observed that gallic acid, with an inhibition of 85.22% at a concentration of 1600 µg/mL, had a higher percentage inhibitory activity against DPPH than the crude essential oils and ascorbic acid. The blend showed a higher DPPH scavenging activity than *M. myristica* at all concentrations, while other crude EOs recorded a higher activity. Table 7 recorded the IC_{50} values of the crude essential oils, the blend, and the standards. It was observed that *X. aethiopica*, with the least IC_{50} value of 796.56 µg/mL, had a higher DPPH inhibition than other crude essential oils, the blend as well as ascorbic acid. *M. myristica*, with an IC_{50} of 1119.35 µg/mL, had the least DPPH inhibition, with only it having a higher IC_{50} than the blend.

ABTS

The percentage inhibitory activities of ABTS radical scavenging showed that *S. aromaticum* had a higher inhibition of 42.87% at a concentration of 1600 µg/mL, while the blend had the least inhibition of 34.90% (Table 8). *S. aromaticum* with an IC_{50} of 1746.96 µg/mL had a higher inhibition than other crude essential oils, while the blend of the essential oil with an IC_{50} of 2309.58 µg/mL showed the least ABTS radical scavenging activity (Table 9). Gallic acid, having an IC_{50} of 1471.11 µg/mL, showed a higher ABTS radical scavenging inhibition than all the essential oils and ascorbic acid.

Lipid Peroxidation

The percentage of lipid peroxidation ranged from 69.00 to 66.44% with a concentration of 1600 µg/mL. The blend recorded the highest inhibition of 76.80% compared to the crude EOs (Table 10). Table 11. displays the IC_{50} observed for the essential oils and standards. The values ranged from 604.39 to 922.00 µg/mL, where the blend of essential oils had the highest lipid peroxidation inhibition.

Table 6. Percentage Inhibitory Activity of DPPH by the essential oils, Blend and Standards.

Samples	*S. aromaticum*	*M. myristica*	*X. aethiopica*	Blend	Gallic Acid	Ascorbic Acid
Concentration (μg/mL)						
100	9.95±1.52^{b}	7.73±0.11^{a}	14.09±0.65^{c}	10.32±0.65^{b}	13.48±0.23^{c}	9.42±0.11^{b}
200	24.53±0.22^{b}	24.42±0.32^{b}	31.93±0.76^{d}	23.05±0.11^{a}	30.02±0.22^{d}	26.34±0.65^{c}
400	38.82±0.32^{b}	33.08±0.87^{a}	49.16±0.87^{d}	34.07±0.97^{a}	48.47±1.19^{d}	45.33±0.87^{c}
800	54.36±0.65^{b}	47.78±1.52^{a}	57.43±0.87^{b}	48.09±3.90^{a}	66.08±0.98^{c}	56.66±0.22^{b}
1600	67.23±0.65^{b}	60.95±1.30^{a}	71.25±0.43^{c}	61.26±2.38^{a}	85.22±0.97^{d}	70.13±0.65^{c}

*Values here are the mean ± standard deviation. Means with different letters in a row are significantly different at $p<0.05$.

Table 7. IC_{50} for DPPH Radical Scavenging Potential of the Essential Oils, Blend, and Standards.

EO/Standards	Concentration IC_{50}(μg/mL)
S. aromaticum	957.35±5.32^{d}
M. myristica	1119.35±4.12^{e}
X. aethiopica	796.56±6.17^{b}
Blend	1092.58±7.32^{e}
Gallic Acid	662.56±8.21^{a}
Ascorbic Acid	871.71±4.81^{c}

*Values here are the mean ± standard deviation. Means with different letters in a row are significantly different at $p < 0.05$.

Table 8. Percentage Inhibitory Activity of ABTS by the Essential Oils, Blend, and Standards.

Samples	*S. aromaticum*	*M. myristica*	*X. aethiopica*	Blend	Gallic Acid	Ascorbic Acid
Concentration (μg/mL)						
100	3.79±0.43^{c}	3.26±1.18^{c}	0.83±0.97^{a}	1.52±0.86^{a}	5.46±1.29^{d}	2.20±0.10^{b}
200	13.88±0.32^{bc}	12.37±0.5^{b}	9.48±1.39^{a}	11.46±1.29^{b}	14.11±0.21^{c}	11.31±0.97^{b}
400	26.40±1.07^{c}	24.28±1.0^{bc}	18.29±0.75^{a}	17.75±0.86^{a}	27.16±0.64^{c}	21.70±0.42^{b}
800	34.14±0.43^{c}	31.49±0.7^{b}	27.39±0.75^{a}	26.25±0.64^{a}	40.06±0.21^{d}	31.34±1.18^{b}
1600	42.87±0.11^{c}	41.40±2.3^{c}	37.71±0.75^{b}	34.90±1.72^{a}	49.01±0.86^{d}	41.65±0.32^{c}

*Values here are the mean ± standard deviation. Means with different letters in a row are significantly different at $p < 0.05$.

Table 9. IC_{50} Values for ABTS Radical Scavenging Potential of the Essential Oils, Blend, and Standards.

EO/Standards	Concentration IC_{50}(μg/mL)
S. aromaticum	1746.96±8.10^{b}
M. myristica	1891.36±5.20^{d}
X. aethiopica	2054.45±3.33^{e}
Blend	2309.58±6.12^{f}
Gallic Acid	1471.11±3.42^{a}
Ascorbic Acid	1803.04±6.21^{c}

*Values here are the mean ± standard deviation. Means with different letters in a row are significantly different at $p < 0.05$.

Table 10. Percentage Inhibitory Activity of Lipid Peroxidation by the Crude Essential Oils, Blend, and Standards.

Samples	*S. aromaticum*	*M. myristica*	*X. aethiopica*	Blend	Gallic Acid	Ascorbic Acid
Concentration (μg/mL)						
100	8.26±1.20^{b}	5.40±0.75^{a}	8.40±0.60^{b}	7.90±0.75^{b}	9.22±0.15^{c}	8.47±1.20^{b}
200	21.61±1.20^{b}	17.70±1.05^{a}	26.40±0.15^{c}	23.90±1.20^{b}	35.80±0.00^{d}	26.59±0.75^{c}
400	42.70±0.75^{b}	37.30±3.90^{a}	47.00±2.10^{c}	43.54±0.75^{b}	59.00±0.75^{d}	48.00±1.05^{c}
800	59.90±1.35^{b}	57.20±0.60^{a}	60.50±1.65^{c}	61.90±1.80^{c}	65.25±0.35^{d}	64.40±0.30^{d}
1600	75.42±1.80^{c}	69.00±3.15^{a}	71.06±2.55^{b}	76.80±2.55^{c}	86.44±0.30^{e}	79.90±0.80^{d}

*Values here are the mean ± standard deviation. Means with different letters in a row are significantly different at $p < 0.05$.

Table 11. IC$_{50}$ Values for Lipid Peroxidation Potential of the Essential Oils, Blend, and Standards.

EO/Standards	Concentration IC$_{50}$(µg/mL)
S. aromaticum	834.88 ± 5.12^{e}
M. myristica	922.00 ± 2.24^{d}
X. aethiopica	837.22 ± 4.28^{c}
Blend	827.22 ± 3.13^{c}
Gallic Acid	604.29 ± 7.12^{a}
Ascorbic Acid	740.48 ± 5.24^{b}

*Values here are the mean ± standard deviation. Means with different letters in a row are significantly different at $p < 0.05$.

Nitric Oxide

The percentage inhibitory activities of each crude essential oil, the blend, and the standards against nitric oxide were recorded in Table 12. The percentage inhibition of nitric oxide at 1600 µg/mL ranges from 52.92 to 65.89% with the essential oil of *S. aromaticum* recording the highest inhibition of 57.65% of nitric oxide among the essential oils. The IC$_{50}$ values obtained from the inhibition of nitric oxide by all of the essential oils, as well as the standards, are presented in Table 13. The crude essential oil of *S. aromaticum* (1104.62 µg/mL) exhibited the highest level of inhibitory action, whereas the essential oil of *M. myristica* (1335.00 µg/mL) had the lowest inhibitory action.

Table 12. Percentage Inhibitory Activity of Nitric Oxide by the Crude Essential Oils, Blend, and Standards.

Samples Concentration (µg/mL)	*S. aromaticum*	*M. myristica*	*X. aethiopica*	Blend	Gallic Acid	Ascorbic Acid
100	13.92 ± 0.42^{d}	9.97 ± 0.74^{a}	10.94 ± 0.42^{a}	11.39 ± 2.12^{b}	13.87 ± 0.53^{d}	12.44 ± 0.64^{c}
200	26.37 ± 0.85^{c}	18.22 ± 1.38^{a}	22.11 ± 1.80^{b}	19.72 ± 1.59^{a}	28.71 ± 0.11^{d}	23.61 ± 0.53^{bc}
400	38.76 ± 0.74^{c}	26.39 ± 0.85^{a}	32.38 ± 0.42^{b}	31.03 ± 0.64^{ab}	39.51 ± 0.53^{d}	32.68 ± 0.85^{b}
800	50.37 ± 1.06^{d}	42.20 ± 2.65^{a}	45.37 ± 0.11^{c}	44.45 ± 1.17^{b}	50.30 ± 0.53^{d}	44.98 ± 0.00^{b}
1600	57.65 ± 0.95^{c}	54.42 ± 0.42^{b}	55.10 ± 0.74^{bc}	54.95 ± 0.74^{b}	65.89 ± 0.74^{d}	52.92 ± 0.21^{a}

*Values here are the mean ± standard deviation. Means with different letters in a row are significantly different at $p < 0.05$.

Table 13. IC$_{50}$ Values for Nitric Oxide Ion Scavenging Potential of the Crude Essential Oils, Blend, and Standards.

EO/Standards	Concentration IC$_{50}$(µg/mL)
S. aromaticum	1104.62 ± 6.32^{b}
M. myristica	1335.00 ± 4.18^{d}
X. aethiopica	1289.23 ± 5.36^{c}
Blend	1285.19 ± 7.46^{c}
Gallic Acid	979.00 ± 6.12^{a}
Ascorbic Acid	1326.67 ± 8.32^{d}

*Values here are the mean ± standard deviation. Means with different letters in a row are significantly different at $p < 0.05$.

Anti-inflammatory Activities

Lipoxygenases Inhibition

The percentage inhibitory activities of lipoxygenases by the crude essential oils, the blend, and the standard were observed in Table 14. The result showed that *S. aromaticum,* with a percentage inhibition of 67.11% had the highest activity of all the essential oils at 1600 µg/mL. The essential oil blend exhibited the least inhibition of lipoxygenases at all concentrations. The IC$_{50}$ values obtained for the lipoxygenase assay with all of the essential oils, as well as the standard, are presented in Table 15. *S. aromaticum* with an IC$_{50}$ of 859.63 µg/mL showed a higher inhibition than the rest of the crude essential oils, while the blend with an IC$_{50}$ of 3093.46 µg/mL recorded the least lipoxygenase inhibition. The standard ibuprofen had an IC$_{50}$ of 767.67 µg/mL, which indicated a higher lipoxygenase inhibition than all the crude and the blend of the essential oils.

Membrane Stability Assay

At a concentration of 1600 µg/mL, the membrane stability inhibition ranged from 36.96 to 78.26%. The blend, with a percentage inhibition of 40.22%, showed a superior inhibition than *M. myristica* (36.96%). *S. aromaticum* recorded membrane stability inhibition of 45.65%, which was the highest percentage of inhibitory activity of all the crude essential oils and the blend. Table 16. It was also revealed that the standard (Ibuprofen) with a percentage inhibition of 78.26% had higher inhibition than all the crude essential oils and the blend at a concentration of 1600 µg/mL. Table 17. revealed the IC$_{50}$ of the membrane stability assay of the essential oils and ibuprofen. *S. aromaticum,* having the least IC_{50} of 1134.90 µg/mL, showed a higher membrane stability assay than the rest of the crude essential oils, as well as the blend.

Table 14. Percentage Inhibitory Activity of Lipoxygenases by the Crude Essential Oils, Blend, and Standard.

Samples Concentration (µg/mL)	*S. aromaticum*	*M. myristica*	*X. aethiopica*	Blend	Ibuprofen
100	25.12 ± 0.70^{d}	19.26 ± 0.58^{b}	22.07 ± 1.52^{c}	5.95 ± 0.94^{a}	25.04 ± 0.35^{d}
200	32.64 ± 1.52^{b}	32.31 ± 0.82^{b}	33.47 ± 5.03^{b}	12.98 ± 1.52^{a}	32.56 ± 0.23^{b}
400	36.69 ± 0.47^{b}	35.37 ± 0.94^{b}	40.58 ± 2.69^{c}	18.35 ± 0.94^{a}	40.17 ± 0.94^{c}
800	58.93 ± 0.35^{d}	39.67 ± 1.87^{b}	50.83 ± 0.35^{c}	24.21 ± 0.82^{a}	60.91 ± 1.29^{d}
1600	67.11 ± 0.94^{d}	43.31 ± 1.40^{b}	58.60 ± 1.29^{c}	28.51 ± 0.82^{a}	71.98 ± 1.99^{e}

*Values here are the mean ± standard deviation. Means with different letters in a row are significantly different at $p < 0.05$.

Table 15. IC_{50} Values for Lipoxygenase Inhibition of the Crude Essential Oils, Blend, and Standard.

EO/Standard	Concentration IC_{50}(µg/mL)
S. aromaticum	859.63 ± 2.12^{b}
M. myristica	1967.50 ± 4.21^{d}
X. aethiopica	1060.95 ± 3.33^{c}
Blend	3093.46 ± 3.44^{e}
Ibuprofen	767.67 ± 5.21^{a}

*Values here are the mean ± standard deviation. Means with different letters in a row are significantly different at $p < 0.05$.

Table 16. Percentage Inhibitory Activity of Membrane by the Crude Essential Oils, Blend, and Standard.

Samples Concentration (µg/mL)	*S. aromaticum*	*M. myristica*	*X. aethiopica*	Blend	Ibuprofen
100	10.86 ± 3.07^{a}	9.78 ± 1.54^{a}	11.96 ± 4.61^{ab}	15.22 ± 0.00^{b}	29.35 ± 7.69^{c}
200	22.83 ± 1.54^{b}	16.30 ± 1.54^{a}	20.65 ± 4.61^{b}	20.65 ± 1.54^{b}	42.30 ± 3.07^{c}
400	29.35 ± 4.61^{b}	22.83 ± 1.54^{a}	28.26 ± 3.07^{b}	29.35 ± 1.54^{b}	53.26 ± 1.54^{c}
800	36.96 ± 3.07^{b}	30.43 ± 3.07^{a}	36.96 ± 3.07^{b}	33.69 ± 1.54^{b}	62.64 ± 1.54^{c}
1600	45.65 ± 6.15^{c}	36.96 ± 3.07^{a}	41.30 ± 3.07^{b}	40.22 ± 1.54^{b}	78.26 ± 3.07^{d}

*Values here are the mean ± standard deviation. Means with different letters in a row are significantly different at $p < 0.05$.

Table 17. IC_{50} Values for membrane stability assay of the Crude Essential Oils, Blend, and Standard.

EO/Standard	Concentration IC_{50}(µg/mL)
S. aromaticum	1134.90 ± 7.12^{b}
M. myristica	2232.11 ± 5.12^{e}
X. aethiopica	1942.35 ± 6.20^{c}
Blend	2102.00 ± 4.70^{d}
Ibuprofen	519.52 ± 5.20^{a}

*Values here are the mean ± standard deviation. Means with different letters in a row are significantly different at $p < 0.05$.

Xanthine Oxidase Inhibition

The inhibitory activities of the crude essential oils, the blend, and the standard (ibuprofen) against xanthine oxidase are presented in Table 18. It was observed that the higher the concentration of the essential oils, the higher the percentage inhibition. At a concentration of 1600 µg/mL, it was indicated that *X. aethiopica* (41.69%) had the highest percentage inhibition of xanthine oxidase, while *S. aromaticum* (33.01%) had the least xanthine oxidase inhibition. the blend, with an inhibition of 41.69%, had a higher activity than *S.aromaticum* and *M. myristica*. It was revealed that *S.aromaticum* with an IC_{50} of 1579.78 µg/mL had the least inhibition activity against xanthine oxidase (Table 19). The result showed that only *X. aethiopica,* with an IC_{50} of 1251.78 µg/mL, exhibited a higher inflammatory activity compared to other EOs.

Table 18. Percentage Inhibitory Activity of Xanthine Oxidase by the Crude Essential Oils, Blend, and Standard.

Samples Concentration (µg/mL)	*S. aromaticum*	*M. myristica*	*X. aethiopica*	Blend	Ibuprofen
100	6.24 ± 0.75^{b}	8.14 ± 0.25^{c}	9.38 ± 0.33^{c}	4.28 ± 0.50^{a}	8.02 ± 0.58^{c}
200	12.70 ± 0.50^{a}	14.85 ± 0.00^{b}	16.45 ± 0.08^{b}	15.38 ± 0.08^{b}	19.06 ± 0.25^{c}
400	19.18 ± 1.25^{a}	21.91 ± 0.92^{a}	25.24 ± 0.25^{b}	22.51 ± 0.25^{a}	32.01 ± 2.09^{c}
800	27.19 ± 0.50^{a}	28.62 ± 0.33^{a}	34.08 ± 0.34^{c}	30.99 ± 0.61^{b}	45.07 ± 0.25^{d}
1600	33.01 ± 1.34^{a}	35.27 ± 0.50^{a}	41.69 ± 0.16^{b}	37.71 ± 0.41^{ab}	51.84 ± 0.58^{c}

*Values here are the mean ± standard deviation. Means with different letters in a row are significantly different at $p < 0.05$.

Table 19. IC_{50} Values for Xanthine Oxidase inhibition of the crude Essential Oils, Blend, and Standard.

EO/Standard	Concentration IC_{50}(µg/mL)
S. aromaticum	1579.78 ± 4.12^{d}
M. myristica	1551.51 ± 3.38^{d}
X. aethiopica	1251.78 ± 2.31^{b}
Blend	1311.11 ± 1.87^{c}
Ibuprofen	855.22 ± 1.20^{a}

*Values here are the mean ± standard deviation. Means with different letters in a row are significantly different at $p < 0.05$.

Antidiabetic Activities

α-amylase Inhibition

Table 20. revealed the percentage inhibitory activities of each of the crude essential oils, the blend, and the standard (Acarbose) against α-amylase. It was observed that with a concentration of 1600 µg/mL, the blend of the crude essential oils recorded a percentage α-amylase inhibition of 54.45% which was the highest obtained, while the essential oil of *M. myristica* recorded the least inhibitory activity of 30.04%. It was also observed that the standard acarbose (65.11%) had a higher percentage inhibition than all the crude essential oils and the blend. The result of the anti-diabetic properties of individual crude essential oils and blends using the α-amylase assay with the inhibition concentration at 50% (IC_{50}) is shown in Table 21. The lowest IC_{50} value of the essential oils against α-amylase was 1250.69 µg/mL obtained in the blend essential oil, while the highest IC_{50} of 2703.00 µg/mL was recorded for the essential oil of *M. myristica*. This indicated that the blend of essential oils had a better antidiabetic activity regarding α-amylase than the other essential oils.

Table 20. Percentage Inhibitory Activity of Alpha-amylase by the Crude Essential Oils, Blend, and Standard.

Samples Concentration (µg/mL)	*S. aromaticum*	*M. myristica*	*X. aethiopica*	Blend	Acarbose
100	8.77 ± 1.73^{b}	5.21 ± 0.22^{a}	5.14 ± 1.19^{a}	8.97 ± 0.33^{bc}	14.19 ± 0.54^{d}
200	17.64 ± 2.60^{b}	11.43 ± 1.19^{a}	17.41 ± 1.08^{b}	18.17 ± 0.54^{b}	24.54 ± 0.22^{c}
400	23.75 ± 1.52^{b}	18.56 ± 1.52^{a}	28.14 ± 0.98^{c}	29.45 ± 0.87^{c}	37.88 ± 0.65^{d}
800	34.13 ± 1.19^{b}	30.75 ± 1.63^{a}	34.59 ± 1.19^{b}	47.47 ± 0.98^{c}	50.69 ± 0.54^{cd}
1600	44.40 ± 2.49^{b}	30.04 ± 0.65^{a}	44.94 ± 1.74^{b}	54.45 ± 1.58^{c}	65.11 ± 0.76^{d}

*Values here are the mean ± standard deviation. Means with different letters in a row are significantly different at $p < 0.05$.

Table 21. IC_{50} Values for Alpha-amylase Inhibition of the Crude Essential Oils, Blend, and Standard.

EO/Standard	Concentration IC_{50}(µg/mL)
S. aromaticum	1799.52 ± 2.60^{cd}
M. myristica	2703.00 ± 1.70^{e}
X. aethiopica	1735.00 ± 3.20^{c}
Blend	1250.69 ± 3.10^{b}
Acarbose	1002.26 ± 2.20^{a}

*Values here are the mean ± standard deviation. Means with different letters in a row are significantly different at $p < 0.05$.

α-glucosidase Inhibition

The percentage inhibitory activities of each crude essential oil, the blend, and the standard (Acarbose) against α-glucosidase are obtained in Table 22. It was observed that the percentage inhibition of α-glucosidase increased with concentration, while a concentration of 1600 µg/mL recorded the highest inhibition. The blend of essential oils had 76.80% inhibition with a concentration of 1600 µg/mL, which is closely followed by the standard acarbose with a percentage inhibition of 58.67%. The least inhibition was observed in the essential oil of *X. aethiopica* at 33.38%. The IC_{50} values of α-glucosidase for each of the essential oils and the standard are recorded in Table 23. Essential oil of *S. aromaticum* with the highest IC_{50} value of 3908.00 µg/mL had the least anti-diabetic activity, while the blend essential oil with an IC_{50} of 1080.56 µg/mL had the highest α-glucosidase inhibition.

Table 22. Percentage Inhibitory Activity of Alpha-glucosidase by the Crude Essential Oils, Blend, and Standard.

Samples Concentration (µg/mL)	*S. aromaticum*	*M. myristica*	*X. aethiopica*	Blend	Acarbose
100	8.89±0.21^{c}	7.07±0.93^{b}	5.98±0.41^{a}	7.14±0.41^{b}	11.81±0.62^{d}
200	11.81±0.21^{a}	13.00±0.62^{b}	15.96±0.31^{b}	10.79±0.21^{a}	21.28±0.21^{c}
400	21.28±0.62^{a}	24.93±0.21^{b}	25.36±1.24^{b}	22.38±1.86^{a}	32.94±0.62^{c}
800	28.28±1.86^{a}	31.71±0.31^{b}	32.51±0.82^{b}	50.61±1.24^{d}	45.55±0.10^{c}
1600	33.38±0.83^{a}	40.45±0.10^{b}	38.19±1.13^{b}	76.80±0.41^{d}	58.67±0.52^{c}

*Values here are the mean ± standard deviation. Means with different letter in a row are significantly different at $p < 0.05$.

Table 23. IC_{50} Values for Alpha-glucosidase Inhibition of the Crude Essential Oils, Blend, and Standard.

EO/Standards	Concentration IC_{50}(µg/mL)
S. aromaticum	3908.00±0.80^{e}
M. myristica	1969.00±2.30^{c}
X. aethiopica	2112.22±8.12^{d}
Blend	1080.56±7.30^{a}
Acarbose	1173.45±10.20^{b}

*Values here are the mean ± standard deviation. Means with different letters in a row are significantly different at $p < 0.05$.

DISCUSSION

S. aromaticum essential oil extracted in this study yielded 11.34% which was higher than what was obtained by Selles et al. (2020), who obtained 10.34% yield. Amanda et al. (2021) reported a 3.8% yield. The yield of *M. myristica* essential oil obtained in this study was revealed to be 2.74% which was higher than what was obtained by Ekere et al. (2017), who reported a yield of 0.66% for the essential oil of *M. myristica* but not significantly different from what was obtained by Owokotomo & Ekundayo, (2012), who reported a yield of 2.16%. *X. aethiopica* was reported by Alphonse et al. (2018) to yield 4.2% which was higher than what was reported in this study for *X. aethiopica*, which yielded a value of 1.44%. The differences in the yield from other studies could be a result of harvest, geographical origin, extraction method, and particle size (Selles et al. 2020).

Essential oils are made up of a wide variety of components; these components may be responsible for the synergistic (positive combined effort) properties exhibited by the extract. In some situations, some components present in the extract may have anti-desire effects on the extracts, resulting in an antagonistic (reduced combined effort) effect on the extract activities (Manindra et al., 2011).

The research reported eugenol (75.08%) in the essential oil from the bud of *S. aromaticum*, isocaryophyllene (29.36%) in the essential oil from the seeds of *M. myristica*, isospathulenol (8.67%) in the essential oil from the pod of *X. aethiopica*, and eugenol (34.25%) in the blend essential oil as the major components. Several studies have determined the chemical composition of the three essential oils. Ainane et al. (2019) reported that eugenol (17.60%), 1,1,4,8-tetramethyl-cis, cis,4,7,10-cycloundecatriene (27.7%), Caryophyllene oxide (24.3%), Caryophyllene (4.22%) and Humulene epoxide II (3.93%) were the five main components of a sample of *S. aromaticum* essential oil from morocco; Kaur & Kaushal, (2019) reported eugenol with a component of 76.8% very close to what was reported in this study, 75.10% was also reported by Simiat et al. (2017). Awojide et al. (2024) reported eugenol (76.13%) as the major compound found in the essential oil of *S. aromaticum,* which was not significantly different from what was observed in the essential oil of *S. aromaticum* of the present study. Isocaryophyllene (29.36%) and Germacrene D-4-ol (20.31%) were reported by Ainane et al. (2019) to be the major compounds found. The essential oil of *M.myristica* in a sample from Nigeria, Awojide et al. (2023), reported sabinol (20.95%), n-hexadecanoic acid (7.66%), linalool (9.11%), and Trans-13-octadecenoic acid (25.18%) as the major constituents of the essential oil of *M. myristica*. Alphonse et al. (2018) revealed that the main components of *X. aethiopica* essential oil were β-pinene (32.16%), β-phellandrene (10.71%), Z-γ-bisabolene (10.07%), and α-pinene (7.39%). The provenance of the fruits, which was not always known, could be one of the causes of this variation; Awojide et al. (2023) mentioned that the treatments of the fruits received after harvesting may be another factor responsible for the variations.

Phenolic contents were detected in all the essential oils, with the highest phenolic constituent observed in *S.*

aromaticum (182.46 mg GAE/g Extract), this was higher than what was observed in the work of Trifan et al. (2021), who reported a total phenolic content of 113.86 mg GAE/g Extract. El Ghallab et al. (2019), also reported the presence of phenolic content in *S. aromaticum.* Nkwocha et al. (2018) reported the presence of six phytochemicals obtained in the study of the essential oil of *M. myristica* (flavonoid was not determined). The values of phenolic content in this study were found to be greater than the values obtained for flavonoids; the same was reported by Hemalatha et al. (2016) and Nkwocha et al. (2018). Aguoru et al. (2016) also reported the presence of alkaloids, saponins, tannins, flavonoids, and steroids in the seeds of *X. aethiopica*. The phytochemicals present in the crude essential oils were present in the blend of the essential oils, but the values obtained for proanthocyanin, saponin, and terpenoid were the least in the essential oil blend. The blend of the essential oils may either increase or reduce the biological activity due to interaction between the components, which may be responsible for the variable values obtained (Romulo et al., 2020).

Antioxidants are known to be responsible for the defense mechanisms of the body against diseases associated with free radical attacks. Plant extracts have been documented to help prevent diseases caused by oxidative stress (Moharram & Youssef, 2014). Antioxidants work either by breaking down antioxidants, which react with lipid radicals and convert them into more stable products (Miguel, 2010) or by capturing free radicals and stopping the chain reactions (Moharram & Youssef, 2014). The result of this research indicated that while the blend resulted in a synergistic response as an antioxidant with respect to some of the essential oils, it was antagonistic to some. In the assessment of the DPPH scavenging ability of the essential oil and the blend, the blend was only synergistic to *M. myristica*. The blend had 61.26% inhibition of DPPH, higher than 60.95% obtained for *M. myrisitca,* but significantly not different; the same trend was reported for nitric oxide inhibition. The lower value of phenolic content present in the blend and *M. myristica* compared with those of other essential oils may be responsible for the lower DPPH scavenging activity observed. According to Zeb (2020), phenolic compounds have been attributed to have a strong antioxidant potential. The higher DPPH scavenging ability of *X. aethiopica* could be a result of the compound chavibetol observed in the essential oil. Chavibetol has been reported by Singh et al. (2009) to possess antioxidant properties, which could also have been responsible for the higher terpenoid observed in the essential oil, which is also known to have a wide spectrum as an antioxidant (Gutiérrez-del-Río et al., 2021). The presence of chavibetol in the blend could also contribute to the higher activities displayed than the essential oil of *M. myristica*.

For ABTS scavenging activities of the essential oils and the blend, the blend produces a percentage inhibition of 34.90% which was the least compared to other essential oils. The lipid peroxidation activity indicated that the blend exhibited a synergistic response, producing the highest lipid peroxide inhibition of 76.80%. The different responses of the indicators to the essential oils could be a result of the different mechanisms of action, which may be brought about by the different chemical components observed in the different essential oils (Miguel, 2010). *X. aethiopica* had higher DPPH scavenging activity than other essential oils, and the blend, *S. aromaticum,* was more effective in the inhibition of ABTS radical scavenger and nitric oxide oxidation, but the blend had the highest lipid peroxidation. Eugenol, having the highest composition in *S. aromaticum*, and the blend may be responsible for this activity observed, this was revealed in a study by Han and Parker (2017). In general, the antioxidant activities differ, depending on the test employed (Chebbac et al., 2013). The value of IC_{50} reported in this study for the DPPH assay was higher than that reported by Selles et al. (2020). Amanda et al. (2021) also reported the ABTS radical scavenging ability of *S. aromaticum* essential oils. Lucrece et al. (2018) reported that the evaluation of the antioxidant activity indicated that *S. aormaticum* had better antioxidant activity compared to *M. myristica*. This is in tandem with what was reported in this work. The synergistic and antagonistic antioxidant activity was evident in the blend.

Unlike in the case of antidiabetic activity, where the blend of the essential oils was more effective in the inhibition of the two different antidiabetic indicators, the essential oils subjected to the anti-inflammatory activity recorded a different trend for the three indicators used. For the lipoxygenases assay, the blend recorded the least inhibition of lipoxygenases (28.51%), while the highest activity of lipoxygenases inhibition was observed in the essential oil of *S. aromaticum* (67.11%). *S. aromaticum* also recorded the highest inhibition in the membrane stability at 45.65% but the least activity of 39.96% was exhibited by *X. aethiopica* essential oil. This trend in the variation of the effectiveness as an anti-inflammatory agent for the indicators was also observed by İlhami et al. (2012), who reported variation of the effectiveness of the different extracts on antioxidant indicators. This variation could be as a result of the different modes of action possibly produced by the differences in the chemical compounds of the different essential oils (Miguel, 2010). Eugenol, which was the most abundant component observed in the essential oil of *S. aromaticum,* may have been responsible for the anti-inflammatory activities observed here. According to Patlevič et al. (2016), eugenol was observed to exhibit anti-inflammatory activity effects in acute lung injury caused by lipopolysaccharide. The high abundance of flavonoids in the essential oil of *X. aethiopica* may have contributed to the anti-inflammatory properties. Ginwala et al. (2019) reported that flavonoids provide anti-inflammatory activity by lowering the formation of reactive oxygen species. A high content of tannin present in *S. aromaticum* may have also contributed to the higher anti-inflammatory activity observed in two of the indicators (Patlevič et al., 2016; Ambreen & Mirza, 2020). The blend of the essential oils recorded the least activity in respect to lipoxygenases inhibition alone, but showed a higher activity than *M. myristica* for the membrane stability assay and higher activity than *S. aromaticum* and *M. myristica* in the xanthine oxidase activity. The blend, therefore, showed synergistic and antagonistic activities with respect to some anti-inflammatory indicators. The differences in the activities may depend on the composition and ratio of the components observed in each oil (Pandur et al., 2021).

The result of the antidiabetic activities of the different essential oils using α-amylase and α-glucosidase assay indicated that the blend of essential oils recorded the least IC_{50} value of 1250.69 µg/mL and 1080.56 µg/mL, respectively, compared to the other essential oils. This is indicative of a better antidiabetic potential of the blend of essential oils than observed for the crude essential oils of *S. aromaticum*, *M. myristica,* and *X. aethiopica*. The antidiabetic activity observed could be attributed to the presence of flavonoids, tannins, saponins, phenolic content, and steroids in the essential oils (Tadesse et al. 2017; Gowd et al., 2017). The higher antidiabetic activity recorded in the blend could be a result of the synergy between eugenol and chavibetol, an isomer of eugenol (Vandana & Shalini, 2014); both have been reported to possess antidiabetic activity (Al-Trad et al., 2019). *Piper betle,* which has been attributed to possess antidiabetic activity, has chavibetol to be the highest component (53.1%), and it was touted to be responsible for the activity (Rekha et al., 2014; Thirugnanasambandam et al., 2022).

CONCLUSION

In this study, the medicinal activities of the blend of the essential oils of *S. aromaticum, M. myristica* and *X. aethiopica* were compared with those of the crude essential oils. The study showed varied components in the blend, compared to the crude essential oils. The results obtained from this study showed that the essential oil blend has synergistic efficacy in several of the medicinal assays conducted, indicating a potential better therapeutic as antioxidant and anti-diabetic properties compared to the crude essential oils.

LIST OF ABBREVIATIONS

IC_{50}- Inhibitory Concentration at 50%; DPPH- 2,2 diphenyl-1-picryhydray; ABTS- 2,2-azino-bis-(3-ethylbenzothiazoline-6-sulphonic acid; EOs- Essential Oils; GC-MS- Gas Chromatography-Mass Spectrometry.

REFERENCES

Afolabi, O. B., Oloyede, O. I., Aluko, B. T. & Johnson, J. A. 2021. Biosynthesis of magnesium hydroxide nanomaterials using *Monodora myristica*, antioxidative activities and effect on disrupted glucose metabolism in streptozotocin-induced diabetic rat. Food Bioscience, 41, pp. 101-123. https://doi.org/10.1016/j.fbio.2021.101023

Aguoru, C., Pilla, C. & Olasan, J. 2016. Phytochemical screening of Xylopia aethiopica with emphasis on its medicinally active principles. Journal of Medicinal Plant Research.

Ainane, A., Khammour, F., Charaf, S., Elabboubi, M., Elkouali, M., Talbi, M., Benhima, R., Cherroud, S., & Ainane, T. 2019. Chemical composition and insecticidal activity of five essential oils: Cedrus atlantica, Citrus limonum, Rosmarinus officinalis, Syzygium aromaticum and Eucalyptus globules. Materials Today: Proceedings, 13, pp. 474-485. doi:10.1016/j.matpr.2019.04.004

Akram, M., Adetunji, C. O., Mohiuddin, E., Oladosun, T. O., Ozolua, P., Olisaka, F. N., Egbuna, C., Olugbenga, S. M., Adetunji, J. B. & Hameed, L. 2021. Prospects of Phytochemicals for the Treatment of Helminthiasis. In Neglected Tropical Diseases and Phytochemicals in Drug Discovery; Eds.; Wiley: New Jersey, pp. 199-223. DOI: 10.1002/9781119617143.ch7

Alghazzaly, A. M., El-Sherbiny, G. M., Moghannemm, S. A. & Sharaf, M. H. 2022. Antibacterial, antibiofilm, antioxidants and phytochemical profiling of Syzygium aromaticum extract. Egypt. Journal of Aquatic Biology Fish. 26, pp. 207-218.

Alphonse, S. T., Thierry, M. N. B., Pierre, M. J. D. & Leopold T. N. 2018. Essential oil of Xylopia aethiopica from Cameroon: Chemical composition, antiradical and in vitro antifungal activity against some mycotoxigenic fungi. Journal of King Saud University - Science, 30(4), pp. 466-471, https://doi.org/10.1016/j.jksus.2017.09.011

Al-Trad, B., Alkhateeb, H., Alsmadi, W. & Al-Zoubi, M. 2019. Eugenol ameliorates insulin resistance, oxidative stress and inflammation in high fat-diet/streptozotocin-induced diabetic rat. Life sciences, 216, pp. 183-188. https://doi.org/10.1016/j.lfs.2018.11.034

Alzarea, S. I., Elmaidomy A. H., Saber H., Musa A., Al-Sanea M. M., Mostafa E. M., Hendaway O. M., Youssif K. A., Alanazi A. S., Alharbi M., Sayed A. M. & Abdelmohsen U. R. 2021. Potential anticancer lipoxygenase inhibitors from the red sea-derived brown algae *sargassum cinereum*: an in-silico-supported in-vitro study. Antibiotics 10, pp. 416.

Amanda, M. T., João, V. S., Juan, M. P. F., Ana, L. A., Kátia, S. C., Nestor, E. M. F., Adenilde, N. M. & Fernando, A. 2021. "GC-MS Characterization of Antibacterial, Antioxidant, and Antitrypanosomal Activity of *Syzygium aromaticum* Essential Oil and Eugenol", Evidence-Based Complementary and Alternative Medicine, 21, pp. 1-12. https://doi.org/10.1155/2021/6663255

Ambreen, M. & Mirza, S. A. 2020. Evaluation of anti-inflammatory and wound healing potential of tannins isolated from leaf callus cultures of Achyranthes aspera and Ocimum basilicum. Pakistan Journal of

Pharmaceutical Sciences, 33(1(Supplementary)), pp. 361-369.

Awojide, S. H., Fadunmade, E. O., Adegboye, A. A., Oyewole, K. A., Adedotun, I. S., Adeyemo, A. G. & Ayeni, J. V. 2024. A comparative study on the synergistic activities of fractions and crude essential oil of *Syzygium aromaticum*. Bulletin of the National Research Centre 48, pp. 47. https://doi.org/10.1186/s42269-024-01205-2

Awojide, S., Fadunmade, E., Oyewole, K., Adeyemo, A., Ogunniran, T., Ademikanlu, D. & Adeleke, A. 2023. Monodora Myristica Essential Oils Bioactivity against Two Grain Storage Insects. 6. pp. 123-129.

Ayala A., Mario F. M. & Sandro A. 2014. Lipid Peroxidation: Production, Metabolism, and Signaling Mechanisms of Malondialdehyde and 4-Hydroxy-2-Nonenal. Oxidative Medicine & Cellular Longevity, 36(4), pp. 38-42.

Batiha, G. E., Alkazmi, L. M., Wasef, L. G., Beshbishy, A. M., Nadwa, E. H. & Rashwan, E. K. 2020. Syzygium aromaticum L. (Myrtaceae): Traditional Uses, Bioactive Chemical Constituents, Pharmacological and Toxicological Activities. Biomolecules, 10(2), pp. 202. https://doi.org/10.3390/biom10020202

Bhaskar, H. & Balakrishnan, N. 2009. In Vitro Antioxidant Property of Laticiferous Plant Species from Western Ghats Tamilnadu, India. International Journal of Health Research, 2, pp. 163-170.

Bunse, M., Daniels, R., Gründemann, C., Heilmann, J., Kammerer, D. R., Keusgen, M., Lindequist, U., Melzig, M. F., Morlock, G. E., Schulz, H., Schweiggert, R., Simon, M., Stintzing, F. C. & Wink, M. 2022. Essential Oils as Multicomponent Mixtures and Their Potential for Human Health and WellBeing. Frontier Pharmacology, 13, pp. 956541. doi: 10.3389/fphar.2022.956541

Chebbac, K., Benziane O. Z., El-Moussaoui, A., Chebaibi, M., Salamatullah, A. M., Lafraxo, S. & Bourhia, M. 2023. In Vitro and In Silico Studies of Antimicrobial, and Antioxidant Activities of Chemically Characterized Essential Oil of Artemisia flahaultii L. (Asteraceae). Life, 13(3), pp. 779. MDPI AG. Retrieved from http://dx.doi.org/10.3390/life13030779

Chen, F., Du, X., Zu, Y., Yang, L. & Wang, F. 2016. Microwave-assisted method for distillation and dual extraction in obtaining essential oil, proanthocyanidins and polysaccharides by one-pot process from Cinnamomi cortex. Separation & Purification Technology, 164, pp. 1-11.

Cimino, C., Maurel, O. M., Musumeci, T., Bonaccorso, A., Drago, F., Souto, E. M. B., Pignatello, R. & Carbone, C. 2021. Essential Oils: Pharmaceutical Applications and Encapsulation Strategies into Lipid-Based Delivery Systems. Pharmaceutics, 13(3), pp. 327. https://doi.org/10.3390/pharmaceutics13030327

Dawood, M. A., El Basuini, M. F., Yilmaz, S., Abdel-Latif, H. M., Alagawany, M., Kari, Z. A., Abdul Razab, M. K. A., Hamid, N. K. A., Moonmanee, T. & Van Doan, H. 2022. Exploring the roles of dietary herbal essential oils in aquaculture: A review. Animals. 12, pp. 823.

Ejikeme, C. M., Ezeonu, C. S., & Eboatu, A. N. 2014. "Determination of physical and Phytochemical constituents of some tropical timber indigeneous to Niger Delta Area of Nigeria", European scientific journal,10(18), pp. 247-270.

Ekeanyanwu, R. C., Nkwocha, C. C. & Ekeanyanwu, C. L. 2021. Behavioural and biochemical indications of the antidepressant activities of essential oils from *Monodora myristica* (Gaertn) seed and *Xylopia aethiopica* (Dunal) fruit in rats. *IBRO Neuroscience Report*, 10, pp. 66-74.

Ekere, N. R., Odoemelam, C., Ihedioha, J. N., & B. Okoye, C. O. 2017. Profile of seed oils from monodora myristica and monodora tenuifoila PLANTS. Journal of Chemical Society of Nigeria, 40(2).

El Ghallab, Y., Al Jahid, A., Jamal, J. E., Haj Said, A. A., Zarayby, L. & Derfoufi, S. 2019. *Syzygium aromaticum* L.: phytochemical investigation and comparison of the scavenging activity of essential oil extracts. Oriental Pharmacy and Experimental Medicine. 20(2), pp. 153-158.

Elshafie, H. S. & Camele, I. 2017. "An Overview of the Biological Effects of Some Mediterranean Essential Oils on Human Health", BioMedical Research International, 17(2), pp. 1-14.

Foda, A. M., Kalaba, M. H., El-Sherbiny, G. M., Moghannem, S. A. & El-Fakharany, E. M. 2022. Antibacterial activity of essential oils for combating colistin-resistant bacteria. Expert Rev. Anti-Infect. Therapeutics 20, pp. 1351-1364.

Ginwala, R., Bhavsar, R., Chigbu, D. I., Jain, P. & Khan, Z. K. 2019. Potential Role of Flavonoids in Treating Chronic Inflammatory Diseases with a Special Focus on the Anti-Inflammatory Activity of Apigenin. *Antioxidants* (Basel, Switzerland), 8(2), pp. 35. https://doi.org/10.3390/antiox8020035

Gowd, V., JiaZ, Q. & Chen, W. 2017. Anthocyanins as promising molecules and dietary bioactive components against diabetes—a review of recent advances. Trends Food Sci Technol. 68(0924-2244), pp. 1-13.

Gutiérrez-del-Río, I., Sara, L., Patricia, M., Luis, F., Álvaro, P., Mateo, T., Elisa, M. M., Claudio, J. V. & Felipe, L. 2021. "Terpenoids and Polyphenols as Natural Antioxidant Agents in Food Preservation" *Antioxidants*, 10(8), pp. 1264. https://doi.org/10.3390/antiox10081264

Han, X. & Parker, T. L. 2017. Anti-inflammatory activity of clove (Eugenia caryophyllata) essential oil in human dermal fibroblasts. Pharmaceutical biology, 55(1), pp. 1619–1622. https://doi.org/10.1080/13880209.2017.1314513

Hemalatha, R., Nivetha, P., Mohanapriya, C., Sharmila, G., Muthukumaran, C. & Gopinath, M. 2016. Phytochemical composition, GC-MS analysis, in vitro antioxidant and antibacterial potential of clove flower bud (Eugenia caryophyllus) methanolic extract. Journal of food science and technology, 53(2), pp. 1189-1198. https://doi.org/10.1007/s13197-015-2108-5

İlhami, G., Mahfuz, E. & Hassan, Y. A. 2012. Antioxidant activity of clove oil – A powerful antioxidant source. Arabian Journal of Chemistry, 5(4), pp. 489-499. https://doi.org/10.1016/j.arabjc.2010.09.016.

Irondi, E. A., Aroyehun, T. M. & Anyiam, A. F. 2023. Phenolics profile, anti-nephrolithiasis, and antioxidant activities of *Monodora myristica* seed: impact of endogenous proteins and lipids. *Food Produce Process* *and Nutrition,* 5, pp. 52. https://doi.org/10.1186/s43014-023-00167-8

Kaur, K. & Kaushal, S. 2019. Phytochemistry and pharmacological aspects of Syzygium aromaticum: A review. Journal of Pharmacognosy and Phytochemistry, 8(1), pp. 398-406.

Kim Y. I., Lee H., Nirmala F. S., Seo H. D., Ha T. Y., Jung C. H. & Ahn J. 2022. Antioxidant Activity of Valeriana fauriei Protection against Dexamethasone-induced Muscle Atrophy. Oxidative & Medicinal Cell Longevity, 32(2), pp. 209-219.

Kruk, J., Hassan, Y. A. E., Kladna, A. & Jacquelyn, E. B. 2019. Oxidative Stress in Biological Systems and Its Relation with Pathophysiological Functions: The Effect of Physical Activity on Cellular Redox Homeostasis. Free Radical, 53(5), pp. 497-521. DOI: 10.1080/10715762.2019.1612059

Leigh-de R. S. & Van, V. S. 2020. Odoriferous therapy: A review identifying essential oils against pathogens of the respiratory tract. Chemistry Biodiversity, 17, pp. 2000062.

Leigh-de, R. S., Viljoen, A. & Van, V. S. 2021. Essential Oil Blends: The Potential of Combined Use for Respiratory Tract Infections. Antibiotics (Basel). 10(12), pp. 1517. doi: 10.3390/antibiotics10121517

Lucrece, E. M., Cecilia, M., Paulin, D. F., Fabrice, T. D., Lakshmi, K. M., Macaire, W. H. & Bandjoun, B. B. 2018. Chemical Composition and Antioxidant Activity of Syzygium aromaticum and Monodora myristica Essential Oils from Cameroon. Journal of Food Stability. 1, pp. 1-13.

Ly, T. T. G., Yun, J., Lee, D. H., Chung, J. S. & Kwon, S. M. 2021. Protective Effects and Benefits of Olive Oil and Its Extracts effects on Women's Health. Nutrients, 13, 4279.

Manindra, M., Kumar, A. A., Zafar Haider, S., & Akash, S. 2011. Essential oil composition and antimicrobial activity of three ocimum species from uttarakhand (Índia). International Journal Pharmacy Pharmaceutical Science, 3, pp. 223.

McCue, P. & Shetty, K. 2005. Antidiabetic and anti-hypertensive potential of sprouted and solid-state bioprocessed soybean. Asian Pacific Journal of Clinical Nutrition. 14, pp. 145-152.

Melo, C., Rosemary, P., Fadel, Y., Oneil, M., Nadjet, C., Sahar, A., Shepherd, C., Thierry, B., Shimin, Z., Thomas, M. Z., Christine, P., José, A., Fernández, R. H., Rodolfo, J. & Adolfina, K. 2021. "Antioxidant, antibacterial, and anti-SARS-CoV Activity of Commercial Products of Xylopia (Xylopia aethiopica)." Journal of Medicinally Active Plants, 10(1), pp. 11-23. DOI: https://doi.org/10.7275/9baf-e988

Miguel, M. G. 2010. Antioxidant and anti-inflammatory activities of essential oils: a short review. Molecules (Basel, Switzerland), 15(12), pp. 9252-9287. https://doi.org/10.3390/molecules15129252

Moharram, H. A. & Youssef, M. M. 2014. Methods for Determining the Antioxidant Activity: A Review. Alex. Journal of Food. Science. & Technology, 11(1), pp. 31-42.

Nkwocha, C., Nworah, F. N., Okagu, I. U., Nwagwe, O. R., Uchendu, N. O., Paul-Onyia, D. B. & Obeta, S. 2018. Proximate and Phytochemical Analysis of Monodora myristica (African Nutmeg) from Nsukka, Enugu State, Nigeria. Journal of Food and Nutrition Research, 6(9), pp. 597-601.

Orchard, A., Kamatou, G., Viljoen, A. M., Patel, N., Mawela, P. & van Vuuren, S. F. 2019. The influence of carrier oils on the antimicrobial activity and cytotoxicity of essential oils. Evidence-Based Complement. Alternative Medicine pp. 6981305.

Owokotomo, A. & Ekundayo, O. 2012. Comparative study of the essential oils of Monodora myristica from Nigeria. European Chemistry Bulletin 1, pp. 263-265.

Owolabi, M. S., Oladimeji, M. O., Lajide, L., Singh, G., Mariwuthu, P. & Isidorov, V. A. 2009. Bioactivity of three plant derived essential oils agianst the maize weevils sitophilus zeamais (motschulsky) and cowpea weevils callosobruchus maculatus (fabricius). Electronic Journal of Environmental, Agricultural & Food Chemistry. 8(9), pp. 828.

Oyedapo, O. O., Akinpelu, B. A., Akinwunmi, K. F., Adeyinka, M. O. & Sipeolu, F. O. 2010. Red blood cell membrane stabilizing potentials of extracts of Lantana camara and its fractions. International Journal of Plant Physiology and Biochemistry, 2(4), pp. 46-51.

Pandur, E., Balatinácz, A., Micalizzi, G., Mondello, L., Horváth, A., Sipos, K. & Horváth, G. 2021. Anti-inflammatory effect of lavender (Lavandula angustifolia Mill.) essential oil prepared during different plant phenophases on THP-1 macrophages. BMC complementary medicine and therapies, 21(1), pp. 287. https://doi.org/10.1186/s12906-021-03461-5

Park Y. S., Jung S. T., Kang S. G., Heo B. G., Arancibia-Avila P., Toledo F., Drzewiecki J., Namiesnik J. & Gorinstein, S. 2008. Antioxidants and proteins in ethylene treated kiwi fruits. Food Chemistry, 107, pp. 640-648.

Patlevič, P., Vašková, J., Švorc Jr, P., Vaško, L. & Švorc, P. 2016. Reactive oxygen species and antioxidant defense in human gastrointestinal diseases," Integrative Medicine Research, 5(4), pp. 250-258.

Rekha V. P. B., Manideep, K., Babita, G., Yarlagadda, B. & Krishna, K. P. 2014. A Review on Piper betle L.: Nature's Promising Medicinal Reservoir. American Journal of Ethnomedicine, 1(5), pp. 276-289.

Samtiya, M., Aluko, R. E., Dhewa, T. & Moreno-Rojas, J. M. 2021. Potential Health Benefits of Plant Food-Derived Bioactive Components: An Overview. Foods (Basel, Switzerland), 10(4), pp. 839. https://doi.org/10.3390/foods10040839

Schaich, K. M., Tian, X. & Xie, J. 2015. Hurdles and pitfalls in measuring antioxidant efficacy: A critical evaluation of ABTS, DPPH and ORAC assays. Journal of Functional Foods. 14, pp. 111-125.

Selles, S. M. A., Kouidri, M., Belhamiti, B. T. & Ait A. A. 2020. Chemical composition, in-vitro antibacterial and antioxidant activities of *Syzygium aromaticum* essential oil. Journal of Food Measurement and Characterization, 14(4), pp. 2352-2358. https://doi.org/10.1007/s11694-020-00482-5

Simiat, O. J., Lateefah, A. A. & Kazeem, A. A. 2017. Phytochemical Screening and Antimicrobial Evaluation of Syzygium aromaticum Extract and Essential oil.

International Journal of Current Microbiology Applied Sciences, 6(7), pp. 4557-4567.

Singh, M., Shakya, S., Soni, V. K., Dangi, A., Kumar, N. & Bhattacharya, S. M. 2009. The n-hexane and chloroform fractions of Piper betle L. trigger different arms of im,mune responses in BALB/c mice and exhibit antifilarial activity against human lymphatic filarid Brugia malayi. International Immunopharmacology, 9, pp. 716-728.

Tadesse, B. T., Ariaya, H., Yalemtsehay, M. & Mekuria, T. 2017. Antidiabetic activity and phytochemical screening of extracts of the leaves of Ajuga remota Benth on alloxan-induced diabetic mice. BMC Complementary and Alternative Medicine. 17 pp. 243. DOI 10.1186/s12906-017-1757-5

Tao, Y., Zhang, Y., Cheng, Y. & Wang Y. 2013. Rapid screening and identification of α-glucosidase inhibitors from mulberry leaves using enzyme-immobilized magnetic beads coupled with HPLC/MS and NMR," Biomedical Chromatography, 27(2), pp. 148–155.

Thirugnanasambandam, R., Anil, K., Sunita, P., Nagalakshmi, V. & Krishnaveni, M. 2022. Phytochemistry & Pharmacological Studies Of Betel Piper. Journal of Pharmaceutical Negative Results, 13(10), pp. 6123-6129. DOI: 10.47750/pnr.2022.13.S10.756

Trifan, A., Zengin, G., Brebu, M., Skalicka-Woźniak, K. & Luca, S. V. 2021. Phytochemical Characterization and Evaluation of the Antioxidant and Anti-Enzymatic Activity of Five Common Spices: Focus on Their Essential Oils and Spent Material Extractives. Plants, 10(12), pp. 2692. MDPI AG. Retrieved from http://dx.doi.org/10.3390/plants10122692

Vandana, D. & Shalini, T. 2014. Review study on potential activity of *Piper betle.* Journal of Pharmacognosy Phytochemistry, 3(4), pp. 93-98.

Wesołowska, A., Paula, J., Danuta, K. & Włodzimierz, P. 2019. "Gas Chromatography-Mass Spectrometry (GC-MS) Analysis of Essential Oils from AgNPs and AuNPs Elicited *Lavandula angustifolia* In Vitro Cultures" Molecules *24*(3), pp. 606. https://doi.org/10.3390/molecules24030606

Yeshi, K. & Phurpa, W. 2022. Essential oils and their bioactive molecules in healthcare. In Herbal Biomolecules in Healthcare Applications; Academic Press: Cambridge, MA, USA, pp. 215-237.

Yin, X., Chávez León, M. A. S. C., Osae, R., Linus, L. O., Qi, L. W. & Alolga, R. N. 2019. *Xylopia aethiopica* Seeds from Two Countries in West Africa Exhibit Differences in Their Proteomes, Mineral Content and Bioactive Phytochemical Composition. Molecules (Basel, Switzerland), 24(10), pp. 1979.

Zeb, A. 2020. Concept, mechanism, and applications of phenolic antioxidants in foods. Journal of Food Biochemistry. doi:10.1111/jfbc.13394

Bulletin of Natural Sciences Research
Vol.15, No. 1, 2025, pp. 27-33.

DOI: https://doi.org/10.5937/bnsr15-61823
Original Scientific Paper

STRUCTURAL AND ELECTROCHEMICAL PROPERTIES OF SYNTHESIZED NANOSTRUCTURED $Ca_{0.9}Er_{0.1}MnO_3$ BY HYDRAZINE NITRITE PROCEDURE

TIJANA B. VLAŠKOVIĆ[1], MILENA ROSIĆ[2], BRANKA B. PETKOVIĆ[1], BOJANA B. LABAN[1*]

[1]Faculty of Sciences and Mathematics, University of Priština in Kosovska Mitrovica, Kosovska Mitrovica, Serbia
[2]Institute of Nuclear Sciences "Vinča", National Institute of the Republic of Serbia, University of Belgrade, Serbia

ABSTRACT

Synthesis, structural, and electrochemical properties of nanostructured powders $Ca_{0.9}Er_{0.1}MnO_3$ with perovskite-type crystal were studied. Nanopowders were prepared by the combustion method using the hydrazine nitrite procedure (HNP), which involves mixing metal nitrate salts (Ca, Mn, Er) in a stoichiometric ratio and varying the quantity of added hydrazine. In this synthetic procedure, the aim is to adjust the amount of hydrazine in order to control the combustion of the reactions, obtain the required amount of fuel energy, but also the amount that will complex the reactants in the mixture. The powders obtained by hydrazine nitrate synthesis were then calcined for 15 minutes at temperatures of 800, 900, and 1000 °C. Characterization of the synthesized and calcined samples was performed using advanced techniques such as X-ray diffraction (XRD), Fourier-transform infrared spectroscopy (FTIR), and electrochemical measurements. The results clearly indicate that the amount of hydrazine added is crucial in preparing the $Ca_{0.9}Er_{0.1}MnO_3$ sample. This highlights the importance of precise hydrazine dosage in optimizing the synthesis process to enhance the material's properties. Further, the electrochemical properties of the obtained perovskite nanopowders were investigated by cyclic voltammetry (CV) and electrochemical spectroscopic impedance (EIS) on perovskite-modified carbon paste electrodes. Electrochemical measurements showed improved electrochemical properties of perovskite-modified carbon paste electrodes compared to bare carbon paste electrode (CPE). The electrode modified with the material synthesized with the smallest amount of hydrazine presented the best results.

Keywords: Perovskites, Hydrazine nitrite procedure, Electrochemical.

INTRODUCTION

Perovskite-type compounds are special materials that share a similar crystal structure and have garnered significant attention in both scientific research and practical applications due to their diverse and unique properties, including ferroelectricity, ferromagnetism, fast-ion conductivity, superconductivity, etc. The term "perovskite-type structure" originates from the mineral calcium titanate ($CaTiO_3$), the first material identified with this specific crystalline structure. It was discovered by geologist Gustav Rose in the Ural Mountains in 1839 and named "perovskite" in honor of the Russian mineralogist Count Lev Alekseevich von Perovsky (Katz, 2020). This name refers to any compound of the formula ABX_3, with a similar ionic crystalline structure. Among various compounds with a perovskite structure, perovskite oxide materials with the general formula ABO_3 attracted the attention of researchers due to their specific chemical and physical properties (Bispo-Jr et al., 2022). The ABO_3 perovskite structure consists of a framework formed by corner-sharing octahedra. Distortions of the octahedra often occur in these structures due to deviations from ideal values of the ion size ratios between the A, B, and O sites of the crystal. Additionally, the A or B cations may exhibit characteristic sizes and valences that can result in oxygen non-stoichiometry, including excess and/or deficiency of oxygen (Kuganathan & Chroneos, 2021).

There are various synthetic methods for the formation of perovskite-type nanomaterials, which can be categorized by three main approaches: solid-state, liquid-state, and gas-state synthesis (Bayode et al., 2024). In this manner, methods such as the mechanical ball-milling method, combustion method, co-precipitation method, and sol-gel chemical method have been employed (Ansari et al., 2020; Bayode et al., 2024; Yadav et al., 2020; Tadić et al., 2016). The challenge is to control the size, crystallinity, morphology, shape, and properties, and to form nanomaterials for specific purposes and from different elements. The choice of methods for perovskite synthesis affects the physical and chemical properties of the material. Additionally, perovskite oxides, due to their multiple oxidation states at the B-site, possess redox properties, and they have been found to have potential applications as electrode materials for electrochemical sensors (Shimizu et al., 1996; Durai & Badhulika, 2022).

---

* Corresponding author:tijanavlaskovicpantovic@gmail.com

Transition metal-containing perovskite oxides exhibit excellent structural flexibility, enabling the placement of various doping cations on either the A or B site while maintaining the perovskite-type framework (Yang et al., 2017; Kuganathan & Chroneos, 2021). Among these materials, $CaMnO_3$ is studied because it has been found to have applications in electrocatalysis, Li-ion batteries, and electronics, among others (Kuganathan & Chroneos, 2021). Doped perovskite manganites have a general formula $A_{1-x}Re_xMnO_3$, where A is an alkali earth element, and Re is a rare-earth element (Rosić et al., 2015; Rosić et al., 2011). In this perovskite-type oxide, manganese can exist in two oxidation states, Mn^{3+} and Mn^{4+}, to maintain charge neutrality. It was found that rare-earth element (Re) atoms occupy the A sites, while smaller cations occupy the B sites (Dukić et al., 2009). Previous work reports that Gd occupies the A sites, because Gd^{3+} is a cation that is significantly larger than the Mn cation, and substitution of Ca with Gd will affect the valence of Mn (Rosić et al., 2011). In undoped $CaMnO_3$, Mn^{4+} ions exhibit antiferromagnetic ordering. However, Gd^{3+} doping introduces Mn^{3+} ions, whose ferromagnetic double exchange interaction with Mn^{4+} leads to the formation of ferromagnetic clusters within an antiferromagnetic matrix (Rosić et al., 2011; Rosić et al., 2015). Additionally, previous research has reported that the substitution of cations in perovskite-type oxides can alter the crystal symmetry from orthorhombic (*Pnma*) to tetragonal (*I4/mcm*) (Srivastava et al., 2015). The incorporation of rare-earth elements into perovskite oxides is primarily governed by ionic size compatibility between host and dopant cations. In $CaMnO_3$, calcium occupies the A-site of the perovskite lattice, with an effective ionic radius of approximately 1.12 Å for Ca^{2+} in 12-fold coordination (Shannon, 1976). Erbium, by comparison, has a smaller ionic radius of about 1.004 Å for Er^{3+} in 8-fold coordination (Shannon, 1976). Despite this size difference, the mismatch remains within the tolerance limits of the perovskite structure, enabling partial substitution of Ca^{2+} by Er^{3+}. Such substitution is expected to induce local lattice distortions, modify the electronic environment, and allow for tuning of functional properties including electrical transport, magnetic ordering, optical response, and defect behavior (Kuganathan & Chroneos, 2021; Xia et al., 2025). The primary objective of this work is to investigate the structural and electrochemical properties of Er^{3+}-doped $CaMnO_3$ oxides, aiming to clarify the role of Er substitution and explore its potential for applications in advanced functional materials, such as thermoelectrics, solid oxide fuel cells, and optoelectronic devices.

In this work, the possibility of forming a nanostructured solid solution with a nominal composition of $Ca_{0.9}Er_{0.1}MnO_3$ was studied using a modified hydrazine nitrite procedure (HNP). Structural and electrochemical properties were investigated.

EXPERIMENTAL

Chemicals

All used chemicals were of analytical grade. Calcium-nitrate tetrahydrate ($Ca(NO_3)_2 \cdot 4H_2O$), Manganese-nitrate hydrate ($Mn(NO_3)_2 \cdot H_2O$), Erbium-nitrate pentahydrate ($Er(NO_3)_3 \cdot 5H_2O$), Hydrazine hydrate ($N_2H_2 \cdot H_2O$), Glassy carbon powder, Liquid paraffin (C_nH_{2n+2}), and Potassium with complex ion $[Fe(CN)_6]^{3-/4-}$, all >99.9% purity (Merck). All solutions were prepared using water purified with a Millipore Milli-Q system.

Synthesis of nanostructured powders

To achieve enhanced control over the stoichiometry, structure, and phase purity of metal oxides, the avoidance of the brute force method remains a fundamental approach in the synthesis of new materials. Starting chemicals used for the HNP (hydrazine nitrate procedure) synthesis of powders were nitrate salts of Ca, Mn, and Er. Hydrazine played a double role as both a complexant and a fuel. The composition of the reacting mixtures was calculated based on the nominal composition of the final reaction product. The principles of propellant chemistry (Patil, 2008) were applied to calculate the composition of the reacting mixtures. In stoichiometric redox reactions between a fuel and an oxidizer, it is essential to define the ratio of the net oxidizing valences of the metal nitrate to the net reducing valences of the fuel. It is essential to gain this understanding to enhance our knowledge and applications in this specific field. By convention, the valencies of nitrogen, oxygen, hydrogen, calcium, erbium, and manganese are set as 0, 2–, 1+, 2+, 3+, and 4+, respectively. Using the valencies of these individual elements, the reducing valence of hydrazine, $N_2H_4H_2O = 2(0)+4(+1)+2(+1)+(-2) = 4$; it works out to be 4+, while $Ca(NO_3)_3$, $Er(NO_3)_3$, and $Mn(NO_3)_3$ work out to be 15–, respectively. We add these values based on Equations (1) and divide them by 4 (the value for hydrazine). For producing one mole of $Ca_{0.9}Er_{0.1}MnO_3$, through the stoichiometric reactions (1), there will be −20.5/4 = 5.125 moles of hydrazine, which is required. According to the chemical equations, $Ca_{0.9}Er_{0.1}MnO_3$ powder was prepared:

$$\begin{aligned}&N_2H_4 \cdot H_2O + 0.9\ Ca(NO_3)_2 \cdot 4\ H_2O + Mn(NO_3)_2 \cdot H_2O + \\ &0.1\ Er(NO_3)_3 \cdot 5\ H_2O + 6.1\ O_2 \rightarrow Ca_{0.9}Er_{0.1}MnO_3 + \\ &6.1\ NO_2 + 8.1\ H_2O.\end{aligned} \tag{1}$$

The starting mixture of the selected composition $Ca_{0.9}Er_{0.1}MnO_3$ was synthesized using a stoichiometric ratio of metal salts and varying amounts of hydrazine compared to the molar ratio from Equation 1. In the HNP method, metal nitrate salts and hydrazine were mixed in a molar ratio: 1 molMn : 1 molCa+Er : 1/6 (0.17 mol) N_2H_4; 1 molMn : 1 molCa+Er : 1/3 (0.33 mol) N_2H_4; and 1 molMn : 1 molCa+Er : 1/2 (0.5 mol) N_2H_4.

In a 1-liter beaker, the calculated masses of the appropriate chemicals were combined and dissolved in a small amount of water, after which three drops of concentrated nitric acid were added. The mixture was heated in the temperature range of 60 – 70 °C. After the reaction was completed, a bulky material was obtained. The second step of the experiment is calcination in an annealing furnace at three different temperatures, 800, 900, and 1000°C. For each sample, we annealed the material for 15 minutes at a given temperature. When applying this method, the most important factor is the molar ratio of hydrazine and nitrate ions in the mixture, as the reaction temperature (due to exothermicity) is higher, resulting in a larger crystal size of the resulting material, i.e., the initial reactants will react more effectively.

RESULTS AND DISCUSSION

XRD Analysis

The XRD patterns of the $Ca_{0.9}Er_{0.1}MnO_3$ powder samples were obtained after combustion reaction (HNP), calcination at 800, 900, and 1000 °C, and different molar ratios are shown in Figure 1a–c.

Following the combustion reaction, the XRD patterns of the resulting powders appeared to be amorphous. This could likely be attributed to inadequate heat generated during the auto-ignition process (Rosić et al., 2011).

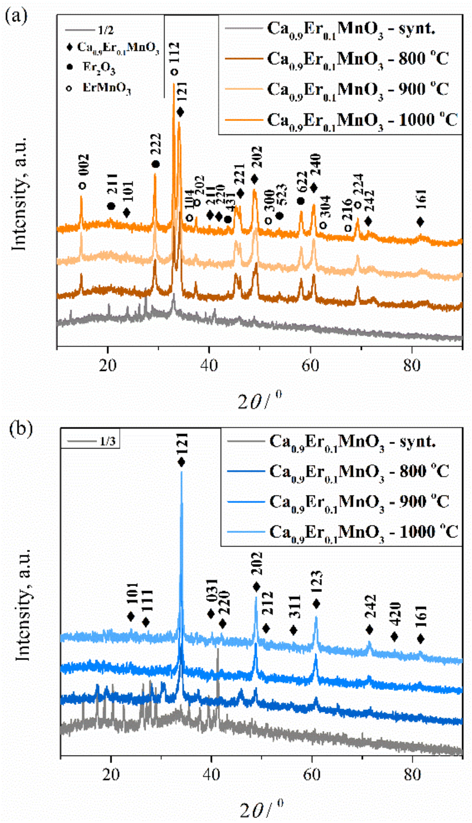

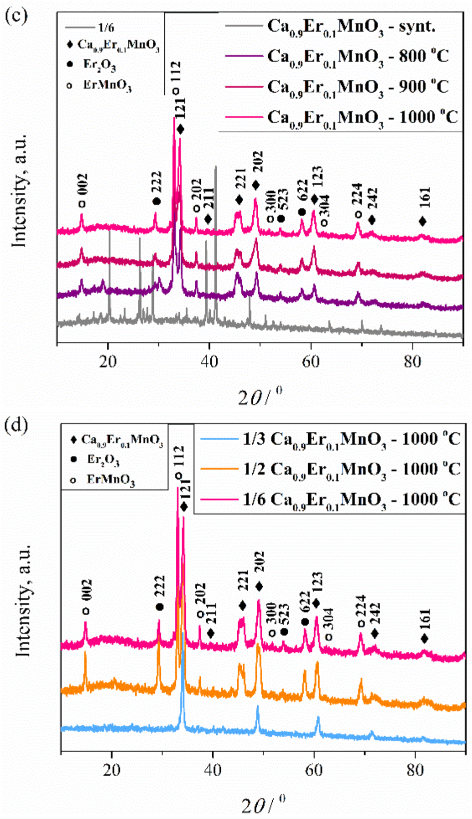

Figure 1. XRD patterns of $Ca_{0.9}Er_{0.1}MnO_3$ powders after combustion, different calcination temperatures, and molar ratios: (a) 1/2-$Ca_{0.9}Er_{0.1}MnO_3$, (b) 1/3-$Ca_{0.9}Er_{0.1}MnO_3$, (c) 1/6-$Ca_{0.9}Er_{0.1}MnO_3$, (d) Comparison of powder samples at the same 1000 °C, but different molar ratios for different amounts of hydrazine: 1/2 – 0.17 molHy, 1/3 – 0.33 molHy, and 1/6 – 0.5 molHy.

XRD patterns of the $Ca_{0,9}Er_{0,1}MnO_3$ powders after calcinations at 800, 900, and 1000 °C with 0.17 and 0.5 mol hydrazine in the initial mixture (Figure 1a and 1c), show the separation of three phases: $CaMnO_3$ (ICSD #153238, *Pnma* N^o 62), $ErMnO_3$ (ICSD #162201, *P 63 c m* N^o185), and ErO_3 (ICSD #33656, *I 21 3* N^o199)(International Crystallographical Database (ICDD)). The formation of these three phases suggests that the violent combustion reaction occurred too rapidly for hydrazine, which serves as both a fuel and a complexant, to effectively perform its dual role. As a result, it did not have sufficient time to bind all the elements present into the perovskite phase. In contrast to the two previously mentioned samples, a monophasic sample was formed in the sample with 0.33 moles of hydrazine in the mixture; an appropriate proportion of fuel was obviously added. Based on the diffractogram (Figure 1b), the calcination temperature for $Ca_{0.9}Er_{0.1}MnO_3$ is in the range of 900 to 1000 °C. A change in the unit cell parameters was observed, but it was not significant due to the small difference in ionic radii between Ca^{2+} and Er^{3+} . The most noticeable changes occurred in the volume and parameter b, while parameters a and c showed negligible differences (see Table 1).

Table 1. Percentage and cell parameters [Å, degree] and volume [$Å^3$] of the unit cell for $Ca_{0.9}Er_{0.1}MnO_3$ phases were observed directly in samples with 0.33 moles of hydrazine in the mixture that have beencalcinated at 900 and 1000 °C, respectively. The data were obtained using the software package Powder Cell (Kraus & Nolze, 1996, http://powdercell-for-windows.software.informer.com/2.4/) and compared with data from the reference (International Crystallographical Database (ICDD)) marked with *.

$CaMnO_3$* ICSD #153238	$Ca_{0.9}Er_{0.1}MnO_3$ 900 °C	$Ca_{0.9}Er_{0.1}MnO_3$ 1000 °C
a=5.2812 b=7.457 c=5.2753 V=207.75	a=5.2766 b=7.5110 c=5.2741 V=209.03	a=5.2723 b=7.4898 c=5.2747 V=208.29
	Rp=5.62 Rwp=7.40 Rexp=0.39	Rp=6.08 Rwp=8.21 Rexp=0.51
	Size 33.32 Strain 0.0029	Size 35.63 Strain 0.0026

While not all peaks are broad, they tend toward that shape and exhibit a moderate intensity, suggesting a nanocrystalline nature, confirmed by a crystallite size of approximately 35 nm. Figure 1d shows a clear difference when visually comparing observed samples.

FTIR spectroscopy

The FTIR spectra of as-prepared and calcinated $Ca_{0.9}Er_{0.1}MnO_3$nanopowders are presented in Figure 2. In Figure 2a, FTIR spectra for as-prepared $Ca_{0.9}Er_{0.1}MnO_3$ are presented using different amounts of hydrazine: 0.17 mol, 0.33 mol, and 0.5 mol.

The FTIR spectra of as-prepared materials (Fig. 2a) show that the band from hydrazine prevails. In contrast, band characteristics of M – O bonds in perovskite (400 – 700 cm^{-1}) are slightly visible, indicating that the reaction is not completed and that there is unreacted hydrazine present in samples. The FTIR spectrum bands come from the vibrational mode of hydrazine: N – H stretching, NH bending, and N – N stretching, and the torsional oscillation (Giguère & Liu, 1952). Pairs of bands at 814 and 855 cm^{-1} are from the symmetric v_6 NH_2 wagging mode, along with the band at 742 cm^{-1} which is due to v_7 wagging mode (Giguère and Liu, 1952). Bands that come from N – H stretching vibrations are positioned at 3475 and 3555 cm^{-1}, bands positioned at 1635 and 1800 cm^{-1} are from N – H bending vibrations (Giguère & Liu, 1952), while bands at 1040, 1319, 1450 cm^{-1} are from nitrates (Mihaylov et al., 2021). The fundamental N – N vibration is an essentially nonpolar bond, it is expected to be weak in the infrared spectrum, and it falls in a region of the NH wagging modes (Giguère & Liu, 1952).

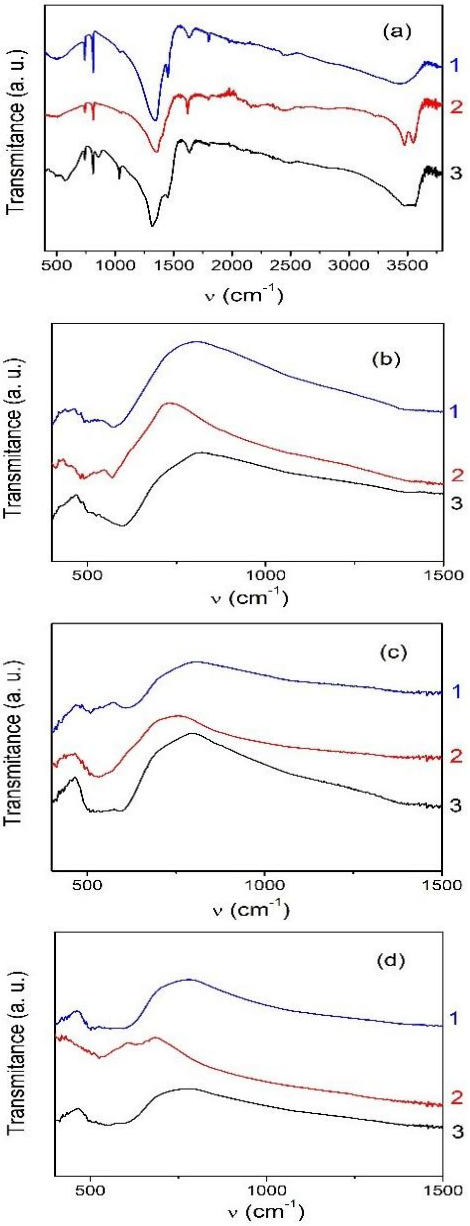

Figure 2. FTIR spectra of $Ca_{0.9}Er_{0.1}MnO_3$nanopowders: a) as-prepared, b) calcinated at 800 °C, c) calcinated at 900 °C, and d) calcinated at 1000 °C, for different amounts of hydrazine: 1 – 0.17 mol Hy, 2 – 0.33 mol Hy, and 3 – 0.5 mol Hy.

After calcination of synthesized materials, at 800, 900, and 1000 °C (Fig. 2 b, c, and d), vibrational modes that come from M – O bonds are more visible, while the band that comes from hydrazine disappears. For M – O bonds (M = Ca, Er, Mn), vibration bands are expected to be in a lower region of wavenumber, 400 – 600 cm^{-1}. From Figure 2 (b, c, and d), observing the spectra in the wavenumber region of 400 – 600 cm^{-1}, it can be seen that changes are presented due to hydrazine concentration and temperature calcination, indicating a structural change in the materials. FTIR results are in good agreement with XRD results. For a more detailed analysis of the FTIR spectra, we selected the spectra of $Ca_{0.9}Er_{0.1}MnO_3$ synthesized with 0.33 mol of hydrazine and calcined at 900 °C.

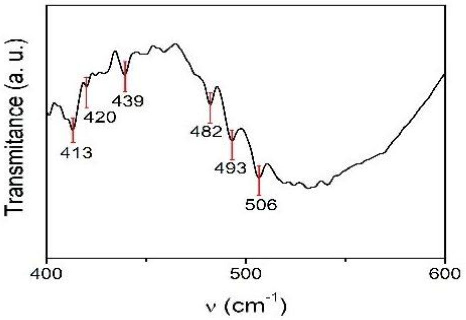

Figure 3. FTIR spectra for $Ca_{0.9}Er_{0.1}MnO_3$ synthesized with 0.33 mol of hydrazine and calcinated at 900 °C.

Figure 3presents the FTIR spectra of the synthesized perovskite material $Ca_{0.9}Er_{0.1}MnO_3$, calcined at 900 °C, within the 400–1000 cm^{-1} range, highlighting the positions of characteristic infrared bands. The observed bands are located at 413, 420, 439, 482, 493, and 506 cm^{-1}, along with a broad band spanning 520–570 cm^{-1}. All identified infrared bands are situated below 700 cm^{-1}, corresponding to vibrations within the Ca–Er–Mn–O framework. These results are consistent with previous FTIR studies of perovskite oxides (Macan et al., 2020, Mary et al., 2024, Rosić et al., 2015, Ansari et al., 2020). It can be observed that no bands appear above 700 cm^{-1} in the FTIR spectra (Fig. 2b, c, and d), indicating the elimination of NO_3^- groups from nitrates and the disappearance of hydrazine-related bands after calcination. The observed bands (Fig. 3) are assigned to O–Mn–O/Mn–O–Mn bending vibrations, and Mn–O asymmetric stretching vibrations of MnO_6octahedra (Macan et al., 2020, Mary et al., 2024). Compared to the position of infrared bands of $CaMnO_3$ (Macan et al., 2020), they are slightly moved due to Er doping, indicating the influence of Er on the crystal lattice.

However, the interpretation of spectra is complicated by the possibility that spectral differences may also arise from variations in the degree of edge-sharing between MnO_6 ctahedra (Julien & Massot, 2003). The full assignment of the bands in the 600–400 cm^{-1} range, therefore, requires further work.

Electrochemical properties of $Ca_{0.9}Er_{0.1}MnO_3$

$Ca_{0.9}Er_{0.1}MnO_3$ samples with different amounts of hydrazine (1 – 0.17 mol Hy, 2 – 0.33 mol Hy, and 3 – 0.5 mol Hy) were employed as electrode modifier and CV and EIS measurements were done in the presence of a stationary 5 mM $K_3[Fe(CN)]_6/K_4[Fe(CN)]_6$ (1:1) mixture as a redox probe in 0.1 M KCl solution. Based on cyclic voltammograms in Figure 4a, all modified electrodes showed improved electrocatalytic behavior compared to bare CPE. It is obvious that the material synthesized with the smallest amount of Hy was the material with the highest current conductivity. Anodic peak related to the oxidation of $Fe^{2+}\rightarrow Fe^{3+}$ was observed at 0.303 V, while the cathodic peak for the opposite reaction was observed at 0.157 V, with peak potential separation, ΔE, of 0.146 V. This suggested that the Fe^{2+}/Fe^{3+} redox couple on the modified carbon paste electrode showed a quasi-reversible behavior.

The CV results were further compared to EIS measurements presented at the graph Fig 4b: the smallest semicircle, formed by points at lower frequencies indicated better conductivity, the promoted electron exchange transfer on the electrode surface and improved catalytic activity.

CVs on different scan rates (10, 25, 50, 75, 100, 125, and 150 mV/s) for the modified electrode with the smallest amount of Hy (1 at CPE) are given in Figure 4c. A derivative linear plot obtained from it, which presents current vs. the square root of scan rate (Fig. 4d), shows that the dominant process at the electrode surface is the diffusion of electroactive species (Fe^{3+}/Fe^{2+}), while absorption and other processes are negligible.The linearity is described by Equation 2 obtained by regression analysis of the results, with an excellent correlation coefficient of 0.997.

$$I(\mathrm{A}) = -5.78\times10^{-6} + 1.31\times10^{-5}\times v^{1/2}(\mathrm{mV/s})^{1/2}; \quad (\mathrm{R}=0.997). \qquad (2)$$

From Figure 4d, and in the same way, recorded and analyzed results obtained from the CV profiles of the other modified electrodes (2 at CPE, 3 at CPE and bare CPE), the active electrode surface has been calculated, using Randles–Sevcik formula (3) for a reversible (and quasi-reversible) process (Rezaei and Damiri, 2008):

$$\mathrm{Ip} = 0.4463\times(\mathrm{F}^3/\mathrm{RT})^{1/2}\times \mathrm{n}^{3/2}\times \mathrm{A}_0\times \mathrm{D}_0^{1/2}\times \mathrm{C}^{1/2}. \qquad (3)$$

where T is 298 K, R is 8.314 J $Kmol^{-1}$, F is 96 480 C mol^{-1}, n is 1, D_0 is 7.6 × 10^{-6} cm^2 s^{-1} and C is 5 mM of $K_3[Fe(CN)]_6/K_4[Fe(CN)]_6$.The active areas of bare CPE and 1, 2 and 3 samples in CPE were $4.88\times10^{-2}cm^2$, 1.02 $\times10^{-2}$ cm^2, 7.30 $\times10^{-2}$ cm^2 and 5.50 $\times10^{-2}$ cm^2, respectively.

Bearing in mind the results obtained by applied electrochemical measurements and calculations, the perovskite nanopowder prepared with the smallest amount of Hy showed up as potentially the most suitable for application in electroanalysis and catalysis, although excellent results and shape of the CV profile are also obtained by a material with slightly more Hy in it (2 at CPE).

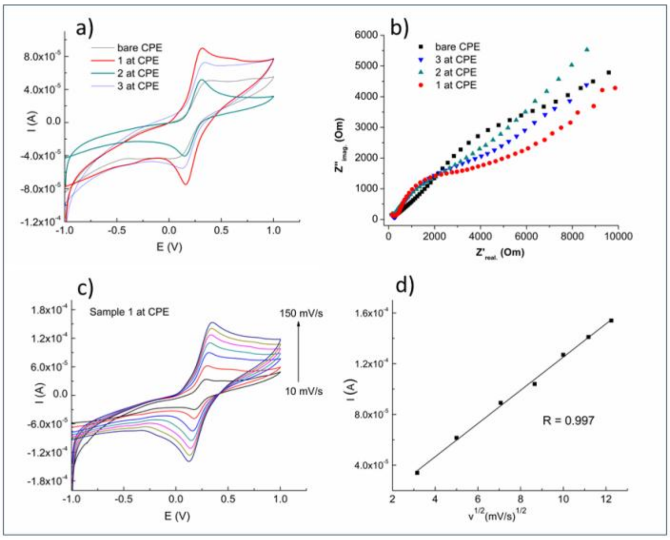

Figure 4. a) CV profiles of bare and perovskite-modified electrodes in in 0.1M KCl test solution containing 5 mM $[Fe(CN)_6]^{3-/4-}$ redox couple (scan rate 50 mV/s); b) EIS measurements in the same test solution; c) CV profiles at modified 1 at CPE in different scan rates (10, 25, 50, 75, 100, 125 and 150 mV/s); d) Graph of I *vs*square root of scan rate obtained from CV profiles on previous figure.

XRD analysis revealed that the sample synthesized with the lowest hydrazine concentration consisted of three phases: $CaMnO_3$, $ErMnO_3$, and Er_2O_3. The enhanced electrical conductivity observed for this material is in line with previous findings that multiphase perovskite systems often surpass their single-phase analogs in electrochemical performance. This improvement can be explained by several factors: the presence of multiple phases creates structural defects and interfacial regions that act as fast diffusion pathways for oxygen ions and charge carriers; secondary oxides contribute additional catalytic functionality; and local modifications of the chemical environment, such as variations in oxygen vacancy concentration and Mn oxidation states, further promote ionic/electronic conductivity and provide active sites for electrochemical reactions (Du et al., 2014). Previous investigations of multiphase $CaMnO_3/CaMn_2O_4$ systems have shown that the presence of phase boundaries and controlled microstructural features plays a critical role in enhancing both bulk and surface transport. Such improvements are directly relevant to electrochemical applications, where they translate into higher electronic conductivity and superior functional performance (Kanas et al., 2022).

CONCLUSION

Nanopowders with the nominal composition $Ca_{0.9}Er_{0.1}MnO_3$ were successfully synthesized by the combustion method using the hydrazine nitrate procedure (HNP). The influence of the hydrazine content on phase formation was systematically investigated. XRD analysis revealed the presence of three crystalline phases, and it was determined that a hydrazine ratio of 0.33 mol provides the most favorable conditions for obtaining a near-monocrystalline structure. FTIR spectra confirmed the incorporation of Er into the perovskite lattice. Thermal treatment studies showed that higher calcination temperatures improved crystallinity and promoted grain growth. Electrochemical measurements demonstrated that the highest electrical conductivity was achieved in the sample prepared with the lowest hydrazine content, which can be attributed to the formation of multiphase perovskite systems.

ACKNOWLEDGMENTS

This research was funded by the Ministry of Science, Technological Development and Innovation of the Republic of Serbia, based on Contract no. 451-03-137/2025-03/200123, Faculty of Sciences and Mathematics University of Priština in Kosovska Mitrovica, Project Number IJ-2301 and 451-03-136/2025-03/200017 through the realization of research theme 1702514 by “Vinča” Institute of Nuclear Sciences—National Institute of the Republic of Serbia, University of Belgrade.

REFERENCES

Ansari, A. A., Adil, S. F., Alam, M., Ahmad, N., Assal, M. E., Labis, J. P. & Alwarthan, A. 2020. Catalytic performance of the Ce-doped $LaCoO_3$ perovskite nanoparticles. Scientific Reports, 10, 15012. https://doi.org/10.1038/s41598-020-71869-z

Bayode, A. A., Ore, O. T., Nnamani, E. A., Sotunde, B., Koko, D. T., Unuabonah, E. I., Helmreich, B. & Omorogie, M. O. 2024. Perovskite Oxides: Syntheses and Perspectives on Their Application for Nitrate Reduction. ACS Omega, 9, pp. 19770-19785. https://pubs.acs.org/doi/10.1021/acsomega.4c01487

Bispo-Jr, A. G., de Morais, A. J., Calado, C. M. S., Mazali, I. O. & Sigoli, F. A. 2022. Lanthanide-doped luminescent perovskites: A review of synthesis, properties, and applications. Journal of Luminescence, 252, 119406. https://doi.org/10.1016/j.jlumin.2022.119406

Du, J., Zhang, T., Cheng, F., Chu, W., Wu, Z. & Chen, J. 2014. Nonstoichiometric Perovskite $CaMnO_3-\delta$ for Oxygen Electrocatalysis with High Activity. Inorganic Chemistry, 53, 9106-9114. https://pubs.acs.org/doi/10.1021/ic501631h

Dukić, J., Bošković, S. & Matović, B. 2009. Crystal structure of Ce-doped $CaMnO_3$ perovskite. Ceramics International, 35, pp. 787-790. https://doi.org/10.1016/j.ceramint.2008.02.023

Durai, L. & Badhulika, S. 2022. Current Challenges and Developments in Perovskite-Based Electrochemical Biosensors for Effective Theragnostics of Neurological Disorders. ACS Omega, 7, pp. 39491-39497. https://pubs.acs.org/doi/10.1021/acsomega.2c05591

Giguère, P. A. & Liu, I. D. 1952. On the Infrared Spectrum of Hydrazine. The Journal of Chemical Physics, 20, pp. 136-140. https://doi.org/10.1063/1.1700155

Julien, C. M. & Massot, M. 2003. Lattice vibrations of materials for lithium rechargeable batteries I. Lithium manganese oxide spinel. Materials Science and Engineering: B, 97, pp. 217-230. https://doi.org/10.1016/S0921-5107(02)00582-2

Kanas, N., Williamson, B. A. D., Steinbach, F., Hinterding, R., Einarsrud, M.-A., Selbach, S. M., Feldhoff, A. & Wiik, K. 2022. Tuning the Thermoelectric Performance of $CaMnO_3$-Based Ceramics by Controlled Exsolution and Microstructuring. ACS Applied Energy Materials, 5, pp. 12396-12407. https://pubs.acs.org/doi/10.1021/acsaem.2c02012

Katz, E. A. 2020. Perovskite: Name Puzzle and German-Russian Odyssey of Discovery. Helvetica Chimica Acta, 103, e2000061. https://doi.org/10.1002/hlca.202000061

Kraus, W. & Nolze, G. 1996. POWDER CELL - a program for the representation and manipulation of crystal structures and calculation of the resulting X-ray powder patterns. Journal of Applied Crystallography, 29, pp. 301-303. https://doi.org/10.1107/S0021889895014920

Kuganathan, N. & Chroneos, A. 2021. Defect and dopant properties in $CaMnO_3$. AIP Advances, 11, 055106. https://doi.org/10.1063/5.0048401

Macan, J., Brleković, F., Kralj, S., Supina, A., Gracin, D., Šantić, A. & Gajović, A. 2020. Soft chemistry synthesis of $CaMnO_3$ powders and films. Ceramics International, 46, pp. 18200-18207. https://doi.org/10.1016/j.ceramint.2020.04.142

Mary, S. B., Mohan, K. S. & Krishnan, M. M. 2024. Effect of A-site and B-site ion substitution on the electrical and thermoelectric properties of nanostructured perovskite $CaMnO_3$. Journal of Materials Science: Materials in Electronics, 35, 600. https://doi.org/10.1007/s10854-024-12351-8

Mihaylov, M. Y., Zdravkova, V. R., Ivanova, E. Z., Aleksandrov, H. A., Petkov, P. S., Vayssilov, G. N. & Hadjiivanov, K. I. 2021. Infrared spectra of surface nitrates: Revision of the current opinions based on the case study of ceria. Journal of Catalysis, 394, pp. 245-258. https://doi.org/10.1016/j.jcat.2020.06.015

Patil, K. C. H., M. S.; Rattan, T.; Aruna, S. T. 2008. Solution Combustion Synthesis of Oxide Materials. Chemistry of Nanocrystalline Oxide Materials. Singapore: World Scientific Publishing Co. Pte. Ltd. https://doi.org/10.1142/6754

Rezaei, B. & Damiri, S. 2008. Voltammetric behavior of multi-walled carbon nanotubes modified electrode-hexacyanoferrate(II) electrocatalyst system as a sensor for determination of captopril. Sensors and Actuators B: Chemical, 134, pp. 324-331. https://doi.org/10.1016/j.snb.2008.05.004

Rigaku 2011. PDXL Integrated X-Ray Powder Diffraction Software. In: RIGAKU (ed.). Tokyo, Japan.

Rosić, M., Kljaljević, L., Jordanov, D., Stoiljković, M., Kusigerski, V., Spasojević, V. & Matović, B. 2015. Effects of sintering on the structural, microstructural and magnetic properties of nanoparticle manganite $Ca_{1-x}Gd_xMnO_3$ (x=0.05, 0.1, 0.15, 0.2). Ceramics International, 41, pp. 14964-14972. https://doi.org/10.1016/j.ceramint.2015.08.041

Rosić, M., Logar, M., Devečerski, A., Prekajski, M., Radosavljević-Mihajlović, A., Kusigerski, V., Spasojević, V. & Matović, B. 2011. Synthesis, structural and magnetic properties of nanostructured $Ca_{0.9}Gd_{0.1}MnO_3$ obtained by modified glycine nitrate procedure (MGNP). Ceramics International, 37, pp. 1313-1319. https://doi.org/10.1016/j.ceramint.2010.12.015

Shannon, R. D. 1976. Revised effective ionic radii and systematic studies of interatomic distances in halides and chalcogenides. Acta Crystallographica Section A, 32, pp. 751-767. https://doi.org/10.1107/S0567739476001551

Shimizu, Y., Komatsu, H., Michishita, S., Miura, N. & Yamazo, N. 1996. Sensing characteristics of hydrogen peroxide sensor using carbon-based electrode loaded with perovskite-type oxide. Sensors and Actuators B: Chemical, 34, pp. 493-498. https://doi.org/10.1016/S0925-4005(97)80021-4

Srivastava, D., Azough, F., Freer, R., Combe, E., Funahashi, R., Kepaptsoglou, D. M., Ramasse, Q. M., Molinari, M., Yeandel, S. R., Baran, J. D. & Parker, S. C. 2015. Crystal structure and thermoelectric properties of Sr–Mo substituted $CaMnO_3$: a combined experimental and computational study. Journal of Materials Chemistry C, 3, pp. 12245-12259. https://doi.org/10.1039/C5TC02318A

Tadić, M., Marković, D., Panjan, M. & Spasojević, V. 2016. Solution combustion synthesis method and magnetic properties of synthesized polycrystalline calcium manganite $CaMnO_{3-\delta}$ powder. Ceramics International, 42, pp. 19365-19371. https://doi.org/10.1016/j.ceramint.2016.09.109

Xia, Z.-R., Li, R.-Q., Liu, F.-F., Tong, Y., Zheng, Q.-H., Ping, Z.-Y., Zhao, W., Zhou, W.-W. & Song, M.-J. 2025. Upconversion and Downconversion Luminescence of $CaLaLiTeO_6$:Mn^{4+}/Er^{3+} Phosphors for Dual-Mode Optical Thermometry and Anti-Counterfeiting Application. Inorganics, 13, 308. https://doi.org/10.3390/inorganics13090308

Yadav, R. S., Kumar, D., Kanwal, M., Singh, A. K. & Rai, S. B. 2020. Synthesis Techniques and Applications of Perovskite Materials. In: TIAN, H. (ed.) Perovskite Materials, Devices and Integration. Rijeka: Intech Open. DOI: 10.5772/intechopen.86794

Yang, P., Tai, B., Wu, W., Zhang, J.-M., Wang, F., Guan, S., Guo, W., Lu, Y. & Yang, S. A. 2017. Tailoring lanthanide doping in perovskite $CaTiO_3$ for luminescence applications. Physical Chemistry Chemical Physics, 19, pp. 16189-16197. https://doi.org/10.1039/C7CP01953J

International Crystallographical Database (ICDD); PDF-2, Release 2023; ICDD: Newtown Square, PA, USA, 2012.

https://icsd.products.fiz-karlsruhe.de/ (accessed on 10 September 2025).

http://powdercell-for-windows.software.informer.com/2.4/ (accessed on 10 September 2025).

Bulletin of Natural Sciences Research
Vol. 15, No. 1, 2025, pp. 34-41.

DOI: https://doi.org/10.5937/bnsr15-55046
Original Scientific Paper

EXPLORING THE NEXUS OF TOURISM DEVELOPMENT, COMMUNITY PERCEPTIONS, AND SUSTAINABILITY IN PROTECTED AREAS

SANJA OBRADOVIĆ STRÅLMAN[1], NIKOLA MILENTIJEVIĆ[2]

[1]Faculty of Sciences, Department of Geography, Tourism and Hotel Management, University of Novi Sad, Novi Sad, Serbia
[2]Faculty of Sciences and Mathematics, Department of Geography, University of Priština, Kosovska Mitrovica, Serbia

ABSTRACT

Sustainable tourism integrates economic, social, and environmental aspects of sustainability. This study investigates the local community's perceptions of tourism development impacts and factors influencing support for sustainable tourism and destination sustainability within Stara Planina Nature Park. Using a Structural Equation Modeling (SEM) approach, using multiple hypothesized relationships across key dimensions, including economic, environmental, social, and infrastructural impacts are examined. The findings highlight the importance of socio-cultural factors in fostering support, while also recognizing the negative impact of environmental and infrastructural concerns. Socio-cultural impacts significantly and positively influenced support for sustainable tourism and destination initiatives, highlighting the role of cultural exchange, tradition preservation, and community identity in garnering local support. These findings align with previous studies, emphasizing the importance of perceived socio-cultural benefits in fostering community backing for tourism development. Effective STD management requires the active involvement of local stakeholders to ensure alignment with local values and environmental goals. Policymakers should focus on enhancing socio-cultural benefits, addressing infrastructural challenges, and effectively communicating economic advantages. Limitations of the study include its cross-sectional design, suggesting the need for longitudinal research to better understand the evolving impact of tourism.

Keywords: Sustainable tourism, Destination sustainability, Local community, Tourism impact, Residents' support, Protected areas.

INTRODUCTION

Tourism development plays a very important role in sustainable development, which offers opportunities and challenges for the local community (Reindrawati, 2024). As tourism globally expands, destinations focus more and more on strategies that will enable a balance of social, economic and environmental impacts to ensure long-term sustainability (Nguyen et al., 2024). The tourism economic benefits include the possibility of employment for locals, an increase in income, and the growth of entrepreneurship, and mainly there are certain social changes and changes in infrastructure (roads, electricity, sewerage, improvement of public services) (Baloch et al., 2023). Contrary to the benefits, the uncontrolled development of tourism can lead to damage to the local ecosystem and certain problems that disrupt community life, which indicates the necessity of sustainable practices (Kapera, 2018).

Local communities are key stakeholders, and necessary for sustainable tourism development (Wondirad & Ewnetu, 2019). The way they see the changes brought by tourism - the impacts of development, whether they are environmental, social, economic or infrastructural, will have a lot to do with their decision whether to support further tourism development or not (Riyanto et al., 2023). The involvement of the local population will not only reflect their attitudes towards the development of tourism but will also strengthen ownership and resilience of sustainable practices (Marzo et al., 2023). When local people are involved in the decision-making process and tourism development activities, it will enable the development to be in accordance with local values, needs and traditions, which will enable a foundation for destination resilience, and lasting tourism development support (Han et al., 2023)

The current study aims to investigate these dynamics in Stara Planina Nature Park (NP), focusing on how local communities perceive and support tourism development across multiple dimensions. In this way, it will contribute to the understanding of these interactions and the local community's importance, and their necessity for achieving sustainable tourism outcomes. Considering the topic's significance, even though a significant number of studies focused on tourism-related community perception (Gautam & Bhalla, 2024; Wondirad & Ewnetu, 2019; Reindrawati, 2024; Uslu et al., 2023), it is very important to examine the attitudes of the local population in protected areas, in order to avoid the negative

---

* Corresponding author: nikola.milentijevic@pr.ac.rs

tourism impacts and degradation. The primary goals of the current study are to create and evaluate a structural equation model (SEM) using a resident-oriented approach, including four-dimensional tourism impacts and tourism development support. Thus, the article adds to the corpus of literature currently available on sustainable tourism by highlighting the importance of community perception and how it influences tourism support. The paper tries to present a theoretical and practical explanation of communities' support in nature protected areas and tourism. The study's conclusions can be utilized by policymakers and community members to draft regulations and take other useful steps that will include communities more and encourage environmental preservation and sustainable development.

This paper first emphasizes local community involvement and support, sustainable tourism and nature protected areas, tourism impacts. The following focuses on factors that result from local community perception of impacts and support and develop research hypotheses. Then, the specifics of the case study, research instrument, and data analysis are discussed. The results were followed by discussions, conclusions and implications for nature protected area sustainable tourism development through community support.

LITERATURE REVIEW

Sustainable tourism development (STD) and nature-protected areas

Sustainable development in protected natural areas (NPAs) primarily focuses on the balance of conservation through tourism development and fulfilling the needs of local communities (Wang et al., 2024). STD points to the importance of protecting biodiversity, cultural heritage and ecosystems while simultaneously focusing on the promotion of responsible tourism that will bring benefits to the local population while minimizing negative impacts (Agarwal et al., 2024). Effective management of STD implies the involvement of local stakeholders, residents and businesses in decision-making processes to ensure that development is in line with environmental goals (Mardiani et al., 2024). Research (Baloch et al., 2023; Han et al., 2023; Pérez-Calderón et al., 2024) has shown that integrating sustainable tourism practices into NPAs can lead to favorable effects of tourism growth, such financial gains for the community, then revenues that will be further used for area protection and heritage preservation. However, to make everything possible it is necessary to involve the local population because ignoring them could lead to rebellions and fatal consequences (Sarr et al., 2020). Therefore, active involvement of the local community in tourism development is essential for fostering sustainable growth, ensuring equitable distribution of benefits, and enhancing residents' sense of ownership and commitment to conservation efforts.

Importance of local community participation and support

Local community participation is very important, if not crucial, for the success and sustainability of tourism in protected areas (Obradović et al., 2022; Wondirad & Ewnetu, 2019). When the local population is involved, development is enabled that takes into account their needs, values, heritage and traditions, while ensuring the promotion of ownership and resilience (Leal Filho et al., 2022; Reindrawati, 2024). When the local support is secured, they will enjoy the „fruits” of tourism development through income, new job opportunities, entrepreneurship, which are vital parts of healthy rural development and retention of young people in the area (Pezeshki et al., 2023). In order to enable conservation and preservation efforts, local involvement is necessary because of their knowledge and practices that can promote sustainable practices and reduce heritage degradation (Obradović et al., 2023). On the contrary, if there is insufficient involvement of locals, it can lead to resistance, which will lead to negative consequences for tourism initiatives, environmental and social sustainability (Mariam et al., 2024). All in all, the local community support is necessary and represents the basis of STD through integrating local perspectives, minimizing conflicts between community interests and tourism objectives, and ensuring long-term benefits (Han et al., 2023; Tong & Yang, 2024).

The local population's support depends mostly on how they view the effects of tourism, whether positive or negative (Riyanto et al., 2023). If the local population sees tourism as something useful, good - for example, it brings new jobs, improves public services and infrastructure, enables the preservation of natural and cultural heritage, there is a greater chance that they will support tourism initiatives (Yayla et al., 2023). Conversely, if they are concerned about negative impacts such as increased crime rates, congestion, degradation of cultural and natural resources, or increased prices, this can lead to resistance (García-Buades et al., 2022). That is why it is necessary to investigate the local population perception towards the effects of tourism, which can help policymakers when forming tourism development strategies that will include the concerns of the locals, promote support and enable development that is in line with sustainability goals and the interests of the local community. For sustainable tourism development plans to be implemented successfully, community cooperation is essential, particularly in places that are protected by nature (Nugroho & Numata, 2020).

Impacts arising from tourism development and the local community's perception

The development of tourism brings many changes that can be economic, social, environmental, etc. and they greatly affect the views of the local population about tourism (Alamineh et al., 2023). When these changes are positive, for example growth and development of the local economy, employment opportunities, improved infrastructure, it will lead to a positive opinion of the locals about tourism and their support for further development (Javadan et al., 2024). On the contrary, when these are negative consequences, for example increased living costs, degradation, congestion, it can often lead to resistance from the local population (Linderova et al., 2021).

How local people view impacts plays a key role in determining their support for tourism initiatives (Han et al., 2023). Previous research (Han et al., 2023; Liu et al., 2023; Su & Swanson, 2019) has shown that when the benefits of development outweigh the costs, the local population is more likely to show support and get involved in the development. On the other hand, negative effects can lead to local opposition that can prevent further development of tourism (García-Buades et al., 2022). Understanding these perceptions is crucial through the definition and development of tourism strategies that enable a balance between the local community benefits and the goals of sustainable development, and which focuses on the inclusion of the local population and therefore supportive of tourism initiatives (Obradović & Tešin, 2023).

Based on the theoretical background, the research model can be proposed (Figure 1) and the following hypotheses can be formulated:

H1. Perception of environmental impacts is reflected in a) support for STD and b) support for a sustainable destination.

H2. Perception of economic impacts is reflected in a) support for STD and b) support for a sustainable destination.

H3. Perception of cultural impacts and social impacts is reflected in a) support for STD and b) support for a sustainable destination.

H4. Perception of infrastructural impacts is reflected in a) STD support and b) sustainable destination support.

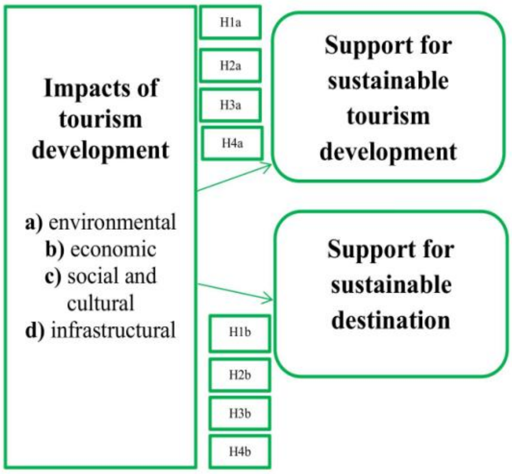

Figure 1. Proposed Research Model and Hypotheses.

MATERIALS AND METHODS

Case Study Area: Stara Planina Nature Park (SPNP)

The SPNP, which is also known as the Balkan Mountain Range, is located in eastern Serbia and stretches across the border with Bulgaria. This nature park, which is in the process of being declared a national park, is recognized for its different ecosystems, numerous species of fauna and flora, waterfalls, valleys, canyons (Institute for Nature Conservation of Serbia, 2024). This protected area is managed to ensure the preservation of biodiversity while supporting sustainable tourism and development (Stankov et al., 2011). In addition to natural values, there are also numerous traditional villages where the local population relies on agriculture, livestock farming, but also on the increasingly growing tourism activities. As part of the PAs network of Serbia, Stara Planina is one of the key destinations for nature-based activities, ecotourism and hiking (Marjanović et al., 2022). Since many endemic species are found here, their preservation is of the utmost importance. Managing the challenges that arise to balance the growth and development of tourism and the preservation of cultural and natural heritage, presents this area as an ideal setting for researching the attitudes of the local population as well as their support for sustainable tourism practices and initiatives. This area has incredible potential for sustainable tourism due to its natural resources, but also cultural, village, folklore and tradition.

Data Collection

The research was conducted in January and February 2021 in four municipalities where SPNP extends: Zaječar, Pirot, Knjaževac and Dimitrovgrad. Due to the restrictions caused by COVID-19, the research was conducted online, by creating a questionnaire in Google Forms and posting it on social media.

The questionnaire was shared primarily through Facebook and Instagram, targeting local community groups, municipal government pages, and forums related to tourism in the selected municipalities. Posts encouraged participants to share the survey within their networks to reach a broader audience.

It was clearly explained to the participants that participation is voluntary, anonymous, and that the results of the survey will be used exclusively for scientific research purposes. While this approach facilitated rapid data collection under pandemic restrictions, it may have introduced sampling biases, as individuals without internet access or social media presence were excluded. Future research should explore complementary methods to ensure inclusivity and mitigate potential limitations.

Questionnaire Design

The questionnaire comprised three main sections:

1. Socio-Demographic Characteristics
2. Tourism Impacts Perception
3. Tourism Development Support (Sustainable Development and Destination Sustainability).

In the second and third section of the questionnaire, statements were adjusted from previous research (Eraqi, 2007; Eshliki & Kaboudi, 2012; Hanafiah et al., 2013; Mureșan et al., 2016), translated into Serbian and first tested on a small number of respondents. When it was determined that the questions were comprehensible, the questionnaire was distributed to the residents of the aforementioned municipalities. These responses were analyzed on a five-point Likert scale. A total of 440 valid questionnaires were collected, margin of error 4.5% and confidence level 95.

Analysis

The data collected from the questionnaires were analyzed using IBM SPSS and AMOS software. To assess validity, Pearson's correlation was evaluated at a 5% significance level. The suitability of the data for factor analysis was confirmed with the Kaiser-Meyer-Olkin (KMO) test, which yielded a value of 0.807, indicating meritorious sampling adequacy. Bartlett's test of sphericity confirmed the reliability of the data with a significant result ($\chi^2(435) = 15.553{,}477$ $p < 0.001$). Common method bias was ruled out, and skewness and kurtosis values were within acceptable ranges. Internal reliability was assessed using Cronbach's Alpha, composite reliability (CR), and average variance extracted (AVE). Descriptive statistics were calculated to profile respondents, and model fit was evaluated using fit indices such as GFI, CFI, RFI, AGFI, SRMR, NFI, TLI, and RMSEA. After confirming validity and reliability, the hypotheses were tested for significance.

RESULTS

Of the total number of respondents who live near STNP, 51% are women, and 49% are men, so it is mostly equal by gender (Table 1). The average age of the respondents is 42 years, and the majority have completed high school and are employed (more than half). Most of the people earn less than average.

When looking at the results shown in Table 2, it can be said that internal consistency is achieved because all alpha values are greater than 0.70 (Hair et al. 2021) even above 0.80.

A SEM model was created, and values were tested to approach the hypotheses' analysis. The model values show that the overall fit is acceptable, reasonable (Kline 2016): $\chi 2$ (122)=319,599, p=0.000, CMIN=2.620, RMSEA=0.071, SRMR=0.019, NFI=0.965, RFI=0.921, IFI=0.971, GFI=0.925, AGFI=0.810, TLI=0.935, CFI=0.971. All items were statistically significant to the factors they belong to, and it can be said that the data set supports a model of six dimensions and 30 items.

Table 1. Sociodemographic attributes of the respondents (n=440).

Gender		**Employment**	
Male	49.0%	Student	5.50%
Female	51.0%	Employed	67.0%
Age		Unemployed	14.80%
		Housewife	5.70%
Average age = 42 Std. = 12.635 Age range (18 – 80)		Retiree	6.82%
		Income	
		Less than average (510€)	60.20%
		Average	33.0%
		More than average	6.80%
Education			
Elementary school	2.30%		
High school	53.40%		
Bachelor's degree	38.0%		
Master's degree/PhD degree	6.30%		

Table 2. Descriptive statistics and measurement model validity.

Variables	Mean	Cronbach's alpha	AVE	CR
EI	3.02	0.876	0.594	0.874
ECI	4.26	0.904	0.512	0.658
SCI	4.36	0.925	0.573	0.755
II	4.07	0.949	0.848	0.750
SSTD	4.42	0.938	0.530	0.705
SSD	4.25	0.922	0.512	0.682

If we look at individual values, you can see that RMSEA is still in the acceptable range, between 0.05 and 0.08, and that the values of NFI, RFI, IFI, GFI, TLI and CFI are above 0.90 (AGFI was slightly lower). the model fit is good and even above the standard cut off points (Kim et al., 2016). When the validity of the model has been established, the next step is to establish construct validity (Hair et al. 2021). To achieve convergent validity of data, factor loadings should be above 0.5 and statistically significant. The values of factor loadings for all items ranged from 0.600 to 0.938, which is an indicator of strong convergent validity. In addition, it is important that the AVE values are above 0.5 and CR above 0.6, which can be seen from Table 2 that it was also achieved.

The results shown in Table 3 show the discriminant validity. As suggested by Hair et al. (2021), if the root of AVE is greater than the correlation value for each dimension, it is considered that discriminant validity has been achieved. As can be seen, each examined dimension shows discriminant validity.

Table 3. Discriminant Validity.

	EI	ECI	SCI	II	SSTD	SSD
EI	0.771					
ECI	0.321	0.715				
SCI	0.204	0.706	0.757			
II	0.097	0.702	0.723	0.921		
SSTD	0.002	0.339	0.505	0.287	0.728	
SSD	0.110	0.341	0.550	0.375	0.701	0.715

* Correlations are off-diagonal elements; the AVE's square root represents diagonal elements.

Since the internal consistency of the data and convergence, as well as the validity of the model and discriminant validity have been determined, it is justified to test the hypotheses. Hypothesis testing was performed based on SEM and CFA analysis and is shown in Table 4.

Table 4. Hypothesis testing.

	Relationship	**Beta**	**Std.Error**	**C.R.(t)**	**Status**
H1a	EI to SSTD	-0.112*	0.042	-2.572	Supported
H1b	EI to SSD	-0.210*	0.045	-5.124	Supported - negative
H2a	ECI to SSTD	0.076	0.082	1.032	Not supported
H2b	ECI to SSD	0.168	0.087	2.401	Not supported
H3a	SCI to SSTD	0.772*	0.070	10.121	Supported
H3b	SCI to SSD	0.805*	0.074	11.158	Supported
H4a	II to SSTD	-0.239*	0.058	3.629	Supported
H4b	II to SSD	-0.101	0.062	-1.622	Not supported

Environmental impacts negatively influence support for sustainable tourism development (β = -0.112*), as do infrastructural impacts (β = -0.239*). However, socio-cultural impacts positively influence support (β = 0.772*), confirming hypotheses H1a, H3a, and H4a. Economic impacts, however, do not significantly influence residents' support, so H2 is not confirmed for either sustainable development or destination support.

Regarding support for a sustainable destination, environmental impacts negatively influence support (β = -0.210*), while socio-cultural impacts positively do so (β = 0.805*), confirming H1b and H3b. Infrastructural impacts (H4b) were not supported.

In total, five out of eight hypotheses were confirmed, with two relationships showing negative influences, as detailed in Table 4 (p-value = 0.001).

DISCUSSION

The findings of this study reveal important insights into the factors influencing residents' support for sustainable tourism development and sustainable destinations. The local population's support for tourism largely hinges on their perception of its impacts. Understanding these perceptions is vital for policymakers to develop tourism strategies that address local concerns, encourage support, and align with sustainability goals and community interests. This approach ensures balanced development that benefits both tourism and the local population.

Environmental impacts were shown to negatively influence support for both sustainable tourism development and destination support. This means that the locals of Stara Planina are concerned about the environmental degradation that tourism may cause and therefore would not support either the destination or its further development.. This highlights the importance of addressing environmental concerns when implementing tourism policies in ecologically sensitive areas. Infrastructural impacts, similarly, were found to negatively affect support for tourism development, indicating that inadequate or inappropriate infrastructure may hinder positive community perceptions.

These findings are in line with Linderova et al. (2021) and García-Buades et al. (2022) who stated that negative consequences, for example degradation, congestion or lack of infrastructure can often lead to resistance from the local population and their lack of support.

On the other hand, socio-cultural impacts were found to have a strong positive influence on support for both sustainable tourism development and destination support. This aligns with prior research (Javadan et al., 2024; Linderova et al., 2021) suggesting that communities tend to support tourism initiatives when they recognize cultural and social benefits, such as increased cultural exchange, preservation of traditions, and enhanced community identity.

Economic impacts, however, were not found to significantly influence support for sustainable tourism or destination development. This lack of a significant relationship contradicts expectations, potentially due to the perceived short-term economic costs or the absence of tangible economic benefits felt by the community. Further research may explore why economic impacts do not play as significant a role in shaping support, particularly in areas where the long-term benefits of tourism are still not fully realized by residents.

These findings confirm five out of eight hypotheses, emphasizing the importance of socio-cultural impacts in fostering community support for sustainable tourism and destination development. The negative influence of environmental and infrastructural impacts suggests that managing these aspects is crucial for sustaining positive attitudes toward tourism development. Infrastructural improvements and environmental protection measures are key to ensuring the success of sustainable tourism initiatives.

CONCLUSION

This study contributes to the theoretical understanding of how different impacts affect local community support for sustainable tourism development and destination sustainability. The results underscore the significant role of socio-cultural factors, while also highlighting the negative effects of environmental and infrastructural concerns. Effective management of STD requires the active participation of local stakeholders, residents, and businesses in decision-making. This involvement ensures that development aligns with environmental goals and addresses local needs, values, and traditions. Local community engagement not only fosters ownership and resilience but also generates economic benefits, such as income, new job opportunities, and entrepreneurship. These factors contribute to healthy rural development and help retain young people in the area, making local support crucial for the long-term success and sustainability of tourism in protected areas.

From a practical standpoint, these findings suggest that policymakers should prioritize socio-cultural benefits, address environmental and infrastructural issues, and ensure that economic benefits are effectively communicated to the local community.

Despite the contribution of these findings, this study has several limitations. First, the cross-sectional design limits the ability to infer causal relationships. Longitudinal studies could provide more insight into how perceptions change over time as communities experience the tangible impacts of tourism development. Additionally, the absence of a significant relationship with economic impacts calls for further exploration of how economic benefits are communicated to local communities. Future research could investigate whether perceived economic benefits take time to materialize and how they are perceived differently across various demographic groups.

REFERENCES

Agarwal, R., Mehrotra, A., Mishra, A., Rana, N. P., Nunkoo, R. & Cho, M. 2024. Four decades of sustainable tourism research: Trends and future research directions. 0International Journal of Tourism Research, 26(2), e2643. https://doi.org/10.1002/jtr.2643

Alamineh, G. A., Hussein, J. W., Endaweke, Y. & Taddesse, B. 2023. The local communities' perceptions on the social impact of tourism and its implication for sustainable development in Amhara regional state. Heliyon, 9(6), e17088. https://doi.org/10.1016/j.heliyon.2023.e17088

Baloch, Q. B., Shah, S. N., Iqbal, N., Sheeraz, M., Asadullah, M., Mahar, S. & Khan, A. U. 2023. Impact of tourism development upon environmental sustainability: a suggested framework for sustainable ecotourism. Environmental Science and Pollution Research International, 30(3), pp. 5917-5930. https://doi.org/10.1007/s11356-022-22496-w

Eraqi, M. I. 2007. Local communities' attitudes towards impacts of tourism development in Egypt. Tourism Analysis, 12(3), pp. 191-200. https://doi.org/10.3727/108354207781626848

Eshliki, S. A. & Kaboudi, M. 2012. Perception of community in tourism impacts and their participation in tourism planning: Ramsar, Iran. Journal of Asian Behavioral Studies, 2(5), pp. 51-64. https://doi.org/10.21834/jabs.v2i5.176

García-Buades, M. E., García-Sastre, M. A. & Alemany-Hormaeche, M. 2022. Effects of overtourism, local government, and tourist behavior on residents' perceptions in Alcúdia (Majorca, Spain). Journal of Outdoor Recreation and Tourism, 39, 100499. https://doi.org/10.1016/j.jort.2022.100499

Gautam, V. & Bhalla, S. 2024. Exploring the relationships among tourism involvement, residents' empowerment, quality of life and their support for sustainable tourism development. Journal of Cleaner Production, 434, 139770. https://doi.org/10.1016/j.jclepro.2023.139770

Hair, J. F., Hult, G. T. M., Ringle, C. M., Sarstedt, M., Danks, N. P. & Ray, S. 2021. Evaluation of reflective measurement models. In Partial least squares structural equation modeling (PLS-SEM) using R (pp. 87-135). Springer. https://doi.org/10.1007/978-3-030-80519-7_4

Han, S., Ramkissoon, H., You, E. & Ja Kim, M. 2023. Support of residents for sustainable tourism development in nature-based destinations: Applying theories of social exchange and bottom-up spillover. Journal of Outdoor Recreation and Tourism, 43, 100643. https://doi.org/10.1016/j.jort.2023.100643

Hanafiah, M. H., Jamaluddin, M. R. & Zulkifly, M. I. 2013. Local community attitude and support towards tourism development in Tioman Island, Malaysia. Procedia - Social and Behavioral Sciences, 105, pp. 792-800. https://doi.org/10.1016/j.sbspro.2013.11.082

Javdan, M., Jafarpour Ghalehteimouri, K., Soleimani, M. & colleagues, 2024. Community attitudes toward tourism and quality of life: A case study of Palangan village, Iran. Discover Environment, 2, Article 117. https://doi.org/10.1007/s44274-024-00154-x

Kapera, I. 2018. Sustainable tourism development efforts by local governments in Poland. Sustainable Cities and Society, 40, pp. 581-588. https://doi.org/10.1016/j.scs.2018.05.001

Kim, H., Ku, B., Kim, J. Y., Park, Y. J. & Park, Y. B. 2016. Confirmatory and exploratory factor analysis for validating the Phlegm Pattern Questionnaire for healthy subjects. Evidence-Based Complementary and Alternative Medicine, 2016, 2696019. https://doi.org/10.1155/2016/2696019

Kline, R. B. 2016. Principles and practice of structural equation modeling (4th ed.). Guilford Press.

Leal Filho, W., Levesque, V., Sivapalan, S., Salvia, A. L., Fritzen, B., Deckert, R., Kozlova, V., LeVasseur, T. J., Emblen-Perry, K., Azeiteiro, U. M., Paço, A., Borsari, B. & Shiel, C. 2022. Social values and sustainable development: community experiences. Environmental Sciences Europe, 34(1), 67. https://doi.org/10.1186/s12302-022-00641-z

Linderová, I., Scholz, P. & Almeida, N. 2021. Attitudes of Local Population Towards the Impacts of Tourism Development: Evidence From Czechia. Frontiers in Psychology, 12, 684773. https://doi.org/10.3389/fpsyg.2021.684773

Liu, Y. L., Chiang, J. T. & Ko, P. F. 2023. The benefits of tourism for rural community development. Humanities and Social Sciences Communications, 10, Article 137. https://doi.org/10.1057/s41599-023-01610-4

Mardiani, E., Adikarya, W. S., Dwyarthi, N. D. M. S. & Guna, B. W. K. 2024. Exploring sustainable tourism development strategies: A case study. Indonesia Journal of Engineering and Education Technology (IJEET), 2(2), pp. 214-220. https://doi.org/10.61991/ijeet.v2i2.40

Mariam, K., Singh, M., Yaja, M. I. & Kumar, A. 2024. Negative perception of the local community towards tourism development. Tourism and Hospitality Management, 30(1), pp. 15-25. https://doi.org/10.20867/thm.30.1.2

Marjanović, M., Milenković, J., Lukić, M., Tomić, N., Antić, A., Marković, R., Atanasijević, J., Božić, D., Buhmiler, S., Radaković, M., Radivojević, A., Milićević, A., Gavrilov, M. & Marković, S. 2022. Geomorphological and hydrological heritage of Mt. Stara Planina in SE Serbia: From river protection initiative to potential geotouristic destination. Open Geosciences, 14(1), pp. 275-293. https://doi.org/10.1515/geo-2022-0340

Marzo, R. R., Chen, H. W. J., Anuar, H., Abdul Wahab, M. K., Ibrahim, M. H., Ariffin, I. A., Ahmad, A. I., Kawuki, J. & Aljuaid, M. 2023. Effect of community participation on sustainable development: An assessment of sustainability domains in Malaysia. Frontiers in Environmental Science, 11, Article 1268036. https://doi.org/10.3389/fenvs.2023.1268036

Mureșan, I. C., Oroian, C. F., Harun, R., Arion, F. H., Poruțiu, A., Chiciudean, G. O., Todea, A. & Dumitraș, D. E. 2016. Local residents' attitude toward sustainable rural tourism development. Sustainability, 8(1), 100. https://doi.org/10.3390/su8010100

Nguyen, T. D., Nguyen, N. T. & Thanh, N. N. 2024. Factors Affecting Sustainable Tourism Development: Evidence from the Central Highlands of Vietnam. Sage Open, 14(2). https://doi.org/10.1177/21582440241240816

Nugroho, P., & Numata, S. 2020. Resident support of community-based tourism development: Evidence from Gunung Ciremai National Park, Indonesia. Journal of Sustainable Tourism, 30(11), pp. 2510-2525. https://doi.org/10.1080/09669582.2020.1755675

Obradović, S., Stojanović, V., Knežević, S. M. & Milić, D. 2022. The importance of local community attitudes for sustainable tourism in protected areas: The case of Tikvara Nature Park, Serbia. Eastern European Countryside, 28(1), pp. 127-153. https://doi.org/10.12775/eec.2022.006

Obradović, S., Stojanović, V. & Milić, D. 2023. The importance of understanding local community attitudes and perceptions regarding nature conservation. Wetlands, 43(2). https://doi.org/10.1007/s13157-022-01652-5

Obradović, S. & Tešin, A. 2023. Local communities' perceptions of tourism planning in natural areas. Tourism and Hospitality, 4(2), pp. 336-354. https://doi.org/10.3390/tourhosp4020021

Pérez-Calderón, E., Miguel-Barrado, V. & Prieto-Ballester, J. M. 2024. Tourism in protected areas in Spain: Perception of sustainable development in protected areas with different levels of protection. Geoheritage, 16, p. 17. https://doi.org/10.1007/s12371-024-00929-x

Pezeshki, F., Khodadadi, M. & Bagheri, M. 2023. Investigating community support for sustainable tourism development in small heritage sites in Iran: A grounded theory approach. International Journal of Heritage Studies, 29(8), pp. 773-791. https://doi.org/10.1080/13527258.2023.2220316

Reindrawati, D. Y. 2023. Challenges of community participation in tourism planning in developing countries. Cogent Social Sciences, 9(1). https://doi.org/10.1080/23311886.2022.2164240

Riyanto, Iqbal, M., Supriono, Fahmi, M. R. A. & Yuliaji, E.S. 2023. The effect of community involvement and perceived impact on residents' overall well-being: Evidence in Malang marine tourism. Cogent Business & Management, 10(3). https://doi.org/10.1080/23311975.2023.2270800

Sarr, B., González-Hernández, M. M., Boza-Chirino, J. & de León, J. 2020. Understanding communities' disaffection to participate in tourism in protected areas: A social representational approach. Sustainability, 12(9), p. 3677. https://doi.org/10.3390/su12093677

Stankov, U., Stojanović, V., Dragićević, V. & Arsenović, D. 2011. Ecotourism: An alternative to mass tourism in Nature Park “Stara Planina.” Journal of the Geographical Institute "Jovan Cvijic," SASA, 61(1), pp. 43-59. https://doi.org/10.2298/IJGI1101043S

Su, L. & Swanson, S. R. 2019. The effect of personal benefits from, and support of, tourism development: The role of relational quality and quality-of-life. Journal of Sustainable Tourism, 28(3), pp. 433-454. https://doi.org/10.1080/09669582.2019.1680681

Tong, J., Li, Y., & Yang, Y. (2024). System construction, tourism empowerment, and community participation: The sustainable way of rural tourism development. Sustainability, 16(1), 422. https://doi.org/10.3390/su16010422

Uslu, A., Erul, E., Santos, J. A. C., Obradović, S. & Custódio Santos, M. 2023. Determinants of residents' support for sustainable tourism development: An empirical study in

Midyat, Turkey. Sustainability, 15(13), p. 10013. https://doi.org/10.3390/su151310013

Wang, W., Ma, T., Russo, I.-R., Sang, W. & Li, B. V. 2024. Editorial: Biodiversity conservation and sustainable development of protected areas. Frontiers in Ecology and Evolution, 12, p. 1454366. https://doi.org/10.3389/fevo.2024.1454366

Wondirad, A. & Ewnetu, B. 2019. Community participation in tourism development as a tool to foster sustainable land and resource use practices in a national park milieu. Land Use Policy, 88, p. 104155. https://doi.org/10.1016/j.landusepol.2019.104155

Yayla, Ö., Koç, B. & Dimanche, F. 2023. Residents' support for tourism development: Investigating quality-of-life, community commitment, and communication. European Journal of Tourism Research, 33, p. 3311. https://doi.org/10.54055/ejtr.v33i.2762

Bulletin of Natural Sciences Research
Vol. 15, No. 1, 2025, pp. 42-47.

DOI: https://doi.org/10.5937/bnsr15-56225
Original Scientific Paper

SPECIFICITY OF GEOGRAPHICAL CONTENT FOR THE APPLICATION OF DEBATE IN GEOGRAPHY LESSONS

IVANA ĐORĐEVIĆ[1*]

[1]University of Belgrade – Faculty of Geography, Belgrade, Serbia

ABSTRACT

Modern geography teaching involves a more intensive use of methods designed to encourage students to learn with reason, to think reasonably and to draw independent conclusions. One of the methods that can contribute to achieving the above goals is certainly the use of debate and its increased implementation in geography lessons. Debating is a form of dialogic method that involves a discussion between two teams and the exploration of a given topic through argumentative practice. The paper analyzes the content of geography lessons that can be learned through debating and its application in the classroom from a theoretical and practical perspective. The first part of the paper is devoted to the theoretical foundations of teaching methods, the conceptual definition of debate, the Karl Popper format and the rules that should be applied in classroom practice. The second part of the paper deals with the application of debate in geography lessons using a content analysis with concrete examples from the subject. The results of the paper show the importance of debate for the development of skills that students in Serbia lack, including argumentative reasoning, public speaking, collaboration and research skills.

Keywords: Teaching methods, Debate, Karl Popper, Geography lessons, Logical thinking.

INTRODUCTION

Although it is said that learning is the result of one's own mental activity, it must be emphasized that it depends on the way teachers teach, i.e. on the teaching methods they use in their work. Among didacticians, pedagogues and other experts there is no unanimous opinion on the definition of the teaching method. The theoretical and practical question of its classification is also not universally valid. Depending on the concept of learning and memory when teaching certain subject matter, the teacher chooses the teaching methods that contribute most to learning efficiency. Care should always be taken to choose the method that most motivates students to conscious activity and independent work. The choice of teaching methods depends mainly on the learning content, the type of lesson, but also on the students (their age and cognitive abilities), the duration of the lesson, the material conditions of the school and other factors (Vranković, 2014).

In geography lessons there are opportunities to use almost all teaching methods, and debate is certainly one of them. Debate as a form of dialogic method is a structured discussion on a specific topic between two teams, one of which advocates a certain point of view while the other rejects it. Its use in geography lessons contributes to the achievement of numerous objectives, the most important of which are: the development of critical thinking, social and communication skills, democratic behavior and self-esteem. Participating in a debate involves engaging with or exploring a topic through the argumentative presentation of positions. Furthermore, debate requires active participation, i.e. its application in the classroom requires activity without passive participants.

The paper is based on the theoretical framework, which refers to previous research in the field of teaching methods and their application in geography education. It then analyzes the characteristics and elements of the debate teaching method, focusing on the Karl Popper format as one of the most commonly used forms of debate in classroom practice. The role of debate in the acquisition of geographical content is a special chapter of the thesis, in which the analysis of content was carried out using concrete examples within the subject.

THEORETICAL FRAMEWORK OF TEACHING METHODS RESEARCH

Considering the basic stages of the teaching process, all teaching methods can be divided into two large groups, namely: a) methods for acquiring knowledge, skills and habits, that is, methods for processing new content and b) methods for determining content (Živković et al., 2015).

Prodanović (1956) divides teaching methods into three groups: verbal-textual (oral presentation and conversation, discussion, work on texts and written papers), illustrative-demonstrational (illustrative papers and demonstrative papers) and laboratory-experimental (laboratory papers and performing experiments). According to Matas (1996), teaching methods are ways of working in teaching. "A teaching method is defined as a learned generalized pattern of behavior that can be applied in different teaching areas with the aim of facilitating and improving learning outcomes" (Vizek-Vidović et al., 2003). Research shows that the main elements of the definition of a teaching method (Terhart, 2001) are: orientation

---

* Corresponding author: ivana.djordjevic@gef.bg.ac.rs

towards the goal of teaching and learning, orientation towards the subject (content) of learning, orientation towards the student (teaching means) and orientation towards the school as an institution (institutional framework). Mattes (2007) defines teaching methods as procedures that the teacher applies in order to structure the course of teaching and achieve defined goals.

Different opinions on the definition of teaching methods arise because they start from different positions and understandings and take different criteria regarding what the method contains. All the definitions of the teaching method mentioned are similar to each other and indicate that the teaching method should mean the path and way of acquiring knowledge, skills and habits in the best possible way with the activity of students and teachers (Živković et al., 2015). The application of teaching methods in direct work depends on the content of each teaching unit. Geography has special and specific methods that teachers use in teaching the curriculum. According to Matas (1996) they are mainly based on observation, data collection, determination, comparison, analysis, interpretation and systematization of knowledge.

RESULTS OF PREVIOUS RESEARCH ON THE APPLICATION OF DEBATE IN EDUCATION

Debate is a form of dialogic teaching method in which students are divided into groups that argue their views on a certain problem with the aim of solving it (Jovanović, 2019). In this way, students expand and connect knowledge from different fields, develop critical thinking and communication skills (Hall, 2011). In the debate, students express their opinions more freely and spontaneously, exchange experiences and research results. In order for the debate to be successful, it is necessary for the students to have certain data, experiences and experiences related to the topic that is the subject of the discussion. However, in addition to knowing the information, it is necessary for the students to be interested in the topic and to have a developed personal attitude about the researched problems. Therefore, the debate itself should be preceded by preparatory activities of the students. Students should be given specific assignments, tasks, preparation instructions, and sources of information on the basis of which they will be adequately prepared for the discussion (Živković et al., 2015).

During the implementation of the debate, it is possible to establish different forms of cognitive and socio-cognitive conflict through the confrontation of students' knowledge and experiences (Brown, 2015). In this way, they develop important intellectual and communicative abilities. The student develops the ability to analyze attitudes in relation to others and the ability to observe problems from the point of view of others (Brophy, 2004). In addition to the cognitive conflict during communication, there is also a relationship of cooperation that manifests itself through the joint construction of new knowledge, attitudes and behavioral habits (Roders, 2003; Ivić et al., 2001).

The opportunity to discuss different points of view on a topic in focus has been recognized in the literature as one of the key factors for acquiring knowledge and developing competencies (Doise et al., 1975; Mugny & Doise, 1978; Doise & Mugny, 1979; Light & Perret-Clermont, 1989; Schwartz, 1995; Schwartz et al., 2000; Howe et al., 2007; Schwartz & Linchevski, 2007; Howe, 2010; Buđevac et al., 2020). However, although the analysis of different points of view is very important for the creation of socio-cognitive conflict (Doise et al., 1975; Mugny & Doise, 1978; Doise & Mugny, 1979; Buđevac et al., 2020) and the subsequent acquisition of new knowledge and development of competencies, this will not happen if understanding is not the product of an argumentative debate – a discussion in which the response to different points of view is an argumentation (Muller Mirza et al., 2009). Today's studies define argumentation, not as the result of dialogue, but as a process that is part of interaction because it is jointly constructed by the interlocutors (Kuhn et al., 1997; Arcidiacono & Perret-Clermont, 2009; Buđevac et al., 2020).

The role of argumentation and reasoned dialogue in the development of new competencies has been extensively documented in the scientific literature, but research conducted in Serbia shows that our students fail to develop this complex and relevant competency to the extent necessary to use it as a tool for learning and development (Buđevac et al., 2020). Although children participate in argumentative exchange early, well before school age (Arcidiacono & Bova, 2013; Pontecorvo & Arcidiacono, 2014), experimental research in an educational context shows that the use of argumentation at an early age is not stable and depends on numerous factors (Muller Mirza et al., 2009). One of our previous studies (Buđevac & Baucal, 2015) also showed that even seven-year-olds were able to spontaneously produce arguments within educational exchanges, without teacher support and without prior systematic preparation. However, another study conducted within the Serbian education system (Branković et al., 2013) showed that our students completely lack systemic support in developing this competence during schooling.

ORGANIZATION AND APPLICATION OF THE KARL POPPER DEBATE IN PRACTICE

The Karl Popper debate format is one of the most popular forms of debate in class, and is named after one of the most prominent philosophers of the 20th century. Debate deals with relevant and often controversial topics and emphasizes developing critical thinking skills and tolerance for different points of view. Debate participants collaborate in teams of three members, and their task is to research arguments for and against the researched topic. Each team has the opportunity to present their arguments and ask questions to the opposing team. At the end of the debate, the judge gives constructive feedback based on what happened in the debate (Scheme 1).

Debate is a team activity, and each team consists of 3 members (Table 1). Affirmative and negative teams have the same time to present their arguments. The judge makes sure that the participants of the debate adhere to the time limits. His role is to indicate to the speakers how much time they have left during the debate. The judges decide the winner of the debate. The debate is judged by an odd number of judges, and the team with the most votes wins. The judges decide on the winner solely on the basis of the success of the arguments. They explain their decision orally, and the evaluation should be neutral and constructive.

Table 1. Implementation of the debate.

Speech A1
N3 interrogates A1
Speech N1
A3 interrogates N1
Speech A2
N1 interrogates A2
Speech N2
A1 interrogates N2
Speech A3
Speech N3

*Source: Croatian Debate Society, 2021.

It is necessary to respect the course of the debate because in this way it is ensured that the debate ends within the time frame of one lesson, and the student who measures the time is responsible for this together with the teacher. Each speaker has a specific role in the debate (Table 2). The first affirmative speaker should present arguments, evidence and define the key concepts of his team. Then there is cross-examination where any member of the negation team asks questions of the member of the affirmation team. Students who ask questions should take care to ask questions in such a way as to make a member of the opposing team admit some of the weaknesses of their positions, and these questions can also be in the sense of demanding explanations of certain parts of the presentation. The main role of the negation team is to express their team's disagreement with the stated thesis or to introduce their own definitions if they think that the affirmative ones are not objective. The first speaker of the negation begins challenging the affirmative case. All elements of the affirmative case that are not disputed by the first speaker of the negation are considered accepted and contribute to the victory of the affirmation. The cross-examination is again approached according to the same rules as in the first cross-examination, with the fact that the roles of the examiner and the examined have been reversed (Croatian Debate Society, 2021).

Affirmation in the second speech has two tasks. First, the speaker should defend his team by answering questions from the opposing team. Second, he should "attack" the team from the negation team. This means that his task is to respond to the arguments of the opposing team and to strengthen his team by further explaining the positions by using the results of the previous cross-examination in the presentation. The second negation team speaker responds to the affirmation team's arguments in terms of strengthening his team, using the results of cross-examination. His task is to build on the arguments with additional explanations, citing specific examples (Croatian Debate Society, 2021).

The third speaker of the affirmation team points out in a few sentences what his team managed to prove in the previous two speeches, and what he managed to dispute in the cross-examination of the negation team. He must not talk about new content that was not analyzed during the debate. He presents his team's conclusion and gives reasons why the affirmative team should win the debate. The third speaker belonging to the negation team is analogous to the third speaker of the affirmative team. The third negation speaker must not present new content, bearing in mind that the affirmative party does not have the opportunity to respond to it. He also summarizes the main arguments, explains them, analyzes and proves why his team was more convincing in each of those arguments (Croatian Debate Society, 2021).

Table 2. Affirmation (A) and negation (N) team.

Tasks of the affirmation team	**Tasks of the negation team**
proves the thesis	disputes the thesis
interprets the thesis and defines key words	accepts the definitions of the affirmation team or rejects them and proposes his own
sets and justifies the criteria	accepts the criteria of the affirmation team or rejects them and proposes his own
present arguments that defend the thesis according to definitions and criteria	challenge the arguments of the affirmative action team
they dispute the arguments of the negation team and "defend" their own	they propose arguments for their position that negate the thesis

*Source: Croatian Debate Society, 2021.

The planned duration of the Karl Popper debate is 60 minutes, which is beyond the time frame of the lesson, so this format is modified in such a way that the duration of the debate fits into the duration of 35 minutes. The teacher uses the remaining 10 minutes of the lesson for the introductory part of the lesson and grading the students with an explanation of the grades. If the teacher wants to evaluate the debate participants, then before the debate itself, he should clearly define the evaluation criteria, whereby winning the debate must not be one of the criteria (Kaluđerović, 2014).

Apart from the time limit, a total of 6 speakers participate in the Karl Popper debate, and the observers of the debate are not included in the discussion. In the modified debate, other students from the class also have the opportunity to participate in an open discussion by asking questions to the members of the affirmative and negative teams and, together with the teacher, share the role of judge in the debate. Students should be introduced to the rules of the debate a few days before the lesson, and they are (Czech Debate Association, 2018):

- 6 speakers participate in the debate, 3 speakers each for the affirmation and negation teams and a student who measures the time;
- students who are not members of the teams write down the questions they want to ask the participants of the debate during the open discussion and together with the teacher participate in the decision on the winner of the debate;
- debate participants should adhere to the debate's time limit;
- after the third speech of the member of the negation team, an open discussion begins in which the teacher and other students from the class participate;
- all students should respect and respect each other and give their vote publicly to the team they think was more convincing in their arguments.

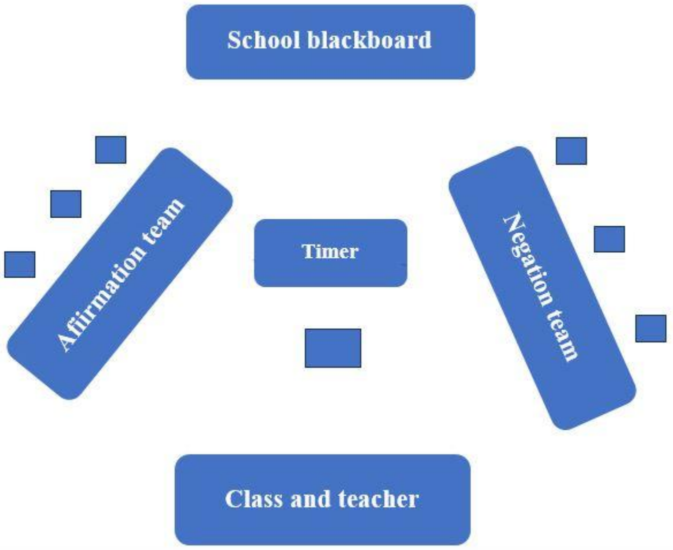

Scheme 1. Seating arrangement during the implementation of the debate. Source: Czech Debate Association, 2018.

After the presentation and cross-examination for a total of 24 minutes, and after the last speech of the third member of the negation team, an open discussion begins that lasts 10 minutes. Debate questions should be specific and clear, requiring a short answer. It is better to ask several questions with the same goal instead of one long question, because that way it will be easier to lead the opponent to the desired answer. After the timer informs about the expiration of 10 minutes of open questioning, the students vote by raising their hands and thus choose the winner of the debate (1 minute). The teacher uses the last 5 minutes for evaluation and ends the lesson with an explanation.

THE ROLE OF DEBATE IN LEARNING GEOGRAPHICAL CONTENT

Studying the elements of the geographical environment, their mutual connections and conditioning, geography has a diverse subject matter of study thanks to the fact that it connects natural and social sciences. Complex geographical topics should be explained to students in a way that will maximally activate them and contribute to the functional acquisition of the content. Thanks to the variety of topics, geographical contents are suitable for teaching because they enable a wide application of forms and methods of work, a large selection and use of teaching aids.

For an essential understanding of the geographical topic, it is important how it is presented to the students, but also which methods are the most effective for more efficient acquisition of the content. The application of debate in the acquisition of knowledge enables the acquired knowledge of students to be more permanent and applicable. Physical-geographic topics are very suitable for teaching using debate. Their methodological particularities come to the fore because they deal with concrete elements of the geographical environment that students can obviously notice or have prior knowledge about. The application of debate in the study of socio-geographic topics can be based on the research of appropriate literature, analysis of statistical data, graphs, interpretation of maps and maximum student activity. Regional-geographic topics are complex for teaching using the debate method because the student needs to know geography as a whole, all its scientific and related disciplines, their specificities and educational value.

When processing geographical content, there are a large number of topics that can be discussed. Playing different social roles in considering a particular problem is of great importance for observing it from different aspects. For example, students can be given a hypothetical situation that a factory is being built in the local area. Teachers arrange students into groups, give instructions, assign roles, monitor the work, provide guidelines, discuss with participants and draw conclusions. Within the group, members based on their professional role (biologist, geographer, chemist, physicist, computer scientist) analyze the problem situation - the construction of a factory in the local area and find arguments for/against. One group develops arguments that the construction of a factory is necessary because of the creation of new jobs. The second group tries to challenge the given thesis by presenting arguments that health is the most important. The third and fourth groups of students define questions that can refute the arguments given by the first and second groups, respectively. This is followed by the realization of the debate, presenting arguments for or against, asking questions to refute the presented arguments, and defending the presented arguments. The fifth group finds a compromise solution to the problem situation based on the arguments of the opposing groups and draws conclusions from the debate.

CONCLUSION

A large number of teaching methods contribute to the effective acquisition of geographical content and its practical application. The dialogic method is one of the most frequently used methods because in the teaching of geography, through conversation, you can study the content and check the acquired knowledge. Debate is a form of dialogic teaching method in which students, divided into groups, oppose different opinions and prove their views on a certain problem with the aim of solving it. Intragroup and intergroup discussion, playing social roles, solving problem situations, forming well-argued positions, mutual respect and appreciation, peer teaching, developing the skill of active listening, proposing solutions, creating new ideas, connecting content between subjects and developing critical thinking, are just some of the advantages of using debate in teaching geography.

In teaching geography, it is possible to discuss various topics from hypothetical and theoretical to practical ones such as ecological, social or economic, but it is important to choose those that contribute to the formation of students' well-argued attitudes. The debate on the topic "Building a factory or preserving the environment" is mentioned in the paper as a teaching activity in which students will be able to highlight the advantages and disadvantages of building a factory in the local environment, and on the other hand, not to pollute the environment. The paper further pointed out that the debate should be based on rules and procedures that enable the successful implementation of the lesson. The application of an interdisciplinary approach contributes to this, which through connecting the content of geography with the content of other teaching subjects, enables students to gain new experiences and knowledge about the researched topic. All of the above highlights the debate as a teaching method suitable for the achievement of educational, educational and functional goals in the teaching of geography.

REFERENCES

Arcidiacono, F. & Bova, A. 2013. Argumentation among family members in Italy and Switzerland: A cross-cultural perspective. In: Y. Kashima, E. S. Kashima, R. Beatson (eds.), Steering the Cultural Dynamics, Melbourne: IACCP, pp. 167-174.

Branković, M., Buđevac, N., Ivanović, A. & Jović, V. 2013. Činioci razvoja viših nivoa čitalačke pismenosti – veštine argumentovanja u školskoj nastavi. Psihološka istraživanja, 16(2), pp. 141-158.

Brofi, Dž. 2004. Nastava. Beograd: Mala pedagoška biblioteka, Pedagoško društvo Srbije.

Brown, Z. 2015. The use of in-class debates as a teachin strategy in increasing students' critical thinking and collaborative learning skills in higher education. Education futures, 7(1), pp. 157-163.

Buđevac, N. & Baucal, A. 2015. The role of argumentation in seven-year-olds joint comprehension of written texts. Teaching Innovations, 28(3), pp. 67-82.

Buđevac, N., Meršnik. M. & Baucal, A. 2020. The role of debate in teaching stem subjects – getting to know the students in a different way. In: Zacłona, Z. & Radovanović, I. (eds.), Educational space. Selected theoretical and practical approaches (pp. 74-82). State University of Applied Sciences in Nowy Sącz, Institute of Pedagogy, Poland; University of Belgrade, Teacher Education Faculty, Serbia.

Czech Debate Association. 2018. Karl Popper Debate Programme Rules. Available at: https://debatovani.cz/wp-content/uploads/2018/11/181119_KP-debate-programme-rules.pdf

Hall, D. 2011. Debate: Innovative Teaching to Enhance Critical Thinking and Communication Skills in Healthcare Professionals. The Internet Journal of Allied Health Sciences and Practice, 9(3), pp. 145-158.

Hrvatsko debatno društvo, 2021. Karl Popper debatni format. Zagreb.

Ivić, I., Pešikan, A. & Antić, S. 2001. Aktivno učenje. Beograd: Ministarstvo prosevete i sporta Republike Srbije, Institut za psihologiju, Ministarstvo za prosvetu i nauku Crne Gore.

Jovanović, S. 2019. Osnove ekološkog obrazovanja. Beograd: Univerzitet u Beogradu – Geografski fakultet.

Kaluđerović, Ž. 2014. Debata u nastavi. Knjiga apstrakata "Projekat debata kao nastavno sredstvo." Novi Sad: Univerzitet u Novom Sadu – Filozofski fakultet.

Matas, M. 1996. Metodika nastave geografije. Zagreb: Hrvatsko geografsko društvo.

Mattes, W. 2007. Nastavne metode. Zagreb: Naklada Ljevak.

Muller Mirza, N., Perret-Clermont, A.-N., Tartas, V. & Iannaccone A. 2009. Psychosocial Processes in Argumentation. In: N. Muller Mirza, A.-N. Perret-Clermont (eds.), Argumentation and Education. Theoretical Foundations and Practices (pp. 67-90). New York: Springer Science + Bussines Media.

Pontecorvo, C. & Arcidiacono, F. 2014. Social interactions in families and schools as context for the development of spaces of thinking: In: T. Zittoun, A. Iannaccone (eds.), Activity of thinking in social spaces (pp. 83-97). New York, NY: Nova Science Publishers.

Prodanović, T. 1956. Problem određivanje pojma nastavne metode i njihove klasifikacije, Beograd.

Roders, P. 2003. Interaktivna nastava. Beograd: Univerzitet u Beogradu-Filozofski fakultet, Institut za pedagogiju i andragogiju.

Terhart, E. 2001. Metode poučavanja i učenja – uvod u probleme metodičke organizacije poučavanja i učenja. Zagreb: Educa.

Vizek-Vidović, V. et. all. 2003. Psihologija obrazovanja. Zagreb: IEP-VERN.

Vranković, B. 2014. Nastavne metode i postignuća učenika osmih razreda iz geografije u zadacima uz grafičke priloge. Acta Geographica Croatica, 39, pp. 77-98.

Živković, Lj., Jovanović, S. & Rudić. V. 2015. Metodika nastave geografije. Beograd: Srpsko geografsko društvo.

Bulletin of Natural Sciences Research
Vol. 15, No. 1, 2025, pp. 48-55.

DOI: https://doi.org/10.5937/bnsr15-57655
Original Scientific Paper

AN IMPROVED CANOPY INTERCEPTION SCHEME INTO BIOGEOCHEMICAL ANALYSIS OF WATER FLUXES IN SUBALPINE CONIFEROUS FOREST (NORTHERN ITALY)

POLINA LEMENKOVA[1*]

[1]Alma Mater Studiorum – University of Bologna, Department of Biological, Geological and Environmental Sciences, Via Irnerio 42, IT-40126 Bologna, Emilia-Romagna, Italy

ABSTRACT

The delicate ecosystems of the Alps' subalpine forests are crucial to water supplies as well as the local and mesoscale climate regulators. Although earlier research has assessed various aspects of the water balance, there is currently a dearth of studies that directly measure every component of the water budget. Furthermore, little is understood about the frequency and impact of fog as well as how forest layout affects water balance. Using the eddy covariance technique, sap flow sensors, phenocam images, throughfall and stemflow gauges, soil moisture sensors, water discharge measurements, and a fog interception gauge, we carried out a thorough investigation of a subalpine coniferous forest at the Renon site in the Italian Alps. Furthermore, we measured the leaf area and lichen occurrence as possible canopy water storage components. Large amount of precipitation was reflected by the canopy interception in spruce and coniferous forest. Although fog alone had no effect on total water intake, it did result in a tiny but noticeable increase in throughfall during mixed fog and rain precipitation events, however this effect seemed to be less significant than in cloud forests that are tropical or subtropical. At the catchment level, the annual balance (November–October) was almost perfectly closed when all input and output components were taken into account. This paper contributes to the ecological monitoring of the Alpine forests in South Tyrol, Northern Italy.

Keywords: Fog, Canopy Interception, Evaporation, Throughfall, Forest, Rainfall, Northern Italy.

INTRODUCTION

Forests are valuable resources in natural systems with high value in ecological, economic, social, and aesthetic services. This includes habitats for biodiversity, the supply of food, medicine, and auxiliary products, recreational opportunities, and aesthetic qualities. Important service of forest for ecosystems consists in the control of the hydrologic cycle and the preservation of soil resources. Forests affect local climate settings by exchanging carbon dioxide, water, and energy, with the atmosphere.

In view of the important link between forests and climate, it is crucial to evaluate the processes of water cycle within forest ecosystems. The statistical models and numerical parameterizations of the climate parameters and Earth's land surface responses provide us with information of how forests contributes to the regulation of local climate through measuring water balance. In hydrological techniques, measurements of the water balance components in forests are typically surrounded by widely accepted oversimplifications and significant uncertainties (Minić, 2001; Ristić Vakanjac et al., 2015; Lemenkova, 2024a). The latter is addressed in ecohydrology by dividing evapotranspiration into transpiration by the vegetation and evaporation from forest interior surfaces (Lemenkova, 2022a; Ahmed et al., 2025; Crișu et al., 2025). Evaporation from canopy interception in forests can currently only be determined indirectly or modeled, even though sapflow sensors and canopy chambers, for example, can detect soil evaporation and tree transpiration directly.

Nevertheless, there are still difficulties to model the correlation between key environmental factors. Aerodynamic modeling of energy exchange was employed in the early attempts to land surface parameterizations. Nevertheless, in these models, the effects of forests vegetation were not explicitly computed neither evaluated. In such models heat flow was controlled by the availability of soil water, and the hydrologic cycle was reduced to a soil water model. Using the traditional Penman-Monteith-equation by a factor of two or more, or the rate of wet canopy evaporation estimated from eddy covariance data (Zhu et al., 2024; Kang et al., 2025) or as the variations between precipitation, throughfall, and stemflow. Existing methods use spatial analysis (Klaučo et al., 2013; Lemenkova, 2024b), statistical techniques for remote sensing data processing (Roljević et al., 2012; Lemenkova, 2021a; Zhang et al., 2025), or hydrogeological and applied engineering approaches to data modelling (Lindh and Lemenkova, 2023; Can et al., 2025; Shaddad et al., 2025).

Forecasting dynamics of climate variables has also become an important aspect of environmental management, as it allows for proactive intervention strategies (Lemenkova, 2021b; 2023a; Cai & Shi, 2025; Ji et al., 2025). Example of an ecological influence on climate in forest ecosystems is

---

[*] Corresponding author: polina.lemenkova2@unibo.it

demonstrated by paired climate simulations, which control and compare climate parameters with changed vegetation patterns. Among the recent effective methods, Machine Learning (ML) and time-series models, which incorporate environmental and climate factors like temperature and humidity, have proven valuable in enhancing prediction accuracy (Lemenkova, 2023c, 2024c; Asghar Rostami et al., 2025; Lee et al., 2025; Mucomole et al., 2025).

Recent research emphasizes various approaches to model and predict behaviour of climate and hydrological variables in forest ecosystems, exploring both statistical and ML models in diverse agricultural contexts (Lemenkova P., 2021c, 2021d, 2022b; Fu et al., 2024; Sharp et al., 2025; Ozdemir & Abdikan, 2025). To solve numerical equations of atmospheric physics and dynamics in forest ecosystems using ML tools, such atmospheric models need calculated variables on energy, moisture, and momentum fluxes at the land surface as boundary conditions. Building on previous findings that use advanced techniques (RS, DL, ML, and time-series models) to provide an integrated method for tracking and predicting connectivity between environmental variables (Lemenkova, 2022c, 2023b; Bilgilioğlu et al., 2024; Olarte et al., 2024), the methodology of this study combines statistical framework, optimized for real-time identification of effects of tree characteristics (age and height of canopy) on water balance in the coniferous forests of the Tyrolean Alps to predict hydro-environmental trends based on the observation data.

METHODS

Study area

In this study, we presented climate model simulations in temperate coniferous forests that show that Alpine forests maintain high rates of evapotranspiration, decrease surface air temperature, and increase precipitation rates. The experiment was conducted in South Tyrol, in the Italian Alps (1735 m a.s.l., 46°35′11″N, 11°26′00″E), Figure 1.

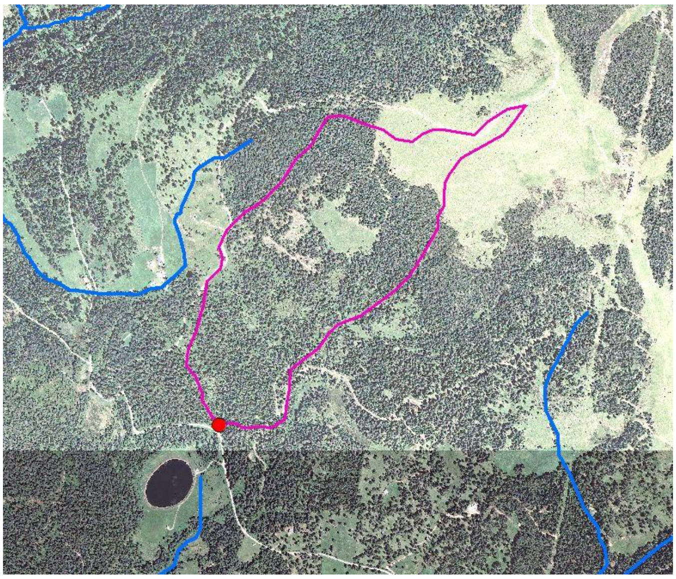

Figure 1. Aerial view of the study area.

The catchment has an area of 0.44 km^2. The water basin was measured on the local digital elevation model using ArcGIS software. The total of 85% spruce [*Picea abies (L) Karst.*], 12% Swiss stone pine (*Pinus cembra L.*), and 3% European larch (*Larix europea L.*) trees made up the tree layer (diameter at breast height (DBH) >5 cm). Individuals of European rowan (*Sorbus aucuparia*) and Scots pine (*Pinus sylvestris L.*) were also uncommon. About 29 meters was the height of the dominating tree. Alpenrose (*Rhododendron ferrugineum L.*) and blueberries (*Vaccinium myrtillus L.*) made up the majority of the understory. *Deschampsia flexuosa (L.)* Trin, or wavy hair-grass, predominated in the intervening grasslands.

Prediction of fog based on meteorological conditions during days with rain, fog and mixed precipitation

In order to understand the weather conditions throughout dry and wet circumstances, and particularly during the days with fog presence (visible below 1 km), meteorological variables measured between 2015 and 2019 were analyzed. The ratio of diffuse to total global radiation, the VPD, and relative air humidity (RH) were chosen to characterize hours and days without precipitation, with fog-only, with rain-only, and with mixed precipitation (fog and rain). The measurement was performed using equipment in Figure 2.

Figure 2. Pulvometers used in the study area: young forest (<30 years, left) and old forest (>200 years, right).

The climate benefits of forests because coniferous trees regulate temperature, control water balance and contribute to balanced albedo. In this regards, forests mitigate negative effects from climate change. Hence, afforestation decreases climate warming. Consequently, it is recommended to continue protection of forest stands in Alpine ecosystems and maintain precious coniferous stands. Such land use policies in Alps should consider the impacts of forest on climate, their effects on water balance at different spatial and temporal scales, and their effectiveness and sustainability as ecosystem service regulator.

The methodology of this study is based on the integrated assessment of climate parameters and the impacts from the young and old forest stands indicated on the cartographic plot, Figure 3. Specifically, this entails an evaluation of albedo, evapotranspiration (ET), transpiration (T), temperature and fog frequency. The evaluation of these parameters in young and old tree stands enables to assess non-linear complex relationships between forest vegetation and climate settings in the coniferous ecosystems of Alps. The geographic impact of these processes varies, because it depends on the time scale of climate forces. For instance, greenhouse gases are also well mixed in the atmosphere and influence global climate which can affect forest and regional impact of the biogeophysical feedbacks.

In turn, the biogeophysical processes influence climate as illustrated below on the models. These processes provided the expected throughfall for a certain precipitation event that included both fog (mixed precipitation) and rain alone. The difference between measured throughfall and the rain-to-throughfall contribution, which was determined by multiplying precipitation by the slope of the throughfall to precipitation equation from rain-only occurrences, was then used to estimate the fog contribution to throughfall for days with mixed precipitation. Using the existing methodology, the impact of fog on throughfall was used to assess its role and contribution. For mixed precipitation and rain-only events, we first calculated a linear regression equation between throughfall and precipitation rates for both stands.

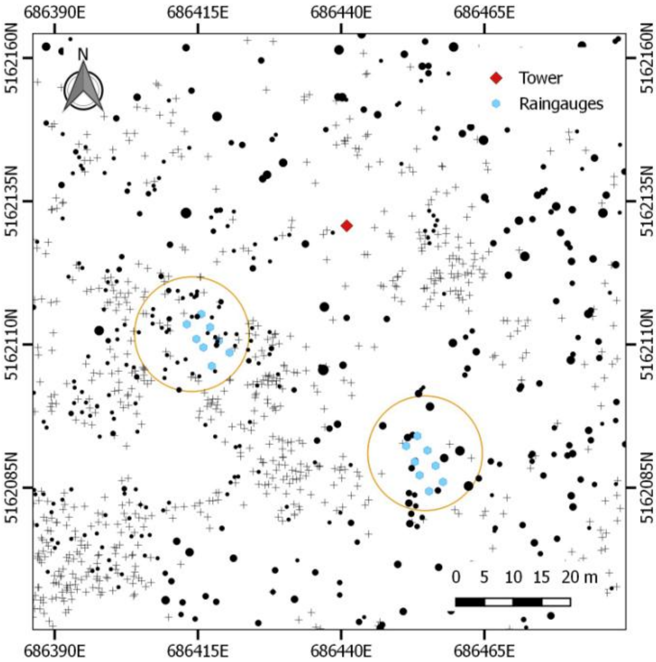

Figure 3. Map (100*100m) showing location of the inspected trees. Software: ArcGIS.

Calculation of Evapotranspiration

Evapotranspiration (ET_EC) was computed using Eddypro software and eddy covariance data in accordance with the ICOS setup. The systematic errors was calculated in the eddy covariance measurements for LE+H at the Renon site to be 17.6% based on the monthly energy balance ratio (EBR) data. It is reasonable to suppose that this mistake is half of the amount in LE (8.8%), and hence in ET, given a Bowen ratio of 1 in the summer. Figure 4 displays the additional elements of the water balance as well as the random error of EC.

Heat balance measurements

In addition to contributing to the terrestrial carbon sink, boreal ecosystems store a significant amount of carbon in soil, permafrost, and wetlands, and mature forests have a low yearly carbon gain. Five spruce trees with a DBH ranging from 23 cm to 57 cm had their sap flow measured in order to determine tree transpiration. Up to ten trees' sap flow measurements dating back to 2016 revealed that these trees behaved in a way that was typical of their size classes. One tissue heat balance sensor (Table 1) was placed at the north side of the trees to reduce mistakes caused by incoming shortwave radiation. Sap flow rates for the entire sapwood depth per unit trunk circumference (kg $^{h-1}$ cm^{-1}) were included into the measuring system. After logging the detected values at 10-minute intervals, we multiplied them by the stem circumference (less the thickness of the bark andphloem measured during sensor testing) to scale them to the tree level.

Computing sap flow

We compared the 95th percentile (P95) of 30-min sap flow rates for 2019 and the prior years to see if wound reactivity and/or resin buildup caused a drop in sap flow while a sensor remained in place for more than a year. We discovered that the P95 sap flow for the two smallest trees had significantly decreased. As a result, we multiplied the P95 [(year of sensor installation)/P95(2019)] ratio to get the rectified sap flow for 2019. A linear correlation between the sap flow of the corresponding tree and eddy covariance evapotranspiration (R2 = 0.57 to 0.66 at a 30-min resolution) was employed to fill up minor data gaps brought on by power outages or transient sensor malfunctions.

Days with precipitation (which we counted as days with mixed precipitation) were frequently accompanied by fog. During a monitoring period of 167 days (from late spring to autumn of 2019), there was fog for 241 hours during 9 days with fog (5%) and 45 days with mixed precipitation (27%).

Meteorological conditions and hydrological components

Flux energy measurements provided in this study confirm that coniferous forests have lower albedo for old forests compared with young forests, greater net radiation, and greater evapotranspiration, particularly during the summer season, producing a shallow, cool, and moist boundary layer. These findings emphasize how crucial are days with both fog and precipitation (mixed precipitation). No fog or mixed precipitation data were obtained during the 254 days of overcast conditions (70%) that were observed in South Tyrol in 2011. According to our 2019 data, 45% of overcast days in 2011 might have been fog days (defined as days with fog and mixed precipitation). For the entire observed time in 2015 and

2019, as well as the common period observed in both years, there were days with dry weather, fog and precipitation (rain or snowfall), and mixed precipitation of fog and rain or snowfall, Table 1.

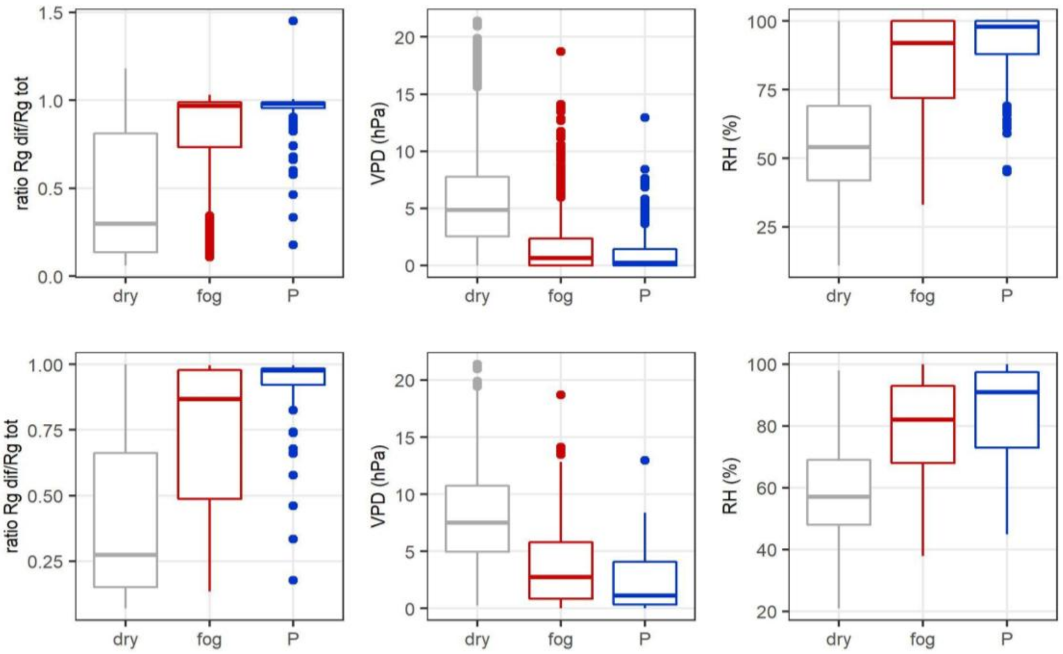

Figure 4. Weather conditions at times of fog (less than 1 km visibility), precipitation, and dry conditions (dry) from 01/01/2015 to 30/08/2015 (top row) and from 25/05/2015 to 30/08/2015 (bottom row) (ratio of diffuse to total global radiation, vapor pressure deficit VPD, and relative air humidity RH).

Table 1. Technical description and accuracy of the instrumentation used to calculate water balance.

Description	Height above	Nr. of sensors	Period of measurements	Instrument uncertainty	Instrument type
Evapotranspiration with Eddy covariance	33.7	1	Long term	±8.8%	Gill HS100 (Gill Instruments Inc.)
Gloval and diffuse radiation	40.3	1	Long term	±5%	DeltaT SPN1 (Delta Devices)
Net radiation	—	1	Long term	—	CNR4net radiometer
—	—	—	—	±0.5% rh	RM Young screen and
Relative humidity	33	1	Long term	—	—
Precipitation - open field	2	1	Long term	±3%	Geonor T200b (Geonor)
Fog frequence (visibility)	32	1	Jan 2015 - Dec 2015	N.A.	Netcam SC5
—	N.A.	1	Jan 2019 - Nov 2019	N.A.	—
Sap flow	DBH	5 spruce trees	Long term	±20% (1)	Tissue heat balance sensors
Temperature inside the canopy	15,23	2	Long term	0.1% at 25 C	Tinytag Data 2; Gemini Datalogger
Humidity inside the canopy	15,23	2	Long term	±3.0% RH at 25 C	Tinytag Data 2; Gemini Datalogger
Precipitation - below canopy, throughfall	0.3	16	Jun-Nov 2019	±1%	Stocker 4523
Precipitation - below canopy, throughfall	0.3	6	Jun-Nov 2019	±1%	Onset (S) RGX + Hobo logger
Precipitation - below canopy, stemflow	0.3	2	Jun-Nov 2020	±1%	Onset (S) RGX + Hobo logger
Soil water content	-0.05, -0.10, -0.20,				
Water discharge	0—2	1	One year (2019)	±0.1%	OTT CTD sensor

The measured values were logged at 10-min intervals and then scaled to the tree level by multiplying them with stem circumference (minus the bark and phloem thickness measured during sensor installation) and integrated them to 30-min and daily sums per tree (L day^{-1}), Table 2.

The systematic error was computed for I in Eq. 2 as well as the equipment accuracy of the measured variables. Given their excellent correlations ($R^2 > 0.87$), linear correlation with operational gauges was used to fill in data gaps caused by logger failure. The manual gauge data, which was absent for the most recent sampling interval, was added using a linear correlation with the automatic gauge results ($R^2 > 0.77$). The study site did not have direct access to long-term fog data. As a result, the information from the 2015 and 2019 was obtained.

Table 2. Meteorological parameters for varied weather conditions (dry and wet) according to the observations: measuring period, time observed and days.

Year	2015 all		2015 common period		2019 all		2019 common period	
period	1.1--30.8.2015		25.5--30.8.2015		25.5--7.11.2019		25.5--30.8.2019	
Time	9:00-17:00		9:00-17:00		0:00-24:00		0:00-24:00	
	days	%	days	%	days	%	days	%
Dry	123	50.6	40	41.2	79	47.3	46	47.4
Fog	72	29.6	31	32.0	9	5.4	2	2.1
rain/snow	11	4.5	6	6.2	34	20.4	31	32.0
mixed precipitation	37	15.2	20	20.6	45	26.9	18	18.6
Total	243	100	97	100	167	100	97	100

Overall, there were 296.5 hours of fog between January and August with 72 days of fog and 37 days of mixed precipitation (109 days; 30% of days were foggy and 15% had mixed precipitation). Days with fog were common in 2019, although there weren't many days with just fog.

RESULTS AND DISCUSSION

Long term precipitation and fog frequency

In this study, we demonstrated the deep links between the coniferous forests and climate throug hevaluated parameters of precipitation and fog frequency. Boreal forests are vulnerable to global warming. In the studied boreal forests of the Alps, there may be loss of evergreen trees and a shift toward deciduous trees due to the climate change. Increased disturbance from fire or insect outbreaks will shift the old coniferous forest to a younger ages. Climate forcing arising from younger stand age may be comparable to that arising from biome shifts. To forecast the incidence of fog in 2019, average radiation, relative humidity, and vapour pressure deficit (VPD) values for days with precipitation, fog, and mixed precipitation in 2015 were computed. When total Rg was high during dry periods, the ratio of total to global radiation (ratio Rg dif/Rg tot) was lower. Conversely, fog and rain had less of an impact on diffuse Rg. The relative air humidity (RH) was lower and VPD was higher during dry conditions than during fog and precipitation, as was to be expected. Compared to the RH and VPD, the Rg dif/Rg tot ratio had more data variability.

When examining time courses, it was found that air temperature (T) and VPD were often lower on foggy and wet days, increased on the first dry days, and then declined once again as the measuring period came to a conclusion. In contrast to T and VPD, relative humidity showed the opposite pattern. According to long-term statistics in Europe, fog caused the temperature to rise at night while decreasing during the day; this suggests that the temperature is more sensitive at night.

Tree transpiration and canopy evapotranspiration

The division of net radiation into sensible and latent heat fluxes varies among boreal forests. Compared to deciduous broadleaf forests, conifer forests produce higher rates of sensible heat exchange and deep atmospheric boundary layers because they have a lower midsummer evaporative fraction, which is the ratio of latent heat flow to accessible energy. Thus, with just one 5-day dry spell at the end of June and another 13 days in mid-September, rainfall events happened fairly often over the whole 2019 measuring period, despite the fact that the precipitation totals in June were lower than the long-term average (Figure 4).

Synthesis of flux data from boreal and temperate Alpiine regions in various stages of ecosystem development (old and young stands) is essential to understand the functioning of forests. It enables to better understand the variations of climate responses across gradients of climate, soils, land cover types, and plant functional patterns. Hence, time courses of T and ET showed good correspondence with similar responses to weather conditions and an overall decrease beginning in late September, but the transpiration of the old (Tof) and young stand (Tyf), as determined by sap flow measurements, was low in comparison to canopy evapotranspiration from eddy covariance, which applied to both stands. The Tyf was higher than Tof as the new stand's higher tree density and smaller projected crown area more than made up for the old stand's larger sap flow from massive single trees. As a result, for both forest types, the Tyf to ET regression line sloped higher than the Tof to ET one. The association between T and ET had an R2 value greater than 0.9. On the other hand, there was no correlation between P and ET or T.

Flux measurements illustrate the potential for changes in species composition, arising from change in the climate regime, to affect water cycle in forests. For example, we found that ET was higher on dry days (55% of total ET in 48% of days) and suppressed, particularly on days with mixed precipitation (17% of total ET in 26% of days), when we divided the days into dry, mixed precipitation (fog and precipitation), and rainfall-only (Table 2). This is due to fog lowering ET, as seen in cloud forests, and also because mixed precipitation days were more frequent in autumn, when ET was normally lower due to phenology (senesced grasses) and lower temperatures.

Although the LAI in both stands was identical, the new stand had higher throughfall rates in relation to precipitation than the old stand. Because the manual gauges covered a larger small-scale fluctuation of PAI/LAI, their throughfall variability was higher than that of the automatic ones. A strong linear correlation ($R^2 > 0.93$) was found between throughfall and precipitation for both stands and no clear increase in throughfall ratio with P. The last data point with the highest amount of throughfall and P was clearly above the linear regression line, indicating that the limits of the canopy’s interception capacity were reached. The correlation between old and young forest stand throughfall is very high.

The same water components, divided into roughly monthly intervals (adjusted to the manual throughfall gauges' sampling periods), show that P rose from June to October and ET peaked in September before sharply declining after that.

Except for June in the old stand, the Tf/P ratio was higher in the fall (September and October) than in the summer, and as a result, the interception rate (I/P) was lower.

Throughfall rates were much greater on days with mixed fog and rain precipitation, whereas interception rates (I/P) were lower on days with rain only. This was discovered by examining throughfall rates at a daily resolution and differentiating by precipitation type. Fog was blamed for this Tf excess (Tf/P = 0.28 for the young stand and Tf/P = 0.27 for the old stand). In addition to having more mixed precipitation days in the fall, this should be linked to greater P. Furthermore, stemflow, which was comparable for both stands, rose between June and October but was still too low overall to significantly affect the water balance. Variations in height and air temperature could account for the Alpine forest's reduced contribution. This finding supports our theory that fog may very slightly affect the seasonal and annual water budget.

Water partitioning and balance at catchment level

Over the course of the 5-month measurement period, we noticed a number of variations in the ecosystem water partitioning between the young and old forest (Table 3).

Table 3. Meteorological parameters for forest with young and old stands. Water components at canopy level for five months, from 2019-5-30 (DOY 150) to 2019-11-07, are approximately separated into months based on the manual throughfall gauges' sampling dates.

Days with mixed precipitation	**young forest**	**old forest**
P measured (mm)	460 ± 35	460 ± 35
Total Tf measured (mm)	292 ± 26	216 ± 11
Tf from rain only events (mm)	243 ± 7	184 ± 8
Fog in mixed events (mm)	70 ± 15	53 ± 5
measured Tf/P (%)	64	47
estimated rain-only Tf/P (%)	53	40
estimated fog Tf/P (%)	15	12
rain contribution to Tf (%)	83	84
fog contribution to Tf (%)	24	24

The young forest had higher levels of transpiration and throughfall. As a result, the young stand had reduced interception, which was determined by subtracting Tf from Sf and then subtracting total P. Interception was responsible for a significant portion of ET (54% in the ancient forest and 33% in the young forest), as intercepted water eventually evaporates back to the sky. Rainfall water can return to the atmosphere more quickly by evaporation, which is a component of the water cycle, rather than via the soil or plant life. When compared to other conifer forests studied in the literature, where T/ET, T/P, and T/potential ET ratios range from 15% to 75%, the ratios of transpiration measured with sap flow to evapotranspiration from eddy covariance (T/ET = 22% for of, 31% for yf) or total precipitation (T/P = 24% for of, 34% for yf) were low for both stands. However, in contrast to I/P reported values of 17–45%, our high ratios of interception to precipitation (I/P = 54% for of, 33% for yf) and ET (I/ET = 51% for of, 31% for yf) were in the upper range.

CONCLUSION

Much of our understanding of how forest impacts climate, and our ability to mitigate climate change, comes from simulation and modelling techniques. Models of climate and the forest biosphere are simplifications of complex physical, chemical, and biological processes in the boreal forest ecosystems. Using such modelling techniques, this study shows that forest age and height are potential climate regulators in the coniferous forests.

Extrapolation of process-level functioning of forest ecosystem functioning was gained from modelling experiments and field studies. Here, the biosphere models were constrained with observational data across a scale from in situ measurements, flux heat computations of ecosystem functioning and syntheses of ecosystem research. The low transpiration/ET ratios can be explained by modelled link between forest ecosystems and climate parameters. Calculated as the residual of ET (Eddy covariance) - T - I, the evapotranspiration of the soil and understory was higher in the young stand, where the interception was significantly lower. Additional information might be obtained by an independent measurement of soil/understory ET utilizing canopy chambers or small-scale lysimeters. The water balance was completed by discharge (DC) and change in soil moisture (dSWC); since both were only measured for the entire forest, the same values were applied to both types of forests. Compared to T and Esu, DC and dSWC were both insignificant. Before the measuring period began, the majority of the discharge happened during the spring snowmelt. Only on short time scales do changes in soil moisture matter when calculating the water balance, and they have essentially leveled out during measurement period.

The temperate coniferous forests in the Alps are linked with climate forces. The biogeophysical parameters such as low albedo during winter and ET during summer influence annual mean T. Higher albedo with loss of forest cover could offset carbon emission so that the net climatic effect of temperate deforestation is negligible, or reduced ET with loss of trees could amplify biogeochemical warming. Although the amount of water input from fog only events at our site was unknown, fog was projected to contribute 24% more throughfall than rain-only events, indicating a clear contribution to mixed fog and rain precipitation. Importantly, previous studies did not take fog into account. Therefore, fog is the missing link in our current findings to comprehend both the decrease of evaporative conditions during dry periods in the studied Alpine environment and the recharge of soil water during days with mixed precipitation.

The ability of the intercepted water to function as a climate regulator at the local and mesoscale is climatologically significant, in addition to the physiological element of the plant's water use. By emitting 44.2 W m^{-2} of latent heat instead of sensible heat, one millimeter of water at 20 °C lowers the temperature and increases the amount of water vapor in the atmosphere.

REFERENCES

Asghar Rostami, A., Taghi Sattari, M., Apaydin, H. & Milewski, A. 2025. Modeling Flood Susceptibility Utilizing Advanced Ensemble Machine Learning

Techniques in the Marand Plain. Geosciences, 15, 110. https://doi.org/10.3390/geosciences15030110

Ahmed, A., Rotich, B. & Czimber, K. 2025. Climate Change as a Double-Edged Sword: Exploring the Potential of Environmental Recovery to Foster Stability in Darfur, Sudan. Climate, 13, 63. https://doi.org/10.3390/cli13030063

Bilgilioğlu, S. S., Gezgin, C., Iban, M. C., Bilgilioğlu, H., Gündüz, H. I. & Arslan, Ş. 2025. Explainable Sinkhole Susceptibility Mapping Using Machine-Learning-Based SHAP: Quantifying and Comparing the Effects of Contributing Factors in Konya, Türkiye. Appl. Sci, 15, 3139. https://doi.org/10.3390/app15063139

Cai, Y. & Shi, X. 2025. A Comparative Study on the Methods of Predictor Extraction from Global Sea Surface Temperature Fields for Statistical Climate Forecast System. Atmosphere, 16, 349. https://doi.org/10.3390/atmos16030349

Can, M., Vaheddoost, B. & Safari, M. J. S. 2025. Data Reconstruction for Groundwater Wells Proximal to Lakes: A Quantitative Assessment for Hydrological Data Imputation. Water, 17(5), 718. https://doi.org/10.3390/w17050718

Crișu, L., Zamfir, A.-G., Vlăduț, A., Boengiu, S., Simulescu, D. & Mititelu-Ionuș, O. 2025. Assessing Vegetation Response to Drought in the Central Part of Oltenia Plain (Romania) Using Vegetation and Drought Indices. Sustainability, 17, 2618. https://doi.org/10.3390/su17062618

Fu, Y., Tan, H., Kou, W., Xu, W., Wang, H. & Lu, N. 2024. Estimation of Rubber Plantation Biomass Based on Variable Optimization from Sentinel-2 Remote Sensing Imagery. Forests, 15, 900. https://doi.org/10.3390/f15060900

Ji, P., Su, R., Wu, G., Xue, L., Zhang, Z., Fang, H., Gao, R., Zhang, W. & Zhang, D. 2025. Projecting Future Wetland Dynamics Under Climate Change and Land Use Pressure: A Machine Learning Approach Using Remote Sensing and Markov Chain Modeling. Remote Sens., 17, 1089. https://doi.org/10.3390/rs17061089

Kang, M., Cho, S., Kim, S. J., Kim, E. & Kang, M. 2025. Deviations in evapotranspiration measurements between enclosed- and open-path eddy covariance systems. Hydrological Sciences Journal, pp. 1-9. https://doi.org/10.1080/02626667.2025.2463619

Klaučo, M., Gregorová, B., Stankov, U., Marković, V. & Lemenkova, P. 2013. Determination of ecological significance based on geostatistical assessment: a case study from the Slovak Natura 2000 protected area. Central European Journal of Geography. 5, pp. 28-42. https://doi.org/10.2478/s13533-012-0120-0

Lee, J., Han, J., Engel, B. & Lim, K. J. 2025. Web-Based Baseflow Estimation in SWAT Considering Spatiotemporal Recession Characteristics Using Machine Learning. Environments, 12, 94. https://doi.org/10.3390/environments12030094

Lemenkova, P. 2021a. Evaluating land cover types from Landsat TM using SAGA GIS for vegetation mapping based on ISODATA and K-means clustering. Acta agriculturae Serbica, 26(52), pp. 159-165. https://doi.org/10.5937/AASer2152159L

Lemenkova, P. 2021b. Mapping environmental and climate variations by GMT: A case of Zambia, Central Africa. Zemljište i biljka, 70(1), pp. 117-136. https://doi.org/10.5937/ZemBilj2101117L

Lemenkova, P. 2021c. ISO Cluster classifier by ArcGIS for unsupervised classification of the Landsat TM image of Reykjavík. Bulletin of Natural Sciences Research, 11(1), pp. 29-37. https://doi.org/10.5937/bnsr11-30488

Lemenkova, P. 2021d. Distance-based vegetation indices computed by SAGA GIS: A comparison of the perpendicular and transformed soil adjusted approaches for the LANDSAT TM image. Poljoprivredna tehnika, 46(3), pp. 49-60. https://doi.org/10.5937/PoljTeh2103049L

Lemenkova, P. 2022a. Evapotranspiration, vapour pressure and climatic water deficit in Ethiopia mapped using GMT and TerraClimate dataset. Journal of Water and Land Development, 54(7-9), pp. 201-209. https://doi.org/10.24425/jwld.2022.141573

Lemenkova P. 2022b, Mapping Ghana by GMT and R scripting: advanced cartographic approaches to visualize correlations between the topography, climate and environmental setting, Advances in Geodesy and Geoinformation, 71, 1, e16. https://doi.org/10.24425/gac.2022.141169

Lemenkova, P. 2022c. GRASS GIS Scripts for Satellite Image Analysis by Raster Calculations Using Modules r.mapcalc, d.rgb, r.slope.aspect. Tehnički vjesnik, 29, 6, pp. 1956-1963. https://doi.org/10.17559/TV-20220322091846

Lemenkova P. 2023a. Monitoring Seasonal Fluctuations in Saline Lakes of Tunisia Using Earth Observation Data Processed by GRASS GIS, Land, 12, 11, 1995. https://doi.org/10.3390/land12111995

Lemenkova, P. 2023b. Mapping Wetlands of Kenya Using Geographic Resources Analysis Support System (GRASS GIS) with Remote Sensing Data. Transylvanian Review of Systematical and Ecological Research, 25, 2, pp. 1-18. https://doi.org/10.2478/trser-2023-0008

Lemenkova P. 2023c. A GRASS GIS Scripting Framework for Monitoring Changes in the Ephemeral Salt Lakes of Chotts Melrhir and Merouane, Algeria. Applied System Innovation, 6, 4, 61.

Lemenkova, P. 2024a. Artificial Intelligence for Computational Remote Sensing: Quantifying Patterns of Land Cover Types around Cheetham Wetlands, Port Phillip Bay, Australia. Journal of Marine Science and Engineering, 12, 8, 1279. https://doi.org/10.3390/jmse12081279

Lemenkova, P. 2024b. Support Vector Machine Algorithm for Mapping Land Cover Dynamics in Senegal, West Africa, Using Earth Observation Data. Earth, 5, pp. 420-462. https://doi.org/10.3390/earth5030024

Lemenkova, P. 2024c. Machine learning methods of satellite image analysis for mapping geologic landforms in Niger: A comparison of the Aïr mountains, Niger River basin and Djado Plateau. Podzemni radovi, 45, pp. 27-47. https://doi.org/10.5937/podrad2445027L

Lindh, P. & Lemenkova, P. 2023. Effects of Water—Binder Ratio on Strength and Seismic Behavior of Stabilized Soil from Kongshavn, Port of Oslo. Sustainability, 15(15), 12016. https://doi.org/10.3390/su151512016

Minić, V. 2001. Hydrogeological influence of the Rautovac stream basin upon the quality of the Niška Banja thermal waters. Acta medica Medianae, 40(4), pp. 5-37.

Mucomole, F. V., Silva, C. A. S. & Magaia, L. L. 2025. Experimental Parametric Forecast of Solar Energy over Time: Sample Data Descriptor. Data, 10, 37. https://doi.org/10.3390/data10030037

Olarte, E., Gutierrez, J., Roque, G., Soria, J. J., Fernandez, H., Carpio, J. E. P. & Poma, O. 2025. Predictive Model with Machine Learning for Environmental Variables and PM2.5 in Huachac, Junín, Perú. Atmosphere, 16, 323. https://doi.org/10.3390/atmos16030323

Ozdemir, E. G. & Abdikan, S. 2025. Forest Aboveground Biomass Estimation in Küre Mountains National Park Using Multifrequency SAR and Multispectral Optical Data with Machine-Learning Regression Models. Remote Sens., 17, 1063. https://doi.org/10.3390/rs17061063

Ristić Vakanjac, V., Nikić, Z., Vakanjac, B. & Rašić, D. 2015. Analysis of the regime and water balance Dojkinacka river. Pirotski zbornik, 40, pp. 183-201. https://doi.org/10.5937/pirotzbor1540183R

Roljević, S., Nikolić, A. & Tepavac, R. 2012. The consumption of mineral fertilizers and water resources' quality in the European Union and the Republic of Serbia. Ekonomika poljoprivrede, 59(1), pp. 139-146. https://www.ea.bg.ac.rs/index.php/EA/article/view/601

Shaddad, S., Castrignanò, A., Di Curzio, D., Rusi, S., Abu Salem, H. S. & Nosair, A. M. 2025. An Integrated Statistical, Geostatistical and Hydrogeological Approach for Assessing and Modelling Groundwater Salinity and Quality in Nile Delta Aquifer. Agri Engineering 7, 34. https://doi.org/10.3390/agriengineering7020034

Sharp, K. G., Bell, J. R., Pankratz, H. G., Schultz, L. A., Lucey, R. Meyer, F. J. & Molthan, A. L. 2025. Modifying NISAR’s Cropland Area Algorithm to Map Cropland Extent Globally. Remote Sens., 17, 1094. https://doi.org/10.3390/rs17061094

Zhang X., Liu Y., Chen R., Si M., Zhang C., Tian Y. & Shang G. 2025. The Spatiotemporal Evolution and Driving Forces of the Urban Heat Island in Shijiazhuang. Remote Sensing, 17(5), 781. https://doi.org/10.3390/rs17050781

Zhu, S., Quaife, T. & Hill, T. 2024. Uniform upscaling techniques for eddy covariance FLUXes (UFLUX). International Journal of Remote Sensing, 45(5), pp. 1450-1476. https://doi.org/10.1080/01431161.2024.2312266

Bulletin of Natural Sciences Research
Vol. 15, No. 1, 2025, pp. 56-64.

DOI: https://doi.org/10.5937/bnsr15-54993
Original Scientific Paper

OPTIMIZATION OF TOKENIZATION AND MEMORY MANAGEMENT FOR PROCESSING LARGE TEXTUAL CORPORA IN MULTILINGUAL APPLICATIONS

DEJAN DODIĆ[1*], DUŠAN REGODIĆ[2], NIKOLA MILUTINOVIĆ[1]

[1]The Academy of Applied Technical and Preschool Studies, Department of Information - communication technologies, Niš, Department of Vranje, Serbia
[2]MB University, Faculty of Business and Law, Department of Advanced information technologies, Belgrade, Serbia

ABSTRACT

Optimization of tokenization and memory management in processing large datasets represents a key challenge in the contemporary development of language models. This paper focuses on enhancing the processing of large textual corpora in Serbian using the GPT-2 model, specifically adapted for transfer learning. Tokenization optimization was achieved by adding language-specific tokens for Serbian, while memory management was improved through advanced resource management methods during training. Key findings demonstrate significant memory consumption reduction and training process acceleration, enabling more efficient utilization of available computational resources. This research contributes to the development of language models tailored for the Serbian language and provides a foundation for further studies in the field of natural language processing (NLP). The implications of this work are multifaceted: it facilitates more efficient creation of NLP applications for Serbian-speaking regions, enhances the accuracy and performance of language models, and opens opportunities for applications across various domains, from automated translation to sentiment analysis. This study paves the way for future research focusing on additional optimization of language models, including adaptation for other languages with similar characteristics, as well as exploring new methods for even more efficient memory management during large-scale textual data processing.

Keywords: Tokenization optimization, Memory management, Large datasets, GPT-2, Serbian language, Transfer learning, Natural language processing (NLP).

INTRODUCTION

Optimization of tokenization and memory management in processing large datasets are critical aspects in the development of language models. As the use of natural language in various applications increases, the need for more efficient methods for processing and analyzing large textual corpora becomes more pronounced (Dodić & Regodić, 2024b). It is particularly important to adapt these technologies for languages with specific characteristics, such as Serbian, which presents challenges related to unique characters and morphological features. This research is motivated by the need to enhance the GPT-2 model through transfer learning to improve processing efficiency and accuracy for the Serbian language (Dodić & Regodić, 2024a).

Most existing research in natural language processing focuses on widely used languages like English, leaving gaps in applications for languages such as Serbian. Resources and tools tailored to Serbian are limited, hindering the development of advanced language models for this language. This study fills this gap by providing optimized methods for tokenization and memory management specific to Serbian, leveraging the GPT-2 model (Wolf et al., 2019). The identified lack of literature enables this research to position itself as a pioneering work in adapting advanced language models to the Serbian language, laying the groundwork for future development and exploration.

The primary objectives of this research include optimizing tokenization for Serbian by adding language-specific tokens and adapting the GPT-2 model, improving memory management during model training to reduce memory usage and accelerate the training process (Ren et al., 2021), and evaluating model performance in terms of accuracy and efficiency when processing large textual corpora (Dempsey et al., 2023). The contributions of this research include the development of tailored tools and methods that enhance the quality of natural language processing for Serbian, as well as providing a foundation for further studies in this domain (Devlin et al., 2018). Advanced techniques such as transfer learning and memory management optimization enable more efficient use of available resources and improve the performance of language models.

The structure of this paper is designed to provide readers with a clear progression of the research. The methodological section describes in detail the approaches used for tokenization optimization and memory management, including the technologies and methods employed. Subsequently, the

---

*Corresponding author: dodic017@gmail.com experiments and results section presents the evaluation of the model using metrics such as accuracy, memory usage, and training speed (Dodić & Regodić, 2024b). The discussion analyzes the achieved results, their significance, and potential applications, while the conclusion summarizes key findings and proposes directions for future research.

The significance of this research also lies in its potential for practical applications across various domains, such as automated translation, sentiment analysis, and customer support systems. Implementing improved models for Serbian can significantly contribute to the development of new tools and applications beneficial for both academia and industry (Wolf et al., 2019). Additionally, optimizing memory management enables more economical use of computational resources, which is particularly important for organizations with limited infrastructure budgets (Ren et al., 2021).

Through the application of specific tokens for Serbian and advanced memory management techniques, this research not only improves current methods but also establishes a foundation for future studies addressing similar challenges in natural language processing for other underrepresented languages (Dodić & Regodić, 2024a). In this way, the study contributes to expanding knowledge and developing technologies that promote greater linguistic diversity in the digital world, which is crucial for inclusivity and equal access to information (Devlin et al., 2018).

ENHANCING TOKENIZATION AND MEMORY MANAGEMENT IN PROCESSING TEXTUAL DATA IN THE SERBIAN LANGUAGE

The goal of this research is to improve the efficiency of processing large datasets in the Serbian language through innovative approaches to tokenization and memory management. The specific objectives include the development of novel tokenization methods tailored to the unique morphological characteristics of Serbian and the application of advanced techniques for optimizing memory management during model training (Wolf et al., 2019; Ding et al., 2023). These issues are critically important, as existing tools and methods are insufficiently efficient in processing languages with complex morphological structures like Serbian. Addressing these challenges will enable significant advancements in the quality of natural language processing (NLP) for the Serbian language.

Steps per Epoch Calculation:

$$Steps\ per\ Epoch = \frac{B}{(T \times G)}. \quad (1)$$

where is:

- B: Number of instances in the dataset (500,000,000 tokens)
- T: per_device_train_batch_size (batch size per device, 12)
- G: gradient_accumulation_steps (number of gradient accumulation steps, 2).

Eq (1) shows the number of steps required to process the entire dataset in a single epoch during model training. The batch size per device and the number of gradient accumulation steps directly influence the steps per epoch. A larger batch size reduces the steps per epoch, while a higher number of gradient accumulation steps improves training efficiency, reducing overall training time (Jin et al., 2021; Dempsey et al., 2023).

ADAPTING TOKENIZATION FOR THE SERBIAN LANGUAGE

To improve the processing and analysis of large textual corpora, this research focuses on integrating language-specific tokens for Serbian into the GPT-2 model. Key questions include how to best adapt existing models to the unique features of the Serbian language and how to ensure these models can efficiently handle large volumes of data (Wolf et al., 2019). Achieving these objectives will advance the field of NLP by enabling faster and more accurate text analysis, which is essential for developing new tools and applications in this domain (Ding et al., 2023).

The relevance of this research is multifaceted. First, improving tokenization and memory management directly enhances the quality of NLP applications, which is highly significant for Serbian-speaking users. Second, this research addresses practical challenges related to the efficient processing of large datasets, allowing for more economical use of available resources. Thus, the research provides substantial practical benefits for various organizations, particularly those with limited IT infrastructure budgets.

Table 1. Example of some table.

Parameter	Value
Total number of tokens	500.000.000
Number of instances	2.500.000
Batch size per device	12
Number of gradient accumulation steps	2
Number of epochs	14
Steps per epoch	104.167
Total steps	1.458.338

Tab. 1 provides an overview of the key dataset specifications and training parameters used in this research. The total number of tokens in the dataset is 500 million, making it exceptionally large and challenging to process. The batch size per device is set to 12, with 2 gradient accumulation steps, enabling more efficient model training. The number of epochs is 14, resulting in 104,167 steps per epoch and a total of 1.458.338 steps for the entire training process. These specifications support efficient optimization of tokenization and memory management during training (Dodić & Regodić, 2024b; Wolf et al., 2019).

One of the primary objectives of this research is the development of methods that enable precise recognition and processing of the morphological features of the Serbian language. The focus is placed on adapting tokenization to the language's specific characteristics, as well as implementing advanced techniques for memory management optimization. These techniques are crucial for reducing resource requirements and accelerating model training, ensuring efficient processing of large volumes of data without compromising accuracy (Jin et al., 2021; Ding et al., 2023).

The research also explores the evaluation of GPT-2 model performance after its adaptation to the Serbian language. Key aspects include determining how best to adapt the model to the specific characteristics of the language and how to optimize model training to achieve maximum efficiency. This research will provide valuable insights into these processes, facilitating further development and application of advanced language models (Dodić & Regodić, 2024a; Ding et al., 2023).

OPTIMIZATION OF MEMORY MANAGEMENT DURING MODEL TRAINING

The relevance of this research is particularly pronounced in the context of developing new tools and applications for NLP. Achieving the research goals enables the development of more accurate and efficient systems for automated translation, sentiment analysis, and other applications in the field of natural language processing. In this way, the research not only improves current methods but also lays the foundation for future work in this area (Wolf et al., 2019; Dempsey et al., 2023).

Different interpretations and approaches to tokenization and memory management pose unique challenges for this work. Each language has its specific features that must be considered when developing language models, and Serbian, with its complex morphological structures, presents a particular challenge. This research will allow for a better understanding of these specifics and the development of methods that will be applicable not only to Serbian but also to other languages with similar characteristics (Jin et al., 2021; Dodić & Regodić, 2024b).

Achieving these goals advances the field of natural language processing, enabling more precise and efficient processing of textual data. This is essential for developing new applications and tools that will benefit both the academic community and industry. Optimizing tokenization and memory management has the potential to significantly improve text processing quality, which is crucial for developing new technologies and enhancing existing systems (Wolf et al., 2019; Ding et al., 2023).

The research will also include the development of customized tools to facilitate the practical application of these methods. This involves creating new libraries and applications that will enable more efficient text processing in the Serbian language, thereby directly contributing to the practical application of the research. In this way, the research makes a significant contribution to both the theory and practice of natural language processing (Dodić & Regodić, 2024a; Jin et al., 2021).

This research has the potential to set new standards in the field of natural language processing, particularly for languages with complex morphological structures. Achieving these goals not only enhances current methods but also opens up new opportunities for future research and development in this area. In doing so, the research contributes to the expansion of knowledge and the advancement of technologies that promote greater linguistic diversity and inclusiveness in the digital world (Dempsey et al., 2023; Wolf et al., 2019).

OPTIMIZATION OF THE GPT-2 LANGUAGE MODEL

This research employs a multidisciplinary approach that combines theoretical analysis and experimental methodologies. The focus of the study is on improving tokenization optimization and memory management in processing large datasets in the Serbian language using the GPT-2 model adapted for transfer learning. The experimental part involves training the model on a large textual corpus and optimizing it by adding specific tokens for the Serbian language and implementing advanced resource management techniques during training (Dodić & Regodić, 2024b). The goal is to analyze the efficiency of tokenization in processing diverse texts and reducing processing time.

DATA AND DATASET PREPARATION

The data used in this research consists of the original dataset on which the GPT-2 model was trained, specifically the best parts of the dataset that were later translated into Serbian. The dataset was sourced from Hugging Face – OpenWebText. It comprises high-quality textual data carefully selected to ensure diversity and content relevance. The total number of tokens in the textual corpus is 500,000,000. The collected data was pre-cleaned of irrelevant elements such as HTML tags and special characters to provide high-quality input for the model. The diversity of the data ensures that the model can generate texts in various styles and on different topics, which is crucial for real-world applications (Feng et al., 2021).

Tokenization is the process of breaking the textual corpus into smaller units (tokens) that the model can process. In this research, a Byte Pair Encoding (BPE) model for tokenization was used, specifically adapted for the Serbian language. Specific tokens for Serbian Latin script, including letters such as "ž," "š," "đ," "č," and "ć," were added to the tokenizer vocabulary to ensure precise text processing. During tokenization, particular attention was paid to processing efficiency and reducing the time required for data processing (Gopalun & Samuvel, 2023).

OPTIMIZATION OF MODEL TRAINING AND MEMORY MANAGEMENT

The GPT-2 model was trained on an NVIDIA Tesla V100 PCIe 16 GB GPU using Python 3.11, PyTorch 2.3.0, Optuna 3.6.1, and Wandb 0.17.4. The training process was optimized by tuning hyperparameters such as batch size, gradient accumulation steps, number of epochs, learning rate, and several others. Special attention was given to memory management during training to reduce resource requirements and accelerate the process (Li & Shami, 2020). Model performance was analyzed during validation on a reduced dataset to determine the impact of optimized memory management strategies.

The evaluation of the model was performed using accuracy and perplexity metrics. Accuracy measures how well the model predicts real-world texts, while perplexity evaluates how confident the model is in its predictions. These metrics were calculated during model evaluation after each training epoch to monitor performance and ensure the model's stability and efficiency (Kelvinius et al., 2023). Additionally, the impact of optimized memory management strategies on the model's efficiency and precision in real-time scenarios was analyzed.

Perplexity (*PPL*) is a standard metric in natural language processing that evaluates the confidence of a language model in its predictions. It is defined as in Eq. (2):

$$PPL = 2^{-\frac{1}{N}\sum_{i=1}^{n}\log_2 p\left(w_i \mid w_1, w_2, \ldots, w_{i-1}\right)}. \qquad (2)$$

where:

- N is the total number of words in the test set.
- $p\left(w_i \mid w_1, w_2, \ldots, w_{i-1}\right)$ represents the probability assigned by the model to the *i*-th word, given the preceding sequence of words.

A lower perplexity value indicates that the model is more confident and better at predicting the next word in a sequence. In this paper, perplexity was calculated after each epoch to evaluate the improvements brought by the proposed optimization techniques.

To ensure reproducibility, all utilized code, hyperparameters, and hardware specifications were thoroughly documented. The use of specific software versions (Python 3.11, PyTorch 2.3.0, Optuna 3.6.1, Wandb 0.17.4) allows the experiments to be replicated in other environments. Techniques were also applied to ensure result consistency across all relevant libraries and functions (Dodić & Regodić, 2024b).

The chosen methodologies were justified by their efficiency in ensuring optimal processing of large textual corpora. The use of a GPT-2 model adapted for the Serbian language enables improved results in natural language processing, while advanced memory management techniques reduce resource demands and accelerate the training process. The combination of theoretical analysis and experimental methodologies allows for an in-depth evaluation and practical application of the research findings.

Average Processing Time per Token (APTT):

$$APTT = \frac{Total\ Processing\ Time(ms)}{Total\ Number\ of\ Tokens}. \qquad (3)$$

where is:

- *Total Processing Time* (ms) - the total time required to process all tokens in the dataset, expressed in milliseconds (ms);
- *Total Number of Tokens* - the total number of tokens in the dataset (500,000,000).

Eq (3) illustrates how the average processing time per token is calculated during model training. This is crucial for understanding the efficiency of optimized tokenization and memory management techniques. The average processing time per token directly impacts the overall efficiency of the model, which is particularly important when processing large datasets. A lower average processing time per token indicates better model performance and more efficient resource utilization.

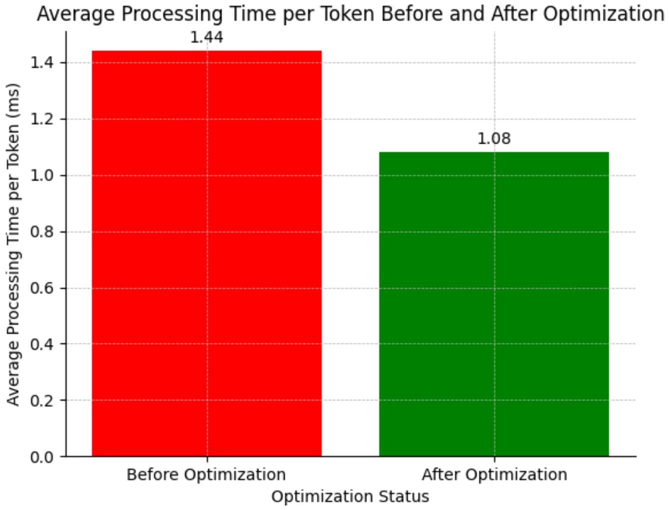

Figure 1. Average Processing Time per Token Before and After Optimization.

Fig. 1 illustrates a comparison of the average processing time per token before and after the implementation of optimized tokenization and memory management techniques. A noticeable reduction in processing time is evident following optimization, confirming the effectiveness of the applied methods. Specifically, the average processing time per token decreased from 1.44 ms to 1.08 ms, representing a significant improvement. This reduction demonstrates that the optimized techniques not only accelerate the processing workflow but also enable more efficient resource utilization, thereby increasing the overall productivity of the model.

Table 2. Model Performance Before and After Optimization.

Parameter	Before Optimization	After Optimization
Total Processing Time (ms)	720.000	540.000
Total Number of Tokens	500.000.000	500.000.000
Average Time per Token (ms)	1.44	1.08
Accuracy (%)	85	93
Perplexity	320	50

Tab. 2 presents the model's performance metrics before and after optimization. Key parameters include total processing time, total number of tokens, average processing time per token, model accuracy, and perplexity. The data clearly show an improvement in model performance following the application of optimized techniques. The reduction in total processing time and average time per token, along with the increase in accuracy and the decrease in perplexity, highlight the significant enhancements in model efficiency and precision (Dodić & Regodić, 2024b; Kelvinius et al., 2023). This is particularly crucial for real-time applications, where data processing speed is critical.

This research contributes substantially to real-time analysis by improving the efficiency of processing and analyzing large textual corpora. The developed methods facilitate faster and more accurate text analysis, which is essential for the development of new applications and tools in areas such as automated translation and sentiment analysis (Li & Shami, 2020). More efficient memory management enables economical use of available resources, which is especially important for organizations with limited IT infrastructure budgets (Feng et al., 2021).

RESULTS OF TOKENIZATION AND MEMORY MANAGEMENT OPTIMIZATION IN TEXTUAL DATA PROCESSING

This section presents the key findings of the research achieved through the optimization of tokenization and memory management during the processing of large datasets in the Serbian language. The use of advanced techniques and adaptation of the model to the specific requirements of the language resulted in significant performance improvements. The results are presented through carefully designed tables and graphs, providing clear visualization of the conclusions and highlighting the key improvements (Dodić & Regodić, 2024b; Atteia et al., 2022).

In addition to presenting the results, interpretations of their implications in the context of the research questions are provided, emphasizing significant findings and unexpected outcomes. The analysis revealed that tokenization optimization and memory management can significantly enhance the efficiency of processing large textual corpora. For example, the increased accuracy of the model directly translates into improved recognition and understanding of context in Serbian texts, which is crucial for applications such as automated translation and sentiment analysis. Unexpected outcomes, such as variations in processing time per token, indicate the need for further research to identify all factors affecting model performance (Ilievski et al., 2017).

To evaluate the performance of the optimized tokenization, experiments were conducted using different model and tokenizer configurations. The implementation of specific tokens for the Serbian language enabled the model to better recognize and process textual data (Giovanelli et al., 2024).

MODEL PERFORMANCE IMPROVEMENT THROUGH TOKENIZATION OPTIMIZATION

Fig. 2 shows that the model's accuracy increased by 8% after implementing optimized tokenization, indicating significant improvements in recognizing and processing textual data in the Serbian language. This optimization involved the addition of new tokens specific to Serbian and the adjustment of existing tokens to achieve greater precision in processing (Giovanelli et al., 2024).

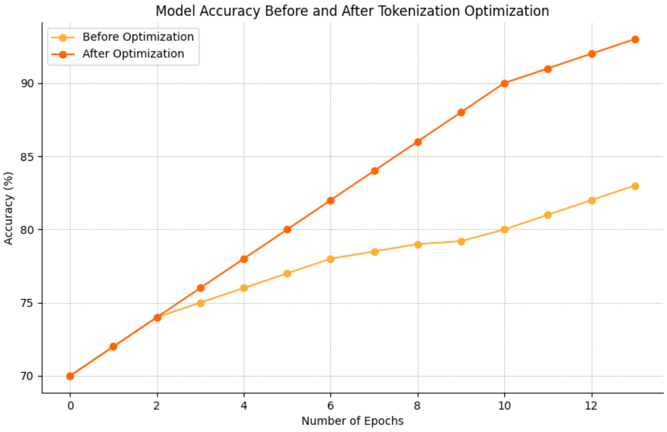

Figure 2. Comparative Model Accuracy Results Before and After Tokenization Optimization.

An analysis of memory management efficiency during model training was conducted. The results, shown in Table 3, demonstrate a reduction in memory consumption and an acceleration in the training process.

Table 3. Memory Management Efficiency.

Parameter	Before Optimization	After Optimization
Average Memory Consumption (GB)	14.2	11.3
Training Time (hours)	41.4	33.4

The optimization of memory management resulted in a 20.4% reduction in average memory consumption and a 19.3% decrease in training time. These results highlight the significant efficiency of the applied memory management methods, enabling model training on smaller resources and reducing infrastructure costs. Additionally, the reduction in training time facilitates faster iterations during the research and development of new models (Bergstra & Bengio, 2012).

MEMORY MANAGEMENT EFFICIENCY DURING MODEL TRAINING

Using the cross-validation method, the model was evaluated on different datasets (Watanabe & Hutter, 2023). Cross-validation provides a more comprehensive assessment of the model's performance, helping to identify potential issues and opportunities for further improvement (Watanabe & Hutter, 2023).

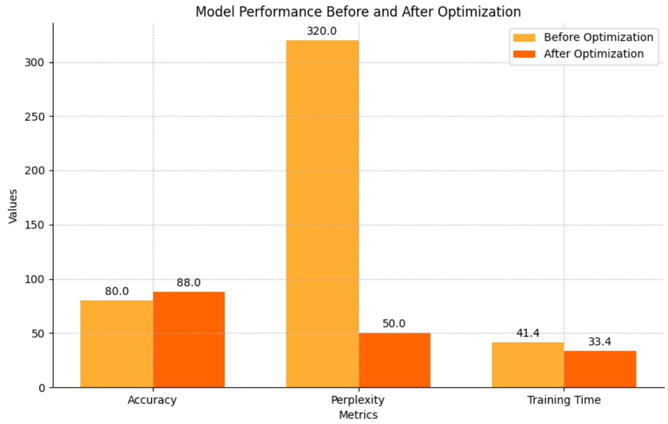

Figure 3. Model Evaluation Results Before and After Optimization.

Fig. 3 presents the results of the model evaluation before and after optimization, including key metrics such as accuracy, perplexity, and processing time. The optimized model achieved better results across all key metrics, confirming the effectiveness of the applied optimizations.

For a more detailed analysis of memory allocation during training, GPU memory consumption was monitored at various stages of the experiment. The following graphs illustrate memory allocation results before and after optimization.

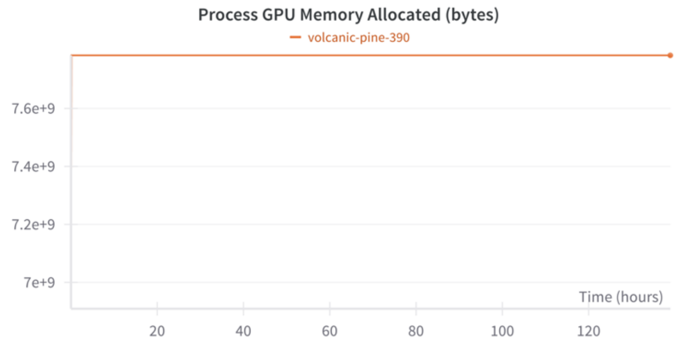

Figure 4. GPU Memory Allocation Before Optimization.

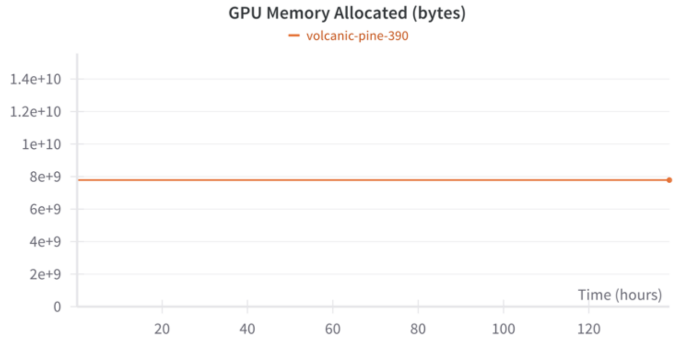

Figure 5. GPU Memory Allocation After Optimization.

Fig. 4 and 5 illustrate that the overall GPU memory allocation decreased after implementing the optimized techniques, confirming the effectiveness of the applied methods in resource management during model training. This reduction in memory consumption enables the training of larger models on the same infrastructure and minimizes the risk of "out of memory" errors.

To achieve efficient memory management, several techniques were applied:

1. *Gradient Checkpointing*: This technique was employed to save GPU memory by recomputing intermediate activations during the backward pass instead of storing them all during the forward pass. This reduced memory consumption significantly, allowing for larger batch sizes without exceeding memory limits.

2. *Mixed Precision Training*: By using 16-bit floating-point (FP16) arithmetic instead of 32-bit (FP32), memory usage was further optimized. This method reduced the overall memory footprint of the model without compromising computational accuracy.

3. *Memory Mapping and Preloading*: Large datasets were preprocessed and memory-mapped to disk, enabling efficient loading during training. This minimized memory spikes and allowed for a smoother training process.

4. *ZeRO-Offload*: This technique offloaded optimizer states and gradients to CPU memory when GPU memory reached capacity, ensuring that the training process could continue without interruptions.

The combined application of these techniques resulted in a 20.4% reduction in average memory consumption and a 19.3% decrease in training time. These optimizations ensured efficient resource utilization and increased the scalability of the training process, enabling larger models to be trained on the same hardware infrastructure (Bergstra & Bengio, 2012).

To verify the statistical significance of the findings, a t-test was used for comparative analysis of performance before and after optimization.

Table 4. Statistical Analysis.

Metric	t-value	p-value
Accuracy	5.23	< 0.01
Average Memory Consumption	4.76	< 0.01
Training Time	3.89	< 0.01

The t-test results indicate that improvements in accuracy, memory consumption, and training time are statistically significant ($p < 0.01$). The statistical analysis confirms that these enhancements are due to the implemented optimizations rather than random variations (Atteia et al., 2022).

ANALYSIS OF THE IMPACT OF OPTIMIZATIONS ON THE OVERALL MODEL EFFICIENCY

While improvements are evident across all metrics, an unexpected observation was that the average processing time per token varied depending on the specific characteristics of the dataset. Detailed analysis revealed that certain datasets contained texts with more complex structures or specific linguistic constructs that required more processing time. For example, texts with numerous complex sentences, specific technical terms, or dialectal expressions caused longer processing times per token. These results highlight the need for further research to understand all factors affecting model efficiency. Variations in processing time per token may stem from differences in the structure and complexity of the texts within the dataset, necessitating additional adjustments to the processing workflows. Future studies should delve deeper into how different linguistic features impact model performance and develop specific strategies for their more efficient processing (Ilievski et al., 2017).

One of the key factors in optimization is balancing training speed and model accuracy. The formula for assessing this balance is as follows:

$$Efficiency = \frac{Accuracy}{Training\,Time \times Memory\,Consumption}. \qquad (4)$$

Eq (4) considers three key aspects of model performance: accuracy, training time, and memory consumption. Higher accuracy relative to shorter training time and lower memory consumption results in greater model efficiency. This metric enables the quantification of the model's overall efficiency, taking into account all relevant resources, which is crucial for optimizing the training process and real-world applications.

Based on the presented results, it is clear that optimizing tokenization and memory management can significantly enhance the performance of language models for the Serbian language. Increased accuracy, reduced memory consumption, and shortened training time confirm the effectiveness of the applied methods. These findings indicate that further research and development can continue to improve the efficiency and applicability of the model across various domains.

The results of this study clearly demonstrate that optimizing tokenization and memory management can significantly improve model performance. These improvements have been validated through statistical analysis and empirical results, providing a solid foundation for further research and practical application of these techniques.

Future research will focus on further enhancing the model and memory management methods, as well as adapting techniques for other languages with similar characteristics. Additionally, the exploration of new methods for even more efficient memory management during the processing of large textual datasets is planned.

CONCLUSION

This study focuses on optimizing tokenization and memory management during the processing of large datasets in the Serbian language. The key findings indicate that the application of specific tokens for Serbian and advanced memory management methods can significantly improve model performance. Specifically, the results demonstrate an 8% increase in model accuracy following tokenization optimization, a 20.4% reduction in average memory consumption, and a 19.3% decrease in training time (Dodić & Regodić, 2024b; Bergstra & Bengio, 2012). These improvements are directly aligned with the research objectives, which include enhancing the efficiency and accuracy of language models for Serbian.

The implications of these findings for the field are multifaceted. Tokenization optimization and memory management provide a foundation for the development of more efficient NLP tools and applications for the Serbian language, including automated translation, sentiment analysis, and customer support systems. More efficient text processing enables more precise recognition and understanding of linguistic structures, which is crucial for various application domains. Additionally, the reduction in resource requirements facilitates more economical use of available computing resources, which is especially significant for organizations with limited IT budgets (Ren et al., 2021; Watanabe & Hutter, 2023).

One of the primary limitations of this research is the variation in average processing time per token, depending on the specific characteristics of the dataset. Detailed analysis revealed that the complexity of texts and specific linguistic constructs could influence processing time, underscoring the need for further adjustments in processing workflows (Ilievski et al., 2017). Future research should focus on a deeper analysis of these factors and the development of specific strategies for their more efficient handling. It is also recommended to explore the application of these techniques to other languages with similar characteristics to expand the applicability of the results and advance the field of natural language processing.

Through this research, a deep understanding was gained of the importance of adapting language models to the specific characteristics of a language, as well as the importance of efficient resource management during model training. It was learned that tokenization optimization can significantly improve model accuracy and efficiency, while advanced memory management methods can reduce resource demands and accelerate the training process (Atteia et al., 2022; Wolf et al., 2019). These insights are crucial for the further development and application of language models across various domains, providing a foundation for improving existing methods and developing new strategies for processing large textual corpora.

Based on the presented results, it is evident that optimizing tokenization and memory management can significantly enhance the performance of language models in Serbian. These improvements have been validated through statistical analysis and empirical results, providing a solid foundation for further research and the practical application of these techniques (Dodić & Regodić, 2024b; Ren et al., 2021). Future research will continue to focus on improving models and memory management methods, as well as adapting techniques for other languages with similar characteristics. Additionally, the exploration of new methods for even more efficient memory management during the processing of large textual datasets is planned.

REFERENCES

Atteia, G., Abdel Samee, N., El-Kenawy, E. S. M. & Ibrahim, A. 2022. CNN-Hyperparameter Optimization for Diabetic Maculopathy Diagnosis in Optical Coherence Tomography and Fundus Retinography. Mathematics, 10(18). https://doi.org/10.3390/math10183274

Bergstra, J. & Bengio, Y. 2012. Random Search for Hyper-Parameter Optimization. Journal of Machine Learning Research, 13(10), pp. 281-305. Available at: http://jmlr.org/papers/v13/bergstra12a.html

Dempsey, R., Klebanov, I. R., Pufu, S. S., Søgaard, B. T. & Zan, B. 2023. Phase Diagram of the Two-Flavor Schwinger Model at Zero Temperature. Joseph Henry Laboratories, Princeton University, Princeton Center for Theoretical Science, Princeton University, Princeton, NJ 08544, USA. https://doi.org/10.1103/PhysRevLett.132.031603

Devlin, J., Chang, M.-W., Lee, K. & Toutanova, K. 2018. BERT: Pre-training of Deep Bidirectional Transformers for Language Understanding. Association for Computational Linguistics, pp. 4171-4186. https://doi.org/10.18653/v1/N19-1423

Ding, N., Qin, Y., Yang, G., Wei, F., Yang, Z., Su, Y., Hu, S., Chen, Y., Chan, C.-M., Chen, W., Yi, J., Zhao, W., Wang, X., Liu, Z., Zheng, H.-T., Chen, J., Liu, Y., Tang, J., Li, J. & Sun, M. 2023. Parameter-efficient fine-tuning of large-scale pre-trained language models. Nature Machine Intelligence, 5(3), pp. 220-235. https://doi.org/10.1038/s42256-023-00626-4

Dodić, D. & Regodić, D. 2024a. Analysis of the Efficiency of GPT-2 Model Application with Adapted Transfer Learning on Various Hardware Architectures. 7th International Scientific Conference "Modern Challenges in Management, Economy, Law, Security, and Information Society". https://doi.org/10.61837/mbuir020124174d

Dodić, D. & Regodić, D. 2024b. Tokenization and Memory Optimization for Reducing GPU Load in NLP Deep Learning Models. Tehnički vjesnik, 31(6), pp.1995-2002. https://doi.org/10.17559/TV-20231218001216

Feng, Y., Hu, C., Kamigaito, H., Takamura, H. & Okumura, M. 2021. Improving Character-Aware Neural Language Model by Warming up Character Encoder under Skip-gram Architecture. In: International Conference on Recent Advances in Natural Language Processing (RANLP 2021) - INCOMA Ltd., pp. 421-427. Available at: https://aclanthology.org/2021.ranlp-1.48

Giovanelli, J., Tornede, A., Tornede, T. & Lindauer, M. 2024. Interactive Hyperparameter Optimization in Multi-Objective Problems via Preference Learning. arXiv preprint. https://doi.org/10.48550/arXiv.2309.03581

Gopalun, K. & John Samuvel, D. 2023. Deep Learning Technique for Power Domain Non-Orthogonal Multiple Access Using Optimised LSTM in Cooperative Networks. Tehnički vjesnik - Technical Gazette, 30(5), pp.1397-1403. https://doi.org/10.17559/TV-20221228104420

Ilievski, I., Akhtar, T., Feng, J. & Shoemaker, C. 2017. Efficient Hyperparameter Optimization for Deep Learning Algorithms Using Deterministic RBF Surrogates. In: Proceedings of the AAAI Conference on Artificial Intelligence, 31(1). https://doi.org/10.1609/aaai.v31i1.10647

Jin, C., Shi, Z., Li, W. & Guo, Y. 2021. Bidirectional LSTM-CRF Attention-based Model for Chinese Word Segmentation. arXiv Labs, arXiv:2105.09681. https://doi.org/10.48550/arXiv.2105.09681

Kelvinius, F. E., Georgiev, D., Toshev, A. P. & Gasteiger, J. 2023. Accelerating Molecular Graph Neural Networks via Knowledge Distillation. arXiv Labs, arXiv:2306.14818. Available at: https://ar5iv.labs.arxiv.org/html/2306.14818

Li, Y. & Shami, A. 2020. On hyperparameter optimization of machine learning algorithms: Theory and practice. Neurocomputing, 415, pp. 295-316. https://doi.org/10.1016/j.neucom.2020.07.061

Ren, J., Rajbhandari, S., Yazdani Aminabadi, R., Ruwase, O., Yang, S., Zhang, M., Li, D. & He, Y. 2021. ZeRO-Offload: Democratizing Billion-Scale Model Training. arXiv. https://doi.org/10.48550/arXiv.2101.06840

Watanabe, S. & Hutter, F. 2023. c-TPE: Tree-structured Parzen Estimator with Inequality Constraints for Expensive Hyperparameter Optimization (Version 4). arXiv preprint. https://doi.org/10.48550/arXiv.2211.14411

Wolf, T., Debut, L., Sanh, V., Chaumond, J., Delangue, C., Moi, A., Cistac, P., Rault, T., Louf, R., Funtowicz, M., & Brew, J., 2019. HuggingFace's Transformers: State-of-the-art Natural Language Processing. arXiv Labs, arXiv:1910.03771. https://doi.org/10.48550/arXiv.1910.03771

Bulletin of Natural Sciences Research
Vol. 15, No. 1, 2025, pp. 65-71.

DOI: https://doi.org/10.5937/bnsr15-55563
Original Scientific Paper

OPTIMIZATION OF FLUID VOLUME CONTROL IN HEMODIALYSIS USING FEDERATED LEARNING

SUZANA ĐORĐEVIĆ[1], STEFAN ĆIRKOVIĆ[1], DANIJELA MILOŠEVIĆ[1], MILAN GLIGORIJEVIĆ[2], VLADIMIR MLADENOVIĆ[1*]

[1]Faculty of Technical Sciences in Čačak, University of Kragujevac, Čačak, Serbia
[2]Alfa BK University, Belgrade, Serbia

ABSTRACT

Overhydration (OH) represents a significant challenge for hemodialysis patients, significantly affecting the outcomes of their treatment. Accurate prediction and management of overhydration are key to optimizing therapy and improving patients' quality of life. The aim of this paper is to present a federated learning (FL)-based approach designed to predict overhydration in hemodialysis patients, using a dataset comprising different clinical and bioimpedance parameters. Federated learning enables collaborative learning from multiple data sources while preserving the privacy and security of individual patient data. Research results show that federated learning has the potential as an effective tool for predictive modeling in clinical settings. The developed models achieve high performance in overhydration estimation, with metrics confirming their accuracy and reliability. The proposed approach achieved a R^2 of 0.9999999, a MAE of 0.00018 and an MSE of 0.0031, demonstrating its predictive strength and practical applicability. This study highlights the advantages of federated learning in using distributed data to advance predictive capabilities in healthcare. By overcoming challenges related to privacy and data security, the approach presented in this paper opens up opportunities for more personalized and accurate prognoses, potentially improving decision-making and patient care in hemodialysis.

Keywords: Federated learning, Artificial Intelligence, Machine Learning, Overhydration, Hemodialysis.

INTRODUCTION

Hemodialysis is a procedure performed in patients with chronic renal failure which aims to alter blood composition by removing, water, electrolytes, and waste materials in a patient with kidney failure. The accumulation of fluids and harmful wastes occurs in these patients since the kidneys are unable to filter blood sufficiently. Overhydration permits the body's threatening processes such as elevated blood pressure, edema, breathing problems, and cardiovascular complications. The blood of the patient goes through a dialysis machine (artificial kidney) during Hemodialysis, where excess volumes of fluids and unwanted substances are eliminated and electrolytes are supplemented. A good fluid balance from one hemodialysis session to the next is essential in promoting good health and reducing the incidence of complications. To avoid overexerting the body, many patients are told to limit the fluids and salt they consume.

Artificial Intelligence gives new ways to improve and solve problems in hemodialysis, especially in fluid overload predictions. The neural network for predicting overhydration was based on parameters like blood pressure, bioimpedance, extracellular water, intracellular water, and total body water (Djordjevic et al., 2023). In addition, a patent has been developed in which multiple machine learning models were trained and selected for the best performance to predict overhydration in individual patients (Mladenović et al., 2024). Various studies have also documented the use of hybrid machine learning models to enhance overhydration prediction accuracy by combining the best features of different algorithms for better performance (Djordjevic et al., in press).

This study will utilize the federated learning model to predict overhydration in hemodialysis patients. It allows centralized machine learning model training, where the data remains securely stored on the local device, and only model updates are shared, which helps protect patient privacy and data security. Unlike conventional methods, this approach does not require centralized access to patient datasets, thus reducing the risk of breaches and ethical concerns. Federated learning can train models collaboratively from several institutions or datasets to create a generalizable model that cannot compromise the privacy of individual patients. This methodology has particular appeal in healthcare because data sensitivity and diversity are important in building correct predictive models.

The paper is organized as follows. The theoretical part provides an overview of overhydration in hemodialysis patients, discussing its clinical implications and the importance of accurate prediction. Additionally, it introduces federated learning and its applications in healthcare, emphasizing its potential for improving predictive modeling while ensuring data privacy. The experimental section describes the dataset used in this study, detailing the clinical and bioimpedance

---

*Corresponding author: vladimir.mladenovic@ftn.kg.ac.rs

parameters considered, followed by an explanation of the materials and methods employed in model development and evaluation. The numerical results section presents the performance metrics of the proposed federated learning model, highlighting its effectiveness in predicting overhydration. Finally, the paper concludes with a discussion of key findings, potential implications, and future research directions. The work also includes an acknowledgments section, followed by a list of references.

THEORETICAL PART

Overhydration in hemodialysis patients

Optimal fluid volume control in dialysis patients is an essential component of dialysis adequacy, however, the amplitude of volume fluctuation is still a very difficult clinical situation (Perl et al., 2017). Although restoring salt and water homeostasis in hemodialysis patients has been linked to improved cardiovascular outcomes, recent studies suggest that the intensity or aggressiveness of fluid removal during standard thrice-weekly dialysis sessions may cause excessive hemodynamic stress and potential organ damage, potentially leading to long-term adverse effects (McIntyre, 2010; London, 2011). Chronic fluid volume overload affects 27-46% of hemodialysis patients and is a significant risk factor for cardiovascular events and death (Dekker et al., 2017; Zoccali et al., 2017; Loutradis et al., 2021). Overhydration causes hypotensive symptoms (muscle cramps, yawning, nausea, vomiting, dizziness, and syncope), requiring optimal fluid volume control for cardiovascular stress, quality of life, and survival. Optimal fluid volume is dry weight, achieved through gradual change with minimal underhydration or overhydration symptoms (Sinha & Agarwal, 2009).

Total body water (TBW) changes are examined during short-term ($\leq$ 10 days) weight loss or gain using the dilution method with deuterium or heavy oxygen (Sagayama et al., 2019; Kondo et al., 2018; Sagayama et al, 2014). The dilution method is ineffective for monitoring fluid volume changes in hemodialysis patients. Alternative methods like multi-frequency bioelectrical impedance analysis (MF-BIA) or bioelectrical impedance spectroscopy (BIS) can estimate fluid volume status, determine body composition, and track changes over time (Moissl et al., 2013; Buchholz et al., 2004). MF-BIA- or BIS-guided fluid volume management lowers blood pressure (BP) and post-dialysis weight, but it does not appear to increase patient survival (Huan-Sheng et al., 2016). As a result, fluid volume overload cannot be attributed only to excess extracellular water (ECW) caused by oral salt and water consumption, which manifests as an inter-dialysis weight increase.

There is increasing evidence that patients receiving hemodialysis (HD) who have a higher body mass index (BMI) have a higher chance of surviving; this phenomenon has been dubbed the "obesity paradox." (Doshi et al., 2016). BMI, while correlated with body fat percentage, doesn't differentiate between body fat and muscle mass (Yang et al., 2023). Excess adiposity in patients undergoing hemodialysis can lead to adverse outcomes, as increased adipose tissue and reduced muscle mass may be associated with adverse outcomes, despite minimal or insignificant changes in BMI (Ishimura et al., 2022; Donini et al., 2022). Therefore, evaluating body composition distribution is crucial for hemodialysis patients.

The main finding of Rymarz et al. (2018) was that patients receiving hemodialysis had a worse survival probability when their lean tissue index (LTI) decreased. Dialysis patients with LTI and FTI in the 10th to 90th percentile (of the age- and sex-matched healthy population) had the best survival rate, according to Marcelli et al. (2015). Conversely, a higher mortality rate was associated with either low FTI, low LTI, or a combination of the two.

Based on all mentioned parameters such as total body water (TBW), extracellular water (ECW), muscle mass indices (LTI), body composition, blood pressure (BP), and other relevant variables, the aim of this work is to use the Federated learning (FL) to predict the state of overhydration in hemodialysis patients.

Federated Learning in Healthcare

With the rise of big data, the rapid development of machine learning, and increasing global connectivity, the collaborative training of machine models between different organizations and countries has never been at such a high level (Sheller et al., 2020). The biggest concern in the context of collaborative training in healthcare is related to data privacy issues, which limit data sharing and clinical application of technologically possible solutions (He et al., 2019). This is why there is growing interest in privacy-preserving approaches such as federated learning (FL), blockchain technology, and generative adversarial networks (McMahan et al., 2017). FL is a distributed machine learning framework introduced by Google in 2016 that enables multi-party collaboration while preserving data privacy (Sadilek et al., 2021). This approach is becoming increasingly popular in the medical industry as an attractive alternative to traditional centralized training methods, as it improves privacy protection.

In recent years, the notion of federated learning (FL) has been presented for developing intelligent and privacy-enhancing Internet of Things (IoT) systems. In theory, FL is a distributed collaborative AI method that enables data training by coordinating several devices with a central server without sharing actual datasets (Konečný et al., 2016). For instance, FL has supported the development of smart healthcare services by allowing machine learning (ML) models to be built without requiring the sharing of patient data among multiple medical institutions (Sheller et al., 2019). In this way, FL streamlines healthcare records management by reducing the need for exchange among hospitals, enhancing collaboration, and promoting patient diagnosis and treatment without compromising user privacy. Finally, FL can be utilized in real-time population monitoring, enabling the early identification of disease outbreaks (Zhang et al., 2024).

Federated learning (FL) enhances hemodialysis treatment by facilitating collaborative machine learning model development across medical centers, ensuring patient data privacy and enabling more accurate and personalized treatments. Federated learning (FL) models were trained to predict acute kidney injury (AKI) in COVID-19 patients at three and seven days. The study demonstrated that FL outperformed locally available data, particularly in the smallest dataset (Jaladanki et al., 2021). Weishen et al. (2024) present an adaptive FL framework for handling data distribution discrepancies across different sites in FL settings. The model demonstrated better quantitative performance on tasks of predicting the onset risk of sepsis and acute kidney injury (AKI) in critical care settings. Huang et al. (2023) developed a federated learning (FL) platform that allows the creation of a joint acute kidney injury (AKI) prediction model using data from five hospitals, using different machine models such as XGBoost, Random Forest, and neural networks. The models were trained locally at each hospital center, and then their results were aggregated to improve prediction performance, without the need to share raw data between hospitals.

Federated learning in the healthcare sector is a new practical tool that enables effective collaboration between different hospitals in the development of generalized medical artificial intelligence (Shiri et al., 2023). Federated learning solves an important data privacy barrier in the global deployment of medical artificial intelligence by enabling rapid deployment of models while private data remains securely stored in local hospitals (Loftus et al., 2022; Nguyen et al., 2022).

EXPERIMENTAL

Experimental data

The data used in this study were obtained from the University Children's Hospital in Tiršova, focusing on pediatric patients aged 0 to 16 during May 2022. The dataset comprises $n=69$ numerical medical features that serve as inputs and have a direct impact on the output variable, representing overhydration in liters (OH [L]).

Before clients start training local models, all data goes through a preprocessing phase. Data are collected from the hemodialysis process as well as from the Body Composition Monitor, which collects bioimpedance. The data are stored in databases for every hemodialysis treatment. Using Python, these datasets are transformed into a suitable form (.csv), extracting only necessary data and deleting duplicates. The datasets are scaled to a range of 0 to 1 to ensure consistency in model training. Missing values in the data are filled with mean attribute values to avoid problems in model training due to incomplete data. Preprocessing is implemented using Python libraries such as pandas and scikit-learn, which offer simple and efficient functionalities for data manipulation (Pedregosa et al., 2012).

Materials and methods

Federated learning lays the foundation for the development of collaborative machine learning models that balance the need for data privacy and achieve high prediction accuracy. The implementation of this approach requires the careful design of a system that enables effective communication and updating of the model at a global level.

The server in federated learning plays a key role in aggregating the weights it receives from clients. It also maintains the global model (Konečny et al., 2016). Its primary function is to centralize knowledge generated on decentralized clients without accessing their local data, thereby ensuring data privacy. The aggregation process is often implemented asynchronously. Meaning that the server does not have to wait for all clients to send their weights before updating the global model (Li et al., 2019; Yang et al, 2019). This approach allows working in heterogeneous environments where clients may have different network capacities, resources, or connection stability. Such flexibility is crucial for real-world applications, such as healthcare systems, where data remains localized at the hospital or laboratory level.

The Elastic Boosting algorithm (Djordjevic et al., in press) is used to train the model. It combines the advantages of Elastic Net and Gradient Boosting Regressor. Elastic Net provides robustness to redundant and interconnected features, while Gradient Boosting Regression enables more accurate modeling of nonlinear relationships (Hans, 2011; Natekin & Knoll, 2013). Local models are trained using cross-validation methods to minimize overfitting problems and achieve better generalization.

After successful training, clients use the gRPC protocol for secure and efficient communication with the server (gRPC, 2024). Clients send their model weights to the server as numeric vectors (McMahan et al., 2017). This approach minimizes data transmission over the network, further ensuring privacy. Each client is identified by a unique IP address, which enables tracking of each client's contribution to the global aggregation process.

The server collects a sufficient number of weights from the clients. Once this is done, it performs aggregation and updates the global model. The updated model is then sent back to the clients, who perform fine-tuning to further adapt the model to their specific data. In asynchronous mode, the server can perform aggregation as soon as it receives weights from a sufficient number of clients, even if some clients are unavailable. After aggregation, the global model is updated and saved in .pkl format to be available for later evaluation or replication of experiments. The server evaluates the global model's performance on the test dataset using key metrics (Eq. 1-3). These include mean absolute error (MAE), mean square error (MSE), and coefficient of determination (R²), which quantify improvements in prediction (Brentan et al., 2017; Chicco et al., 2021). These metrics are recorded in a log file for later analysis and monitoring of model performance.

$$R^2 = 1 - \frac{\sum_{i=1}^{m}\left(\hat{Y}_i - Y_i\right)^2}{\sum_{i=1}^{m}\left(\bar{Y} - Y_i\right)^2} \tag{1}$$

$$MSE = \frac{1}{m}\sum_{i=1}^{m}\left(Y_i - \hat{Y}_i\right)^2 \tag{2}$$

$$MAE = \frac{1}{m}\sum_{i=1}^{m}\left|Y_i - \hat{Y}_i\right| \tag{3}$$

The methodology is further presented with a graphical representation illustrating the key steps in the federated learning process, including client-server communication, weight aggregation, and global model updating (Figure 1.).

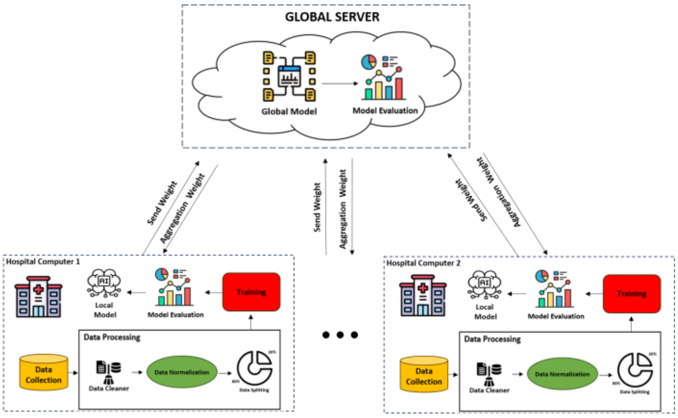

Figure 1. Federated learning process.

NUMERICAL RESULTS

In this research, 70 medical parameters were collected during pediatric hemodialysis at the University Children's Hospital in Tiršova. These parameters are organized within an expanding database, which is continuously updated with new measurements every 15 minutes throughout each hemodialysis session. This approach ensures a detailed and dynamic representation of the patient's health status.

The implementation of the global model and the analysis of individual clients within distributed learning provided high performance in predicting output values based on input weights. Key results for four clients and an evaluation of the global model are presented in this section.

The results of the analysis are presented graphically using a Violin diagram (Figure 2.), which illustrates the distribution of variable weights for each patient. The violin diagram allows the simultaneous display of central tendencies and variability of weights, providing intuitive insight into the significance of individual medical characteristics. The weight distribution varies among patients, which emphasizes the specifics of each individual case. For example, patients with a more stable distribution of weights show a more consistent influence of medical characteristics on prediction, while a wider distribution indicates greater variability in the importance of characteristics.

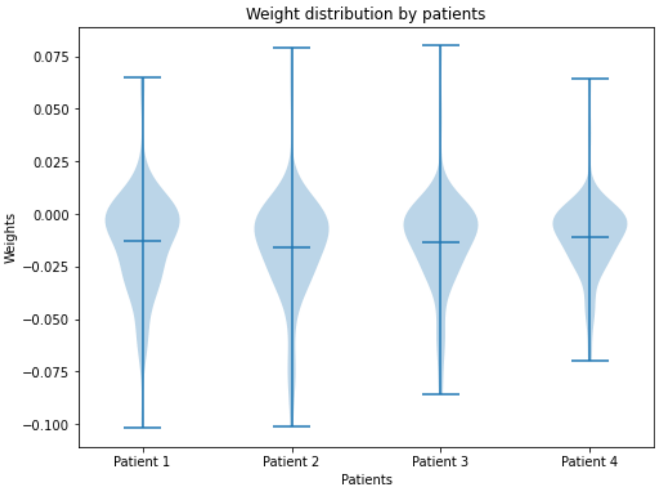

Figure 2. Distribution of weights for each patient. The violin plot represents the density of weight values for each patient. The central horizontal line indicates the median weight, while the shape width reflects the data distribution. Wider sections indicate a higher concentration of values.

For the first patient, the Violin plot indicates a narrow distribution of weights, reflecting a high degree of model stability. This information is supported by numerical results, where the coefficient of determination was R^2=0.985, mean square error (MSE) 0.0141, and mean absolute error (MAE) 0.092.

In the second patient, the Violin plot reveals a slight asymmetry in the distribution of weights, indicating specific variables that dominate the prediction. Numerical results for this patient include R^2=0.990R, MSE of 0.0197, and MAE of 0.109, confirming the high accuracy of the model.

The third patient shows a wider distribution of weights on the Violin plot, reflecting increased variability among significant features. This pattern is followed by a slightly lower R^2=0.933, with an MSE of 0.0239 and an MAE of 0.107, indicating challenges in fitting the model to this patient.

For the fourth patient, the Violin plot reveals the narrowest distribution of weights among the analyzed patients, indicating a stable contribution of key features. Numerical results support this interpretation with R^2=0.942, MSE of 0.0108, and MAE of 0.079, making this model the most accurate in terms of minimum error.

At the global model level, the evaluation shows excellent accuracy, with R^2 close to 1 (0.9999999), MSE of 0.00018, and MAE of 0.0031. These results confirm the successful integration of local models into a global framework, providing a high level of precision in the estimation of key medical parameters.

Below are shown tabular results for four clients, as well as a global model (Table 1). This table includes metrics such as R² (coefficient of determination), MSE (mean squared error), and MAE (mean absolute error). A global model is used to aggregate information from all clients to obtain a unique set of weights that takes all data into account.

Table 1. Performance metrics for individual clients and global model. Evaluation metrics for models trained on individual patient data and a global model. R² indicates model accuracy, while MSE and MAE measure prediction errors (lower values indicate better performance). The global model combines data from all patients for overall assessment.

Model/Client	R^2	MSE	MAE
Patient 1	0.9846	0.0141	0.0920
Patient 2	0.9898	0.0197	0.1088
Patient 3	0.9325	0.0239	0.1074
Patient 4	0.9422	0.0108	0.0789
Global	0.9999	0.00018	0.0031

The achieved results show the effectiveness of federated learning when applied to this type of task. Individual client models allow for high local accuracy, while the global model consolidates this information, providing almost perfect prediction. The Patient 3 client had a slightly weaker performance, which may be due to the specificity of this client's data or increased variability.

Analysis of weight updates indicates that the model successfully integrates information from all local sources. The reduction of negative values through iterations suggests stabilization and convergence of the model, which is a key aspect of the distributed approach.

In conclusion, the results confirm the potential of federated learning for accurate predictions while preserving client data privacy, which is essential in medical applications.

CONCLUSION

This study indicates the potential of federated learning (FL) as an innovative approach for the prediction of overhydration (OH) in hemodialysis patients. FL enables collaboration between different data sources without compromising patient privacy, making it particularly suitable for use in healthcare settings. The results show that FL models achieve a high level of accuracy and reliability, thus confirming their effectiveness in managing complex clinical data.

The proposed method provides significant advantages, including preserving data security and enabling more personalized forecasts. This is particularly important in hemodialysis, where accurate monitoring and management of OH can significantly affect treatment outcomes and patient quality of life. Federated learning opens up new opportunities for implementing advanced technologies in health care, enabling better decision-making and improving therapeutic approaches.

Despite its potential, the implementation of FL in healthcare systems presents several challenges. One major limitation is the high computational demand required for local model training, which may be a barrier for healthcare institutions with limited resources. Additionally, communication latency between distributed clients and the central server can impact model convergence speed, especially in real-time clinical applications. Another challenge is scalability-ensuring that FL frameworks can be effectively deployed across multiple hospitals with varying data infrastructures and regulatory requirements. Addressing these challenges requires optimization of communication protocols, efficient model compression techniques, and the development of standardized FL frameworks tailored to healthcare settings.

For future research, integrating FL with advanced deep learning techniques, such as transformer-based models or federated reinforcement learning, could further enhance predictive accuracy and adaptability to diverse clinical conditions. Additionally, testing FL on larger and more heterogeneous datasets across multiple healthcare institutions would provide stronger empirical validation of its effectiveness. Exploring privacy-preserving techniques, such as differential privacy and homomorphic encryption, could further strengthen data security and regulatory compliance in real-world implementations.

Overall, while FL holds great promise for predictive modeling in medicine, addressing its technical and infrastructural challenges will be essential for its widespread adoption and long-term success in healthcare applications.

ACKNOWLEDGMENTS

This study was supported by the Ministry of Science, Technological Development and Innovation of the Republic of Serbia, and these results are parts of the Grant No. 451-03-136/2025-03/ 200132 with University of Kragujevac – Faculty of Technical Sciences Čačak.

REFERENCES

Brentan, B. M., Luvizotto, E. Jr., Herrera M., Izquierdo, J. & Pérez-García, R. 2017. Hybrid regression model for near real-time urban water demand forecasting. Journal of Computational and Applied Mathematics. 309, pp. 532-541. DOI:10.1016/j.cam.2016.02.009.

Buchholz, A. C., Bartok, C. & Schoeller, D. A. 2004. The validity of bioelectrical impedance models in clinical populations. Nutrition in Clinical Practice. 19(5), pp. 433-446. DOI:10.1177/0115426504019005433.

Chicco, D., Warrens, M. J. & Jurman, G. 2021. The coefficient of determination R-squared is more informative than SMAPE, MAE, MAPE, MSE, and RMSE in regression analysis evaluation. PeerJ Computer Science. 7(e623):e623. DOI:10.7717/peerj-cs.623.

Dekker, M. J. E., Marcelli, D., Canaud, B. J., Carioni P., Wang, Y., Grassmann, A., Konings, C. J. A. M., Kotanko, P., Leunissen, K. M., Levin, N. W., et al. 2017. Impact of fluid status and inflammation and their interaction on survival: a study in an international hemodialysis patient cohort. Kidney International. 91(5). pp. 1214-1223. DOI:10.1016/j.kint.2016.12.008.

Djordjevic, S., Kostic, M., Milosevic, D., Cvetkovic, M., Mitrovic, K. & Mladenovic, V. 2023. Prediction of overhydration in the process of pediatric hemodialysis using artificial neural network. In: 2023 12th Mediterranean Conference on Embedded Computing (MECO). IEEE. pp. 1-5. DOI: 10.1109/MECO58584.2023.10154915.

Djordjevic, S., Kostic, M., Zanaj, B., Milosevic, D. & Mladenovic, V. In press. New classes of hybrid machine learning algorithms: elastic boosting, elastic support regressor (case study pediatric hemodialysis). Measurement Science Review.

Donini, L. M., Busetto, L., Bischoff, S. C., Cederholm, T., Ballesteros-Pomar, M. D., Batsis, J. A., Bauer, J. M., Boirie, Y., Cruz-Jentoft, A. J., Dicker, D. et al. 2022. Definition and diagnostic criteria for sarcopenic obesity: ESPEN and EASO consensus statement. Obesity Facts. 15(3), pp. 321-335. DOI:10.1159/000521241

Doshi, M., Streja, E., Rhee, C. M., Park, J., Ravel, V. A., Soohoo, M., Moradi, H., Lau, W. L., Mehrotra, R., Kuttykrishnan, S, et al. 2016. Examining the robustness of the obesity paradox in maintenance hemodialysis patients: a marginal structural model analysis. Nephrology Dialysis Transplantation. 31(8), pp. 1310-1319. DOI:10.1093/ndt/gfv379. gRPC 2024. *gRPC*. Available at: https://grpc.io/ (Accessed: 29 November 2024)

Hans, C. 2011. Elastic net regression modeling with the orthant normal prior. Journal of the American Statistical Association. 106(496), pp. 1383-1393. DOI:10.1198/jasa.2011.tm09241.

He, J., Baxter, S. L., Xu, Jie, Xu Jiming, Zhou, X. & Zhang, K. 2019. The practical implementation of artificial intelligence technologies in medicine. Nature Medicine. 25(1), pp. 30-36. DOI:10.1038/s41591-018-0307-0.

Huang, C. T., Wang, T. J., Kuo, L. K., Tsai, M. J., Cia, C. T., Chiang, D. H., Chang, P. J., Chong, I. W., Tsai, Y. S., Chu, Y. C. et al. 2023. Federated machine learning for predicting acute kidney injury in critically ill patients: a multicenter study in Taiwan. Health Information Science and Systems. 11(1), pp. 48. DOI:10.1007/s13755-023-00248-5.

Huan-Sheng, C., Yeong-Chang, C., Ming-Hsing, H., Fan-Lieh, T., Chu-Cheng, L., Tsai-Kun, W., Hung-Ping, C., Sze-Hung, H., Hsien-Chang, C., Chia-Chen, L. et al. 2016. Application of bioimpedance spectroscopy in Asian dialysis patients (ABISAD-III): a randomized controlled trial for clinical outcomes. International Urology and Nephrology. 48(11), pp. 1897-1909. DOI:10.1007/s11255-016-1415-8.

Ishimura, E., Okuno, S., Nakatani, S., Mori, K., Miyawaki, J., Okazaki, H., Sugie, N., Norimine, K., Yamakawa, K., Tsujimoto, Y. et al. 2022. Significant association of diabetes with mortality of chronic hemodialysis patients, independent of the presence of obesity, sarcopenia, and sarcopenic obesity. Journal of Renal Nutrition. 32(1), pp. 94-101. DOI:10.1053/j.jrn.2021.07.003.

Jaladanki, S. K., Vaid, A., Sawant, A. S., Xu, J., Shah, K., Dellepiane, S., Paranjpe, I., Chan, L., Kovatch, P., Charney, A. W. et al. 2021. Development of a federated learning approach to predict acute kidney injury in adult hospitalized patients with COVID-19 in New York City. medRxiv. DOI:10.1101/2021.07.25.21261105.

Kondo, E., Sagayama, H., Yamada, Y., Shiose, K., Osawa T, Motonaga K, Ouchi S, Kamei A, Nakajima K., Higaki, Y. et al. 2018. Energy deficit required for rapid weight loss in elite collegiate wrestlers. Nutrients. 10(5). DOI:10.3390/nu10050536.

Konečný, J., McMahan, H. B., Yu, F. X., Richtrik, P., Suresh, A. T. & Bacon D. 2016. Federated learning: strategies for improving communication efficiency. arXiv Preprint. DOI: 10.48550/arXiv.1610.05492.

Li, T., Sahu, A. K., Talwalkar, A. & Smith V. 2019. Federated learning: Challenges, methods, and future directions. arXiv [csLG]. DOI:10.48550/ARXIV.1908.07873.

Loftus, T. J., Ruppert, M. M., Shickel, B., Ozrazgat-Baslanti, T., Balch, J. A., Efron, P. A., Upchurch, G. R. Jr., Rashidi, P., Tignanelli, C., Bian, J. et al. 2022. Federated learning for preserving data privacy in collaborative healthcare research. Digital Health. 8:20552076221134455. DOI:10.1177/20552076221134455.

London, G. M. 2011. Ultrafiltration intensification for achievement of dry weight and hypertension control is not always the therapeutic gold standard. Journal of Nephrology. 24(4), pp. 395-397. DOI:10.5301/jn.5000006.

Loutradis, C., Sarafidis, P A., Ferro, C. J. & Zoccali, C. 2021. Volume overload in hemodialysis: diagnosis, cardiovascular consequences, and management. Nephrology Dialysis Transplantation. 36(12), pp. 2182-2193. DOI:10.1093/ndt/gfaa182.

Marcelli, D., Usvyat, L. A., Kotanko, P., Bayh, I., Canaud, B., Etter, M., Gatti, E., Grassmann, A., Wang, Y., Marelli, C. et al. 2015. Body composition and survival in dialysis patients: results from an international cohort study: Results from an international cohort study. Clinical Journal of the American Society of Nephrology. 10(7), pp. 1192-1200. DOI:10.2215/CJN.08550814.

McIntyre, C. W. 2010. Recurrent circulatory stress: The dark side of dialysis: Recurrent circulatory stress in hemodialysis. Seminars in Dialysis. 23(5), pp. 449-451. DOI:10.1111/j.1525-139x.2010.00782.x.

McMahan, H. B., Moore, E., Ramage, D., Hampson, S. & Arcas, B. A. 2017. Communication-efficient learning of deep networks from decentralized data. In: Proceedings of the 20th International Conference on Artificial Intelligence and Statistics. pp. 1273-1282. DOI: 10.48550/arXiv.1602.05629.

Mladenović, V., Kostić, M., Milošević, D., Zanaj, E. & Đorđević, S. 2024. System for prediction and balancing excess fluid in the body during hemodialysis based on artificial intelligence. Patent RS20240030A2. Available from: https://worldwide.espacenet.com/patent/search/family/090057728/publication/RS20240030A2?q=pn%3DRS20240030A2

Moissl, U., Arias-Guillén, M., Wabel, P., Fontseré, N., Carrera, M., Campistol, J. M. & Maduell, F. 2013. Bioimpedance-guided fluid management in hemodialysis patients. Clinical Journal of the American Society of Nephrology. 8(9), pp. 1575-1582. DOI:10.2215/CJN.12411212.

Natekin, A. & Knoll, A. 2013. Gradient boosting machines, a tutorial. Front Neurorobot. 7, 21. DOI:10.3389/fnbot.2013.00021.

Nguyen, T. V., Dakka, M. A., Diakiw, S. M., VerMilyea, M. D., Perugini, M., Hall, J. M. M. & Perugini, D. 2022. A novel decentralized federated learning approach to train on globally distributed, poor quality, and protected private medical data. Scientific Reports. 12(1), 8888. DOI:10.1038/s41598-022-12833-x.

Pedregosa, F., Varoquaux, G., Gramfort, A., Michel, V., Thirion, B., Grisel, O., Blondel, M., Müller, A., Nothman, J., Louppe, G. et al. 2012. Scikit-learn: Machine Learning in Python. arXiv [csLG]. DOI:10.48550/ARXIV.1201.0490.

Perl, J., Dember, L. M., Bargman, J. M., Browne, T., Charytan, D. M., Flythe, J. E., Hickson, L. J., Hung, A. M., Jadoul, M., Lee, T. C. et al. 2017. The use of a multidimensional measure of dialysis adequacy-moving beyond small solute kinetics. Clinical Journal of the American Society of Nephrology. 12(5), pp. 839-847. DOI:10.2215/CJN.08460816.

Rymarz, A., Gibińska, J., Zajbt, M., Piechota, W. & Niemczyk, S. 2018. Low lean tissue mass can be a predictor of one-year survival in hemodialysis patients. Renal Failure. 40(1), pp. 231-237. DOI:10.1080/0886022X.2018.1456451.

Sadilek, A., Liu, L., Nguyen, D., Kamruzzaman, M., Serghiou, S., Rader, B., Ingerman, A., Mellem, S., Kairouz, P., Nsoesie, E. O. et al. 2021. Privacy-first health research with federated learning. NPJ Digital Medicine. 4(1), 132. DOI:10.1038/s41746-021-00489-2.

Sagayama, H., Jikumaru, Y., Hirata, A., Yamada, Y., Yoshimura, E., Ichikawa, M., Hatamoto, Y., Ebine, N., Kiyonaga, A., Tanaka, H. et al. 2014. Measurement of body composition in response to a short period of overfeeding. Journal of Physiological Anthropology. 33(1), 29. DOI:10.1186/1880-6805-33-29.

Sagayama, H., Yoshimura, E., Yamada, Y. & Tanaka H. 2019. The effects of rapid weight loss and 3-h recovery on energy expenditure, carbohydrate, and fat oxidation in boxing athletes. The Journal of Sports Medicine and Physical Fitness. 59(6), pp. 1018-1025. DOI:10.23736/S0022-4707.18.08677-2.

Sheller, M. J., Edwards, B., Reina, G.A., Martin, J., Pati, S., Kotrotsou, A., Milchenko, M., Xu, W., Marcus, D., Colen, R. R. et al. 2020. Federated learning in medicine: facilitating multi-institutional collaborations without sharing patient data. Scientific Reports. 10(1), 12598. DOI:10.1038/s41598-020-69250-1.

Sheller, M. J., Reina, G. A., Edwards, B., Martin, J. & Bakas, S. 2019. Multi-institutional deep learning modeling without sharing patient data: a feasibility study on brain tumor segmentation. In: Crimi A, Bakas S, Kuijf H, Keyvan F, Reyes M, van Walsum T, editors. Brainlesion: glioma, multiple sclerosis, stroke and traumatic brain injuries. Lecture Notes in Computer Science. pp. 92-104. DOI: 10.1007/978-3-030-11723-8_9.

Shiri, I., Vafaei Sadr, A., Akhavan, A., Salimi, Y., Sanaat, A., Amini, M., Razeghi, B., Saberi, A., Arabi, H., Ferdowsi, S. et al. 2023. Decentralized collaborative multi-institutional PET attenuation and scatter correction using federated deep learning. The European Journal of Nuclear Medicine and Molecular Imaging. 50(4), pp. 1034-1050. DOI:10.1007/s00259-022-06053-8.

Sinha, A. D. & Agarwal R. 2009. Can chronic volume overload be recognized and prevented in hemodialysis patients? The pitfalls of the clinical examination in assessing volume status. Seminars in Dialysis. 22(5), pp. 480-482. DOI:10.1111/j.1525-139X.2009.00641.x.

Yang, Q., Liu, Y., Chen, T. & Tong, Y. 2019. Federated Machine Learning: Concept and Applications. arXiv [csAI]. DOI:10.48550/ARXIV.1902.04885.

Yang, Y., Zhang, H., Lan, X., Qin, X., Huang, Y., Wang, J., Luo, P., Wen, Z., Li, Y., Kong, Y. et al. 2023. Low BMI and high waist-to-hip ratio are associated with mortality risk among hemodialysis patients: a multicenter prospective cohort study. Clinical Kidney Journal. 16(1), pp. 167-175. DOI:10.1093/ckj/sfac210.

Zhang, F., Kreuter, D., Chen, Y., Dittmer, S., Tull, S., Shadbahr, T., BloodCounts! consortium, Preller, J., Rudd, J. H. F., Aston, J. A. D, et al. 2024. Recent methodological advances in federated learning for healthcare. Patterns. 5(6), 101006. DOI:10.1016/j.patter.2024.101006.

Zoccali, C., Moissl, U., Chazot, C., Mallamaci, F., Tripepi, G., Arkossy, O., Wabel, P. & Stuard, S. 2017. Chronic fluid overload and mortality in ESRD. The Journal of the American Society of Nephrology. 28(8), pp. 2491-2497. DOI:10.1681/ASN.2016121341.

Bulletin of Natural Sciences Research
Vol. 15, No. 1, 2025, pp. 72-77.

DOI: https://doi.org/10.5937/bnsr15-58114
Original Scientific Paper

AN APPLICATION OF RESIDUE NUMBER SYSTEM ARITHMETICS TO SECURE HASH FUNCTIONS DESIGN

MILIJA PAVLOVIĆ[1,⋆], STEFAN PANIĆ[1], BORIS DAMJANOVIĆ[2], NEGOVAN STAMENKOVIĆ[1]

[1]Faculty of Natural Sciences and Mathematics, University of Priština in Kosovska Mitrovica, Kosovska Mitrovica, Serbia
[2]Faculty of Information Technologies and Engineering, Union - Nikola Tesla University, Belgrade, Serbia

ABSTRACT

This paper presents a cryptographic hash function based on the Residue Number System (RNS), designed to enhance security and computational efficiency. The function leverages the parallelism and modular properties of RNS to achieve high-speed processing while maintaining strong diffusion and resistance to various cryptanalytic attacks. Experimental results confirm that the proposed function exhibits a pronounced Avalanche effect, ensuring that minor changes in the input result in significant alterations in the hash output. Additionally, statistical analysis using the ENT test demonstrates a high level of entropy and uniform distribution of hash values, reinforcing the function's unpredictability—an essential characteristic for cryptographic security. The proposed hash function is suitable for applications in digital signatures, data integrity verification, and authentication systems, offering advantages in environments requiring high computational efficiency.

Keywords: Cryptographic hash function, Residue number system, Avalanche effect, Diffusion, Entropy, Parallelism, Modular arithmetic.

INTRODUCTION

The main contribution of this paper is the proposal of RNS to parallelizing hash function operations, to provide speed boost while preserving cryptographic security. The Residue Number System (RNS) is an unconventional numerical system that achieves high efficiency in data processing, thanks to arithmetic based on modular operations (Stamenković, 2019). In recent decades, the application of RNS in digital signal processing, cryptography, and many other areas of modern computing has attracted significant attention (Ananda Mohan, 2016; Omondi & Premkumar, 2007; Szabo & Tanaka, 1967).

It ensures the efficiency of arithmetic operations due to the high degree of parallelization, making it particularly interesting for researchers working on computationally intensive applications. This numerical system is based on converting a large number into several smaller numbers, which are residues obtained as a result of dividing the given number by moduli, where the moduli are pairwise coprime integers (Isupov, 2021).

One of the most significant advantages of RNS lies in the fact that the residues are mutually independent. This means that addition, subtraction, and multiplication operations are reduced to independent operations with shorter residue values, eliminating the need for carry propagation between them and avoiding computationally expensive operations with long bit-lengths (Ananda Mohan, 2016).

When discussing the application of RNS, it is most often associated with Montgomery modular multiplication (Montgomery, 1985). Since the mid-2000s, numerous studies have explored RNS-based Montgomery multiplication and the optimization of cryptosystem design. RNS arithmetic was first utilized in elliptic curve cryptography (ECC) in , and it has also been employed in RSA cryptography (Bajard & Imbert, 2004; Gandino et al., 2011, 2012).

Beyond its applications in asymmetric cryptography, RNS has also been studied in the context of hash functions, where its properties are leveraged to enhance efficiency and security (Naseem et al., 2013). Research shows that using RNS in hashing can improve parallel processing and reduce resource consumption, which is particularly important for hash functions with large input data lengths. Furthermore, certain RNS-based hash function constructions demonstrate increased resistance to specific types of cryptanalytic attacks, making them promising candidates for modern security systems.

HASH FUNCTIONS IN THE CONTEXT OF RNS

Hash functions are a fundamental element of modern cryptographic systems, providing data compression into a fixed size and ensuring information integrity (Rogaway & Shrimpton, 2004). Traditional hashing principles are based on a deterministic transformation of input data into a hash value, which is cryptographically strong if it satisfies the following properties:

- pre-image resistance,
- second pre-image resistance,
- collision resistance.

[⋆] Corresponding author: milija.pavlovic@pr.ac.rs

These characteristics enable hash functions to serve as the foundation for digital signatures, data integrity verification mechanisms, and password storage algorithms (Ambedkar, 2025).

Although traditional hashing methods offer solid security guarantees, their intensive computational complexity can be a limitation in resource-constrained environments, such as IoT devices or embedded systems (Stevens et al., 2017). In this context, an increasing number of studies are exploring the application of unconventional computing techniques, such as the Residue Number System (RNS), which allows carry-free arithmetic, thereby improving processing speed and reducing resource consumption (Köroğlu, 2025).

By applying RNS in the design of hash functions, algorithms can achieve better parallelization of operations, leading to faster hashing without compromising security properties. Moreover, the resistance of RNS to certain cryptanalytic techniques, such as zero-value attacks, makes it promising for the development of new generations of hash functions. Research shows that RNS-based hash functions can be more efficient in high-throughput systems, such as blockchain technologies and data protection in large-scale information infrastructures.

RNS HASH FUNCTION

Let M be a given message of length N bits. The message is segmented into blocks of 128 bits as follows:

1. If N is divisible by 128, the message is divided into $t = \frac{N}{128}$ blocks without any padding.
2. If N is not divisible by 128, the message is divided into $t = \lceil N/128 \rceil$ blocks, where the last block, if shorter than 128 bits, is left-padded with zeros to reach the full length of 128 bits.

Formally, let

$$t = \lceil N/128 \rceil. \tag{1}$$

be the number of blocks. The message M is then represented as a sequence of blocks:

$$M = B_1 \| B_2 \| \dots \| B_t. \tag{2}$$

where for each i, where $1 \leq i < t$, we have

$$B_i = M[(i-1) \cdot 128 : i \cdot 128]. \tag{3}$$

while the last block B_t is formed as

$$B_t = 0^{128-(N \mod 128)} \| M[(t-1) \cdot 128 : N]. \tag{4}$$

where 0^k denotes a sequence of k zeros, and $\|$ denotes concatenation.

Each block B_i is first incremented by a constant value of 255, resulting in a transformed block:

$$B_i' = B_i + 255. \tag{5}$$

After this transformation, a set of moduli $\{x_1, x_2, \dots, x_8\}$ is used, with the following modulus values:

$$\begin{array}{llll} x_1 = 173, & x_2 = 179, & x_3 = 181, & x_4 = 191, \\ x_5 = 193, & x_6 = 197, & x_7 = 199, & x_8 = 211, \\ x_9 = 223, & x_{10} = 227, & x_{11} = 229, & x_{12} = 233, \\ x_{13} = 239, & x_{14} = 241, & x_{15} = 247, & x_{16} = 251. \end{array} \tag{6}$$

The selection of moduli was made with the constraint that the length of the residues must not exceed 8 bits, which implies that the moduli themselves must not be greater than 255 — the largest number that can be represented in an 8-bit system. For this reason, the largest possible prime numbers less than 255 were selected, in order to cover as many distinct residues as possible, reduce the probability of collisions, and preserve the relative primality among the moduli, which is a key property for the correct functioning of the Residue Number System (RNS). The only exception in the set is the number 247, which is not prime, but is relatively prime to all other selected moduli, allowing it to be used without violating the fundamental principles of RNS.

For each modulus x_j, the remainder of the division of the transformed block B_i' is computed, along with the integer quotient:

$$a_{i,j} = B_i' \mod x_j, \quad A_{i,j} = \lfloor B_i'/x_j \rfloor, \quad j \in \{1, 2, \dots, 16\}. \tag{7}$$

These parameters enable further numerical processing within the Residue Number System (RNS) framework, improving computational efficiency and security in the applied algorithm.

After computing the initial set of values $\{a_{i,j}, A_{i,j}\}$, the processing continues through an iterative update of remainders and quotients, enabling more efficient data manipulation within the Residue Number System (RNS) framework. This procedure consists of multiple stages in which previously computed values are used to generate new parameters.

For each modulus x_j, the new remainder is calculated by taking the sum of the previous quotient and remainder modulo x_j:

$$b_{i,j} = (A_{i,j} + a_{i,j}) \mod x_j, \quad j \in \{1, 2, \dots, 16\}. \tag{8}$$

Simultaneously, the new quotient is determined as the integer part of the same expression divided by x_j:

$$B_{i,j} = \left\lfloor \frac{A_{i,j} + a_{i,j}}{x_j} \right\rfloor, \quad j \in \{1, 2, \dots, 16\}. \tag{9}$$

After completing this phase, the obtained values $B_{i,j}$ and $b_{i,j}$ serve as input for the next iteration, where a new set of remainders and quotients is computed using the same principle:

$$c_{i,j} = (B_{i,j} + b_{i,j}) \mod x_j, \quad C_{i,j} = \left\lfloor \frac{B_{i,j} + b_{i,j}}{x_j} \right\rfloor. \tag{10}$$

This process is repeated iteratively across multiple steps, where each subsequent phase utilizes the previously computed values to generate new ones:

$$
\begin{aligned}
&\{d_{i,j}, D_{i,j}\}, \quad \{e_{i,j}, E_{i,j}\}, \quad \{f_{i,j}, F_{i,j}\}, \quad \{g_{i,j}, G_{i,j}\}, \\
&\{h_{i,j}, H_{i,j}\}, \quad \{i_{i,j}, I_{i,j}\}, \quad \{j_{i,j}, J_{i,j}\}, \quad \{k_{i,j}, K_{i,j}\}, \\
&\{l_{i,j}, L_{i,j}\}, \quad \{m_{i,j}, M_{i,j}\}, \quad \{n_{i,j}, N_{i,j}\}, \quad \{o_{i,j}, O_{i,j}\}, \\
&\{p_{i,j}, P_{i,j}\}.
\end{aligned} \tag{11}
$$

By iteratively repeating this procedure, data is successively transformed through multiple stages, enabling optimized processing within the RNS framework. This method reduces computational errors, enhances efficiency, and increases resistance to attacks in applications where the Residue Number System is utilized.

For each iterative step k, where $k \geq 1$, the values of remainders and quotients are updated according to the following relations:

$$
x_{i,j}^{(k)} = (X_{i,j}^{(k-1)} + x_{i,j}^{(k-1)}) \mod x_j, \quad X_{i,j}^{(k)} = \left\lfloor \frac{X_{i,j}^{(k-1)} + x_{i,j}^{(k-1)}}{x_j} \right\rfloor. \tag{12}
$$

The initial values are defined as $x_{i,j}^{(0)} = a_{i,j}$ and $X_{i,j}^{(0)} = A_{i,j}$. This process continues until the final step, where the resulting values $\{p_{i,j}, P_{i,j}\}$ are obtained for each block B_i.

The computation of the final hash is performed through the following steps:

First, the final remainders are determined using the XOR operation. For each modulus x_j, where $j = 1, \ldots, 16$. and the corresponding values $a_j, b_j, c_j, d_j, e_j, f_j, g_j, h_j, i_j, j_j, k_j, l_j, m_j, n_j, o_j, p_j, P_j$, the final remainder rem_j is defined as:

$$
\begin{aligned}
\text{rem}_j = a_j \oplus b_j \oplus c_j \oplus d_j \oplus e_j \oplus f_j \oplus g_j \oplus h_j \oplus i_j \oplus j_j \\
\oplus k_j \oplus l_j \oplus m_j \oplus n_j \oplus o_j \oplus p_j \oplus P_j.
\end{aligned} \tag{13}
$$

where the symbol $\oplus$ represents the XOR operation.

Next, each result is converted into an 8-bit binary representation. If necessary, leading zeros are added to ensure the appropriate length. The resulting binary representation, denoted as b_rem_j, is computed as:

$$
b\_\text{rem}_j = \text{bin}(\text{rem}_j). \tag{14}
$$

where leading zeros are added to ensure an exact length of 8 bits.

Finally, the final hash value hesF is formed by concatenating individual binary representations, formally expressed as:

$$
\begin{aligned}
\text{hesF} = {} & b\_\text{rem}_1 \| b\_\text{rem}_2 \| b\_\text{rem}_3 \| b\_\text{rem}_4 \\
& \| b\_\text{rem}_5 \| b\_\text{rem}_6 \| b\_\text{rem}_7 \| b\_\text{rem}_8 \\
& \| b\_\text{rem}_9 \| b\_\text{rem}_{10} \| b\_\text{rem}_{11} \| b\_\text{rem}_{12} \\
& \| b\_\text{rem}_{13} \| b\_\text{rem}_{14} \| b\_\text{rem}_{15} \| b\_\text{rem}_{16}.
\end{aligned} \tag{15}
$$

where the symbol $\|$ denotes the concatenation operation of binary sequences.

As a result, the final hash hesF is a 128-bit binary sequence, formed by combining all individual binary residues. In Fig. 1. and Fig. 2. we can see a graphical representation of the algorithm.

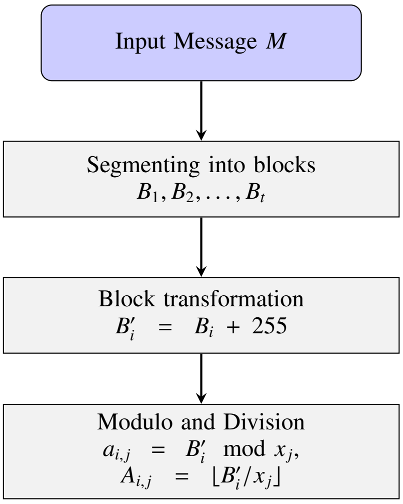

Figure 1. Hashing Process - Part 1: Data Preparation.

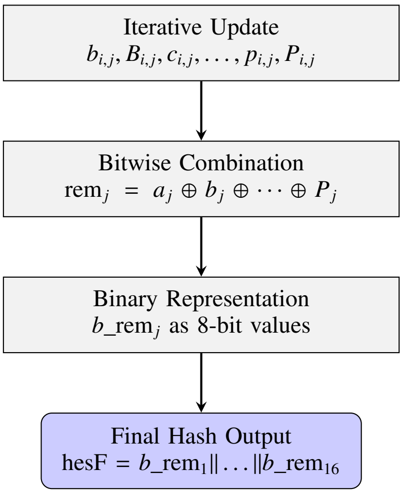

Figure 2. Hashing Process - Part 2: Finalization.

ENT TEST OF RNS HASH FUNCTION

The ENT test is a statistical tool for analyzing data randomness, making it particularly relevant for evaluating cryptographic hash functions. A strong hash function should produce outputs with high entropy, uniform value distribution, and minimal statistical deviations (Walker, 2008).

To determine whether a hash function exhibits the properties of ideal randomness, key parameters of the ENT test, such as entropy, arithmetic mean, Monte Carlo approximation of π, and serial correlation, are used.

Applying the ENT test to hash function outputs allows researchers to identify weaknesses in cryptographic algorithms and verify their suitability for security applications, such as digital signatures, password storage, and data integrity preservation in blockchain technologies.

Entropy (H)

Entropy measures the amount of uncertainty or randomness in a dataset and is defined as:

$$H = -\sum_{i=1}^{n} p_i \log_2 p_i. \tag{16}$$

where p_i is the probability of occurrence of the i-th symbol in the dataset (Cover & Thomas, 1991). The maximum entropy for a completely random binary file is $H = 8$ bits per byte.

Arithmetic Mean ($\bar{x}$)

The arithmetic mean of the bytes in the dataset is calculated as:

$$\bar{x} = \frac{1}{N} \sum_{i=1}^{N} x_i. \tag{17}$$

where x_i are individual byte values, and N is the total number of bytes (Cox & Hinkley, 1980). For perfectly random data, the expected value is 127.5.

Monte Carlo Approximation of π

This test relies on a simulation where random coordinate pairs (x, y) are generated within a unit square. The value of π is estimated using the ratio of points that fall within a circle to the total number of generated points:

$$\pi \approx 4 \times \frac{\text{number of points in the circle}}{\text{total number of points}}. \tag{18}$$

The approximation error indicates deviations in the randomness of the data (Kalos & Whitlock, 2008).

Serial Correlation Coefficient (r)

The serial correlation coefficient measures the correlation between consecutive bytes in a file:

$$r = \frac{\sum (x_i - \bar{x})(x_{i+1} - \bar{x})}{\sum (x_i - \bar{x})^2}. \tag{19}$$

where $\bar{x}$ is the arithmetic mean, and x_i is the value of the i-th byte. Ideally random data should have a value close to 0, while positive or negative values indicate patterns or dependencies between adjacent bytes (Brockwell & Davis, 2002).

Table 1. ENT Test Results for the File `output.bin`.

Parameter	Obtained Value	Expected Value
Entropy (H)	7.999555	8.000
Arithmetic Mean ($\bar{x}$)	128.8689	127.500
Monte Carlo π Approximation	3.101761	3.141593
Serial Correlation (r)	0.002546	0.000

An ENT test was conducted on a sample of 1,000,000 hash functions, and the obtained results are presented in Tab. 1. The entropy is 7.999555 bits per byte, which is very close to the maximum value of 8 bits per byte, indicating a high level of data unpredictability, as expected for well-generated random numbers.

The sample's compressibility is 0%, which aligns with theoretical expectations, as truly random sequences cannot be efficiently compressed.

The arithmetic mean is 128.8689, which is close to the theoretical value of 127.5, with the minor deviation attributed to statistical fluctuations.

The Monte Carlo estimation of π is 3.101761319, with an error of 1.27% compared to the exact value (3.1415926535). This result is consistent with expectations for random data and confirms their good randomness.

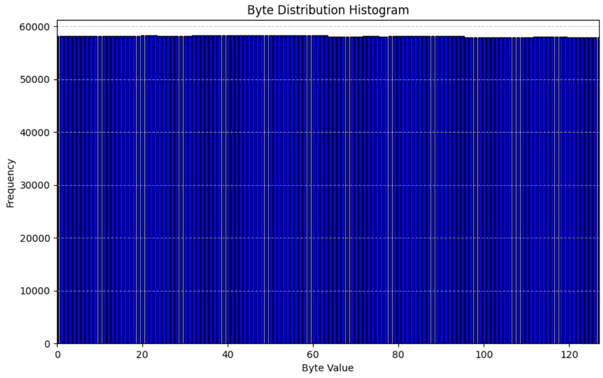

Figure 3. Byte Distribution Histogram (RNS Hash).

The byte distribution histogram shown in Fig. 3. demonstrates a high degree of uniformity, which is a key indicator of the quality of a hash function or a cryptographically secure pseudorandom number generator. The frequencies of all byte values are approximately equal, indicating good diffusion and the absence of bias toward specific values, thereby minimizing the predictability of the output and ensuring strong security. Visual analysis suggests that the data entropy is close to its maximum value, meaning there is no apparent pattern that could be exploited for analysis or attacks. The absence of significant anomalies, such as noticeable peaks or gaps in the byte spectrum, further confirms that the algorithm produces a balanced output without statistical irregularities that could compromise its robustness. The clarity of the visual presentation, with well-defined axes and a grid, facilitates straightforward and precise data interpretation, further emphasizing the reliability and security of the analyzed system.

AVALANCHE EFFECT

The avalanche effect is a crucial property of cryptographic hash functions that ensures minimal changes in input data (e.g., flipping a single bit) result in significant changes to the output hash value. This property is essential for good diffusion, meaning that changing one input bit should affect approximately 50%

of the output bits. The avalanche effect is characterized by two key criteria:

1. Strict Avalanche Criterion (SAC),
2. Bit Independence Criterion.(BIC)(Wang et al., 2012)

For mathematical analysis of these properties, the following definitions are used:

- Input messages: m, n,
- Hamming distance: $D(a, b)$ – number of bit positions where strings a and b differ,
- Hash value: $H(i)$ – output of hash function H for input i,
- Output size: s – fixed length of hash function $H()$ output.

These properties ensure that a hash function properly implements the avalanche effect, which is crucial for its security (Upadhyay et al., 2022).

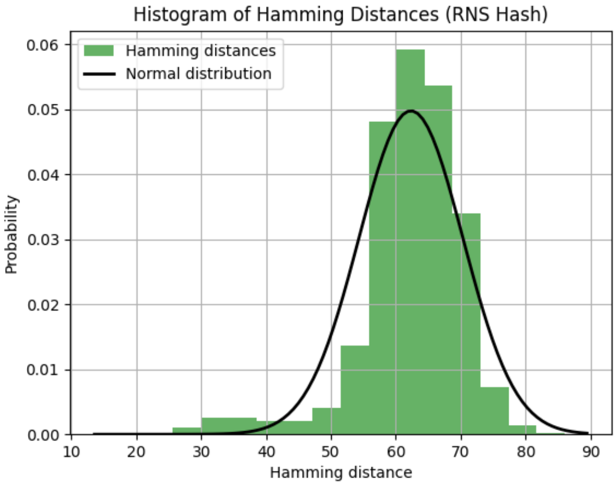

Figure 4. Histogram of Hamming Distances (RNS Hash).

Histogram of Hamming distances shown in Fig. 4. illustrates the distribution of bit changes in the hash output of the RNS hash function. The distribution demonstrates a high level of the avalanche effect, with values concentrated around a mean close to 64, which aligns with the ideal expectation for a 128-bit hash output.

The shape of the distribution follows a normal distribution, confirming that each bit in the hash has approximately an equal probability of changing with minimal input variations. The evident symmetry of the histogram indicates consistent diffusion, while slight variations at the tails do not compromise the overall stability of the algorithm.

The hash function exhibits a high degree of entropy and uniformity in bit changes, suggesting strong robustness for cryptographic applications. The data distribution is well-balanced, without significant anomalies, confirming the reliability of the applied method and its ability to ensure security through a strong avalanche effect.

Table 2. Examples of the Avalanche Effect.

Input Values	RNS Hash Values	Hamming Distances
"Hello World"	D6064077F28E9AC...	-
"hello world"	715FF3A1DBF5CC8F...	65
"hellO worlD"	520C9747994B5DFF...	69
"HELLO WORLD"	F1C4F3C78EC8E321...	65

Tab. 2. presents an analysis of the Avalanche effect by comparing variations of an input string and their corresponding Residue Number System (RNS) hash values. The Hamming distance is used as a metric to quantify the number of bit changes in the hash output when the input undergoes minimal modifications.

The results demonstrate that even small changes in letter case (e.g., lowercase vs. uppercase) lead to significant alterations in the hash values. The measured Hamming distances, ranging from 65 to 69 bits, indicate a strong diffusion property of the RNS-based hashing function, aligning with the expected behavior of a cryptographic hash function. The distribution of distances suggests a high level of randomness and unpredictability, which are desirable characteristics in cryptographic applications.

Furthermore, the table illustrates that the hash function successfully propagates input variations throughout the output space, reinforcing its resilience against pattern detection and potential vulnerabilities. The consistent magnitude of bit changes across different input modifications suggests that the hash function adheres to the strict avalanche criterion (SAC), a fundamental property ensuring security in hashing algorithms.

CONCLUSION

The RNS-based hash function has demonstrated a high level of security characteristics, as confirmed by positive results on the ENT test and a pronounced Avalanche effect. The function's construction, which relies on the Residue Number System (RNS) for parallel and modular data processing, enables efficient and distributed computation, enhancing resistance to certain types of attacks and improving execution speed.

Experimental analysis shows that even the smallest changes in the input data lead to significant alterations in the hash output, indicating strong diffusion and compliance with the Strict Avalanche Criterion (SAC). The results of the ENT test confirm the high entropy of output values, ensuring their uniformity and unpredictability—key properties of a secure hash function.

Due to these characteristics, the RNS-based hash function can be applied in various cryptographic systems, including digital signatures, data integrity verification, and authentication. Its resistance to linear and differential attacks is further strengthened by the modular structure of RNS, making it more difficult to perform reversible analysis or predict outputs based on inputs.

Future research could focus on optimizing the selection of moduli within the RNS to improve the balance of diffusion and processing speed. Additionally, exploring the application of this hash function in resource-constrained environments could provide significant performance advantages due to its parallelism. Further analyses of resistance to side-channel attacks could also contribute to confirming its security robustness.

ACKNOWLEDGMENT

The authors gratefully acknowledge the support from the Serbian Ministry of Science, Technological Development and Innovation (Contract No. 451-03-65/2024- 03/200124). This work has been partially funded by the University of Pristina in Kosovska Mitrovica, Faculty of Science and Mathematics, Serbia, under the project: IJ-2302 (Optimization of neural network).

REFERENCES

Ambedkar, B. R. 2025, Enhancing the Performance of Cryptographic Hash Function Using 2080 Bits Proposed Secure Hash Algorithm 160, International Journal of Scientific Research in Network Security and Communication, 13 (1), pp. 8–11. https://doi.org/10.26438/ijsrnsc.v13i1.264

Ananda Mohan, P. 2016, Residue Number Systems: Theory and Applications.

Bajard, J. & Imbert, L. 2004, A full RNS implementation of RSA, IEEE Transactions on Computers, 53, pp. 769–774. https://doi.org/10.1109/TC.2004.2

Brockwell, P. J. & Davis, R. A. 2002, Introduction to Time Series and Forecasting, 2nd edn. (Springer), pp. 15–1.

Cover, T. M. & Thomas, J. A. 1991, Elements of Information Theory, Wiley Series in Telecommunications. https://doi.org/10.1002/047174882X

Cox, D. R. & Hinkley, D. V. 1980, Theoretical Statistics, Chapman & Hall, pp. 34–38. https://doi.org/10.1201/9780203758486

Gandino, F., Lamberti, F., Montuschi, P., & Bajard, J. 2011, in Computer Arithmetic (ARITH), 2011 20th IEEE Symposium on, pp. 195–204.

Gandino, F., Lamberti, F., Paravati, G., Bajard, J., & Montuschi, P. 2012, An Algorithmic and Architectural Study on Montgomery Exponentiation in RNS, IEEE Transactions on Computers, 61 (8), pp. 1071–1083. https://doi.org/10.1109/TC.2012.84

Isupov, K. 2021, High-Performance Computation in Residue Number System Using Floating-Point Arithmetic, Computation, 9 (2), 9. https://doi.org/10.3390/computation9020009

Kalos, M. H. & Whitlock, P. A. 2008, Monte Carlo Methods, 2nd edn. (Wiley-VCH), pp. 3–12, poglavlje o historijskoj primjeni za sa matematičkom analizom.

Köroğlu, T. 2025, Hash Functions: Design Paradigms, Security, and Algorithmic Analysis, Advances in Computer Engineering, pp. 109–135. https://doi.org/10.5281/zenodo.14579277

Montgomery, P. 1985, Modular multiplication without trial division, Mathematics of Computation, 16, pp. 519–521. https://doi.org/10.1090/S0025-5718-1985-0777282-X

Naseem, M. T., Qureshi, I. M., Cheema, T. A., & ur Rahman, A. 2013, Hash based Medical Image Authentication and Recovery using Chaos and Residue Number System, Journal of Basic and Applied Scientific Research.

Omondi, A. & Premkumar, B. 2007, Residue Number Systems: Theory and Implementation (London, UK)

Rogaway, P. & Shrimpton, T. 2004, in Lecture Notes in Computer Science, Vol. 3152, Advances in Cryptology – CRYPTO 2004 (Berlin, Heidelberg: Springer), pp. 371–388.

Stamenković, N. 2019, Isomorphic Transformation and Its Application to the Modulo (2^n+1) Channel for RNS Based FIR Filter Design, Bulletin of Natural Sciences Research, 9 (2), pp. 25–32. https://doi.org/10.5937/univtho9-21821

Stevens, M., Bursztein, E., & Karpman, P. e. a. 2017, The First Collision for Full SHA-1, Advances in Cryptology - CRYPTO 2017.

Szabo, N. & Tanaka, R. 1967, Residue Arithmetic and Its Application to Computer Technology (New York, NY, USA)

Upadhyay, D., Gaikwad, N., Zaman, M., & Sampalli, S. 2022, Investigating the Avalanche Effect of Various Cryptographically Secure Hash Functions and Hash-Based Applications, IEEE Access, 10, pp. 112473–112486. https://doi.org/10.1109/ACCESS.2022.3215778

Walker, J. 2008, ENT: A Pseudorandom Number Sequence Test Program, Online manual, the original ENT entropy test documentation with statistical foundations.

Wang, Y., Wong, K.-W., Li, C., & Yang, L. 2012, A novel method to design S-box based on chaotic map and genetic algorithm, Physics Letters A, 376 (6-7), pp. 827–833. https://doi.org/10.1016/j.physleta.2012.01.009

Bulletin of Natural Sciences Research
Vol. 15, No. 1, 2025, pp. 78-85.

DOI: https://doi.org/10.5937/bnsr15-59743
Original Scientific Paper

AN INFORMATION-PHYSICAL PERSPECTIVE ON FADING PROCESS TRANSITIONS BASED ON HIGHER ORDER STATISTICS

STEFAN R. PANIĆ[1,⋆]

[1] Faculty of Natural Sciences and Mathematics, University of Priština in Kosovska Mitrovica, Kosovska Mitrovica, Serbia

ABSTRACT

This paper proposes a novel theoretical framework for analyzing fading channels by introducing the concepts of energetic orbits and entropy barriers. Inspired by atomic physics and thermodynamic analogies, here the signal envelope is modeled as a stochastic process whose transitions between different structural regimes (extrema, inflection points, level crossings) correspond to energy quantization events. Each transition is associated with a local information-energy quantum, defined as a product of amplitude displacement and transition count, normalized by local entropy. Furthermore, the ideas of entropic spin and degeneracy of states have been explored, and the dispersion of level-crossing processes, extremum-crossing process, inflection point-crossing process, saddle point-crossing process (LCR, ECR, ICR, SCR) through an autocorrelation-based energetic formalism has been characterized. This approach enables the construction of a layered energetic map of fading dynamics and offers new insights into the structural behavior of wireless signals under stochastic fluctuations.

Keywords: Fading channels, Entropy barriers, Energetic orbits, Crossing statistics, Stochastic signal dynamics.

INTRODUCTION

In modern wireless communications, the fading process represents one of the most critical challenges for maintaining signal integrity and reliability. Fading arises due to the superposition of multiple reflected, refracted, and scattered components of the transmitted signal, leading to time-varying fluctuations in amplitude, phase, and frequency (Simon & Alouini, 2005). These fluctuations can be modeled as stochastic processes with varying statistical properties, depending on environmental and mobility conditions (Stuber, 2001). Classical fading models, such as Rayleigh, Rician, and Nakagami-m, Gamma, Weibull, Hoyt, $\alpha-\mu$, $\kappa-\mu$ and $\eta-\mu$ have been used to characterize signal behavior under different propagation conditions (Panic et al., 2013).

With the advent of 6G and beyond wireless technologies, the demand for ultra-reliable low-latency communication (URLLC), massive machine-type communications (mMTC), and enhanced mobile broadband (eMBB) has led to the need for more refined performance metrics that go beyond traditional outage probability or average bit error rate. In this context, crossing statistics, such as the level crossing rate (LCR) and average fade duration (AFD), have gained prominence as tools to assess the dynamic structure of the fading envelope. These metrics capture how frequently and for how long a signal crosses certain amplitude thresholds, offering a more nuanced understanding of channel behavior in time-sensitive or mission-critical scenarios (Abdi & Nader-Esfahani, 2003).

Building on this perspective, recent theoretical work has extended crossing statistics to include higher-order concepts, such as extremum crossing rate (ECR), inflection point crossing rate (ICR), and saddle crossing rate (SCR). These measures rely on higher-order time derivatives of the fading process and their statistical distributions, enabling a more granular analysis of waveform structure. Despite their potential, a unifying physical or informational interpretation of these metrics remains elusive, especially in connection with signal energetics and system-level implications.

This paper introduces a novel informational-energetic framework that interprets crossing phenomena in fading channels as transitions across entropic barriers and energetic orbital zones. Motivated by analogies to thermodynamic systems, characteristic energy levels associated with crossing statistics has been defined and their interdependence with entropy-like measures and signal variability has been observed. Contribution lies in bridging stochastic signal analysis with conceptual tools inspired by statistical mechanics and information theory, thereby proposing a new lens through which to understand the microstructure of fading dynamics. This framework aims to complement existing analytical methods while offering fertile ground for new interpretations, visualizations, and performance insights in future wireless systems.

SYSTEM MODEL

Let $X(t)$ be a stationary, ergodic random process representing the fading envelope. For a given threshold level u, the LCR quantifies the frequency of signal excursions across level u in both directions, positive and negative crossing (Rice, 1944, 1945):

$$N_u^{(+)} = \int_0^{\infty} \dot{x}\, p_{X,\dot{X}}(u, \dot{x})\, d\dot{x}. \tag{1}$$

and

$$N_u^{(-)} = -\int_{-\infty}^{0} \dot{x}\, p_{X,\dot{X}}(u, \dot{x})\, d\dot{x}. \tag{2}$$

[⋆] Corresponding author: stefan.panic@pr.ac.rs where $p_{X,\dot{X}}(x,\dot{x})$ represents joint probability density function (JPDF) of random process $X(t)$ and its first time derivative $\dot{X}$. The total LCR is in that case then given by:

$$N_u = N_u^{(+)} + N_u^{(-)} = \int_0^{\infty} |\dot{x}|\, p_{X,\dot{X}}(u,\dot{x})\, d\dot{x}. \tag{3}$$

The AFD can be correspondingly derived as (Rice, 1944):

$$\mathrm{AFD}_u = \frac{F_X(u)}{N_u}. \tag{4}$$

where $F_X(u)$ is the cumulative distribution function (CDF) of $X(t)$, while N_u is the total LCR. AFD can be decomposed into upward and downward fade durations as (Tikhonov, 1970):

$$\mathrm{AFD}_u^{(+)} = \frac{F_X(u)}{N_u^{(+)}}, \quad \mathrm{AFD}_u^{(-)} = \frac{F_X(u)}{N_u^{(-)}}. \tag{5}$$

corresponding to upward and downward crossings of level u. Higher-order statistics extend these concepts to the curvature and geometric behavior of the fading process, describing progressively its finer structural properties (Blachman, 1999). ECR quantifies local extrema, ICR captures curvature reversals, and SCR characterizes the sharpness or saddle-like transitions between inflection points. This multiscale statistical perspective is particularly useful in modern communication systems where fine envelope fluctuations directly impact reliability and error dynamics.

As mentioned, ECR counts zero-crossings of $\dot{X}(t)$, capturing local maxima:

$$\eta_u^{\max} = -\int_{-\infty}^{0} \ddot{x}\, p_{X,\dot{X},\ddot{X}}(u,0,\ddot{x})\, d\ddot{x}. \tag{6}$$

and local minima:

$$\eta_u^{\min} = \int_0^{\infty} \ddot{x}\, p_{X,\dot{X},\ddot{X}}(u,0,\ddot{x})\, d\ddot{x}. \tag{7}$$

for observed level u of random process. The total ECR is in that case then given by:

$$\eta_u = \eta_u^{\max} + \eta_u^{\min} = \int_{\infty}^{0} |\ddot{x}|\, p_{X,\dot{X},\ddot{X}}(u,0,\ddot{x})\, d\ddot{x}. \tag{8}$$

In similar manner ICR can be observed as characterization related to curvature transitions (changes in concavity). Number of translations from concave to convex process can be obtained as:

$$\kappa_u^{(+)} = \int_0^{\infty} \dddot{x}\, p_{X,\dot{X},\ddot{X},\,\dddot{X}}(u,\ddot{x},0,\,\dddot{x})\, d\,\dddot{x}. \tag{9}$$

while convex-to-concave translations of random procces u can be expressed as:

$$\kappa_u^{(-)} = -\int_{-\infty}^{0} \dddot{x}\, p_{X,\dot{X},\ddot{X},\,\dddot{X}}(u,\ddot{x},0,\,\dddot{x})\, d\,\dddot{x}. \tag{10}$$

The total ICR is in that case then given by:

$$\kappa_u = \kappa_u^{(+)} + \kappa_u^{(-)} = \int_0^{\infty} |\,\dddot{x}|\, p_{X,\dot{X},\ddot{X},\,\dddot{X}}(u,\ddot{x},0,\,\dddot{x})\, d\,\dddot{x}. \tag{11}$$

The SCR measures the rate at which the third derivative of curvature, $\dddot{X}(t)$, crosses zero, indicating rapid geometric transitions in the signal's shape. It is especially useful in detecting saddle-like behaviors and sharp geometric inflection transitions.

Now let us define SCR as the sum of two directional components: Convex-to-saddle transitions, which can be calculated according to:

$$\chi_u^{(+)} = \int_0^{\infty} x^{(4)}\, p_{X,\dot{X},\ddot{X},\,\dddot{X},X^{(4)}}(u,\dot{x},\ddot{x},0,x^{(4)})\, dx^{(4)}. \tag{12}$$

and Concave-to-saddle transitions, which can be calculated according to:

$$\chi_u^{(-)} = -\int_{-\infty}^{0} x^{(4)}\, p_{X,\dot{X},\ddot{X},\,\dddot{X},X^{(4)}}(u,\dot{x},\ddot{x},0,x^{(4)})\, dx^{(4)}. \tag{13}$$

In that case the total CSR is thus expressed as:

$$\chi_u = \chi_u^{(+)} + \chi_u^{(-)} = \int_0^{\infty} |x^{(4)}|\, p_{X,\dot{X},\ddot{X},\,\dddot{X},X^{(4)}}(u,\dot{x},\ddot{x},0,x^{(4)})\, dx^{(4)}. \tag{14}$$

To extend the concept of AFD to higher-order structural features of the fading process, let us introduce analogous time-domain measures for extrema, inflection points, and saddle geometries, i.e. Average Extrema Duration (AED), Average Inflection Duration (AID) and Average Saddle Duration (ASD). AED metric quantifies the average time between successive extrema (local maxima or minima) below a threshold level u. It is defined as:

$$\mathrm{AED}_u = \frac{P(X<u)}{\eta_u} = \frac{F_X(u)}{\eta_u}. \tag{15}$$

where $F_X(u)$ is the CDF of the fading envelope $X(t)$ and η_u is the total ECR at level u. This metric can be split as:

$$\mathrm{AED}_u^{(\max)} = \frac{F_X(u)}{\eta_u^{\max}}, \quad \mathrm{AED}_u^{(\min)} = \frac{F_X(u)}{\eta_u^{\min}}. \tag{16}$$

to separately quantify the durations between local maxima and local minima.

AID metric measures the average duration between transitions in the curvature of the signal envelope, which correspond to inflection points:

$$\mathrm{AID}_u = \frac{P(X<u)}{\kappa_u} = \frac{F_X(u)}{\kappa_u}. \tag{17}$$

where κ_u is the ICR. Optional directional variants can also be defined:

$$\mathrm{AID}_u^{(+)} = \frac{F_X(u)}{\kappa_u^{(+)}}, \qquad \mathrm{AID}_u^{(-)} = \frac{F_X(u)}{\kappa_u^{(-)}}. \tag{18}$$

For completeness, the same logic can be extended to saddle transitions associated with ASD higher-order derivative crossings:

$$\mathrm{ASD}_u = \frac{F_X(u)}{\chi_u}. \tag{19}$$

where χ_u denotes the SCR, based on zero-crossings of the third derivative of the curvature. It can be decomposed as:

$$\mathrm{ASD}_u^{(\nearrow)} = \frac{F_X(u)}{\chi_u^{(+)}}, \quad \mathrm{ASD}_u^{(\searrow)} = \frac{F_X(u)}{\chi_u^{(-)}}. \tag{20}$$

denoting forward-saddle and backward-saddle transition durations respectively. These generalized duration metrics allow for a multiscale characterization of the temporal structure of the fading process, enabling refined analysis of signal behavior in advanced wireless systems.

In the context of fading processes, the time derivatives of the envelope $X(t)$—such as $\dot{X}(t)$, $\ddot{X}(t)$, and higher orders—are often modeled as zero-mean Gaussian random variables. This assumption is justified for wide-sense stationary and ergodic processes due to the smoothness and symmetry of their autocorrelation structure. Specifically, the variance of the n-th time derivative of $X(t)$, denoted by $\sigma^2_{X^{(n)}}$, is obtained by evaluating the $2n$-th time derivative of the autocorrelation function $R_X(\tau)$ at the origin:

$$\sigma^2_{X^{(n)}} = (-1)^n \left. \frac{d^{2n}}{d\tau^{2n}} R_X(\tau) \right|_{\tau=0}. \tag{21}$$

Assuming zero mean and Gaussianity, the PDF of the n-th time derivative $X^{(n)}$ is:

$$p_{X^{(n)}}(x) = \frac{1}{\sqrt{2\pi\sigma^2_{X^{(n)}}}} \exp\left(-\frac{x^2}{2\sigma^2_{X^{(n)}}}\right). \tag{22}$$

Moreover, for stationary Gaussian processes, time derivatives of even and odd order are uncorrelated and hence statistically independent due to symmetry of the autocorrelation function:

$$\mathbb{E}\left[X^{(n)}(t) \cdot X^{(m)}(t)\right] = 0, \quad \text{for } n + m \text{ odd}.$$

This property simplifies joint PDF formulations used in crossing rate computations involving mixed orders of derivatives.

Let $R_X(\tau)$ denote the ACF of $X(t)$. For isotropic Rayleigh fading:

$$R_X(\tau) = J_0(2\pi f_D \tau). \tag{23}$$

where f_D is the maximum Doppler frequency and $J_0(\cdot)$ is the Bessel function of the first kind. Time derivatives of the process can be computed using:

$$R_{X^{(n)}}(\tau) = \left. \frac{\partial^n}{\partial t^n} \frac{\partial^n}{\partial t'^n} R_X(t - t') \right|_{t=t'}. \tag{24}$$

In example for Rayleigh fading, where the envelope has PDF:

$$p_X(u) = \frac{2u}{\Omega} \exp\left(-\frac{u^2}{\Omega}\right), \quad u \geq 0. \tag{25}$$

the LCR at level u is given by:

$$\nu_u = \sqrt{2\pi} f_D \cdot \frac{u}{\sqrt{\Omega}} \exp\left(-\frac{u^2}{\Omega}\right). \tag{26}$$

where f_D is the maximum Doppler frequency and $\Omega = \mathbb{E}[X^2]$ is the average envelope power. Using the conditional Gaussian approximation, the ECR at level u becomes:

$$\eta_u = 2\sqrt{\frac{6}{\pi}} f_D \cdot \frac{u}{\Omega} \exp\left(-\frac{u^2}{\Omega}\right). \tag{27}$$

where the variances of derivatives are:

$$\sigma^2_{\dot{X}|X} = 2\pi^2 f_D^2 \Omega. \tag{28}$$

$$\sigma^2_{\ddot{X}|X} = 6\pi^4 f_D^4 \Omega. \tag{29}$$

Similarly ICR and SCR values can be determined.

The variance of the number of level crossings $N_u(T)$ during interval $[0, T]$:

$$\mathrm{Var}[N_u(T)] = 2 \int_0^T (T - \tau) \left[R_{N_u}(\tau) - N_u^2\right] d\tau. \tag{30}$$

where $R_{N_u}(\tau)$ is the autocorrelation function of the crossing process:

$$R_{N_u}(\tau) = \int_{-\infty}^{\infty} \int_{-\infty}^{\infty} |\dot{x}_1| |\dot{x}_2| \, p_{X,\dot{X},X',\dot{X}'}(u, \dot{x}_1, u, \dot{x}_2; \tau) \, d\dot{x}_1 \, d\dot{x}_2. \tag{31}$$

The same structure can be used for ECR dispersion:

$$\mathrm{Var}[N_{\dot{X}=0}(T)] = 2 \int_0^T (T - \tau) \left[R_\eta(\tau) - \eta^2\right] d\tau. \tag{32}$$

The variance of the number of extremum crossings $N_{\dot{X}=0}(T)$ in the time interval $[0, T]$ is given by:

$$\mathrm{Var}[N_{\dot{X}=0}(T)] = 2 \int_0^T (T - \tau) \left[R_\eta(\tau) - \eta^2\right] d\tau. \tag{33}$$

where $R_\eta(\tau)$ is the autocorrelation function of the ECR process, expressed as:

$$R_\eta(\tau) = \int_{-\infty}^{\infty} \int_{-\infty}^{\infty} |\ddot{x}_1| |\ddot{x}_2| \, p_{X,\dot{X},\ddot{X},X',\dot{X}',\ddot{X}'}(u, 0, \ddot{x}_1, u, 0, \ddot{x}_2; \tau) \, d\ddot{x}_1 \, d\ddot{x}_2. \tag{34}$$

Similarly, the variance of the number of inflection point crossings $N_{\ddot{X}=0}(T)$ over the interval $[0, T]$ is:

$$\mathrm{Var}[N_{\ddot{X}=0}(T)] = 2 \int_0^T (T - \tau) \left[R_\kappa(\tau) - \kappa^2\right] d\tau. \tag{35}$$

where the autocorrelation function of the ICR process is given by:

$$R_\kappa(\tau) = \int_{-\infty}^{\infty} \int_{-\infty}^{\infty} d\dddot{x}_1 \, d\dddot{x}_2 |\dddot{x}_1| |\dddot{x}_2| \, p_{X,\ddot{X},\dddot{X},X',\ddot{X}',\dddot{X}'}(u, 0, \dddot{x}_1, u, 0, \dddot{x}_2; \tau). \tag{36}$$

Finally, the variance of the number of saddle point crossings $N_{\dddot{X}=0}(T)$ is:

$$\mathrm{Var}[N_{\dddot{X}=0}(T)] = 2 \int_0^T (T - \tau) \left[R_\chi(\tau) - \chi^2\right] d\tau. \tag{37}$$

with the ACF of the SCR process:

$$R_\chi(\tau) = \iint_{-\infty}^{\infty} dx_1^{(4)} dx_2^{(4)} |x_1^{(4)}| |x_2^{(4)}| \cdot p_{X(t),\ddot{X}(t),\dddot{X}(t),X^{(4)}(t),X(t+\tau),\ddot{X}(t+\tau),\dddot{X}(t+\tau),X^{(4)}(t+\tau)}(u, \ddot{x}_1, 0, x_1^{(4)}, u, \ddot{x}_2, 0, x_2^{(4)}). \tag{38}$$

For each fading model, one can identify characteristic envelope levels at which key stochastic rates attain their maxima. Specifically, the saddle crossing rate (SCR) reaches its maximum

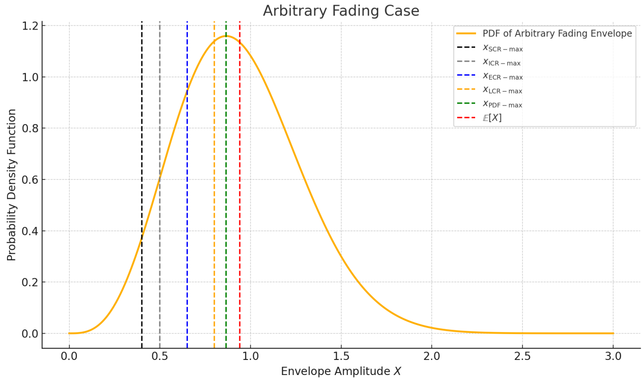

Figure 1. Illustration of the envelope PDF with statistical markers for characteristic crossing metrics.

at the lowest amplitude level, denoted $x_{\mathrm{SCR-max}} = \kappa_{u\,\max}^{-1}(X)$, followed by the inflection crossing rate (ICR) at $x_{\mathrm{ICR-max}}$, the extremum crossing rate (ECR) at $x_{\mathrm{ECR-max}}$, and the level crossing rate (LCR) at $x_{\mathrm{LCR-max}}$. The envelope PDF itself typically peaks at $x_{\mathrm{PDF-max}} = \sigma$, which lies below the statistical mean $\mathbb{E}[X]$. In unimodal and symmetric fading distributions such as Rayleigh or Nakagami-m, this ordering generally holds (see Figure 1):

$$x_{\mathrm{SCR-max}} \leq x_{\mathrm{ICR-max}} \leq x_{\mathrm{ECR-max}} \leq x_{\mathrm{LCR-max}} \leq x_{\mathrm{PDF-max}} \leq \mathbb{E}[X]. \tag{39}$$

This progression reflects a natural gradient from transient and localized features of the envelope (e.g., saddle points) to more stable and probable signal excursions (e.g., mean level crossings).

The entropic envelopes for various crossing-based statistics in fading processes can be formally defined by tracing the loci of their instantaneous local maxima. Each envelope captures a structurally dominant transition zone corresponding to a particular order of derivative behavior in the signal dynamics (Stefanovic et al., 2012).

Let $X(t)$ be a continuous fading process with continuous derivatives up to fourth order. The envelope surfaces corresponding to the maxima of various crossing statistics are defined by:

PDF Envelope:

$$\mathcal{E}_{\mathrm{PDF}} = \arg\max_{x\in\mathbb{R}} \left\{ p_X(x) \;\middle|\; \frac{d}{dx} p_X(x) = 0 \right\}. \tag{40}$$

LCR Envelope:

$$\mathcal{E}_{\mathrm{LCR}}(t) = \arg \max_{\dot{X}(t)=0,\ \ddot{X}(t)<0} X(t). \tag{41}$$

ECR Envelope:

$$\mathcal{E}_{\mathrm{ECR}}(t) = \arg \max_{\dot{X}(t)=0,\ \ddot{X}(t)\neq 0} X(t). \tag{42}$$

ICR Envelope:

$$\mathcal{E}_{\mathrm{ICR}}(t) = \arg \max_{\ddot{X}(t)=0,\ \dddot{X}(t)\neq 0} X(t). \tag{43}$$

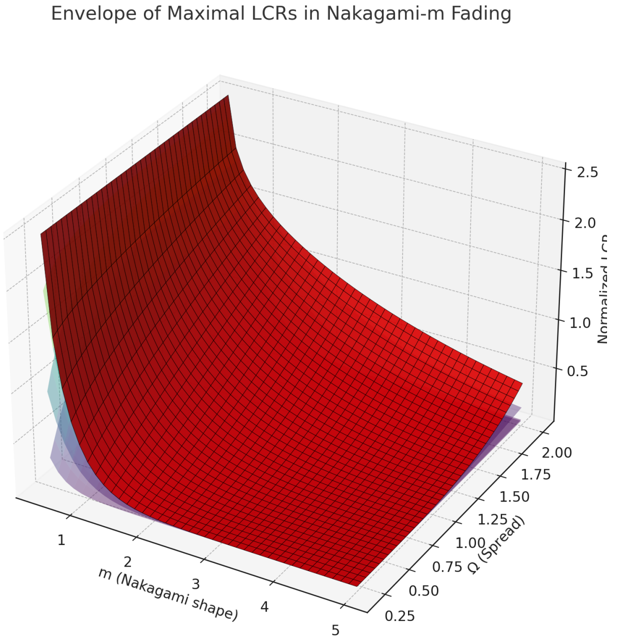

Figure 2. Illustration of the envelope surface of maximums of LCR process of Nakagami-m fading.

SCR Envelope:

$$\mathcal{E}_{\mathrm{SCR}}(t) = \arg \max_{\dddot{X}(t)=0,\ X^{(4)}(t)\neq 0} X(t). \tag{44}$$

These envelopes, individually and collectively, delineate macro-scale statistical boundaries in the signal space and can be interpreted as entropic manifolds — encoding the dominant excursion behavior of the underlying fading process across multiple derivative dimensions. The entropic envelope can be interpreted as a singular solution to a higher-order differential equation that governs the statistical dynamics of the fading process. In this context, the standard statistical measures such as the PDF, LCR, ECR, ICR and SCR represent particular solutions or projections of this governing structure under specific boundary or derivative constraints. While the PDF captures the stationary distribution of the envelope, the derivative-based crossing rates correspond to dynamic transitions across levels of increasing geometric complexity. The envelope thus encodes a global, macro-structural constraint, guiding the formation of localized statistical behaviors and acting as an attractor surface in the space of observable transitions.

Figure 2 illustrates the surface behavior of the normalized LCR in a Nakagami-m fading environment as a function of the fading severity parameter m, the average power Ω, and the signal level u (expressed in decibels). Several semi-transparent LCR surfaces corresponding to fixed values of u are shown to depict the structural variation of the LCR in the 3D parameter space. Overlaid on these surfaces is a prominent red envelope surface that traces the locations of maximum LCR values across all combinations of m and Ω, obtained by solving $\frac{\partial}{\partial u}\mathrm{LCR}(u; m, \Omega) = 0$. This envelope delineates the most probable fluctuation intensities for different fading regimes and serves as a boundary surface separating regions of deterministic behavior from those dominated by stochastic excursions, supporting the concept of entropic zones in fading dynamics.

RESULTS AND DISCUSSION

Entropic Envelopes and Structural Boundaries of Fading Processes

The concept of *entropic envelopes* is proposed as a statistical framework to characterize the structural transitions within stochastic fading processes. These envelopes are defined as boundary surfaces composed of local maxima of key statistical rate functions, namely: PDF, LCR, ECR, ICR, SCR. Each of these rate functions encodes a distinct type of structural behavior of the fading envelope.

- The first boundary, denoted $x_{\text{PDF}}^{\max}$, corresponds to the most probable signal level, i.e., the maximum of the PDF. This point represents the mode of the process and serves as a statistical center of mass for the fading distribution.
- The LCR envelope corresponds to amplitude-level crossings (zero-crossings of the first derivative). Its maximum, $x_{\text{LCR}}^{\max}$, identifies the most likely signal level where crossings of a fixed threshold occur.
- The ECR envelope tracks local maxima and minima by identifying points where the first derivative vanishes and the second derivative is non-zero. The maximum $x_{\text{ECR}}^{\max}$ denotes the dominant structural oscillation scale.
- The ICR envelope captures inflection points (zero-crossings of the second derivative with non-zero third derivative). $x_{\text{ICR}}^{\max}$ marks transitions in curvature and delineates regions of acceleration in signal fluctuation.
- The SCR envelope reflects higher-order geometric transitions by locating points where the third derivative vanishes and the fourth derivative is non-zero. The maximum $x_{\text{SCR}}^{\max}$ defines saddle-like changes in the envelope's trajectory, representing the outermost boundary of structured variation.

The positions of these maxima, ordered as:

$$x_{\text{SCR}}^{\max} \leq x_{\text{ICR}}^{\max} \leq x_{\text{ECR}}^{\max} \leq x_{\text{LCR}}^{\max} \leq x_{\text{PDF}}^{\max}.$$

serve to partition the signal domain into hierarchical *entropic zones*, where each successive zone represents an increased level of local irregularity or complexity in the signal structure.

Physically, these envelopes can be interpreted as phase-like statistical boundaries that separate regions of predictable, smooth envelope behavior from those dominated by rapid transitions and complexity. In this sense, they form a spectrum of stochastic regularity, useful for defining operational regimes in wireless communication systems. From a practical standpoint, entropic envelopes support tasks such as adaptive modulation, outage prediction, and time-frequency signal classification by providing natural demarcations in the dynamics of the fading process.

Orbital Interpretation of Transitions

Each zone defined by the maxima of LCR, ECR, ICR, and SCR can be conceptualized as an orbital level, similar to discrete energy states in quantum mechanical systems. In that way it can be observed that structural patterns in the fading envelope tend to cluster within well-defined entropic zones. The transitions between these zones represent quantum energy-like changes in the statistical configuration of the process.

From this perspective, a crossing from a local minimum to a maximum, or from an extremum to an inflection point, can be seen as a statistical excitation or relaxation. The system exhibits quantized patterns of movement between these zones, governed by the underlying autocorrelation structure and derivative variances.

This analogy provides a powerful framework to analyze the spectral behavior of fading processes. It allows us to assign structural transitions to distinct entropic orbitals, each characterized by a dominant derivative feature and its associated variance. This interpretation supports the development of quantized information models for wireless fading dynamics.

Directional Characterization of Structural Transitions

To provide a finer classification of the structural transitions in the fading envelope, a directional labeling scheme that characterizes the polarity and orientation of each transition event can be introduced. Specifically, transitions are categorized based on whether they represent an ascent (e.g., from an inflection point to a local maximum) or a descent (e.g., from a maximum to a subsequent inflection or minimum). This directionality reflects the temporal asymmetry in the envelope's evolution.

Incorporating this directional information enriches the structural taxonomy associated with the entropic envelope framework. Each entropic zone, defined by features such as maxima, inflections, or saddle points, can now be associated not only with its morphological type but also with the directional trajectory that the envelope follows through it. This dual classification captures both the geometric structure and the dynamical flow of the signal process.

Such directional analysis becomes particularly valuable in environments exhibiting asymmetry or spatial non-stationarity, such as in multi-antenna or frequency-selective fading scenarios. By distinguishing ascending from descending transition paths, this framework enhances the ability to identify transient versus stable phenomena in the signal, improving both analytical insight and predictive capability in practical systems.

Let $X(t)$ be a continuous envelope process defined on the interval $t \in [0, T]$, and let $X^{(n)}(t)$ denote its n-th time derivative. For any structural transition of order n, we define the directional counts:

$$N_{+}^{(n)}(T) = \#\left\{t_i \in [0, T] \;\middle|\; X^{(n)}(t_i) = 0,\ X^{(n+1)}(t_i) < 0\right\}. \quad (45)$$

$$N_{-}^{(n)}(T) = \#\left\{t_i \in [0, T] \;\middle|\; X^{(n)}(t_i) = 0,\ X^{(n+1)}(t_i) > 0\right\}. \quad (46)$$

The total number of directional transitions of order n is then given by:

$$N^{(n)}(T) = N_+^{(n)}(T) + N_-^{(n)}(T). \tag{47}$$

As a concrete example, for the second-order transitions corresponding to local extrema (ECR events), we have:

$$N_+^{(2)}(T) = \#\left\{t_i \in [0,T] \;\middle|\; \dot{X}(t_i) = 0,\ \ddot{X}(t_i) < 0\right\}, \quad \text{(maxima).} \tag{48}$$

$$N_-^{(2)}(T) = \#\left\{t_i \in [0,T] \;\middle|\; \dot{X}(t_i) = 0,\ \ddot{X}(t_i) > 0\right\}, \quad \text{(minima).} \tag{49}$$

This framework thus generalizes to any transition order n, and enables a rigorous classification of the signal's structural dynamics by associating both morphological and directional information with each observed transition.

To quantify the informational complexity of directional transitions, we define an entropy-based metric over the normalized counts of upward and downward events. Let:

$$p_+^{(n)} = \frac{N_+^{(n)}(T)}{N^{(n)}(T)}, \qquad p_-^{(n)} = \frac{N_-^{(n)}(T)}{N^{(n)}(T)}. \tag{50}$$

with $p_+^{(n)} + p_-^{(n)} = 1$. The directional transition entropy is then given by:

$$H_n = -p_+^{(n)} \log_2 p_+^{(n)} - p_-^{(n)} \log_2 p_-^{(n)}. \tag{51}$$

This entropy attains its maximum value $H_n = 1$ when both transition types are equally likely, indicating maximal uncertainty in directionality. Lower values reflect an asymmetry or bias in transition polarity, which may correspond to a directional drift or non-stationarity in the envelope dynamics.

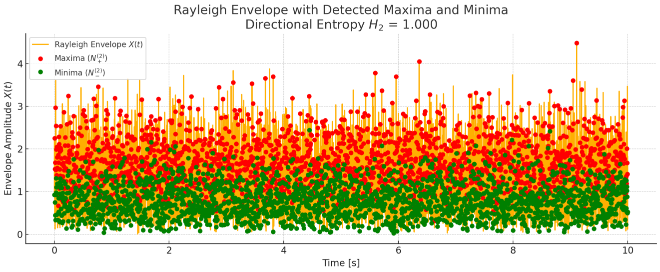

Figure 3. Rayleigh fading envelope with identified local extrema over time.

Red dots at Fig. 3 indicate upward second-order transitions (local maxima), while green dots mark downward second-order transitions (local minima). The underlying signal $X(t)$ is shown in orange. The balance between the number of maxima $N_+^{(2)}$ and minima $N_-^{(2)}$ yields a directional entropy of $H_2 = 1.000$, indicating complete symmetry in the polarity of second-order transitions. This statistical symmetry reflects the ergodicity and isotropy of the Rayleigh fading model and supports the assumption of equal probability for structural ascent and descent events.

Assuming the process $X(t)$ is ergodic and wide-sense stationary over a finite observation window of duration T, the average waiting time between directional transitions of order n can be expressed as:

$$\mathbb{E}[\Delta t_+^{(n)}] = \frac{T}{N_+^{(n)}(T)}. \tag{52}$$

$$\mathbb{E}[\Delta t_-^{(n)}] = \frac{T}{N_-^{(n)}(T)}. \tag{53}$$

where $N_+^{(n)}(T)$ and $N_-^{(n)}(T)$ denote the total number of ascending and descending transitions of the n-th order observed within the interval $[0,T]$. The time horizon T represents the total observation period over which the statistical averages are estimated.
These quantities provide temporal scales over which structural transitions of a given direction and order typically occur. For example, a lower $\mathbb{E}[\Delta t_+^{(2)}]$ implies frequent upward extrema (local maxima), possibly indicating bursty or rapidly varying behavior in the envelope. The full set $\{\mathbb{E}[\Delta t_\pm^{(n)}]\}$ across several n-values can be interpreted as a *temporal fingerprint* of the stochastic structure, with potential applications in classification, anomaly detection, and adaptive system design.

Finally, an entropy-weighted transition index for order n can be defined as:

$$Q^{(n)} = \frac{H_n}{\mathbb{E}[\Delta t^{(n)}]}. \tag{54}$$

where $\mathbb{E}[\Delta t^{(n)}] = T/N^{(n)}(T)$ is the average inter-event duration for all transitions of order n. This metric reflects the *informational flux density* of structural transitions, combining their rate and directional uncertainty. High values of $Q^{(n)}$ indicate both frequent and directionally unpredictable transitions, while lower values point to either sparsity or determinism in the process dynamics.

Entropic-Informational Structure of Derivative Transitions

The entropic-informational structure of a stochastic envelope process is characterized through a hierarchy of statistical transition functions, each associated with a specific time-derivative order of the underlying ACF. These functions namely the LCR, ECR, ICR, SCR, capture the envelope's structural complexity at increasing levels of geometric differentiation.

Each crossing function highlights localized regions of elevated statistical activity, where the envelope exhibits critical morphological features such as amplitude crossings, extrema, curvature sign changes, or higher-order saddle points. These transitions are intrinsically tied to the variances of the corresponding derivatives of the process and reflect the concentration of structural dynamics in specific signal regions.

By systematically analyzing these features, one obtains a compact representation of the envelope's geometric irregularities and their distribution across scales. This derivative-based characterization facilitates rigorous classification of stochastic signals in terms of entropic density and structural coherence, offering valuable insights for tasks such as fading channel modeling, signal classification, and adaptive information encoding in complex wireless environments.

Transition Quanta and Characteristic Energies

Each transition between entropic zones can be quantified using an informational-energy expression, defining the transition quantum as:

$$q_i = \frac{\Delta u_i \cdot \Delta N_i}{p_i \log(p_i)}. \tag{55}$$

where Δu_i is the level excursion, ΔN_i is the number of transitions in that zone, and p_i is the transition probability. The total information quantum can be in that case computed as the inverse harmonic sum:

$$Q^{-1} = \left(\sum_i \frac{1}{q_i}\right)^{-1}. \tag{56}$$

The characteristic energy of the nth-order transition zone is defined through the autocorrelation of the corresponding crossing process:

$$2T \int_0^T (T-\tau)[R_{N^{(n)}}(\tau) - (\nu_u^{(n)})^2]d\tau = H(X^{(n)}) \cdot Q^{-1}. \tag{57}$$

where $H(X^{(n)})$ is the entropy of the nth derivative of the process.

The entropy can be given by:

$$H(X^{(n)}) = \frac{1}{2} + \frac{1}{2}\log(2\pi\sigma^2_{X^{(n)}}). \tag{58}$$

This framework connects transition rates with both informational content and energy expenditure, providing a dual view of envelope complexity.

Structural transitions in fading processes may converge when higher-order features of the envelope become indistinct. Specifically, critical points such as local maxima may gradually lose curvature and merge with neighboring inflection points, thereby collapsing distinct entropic zones into a unified region of statistical indeterminacy. This transition signifies the onset of what can be termed an *entropic continuum*, where discrete morphological events become indistinguishable.

Within this continuum regime, the envelope process exhibits increased stochastic irregularity, characterized by an absence of clear-cut extrema, inflection points, or saddle structures. The geometric regularity of the signal deteriorates, and the fading process approaches a structurally chaotic behavior. Under these conditions, classical descriptors fail to isolate features, and one must instead rely on global metrics such as crossing densities, spectral entropy, or cumulant-based statistics to quantify complexity.

The total number of structural excursions accumulated across all entropic orders provides a macroscopic measure of this complexity:

$$N_{\text{total}} = \sum_i N^{(i)}. \tag{59}$$

where $N^{(i)}$ represents the number of transitions of structural order i. This aggregate count offers a coarse-grained but comprehensive summary of the signal's morphological dynamics.

Entropic Potential and Informational Transition Fields

To characterize the directional bias and local dynamics of structural evolution in fading processes, we introduce the notion of an *entropic potential field*. This scalar function encapsulates the tendency of the signal envelope to transition through distinct morphological states, driven not by classical energy considerations, but by local informational gradients.

Let $\mathcal{U}(x)$ denote the entropic potential at envelope level x. One possible formalization connects $\mathcal{U}(x)$ to the derivative of the autocorrelation function $R_X^{(n)}(\tau)$, or to the derivative of the crossing density function. An alternative formulation ties it to the normalized transition quantum q_i via Eq.55, where Δu_i and ΔN_i denote amplitude and transition count variations within zone i, and p_i is the normalized probability of such transitions. These local information-energy interactions define the entropic geometry of the process.

The entropic potential field defines an informational gradient landscape that directs the evolution of the stochastic envelope between regions of relative stability and instability. Analogous to physical systems, this potential may exhibit local minima, interpreted as informational attractors and local maxima, corresponding to repelling configurations. These structural extrema delineate statistically dominant regimes within the signal space. This framework provides a rigorous basis for enhancing signal processing strategies in adaptive wireless systems, including channel state estimation, predictive modeling, and rate adaptation under non-stationary fading conditions.

Entropic Potential Function for Structural Transitions

For a generic structural transition of order n, the entropic potential function $\mathcal{U}^{(n)}(x)$ can be defined as:

$$\mathcal{U}^{(n)}(x) = -\log\left(\frac{N^{(n)}(x)}{\max_x N^{(n)}(x)}\right). \tag{60}$$

where:

- $N^{(n)}(x)$ is the crossing rate function of order n (e.g., LCR for $n = 1$, ECR for $n = 2$, etc.),
- $\max_x N^{(n)}(x)$ is the global maximum of the crossing rate function over the signal domain x,

Interpretation:

- Low potential values $\mathcal{U}^{(n)}(x) \approx 0$ indicate high likelihood of structural transitions, forming informational *wells*.
- High potential values reflect statistically rare transitions, forming entropic *barriers*.
- The potential profile $\mathcal{U}^{(n)}(x)$ reveals the spatial concentration of structural events and helps delineate the stochastic geometry of the envelope process.

These curves presented at Fig. 4 highlight the *informational landscape* of the signal, where valleys indicate statistically dominant transitions (most likely signal levels), and peaks represent entropic barriers or rare events.

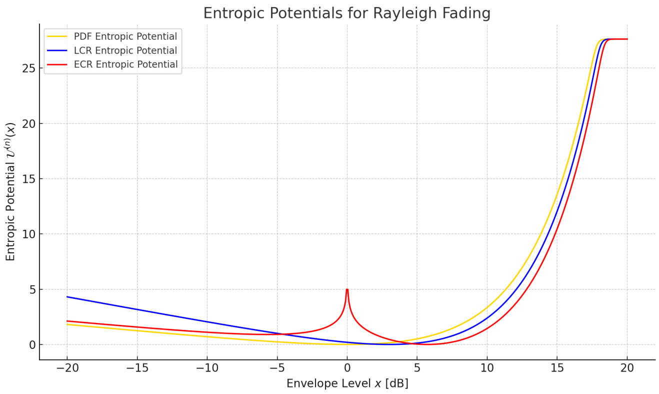

Figure 4. Entropic potentials for Rayleigh fading.

Energy-Entropy Transformation

Two fundamental transformation directions in the study of entropic zones can be identified. The first, energy-to-entropy, observes how structural events such as maxima and saddles can be mapped to entropic zones via their statistical significance. This results in an entropic spectrum that characterizes the process's disorder. The second transformation, entropy-to-energy, aggregates the local information contributions (via $H(X^{(n)})$) across derivative orders to reconstruct energy-like measures. This enables the synthesis of predictive models that treat entropy as a form of latent structural energy. Together, these dual transformations establish a bridge between physical interpretation and information-theoretic representation of stochastic fading envelopes. They offer a unified framework for analyzing complexity and transitions in dynamic systems.

Practical Applications of Study

The entropic envelopes derived from LCR, ECR, ICR, and SCR maxima delineate statistically significant signal regimes, which can inform adaptive modulation and coding strategies. For example, regions corresponding to low entropic potential indicate high transition density and increased signal variability, suggesting the need for robust coding schemes or fallback modulation orders. Conversely, zones with reduced structural activity allow for more aggressive spectral efficiency. Moreover, the entropy-weighted transition index $Q^{(n)}$ and directional entropy H_n provide powerful tools for anomaly detection. Abrupt changes in these metrics over time may signal deviations from normal fading behavior due to interference, obstruction, or hardware faults. In multi-antenna and cooperative systems, the identification of directional asymmetry through $N_{\pm}^{(n)}$ enables intelligent diversity combining by prioritizing channels that exhibit more favorable structural stability. Collectively, these descriptors form a compact statistical signature of the fading environment that can be exploited for real-time adaptation and resilience in dynamic wireless channels.

CONCLUSION

In this work, we introduced a novel framework for the structural analysis of stochastic fading processes through the concept of *entropic envelopes*, which identify and classify the most statistically significant transitions within the signal envelope. By systematically analyzing the local maxima of the LCR, ECR, ICR, SCR, corresponding envelope surfaces are constructed that represent the statistical basis for the fading dynamics. These surfaces highlight regions of high transition density and define operational boundaries within the signal space. Building upon these crossing based features, a directional transition taxonomy based on the sign of higher-order derivatives have been proposed, with introducing quantities such as $N_{+}^{(n)}$, $N_{-}^{(n)}$, and associated waiting times. This helped to define an entropy based index H_n that quantifies the balance of structural transitions, and a derived entropic flux density $Q^{(n)}$, which jointly measures the frequency and unpredictability of such events. Together, these descriptors offer a compact temporal fingerprint of the stochastic envelope process. Furthermore, the notion of an *entropic potential* $U^{(n)}(x)$ has been introduced, analogous to potential energy landscapes, capturing the informational cost of observing a transition at a given signal level x. Finally, an analogy with quantum orbitals was discussed, where structural transitions occupy discrete entropic zones, and degeneracy leads to the merging of these zones into an entropic continuum. This perspective opens new pathways for the quantized modeling of fading dynamics and their application in statistical signal processing and wireless communication system design.

REFERENCES

Abdi, A. & Nader-Esfahani, S. 2003, Expected number of maxima in the envelope of a spherically invariant random process, IEEE Transactions on Information Theory, 49 (6), pp. 1560–1570.

Blachman, N. M. 1999, The distributions of local extrema of Gaussian noise and of its envelope, IEEE Transactions on Information Theory, 45 (7), pp. 2115–2121.

Panic, S., Stefanović, M., Anastasov, J., & Spalević, P. 2013, Fading and interference mitigation in wireless communications (Boca Raton, FL, USA: CRC Press)

Rice, S. O. 1944, Mathematical analysis of random noise, Bell System Technical Journal, 23 (3), pp. 282–332.

Rice, S. O. 1945, Mathematical analysis of random noise—Part II, Bell System Technical Journal, 24 (1), pp. 46–156.

Simon, M. K. & Alouini, M. S. 2005, Digital communication over fading channels, 2nd edn. (Hoboken, NJ, USA: Wiley)

Stefanovic, H., Stefanovic, I., Milic, D., & Stefanovic, D. 2012, in Proceedings of the 11th International Symposium INFOTEH-JAHORINA (Jahorina, Bosnia and Herzegovina: University of East Sarajevo), pp. 1–4.

Stuber, G. L. 2001, Principles of mobile communication, 2nd edn. (Boston, MA, USA: Kluwer Academic)

Tikhonov, V. I. 1970, Excursions in random processes (Moscow, Russia: Nauka), (in Russian)

Bulletin of Natural Sciences Research
Vol. 15, No. 1, 2025, pp. 86-93.

DOI: https://doi.org/10.5937/bnsr15-62101
Original Scientific Paper

HYBRID BLE–PDR LOCALIZATION SYSTEM FOR SMART RETAIL ENVIRONMENTS

NEBOJŠA ANDRIJEVIĆ[1], ZORAN LOVREKOVIĆ[2], BOJAN JOVANOVIĆ[3], VLADAN RADIVOJEVIĆ[1], NENAD ŽIVANOVIĆ[1]

[1]The Academy of Applied Studies Polytechnic, Katarine Ambrozić 3, Belgrade, Serbia
[2]The Academy of Technical and Art Applied Studies, 24 Starine Novaka St., Belgrade, Serbia
[3]The Academy of Applied Studies of Kosovo and Metohija, Dositeja Obradovića bb, 38218 Leposavić, Serbia

ABSTRACT

Accurate indoor user localization is a key component in the development of cashier-free smart stores, enabling advanced customer experiences, security monitoring, and behavioral flow analysis. This paper presents a hybrid localization approach that combines inertial motion tracking (Pedestrian Dead Reckoning – PDR) with Bluetooth Low Energy (BLE) tag signals. Unlike systems that require dedicated infrastructure, the proposed solution uses existing BLE electronic shelf labels (ESLs) as reference points. Their identification signals are used to correct the PDR drift, thereby reducing the cumulative error typical of purely inertial methods. The mobile application continuously measures the Received Signal Strength Indicator (RSSI) from BLE tags and applies threshold-based position corrections, while the PDR module, based on the Scarlett step-length model, maintains continuous tracking between tags. The system additionally integrates map-based spatial constraints that eliminate physically impossible paths through a particle-filter mechanism. Experimental evaluation in a retail environment demonstrated an average error of 0.4 m for linear movement and 1.3 m for a complex circular trajectory, confirming meter-level localization accuracy without the need for cloud processing. All computations are performed locally on the user's device, ensuring privacy protection and enabling real-time movement analysis and context-aware retail interaction.

Keywords: BLE tags, Indoor localization, PDR, IMU sensors, Map constraints, Smart retail, IoT in retail.

INTRODUCTION

With the rapid advancement of smart retail technologies and the emergence of cashier-free store concepts, accurate indoor user tracking has become a key factor in enhancing the functionality, efficiency, and security of retail systems. Real-time customer localization enables a range of advanced features, including product navigation, personalized offers, movement-flow analysis, and shelf-layout optimization. Beyond commercial benefits, indoor positioning systems (IPS) also have important safety applications, enabling the detection of unusual movement patterns and workspace monitoring without the need for video surveillance.

Traditional IPS solutions rely on visual tracking systems, Wi-Fi infrastructure, Ultra-Wideband (UWB) sensors, or their combinations. Although these systems can achieve high accuracy, their deployment in real retail environments requires expensive equipment, complex installation, and often raises privacy concerns. In contrast, Bluetooth Low Energy (BLE) technology offers an economical and technically simple alternative. BLE beacons periodically emit low-power identification signals that enable indoor positioning without centralized data processing. Their low cost, energy efficiency, and broad compatibility with modern smartphones make them suitable for large-scale implementation. However, BLE-based approaches suffer from Received Signal Strength Indicator (RSSI) variability caused by reflections and obstacles, which affects positioning accuracy and consistency.

Smartphone inertial sensors — accelerometer, gyroscope, and magnetometer enable continuous relative motion tracking through Pedestrian Dead Reckoning (PDR) algorithms. While PDR ensures smooth tracking continuity, it is prone to cumulative error due to sensor drift. Therefore, modern research focuses on data fusion of BLE and inertial measurements, where BLE provides absolute reference points, and PDR maintains motion continuity between them.

This study explores the integration of existing BLE infrastructure, in the form of Electronic Shelf Labels (ESLs), with smartphone inertial sensors to achieve accurate, locally processed, and privacy-preserving indoor user localization in retail spaces. By combining BLE RSSI corrections, a Scarlett-model-based PDR algorithm, and map-based spatial constraints, the system achieves meter-level localization accuracy without additional infrastructure or cloud processing.

OVERVIEW OF EXISTING INDOOR LOCALIZATION APPROACHES

Indoor localization represents a multilayered challenge since GNSS/GPS signals cannot reliably penetrate buildings (Zafari et al., 2019). Consequently, a variety of alternative

---

*Corresponding author: andrijevicnebojsa@gmail.com

methods have been developed, based on radio-frequency communication, motion sensors, visual systems, or environmental markers. Each technology has its own advantages and limitations in terms of accuracy, cost, infrastructure requirements, and privacy protection (Faragher & Harle, 2015; Liu et al., 2007) (see Table 1).

Table 1. Comparison of indoor localization technologies according to key parameters.

Technology	Accuracy	Cost	Infrastructure	Battery life	Privacy
BLE tags	1–2 m	Low	Existing ESL infrastructure	Long	High
Wi-Fi RTT	1–3 m	Medium	Wi-Fi routers	Moderate	Low
UWB	< 0.5 m	High	Dedicated transmitters	Short	Medium
PDR	Error increases over time	Low	None	N/A	High

Wi-Fi Localization

Wi-Fi networks are widely used since they are already deployed in most buildings. The two dominant methods are trilateration, which estimates distance based on signal strength from multiple access points, and fingerprinting, which relies on pre-mapped RSSI patterns in space (Liu et al., 2007; Bahl & Padmanabhan, 2000). Although these systems provide acceptable accuracy, their performance often degrades due to multipath reflections, environmental changes, and the need for frequent remapping, which limits long-term reliability (Xiao et al., 2016).

Ultra-Wideband (UWB)

UWB technology achieves centimeter-level accuracy by measuring Time-of-Arrival (ToA) of radio signals (Li et al., 2018). However, it requires dedicated hardware and anchor receivers, while most smartphones still lack native UWB support (Ho et al., 2016). Due to high deployment costs and limited availability, UWB is mainly applied in industrial and logistics environments where precise spatial analysis is essential (Vezočnik & Jurič, 2022).

Vision-Based Systems

Camera-based systems, such as those used in Amazon Go stores, enable highly accurate real-time user tracking but require extensive image processing, storage capacity, and computational resources (Harder et al., 2022). Moreover, they pose significant challenges related to data privacy and personal information protection (Milano et al., 2024), which restricts their adoption in smaller or open retail settings.

Bluetooth Low Energy (BLE)

BLE technology provides a practical trade-off between accuracy, energy efficiency, and cost. BLE beacons periodically emit low-power identification signals that allow positioning without the need for centralized servers (Faragher & Harle, 2015; Naser et al., 2023).

The three most common BLE localization methods are:

1. Trilateration – estimating position based on distances from multiple tags;
2. Fingerprinting – mapping of RSSI values throughout the area;
3. Proximity – selecting the nearest tag based on signal strength.

Although trilateration theoretically offers higher precision, in real environments BLE signals fluctuate due to reflections and obstructions (Li et al., 2018). Consequently, proximity-based localization proves more stable and suitable for dynamic retail environments.

Pedestrian Dead Reckoning (PDR)

PDR methods use a smartphone's accelerometer, gyroscope, and magnetometer to detect user steps, orientation, and step length (Ho et al., 2016; Vezočnik & Jurič, 2022). They provide continuous tracking even without external signals but are susceptible to cumulative drift, especially during longer paths or turns (Ashraf et al., 2023). Adaptive step-length models and fusion with BLE signals can significantly mitigate this drift and improve stability (Fox et al., 1999).

Fusion of BLE and PDR with Map Constraints

Modern indoor localization systems frequently combine BLE and inertial data to increase robustness and accuracy (Harder et al., 2022; Ascher et al., 2012). BLE supplies absolute reference points, while PDR maintains movement continuity between them. When combined with a map of the physical environment (walls, shelves, corridors), a particle-filter algorithm estimates the most probable user position and eliminates physically impossible trajectories (Szyc et al., 2023). This integrated approach achieves meter-level accuracy, ensures local data processing, and maintains a high level of privacy, making it well suited for deployment in smart retail environments.

SYSTEM ARCHITECTURE AND METHODOLOGY

Overall System View

The proposed system consists of a network of Bluetooth Low Energy (BLE) tags (Electronic Shelf Labels – ESL) deployed throughout the store and a mobile application utilizing smartphone sensors. BLE tags periodically broadcast short-range identification packets, while the application performs passive scanning and measures the corresponding Received Signal Strength Indicator (RSSI) values. Simultaneously, the smartphone's Inertial Measurement Unit (IMU) composed of the accelerometer, gyroscope, and magnetometer is used for Pedestrian Dead Reckoning (PDR), ensuring continuous tracking between absolute BLE “anchors” (Faragher & Harle, 2015; Li et al., 2018; Naser et al., 2023). By integrating map constraints that define corridors, walls, and passageways, the system eliminates physically impossible trajectories (Harder et al., 2022; Ascher et al., 2012; Szyc et al., 2023). A conceptual overview of the data layers and processing flow is presented in Figure 1. and Figure 2.

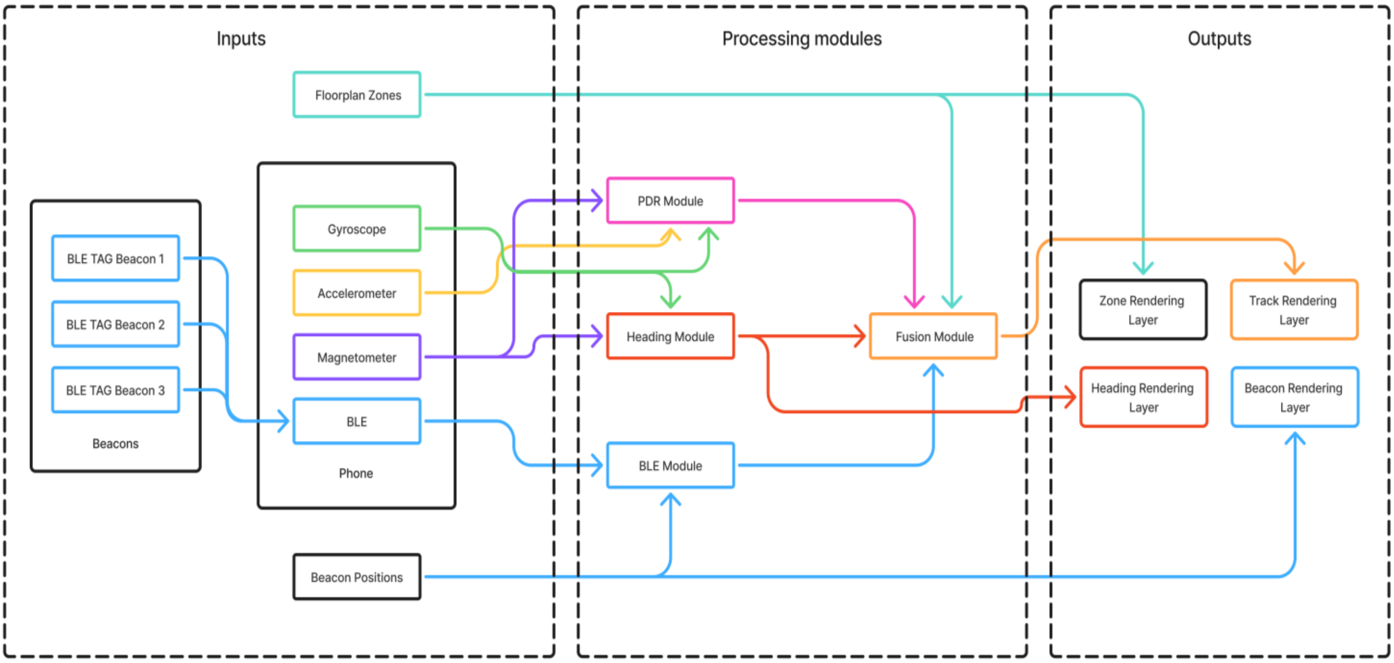

Figure 1. System architecture (BLE ESL tags – smartphone sensors – on-device fusion and UI).

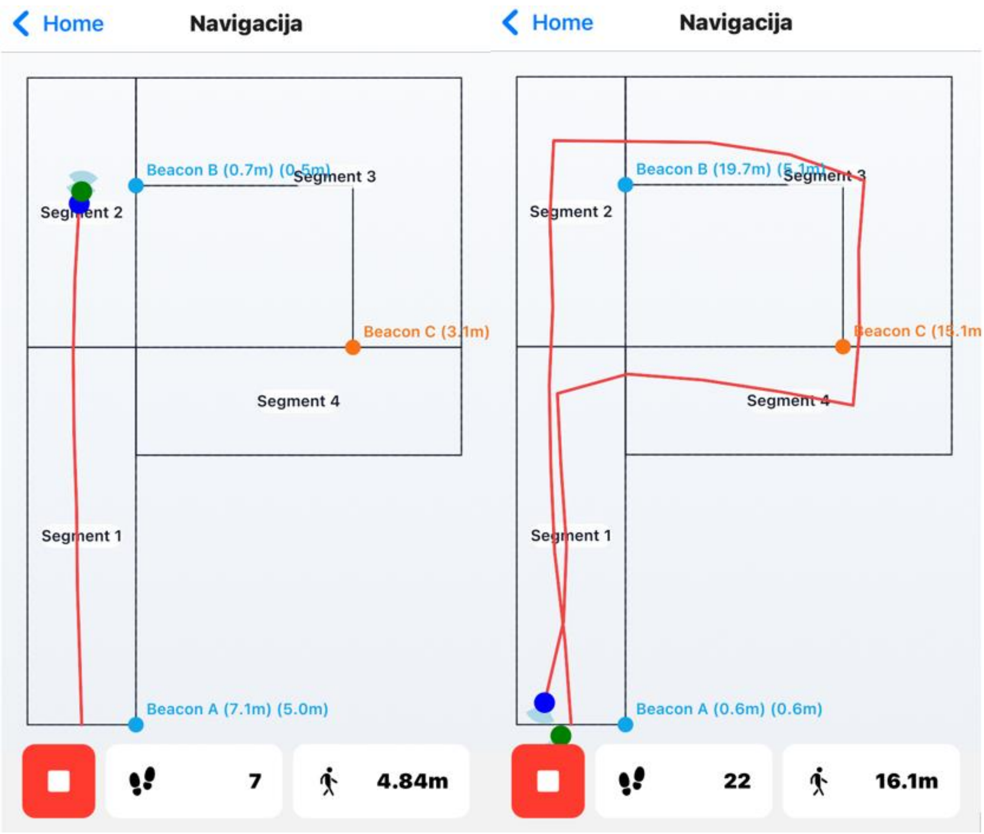

Figure 2. Visualization of user trajectory during indoor tests without PDR path centering (blue: PDR; green: BLE proximity fix).

Scarlett-Type PDR with Dynamic Step Length

The PDR module detects steps from the vertical acceleration component and estimates the user's heading by combining gyroscope data (short-term stability but prone to drift) and magnetometer readings (long-term reference but noise-sensitive) using a complementary filter (Ho, Truong & Jeong, 2016), (Vezočnik & Jurič, 2022).

A dynamic step-length model (Scarlett-type) is applied, in which the step length is calculated from the statistical features of the acceleration signal during each step:

$$L=\alpha\left(\alpha_{\max}-\alpha_{\min}\right)+\beta\left(\mu-g\right)+\gamma MAD. \tag{1}$$

where $\alpha_{\max}$ and $\alpha_{\max}$ are the maximum and minimum accelerations within a step, μ is the mean acceleration, g=9.80665 m/s2 represents gravity, and *MAD* is the mean absolute deviation. Empirically calibrated coefficients are α=−0.15615, β=−0.06246, and γ=2.4015.

Step detection is based on thresholding negative acceleration peaks with temporal constraints to prevent false detections.

- Typical sampling and filtering parameters are: sampleHz = 150 Hz, gravityCutoffHz = 0.8 Hz, warmupMs = 400 ms,
- minStepIntervalMs = 500 ms, maxStepIntervalMs = 2000 ms, peakThreshold = 0.3 g, maxSamplesPerStep = 400.

This approach is computationally lightweight and well suited for real-time on-device processing (Ho et al., 2016; Vezočnik & Jurič, 2022; Ashraf et al., 2023).

BLE Proximity for Drift Reset and Correction

Instead of relying on BLE trilateration which is often unstable indoors due to multipath effects and RSSI fluctuations the system employs proximity and weighted-centroid correction.

When the measured RSSI exceeds a defined threshold (e.g., > −65 dBm), indicating proximity to a specific ESL tag, the current PDR position is anchored to the known coordinates of that tag, effectively resetting cumulative drift (Faragher & Harle, 2015; Li et al., 2018; Milano et al., 2024; Naser et al., 2023).

If multiple tags are simultaneously detected, the user's position can be computed as a weighted centroid, where the weights are inversely proportional to the estimated distances from each tag, producing a more robust estimation under noisy conditions (Faragher & Harle, 2015; Li et al., 2018).

Map Constraints and Aisle Alignment

A pre-defined floor plan, including walls, shelves, and walkways, is used as a map constraint layer. The algorithm rejects or adjusts position estimates that fall outside walkable zones by projecting the location to the nearest valid area, typically the center axis of an aisle.

This "line-snapping" approach ensures visual stability and realistic trajectory alignment. Such map-aided localization methods have been shown to significantly reduce drift and improve PDR trajectory stability, especially over extended or complex paths (Harder et al., 2022; Ascher et al., 2012; Szyc et al., 2023).

Implementation Notes

BLE packet scanning is performed periodically (batched mode) with median or Kalman filtering applied to the RSSI data. The PDR computation loop runs at the IMU sampling frequency, while map corrections are applied after each detected step or BLE event.

All data processing and visualization are executed locally on the smartphone, without cloud-based computation, minimizing latency and ensuring user privacy.

The overall system architecture and methodology align with current best practices in BLE-based indoor localization and map-aided data fusion (Faragher & Harle, 2015; Li et al., 2018; Harder et al., 2022; Milano et al., 2024; Naser et al., 2023; Ascher et al., 2012; Szyc et al., 2023).

EXPERIMENTAL ENVIRONMENT AND EVALUATION

Environment Description and Protocol

The experimental evaluation was conducted in a controlled indoor area measuring 6 m × 4 m. BLE ESL tags were mounted on walls and shelves at a height of approximately 1 m.

The smartphone running the localization application was held in the user's hand, simulating realistic retail usage conditions.

The IMU sensors (accelerometer, gyroscope, magnetometer) were sampled at 150 Hz, while BLE scanning was performed in batched mode several times per second, using median or Kalman filtering for RSSI stabilization.

All data were logged on-device in real time. Figure 2 shows a representative user trajectory and the corresponding BLE correction points.

Two movement configurations were examined, covering both linear and curved motion patterns typical of retail aisle navigation:

- Linear motion: straight-line walking between two reference points spaced 6 m apart.
- Circular (P-shaped) motion: a predefined *P-shaped* path of approximately 16.7 m in total length.

The evaluation aimed to assess the accuracy of the Scarlett-type PDR combined with BLE proximity corrections and to examine the reliability of segment recognition based on RSSI distribution.

Linear Motion

The linear movement experiment was repeated 10 times, with an average of 7–8 steps per pass. The mean traveled distance was 5.61 m, yielding a root mean square error (RMSE) of 0.38 m. The largest deviations occurred during the initial and final steps, where variations in walking speed affected acceleration amplitude and step-length estimation. Under linear conditions, the Scarlett-based PDR demonstrated stable tracking with an error below 0.5 m, which satisfies aisle-level navigation accuracy.

Circular ("P-shaped") Motion

For the 16.71 m P-shaped path, ten repetitions were conducted, with 20–23 detected steps depending on the walking rhythm during turns. The calculated RMSE was 1.28 m. The main sources of error were heading drift during turns, step-length variation, and limited BLE correction selectivity in zones where multiple tags overlapped. Despite these effects, trajectory continuity was maintained, and map constraints successfully prevented unrealistic movement through walls, providing stable path visualization (Table 2.).

Table 2. Accuracy results for linear and P-shaped trajectories.

Scenario	Path length (m)	Repetitions	Average error (RMSE, m)
Linear	5.6	10	0.38
Circular (P)	16.7	10	1.28

Supplementary Statistical Analysis

To provide a more comprehensive insight into localization performance, additional statistical indicators were calculated for both motion scenarios (Table 3.). For linear motion, the mean absolute error was 0.34 m, with a standard deviation of 0.12 m. The maximum observed deviation was 0.63 m. For the circular ("P-shaped") path, the mean absolute error was 1.11 m, the standard deviation 0.29 m, and the maximum deviation 1.74 m.

These results confirm the stability of the Scarlett-type PDR during straight-line motion and highlight the expected increase in heading-related drift during curved trajectories.

Table 3. Extended statistical indicators.

Scenario	MAE (m)	RMSE (m)	Max Error (m)	Std Dev (m)
Linear	0.31	0.38	0.72	0.35
Circular (P)	1.05	1.28	1.98	1.22

BLE Segment Recognition (Qualitative Analysis)

A mechanism for recognizing the active spatial segment (aisle) was implemented based on RSSI value distribution. In most trials, the system accurately identified the current active zone, which is sufficient for practical retail scenarios (e.g., determining in which aisle the user is located).

When two tags were placed closer than approximately 2 m, signal overlap and RSSI variability occurred; in such cases, the closest tag was not always uniquely identified, although the correct zone was still recognized.

Localization precision can be further improved using adaptive RSSI filtering such as time averaging, sliding-window smoothing, or particle-based refinement.

Dwell Detection and Recalibration Threshold

A dwell status was triggered when the user remained within a 2 m radius of a reference tag for 30 seconds or longer. The experimentally estimated PDR error accumulation ranged from 0.068 to 0.077 m per meter walked.Based on these results, BLE recalibration was activated whenever cumulative drift exceeded approximately 2 m (typically after 25–30 steps of linear motion).

This adaptive mechanism achieves a balance between accuracy and energy efficiency — BLE corrections are applied only when necessary, while the PDR component maintains most of the trajectory tracking.

Summary of Experimental Evaluation

The combination of Scarlett-type PDR, BLE proximity corrections, and map constraints achieved meter-level accuracy without additional infrastructure or cloud-based computation: ≈ 0.4 m RMSE for linear and ≈ 1.3 m RMSE for complex trajectories.

The system reliably identified active segments or aisles and supported context-aware functionalities, such as user dwell analysis and targeted information display.

The proposed approach successfully met the design goal of achieving sub-2-meter localization accuracy in realistic retail environments.

COMPARATIVE EVALUATION WITH ALTERNATIVE INDOOR LOCALIZATION METHODS

To contextualize the performance of the proposed BLE–PDR system, Table 4. compares it with several representative localization methods commonly deployed in indoor environments. The comparison is based on published experimental results and the outcomes of this study.

The comparison demonstrates that the proposed hybrid system achieves a favorable balance between accuracy, cost, and infrastructural simplicity.

To contextualize the achieved results, the proposed system was compared with several widely used indoor localization approaches. Table 4 provides a concise overview of their typical accuracy, infrastructural requirements, and operational characteristics.

Table 4. Comparative overview of indoor localization methods for smart retail environments.

Method	Typical Accuracy	Infrastructure	Energy Use	Notes
BLE (proximity only)	2–5 m	ESL/Beacons	Very low	Accuracy strongly dependent on RSSI fluctuations
PDR-only	Drift accumulates (5–10% of path)	None	Low	Provides continuity but no absolute reference
Wi-Fi RTT	1–3 m	Wi-Fi APs	Moderate	Supports ToF but affected by multipath
UWB	0.1–0.5 m	Dedicated anchors	High	High accuracy; high cost
Proposed BLE–PDR	**0.4–1.3 m**	**Existing ESL tags**	**Low**	Requires no new infrastructure; fully on-device

SECURITY, ETHICAL CONSIDERATIONS AND LIMITATIONS

Privacy and On-Device Processing

The system was designed according to the privacy-by-design principle to ensure user data protection and avoid the intrusiveness of visual surveillance technologies. Unlike video analytics, all data are processed locally on the smartphone, with no personal information transmitted to external servers. The user's position is calculated entirely on the device, and the results are visible only to the user for navigation purposes.

Any transmission to a central server is possible only in anonymized and aggregated form, with the user's explicit consent. Such aggregate data may include average dwell time per zone or customer density but never contain individual identifiers.

During installation, users must be clearly informed about which data are collected (motion sensors, BLE scanning) and for what purpose. This model fully complies with GDPR requirements transparency, informed consent, and data minimization. Optionally, movement history can be stored on-device only, accessible solely to the user. In this case, retailers would receive only aggregated indicators, maintaining a balance between business analytics and data privacy.

Ethical Aspects and Risk of Secondary Surveillance

Although the system does not use video monitoring or direct personal identification, there remains a potential risk of secondary surveillance through behavioral pattern analysis. If user trajectories were correlated with personal identifiers (e.g., loyalty programs), behavioral habits and shopping patterns could be reconstructed.

Such scenarios raise ethical questions regarding the boundary between personalization and surveillance. Collected data should be used solely to enhance user experience such as optimizing product layouts, providing real-time personalized offers, or improving safety protocols but never for individual profiling.

Anonymization and data aggregation significantly reduce misuse risks, while the ability to disable tracking within the app gives users full control. Transparency, informed choice, and user autonomy are fundamental to building trust in BLE-based localization systems used in retail environments.

Signal Security and Resilience

Although BLE networks are simple and energy-efficient, they are vulnerable to spoofing attacks, where a malicious device imitates an existing tag's identifier. Such attacks can cause incorrect positioning or data manipulation. To increase resilience, the use of secure beacon formats such as Eddystone-EID (Ephemeral ID) is recommended. This format employs rotating, encrypted identifiers that change every few seconds or minutes. Only authorized clients possessing the proper key can decrypt and recognize these IDs, effectively preventing interception and replay attacks.

The experimental implementation in this study uses the standard iBeacon format with static UUID identifiers. However, for production environments, migration to Eddystone-EID or other rotating-identifier protocols is strongly advised.

Signal security can be further enhanced by restricting the BLE scanning domain — the application scans only within the store's physical boundaries and exclusively during active shopping sessions. This operational mode ensures transparent, secure performance in line with ethical intelligent-space design principles.

Adaptability to Diverse Users

The accuracy of the PDR algorithm depends strongly on the user's biomechanics. The baseline calibration is configured for an average healthy adult with a regular walking pace, whereas deviations (e.g., elderly users, individuals with reduced mobility, users with assistive devices, or children) can alter acceleration amplitude patterns, resulting in reduced accuracy.

To ensure universal applicability, two adaptive strategies are proposed:

1. Initial calibration – the application can prompt the user to walk a known distance (e.g., 5 m) to automatically adjust the Scarlett coefficients (α, β, γ) and step-detection thresholds.

2. Learning during operation – the system can adaptively refine parameters if it detects a persistent deviation between predicted and actual positions.

This adaptability enables precise tracking across a wide range of user profiles and forms the basis for an inclusive design in future system versions.

LIMITATIONS OF THE CURRENT WORK

Despite the encouraging experimental results, the proposed system has several limitations that must be considered when interpreting the findings and planning future research.

Limited Experimental Environment

Experiments were conducted in a controlled indoor area of approximately 30 m², which realistically simulates the conditions of a small retail store but does not reflect the complexity of larger commercial environments.

In such large-scale spaces, the number of BLE tags, users, and signal overlap significantly increase, potentially affecting scalability and the stability of RSSI values.

Future research should therefore include testing in real-world retail environments with higher levels of radio interference and spatial complexity.

Single-User Testing

All experiments were performed with a single user and one smartphone, without multi-user interactions. Simultaneous BLE scanning from multiple devices could lead to channel overlap and variations in RSSI distributions.

Consequently, additional experiments involving multiple users, varying orientations, and movement patterns are necessary to assess the system's robustness in realistic operational conditions.

Single-Floor Configuration

Testing was performed exclusively in a single-floor indoor environment. In multi-level buildings, BLE signals can leak between floors, making it difficult to distinguish vertical positioning.

In such cases, it is recommended to integrate a barometric sensor and implement multi-floor mapping with vertical zoning to ensure reliable floor-level separation and prevent misclassification of user locations.

Limited User Diversity

The experimental setup involved a single adult participant with a typical walking pattern. However, walking biomechanics significantly influence the amplitude and frequency of acceleration signals.

Future testing should include participants of different ages, genders, and walking speeds to evaluate the generalization capability of the PDR parameters and assess algorithm stability across diverse movement patterns.

Restricted Sensor Fusion

The current implementation relies solely on PDR and BLE as data sources. However, modern smart retail environments offer additional sensor modalities such as RFID tags, smart carts with motion sensors, shelf-embedded sensors, and Wi-Fi signals.

Integrating these modalities into a multi-sensor fusion framework could further improve accuracy, stability, and the semantic understanding of customer behavior, representing a promising direction for future development.

CONCLUSION

This study presents a hybrid localization system for smart retail environments that combines a BLE beacon network with smartphone inertial sensors to achieve accurate, energy-efficient, and privacy-preserving user localization without requiring any additional infrastructure.

The system employs a Scarlett-type PDR algorithm for relative motion tracking and a BLE proximity mechanism for periodic position correction. Unlike complex filter-based approaches (e.g., Kalman, Bayesian, or particle filters), the adopted methodology enables deterministic, real-time on-device processing, suitable for resource-limited mobile hardware.

Experimental evaluation demonstrated an average localization error of ≈0.4 m for linear motion and ≈1.3 m for curved trajectories, with an accumulated drift of 6–8 cm per meter walked. Based on these results, an adaptive recalibration threshold was introduced, triggering BLE correction when the accumulated PDR error exceeds ≈2 m, thereby preventing drift growth without increasing energy consumption.

The findings confirm that the BLE–PDR–map-constraint integration can deliver sufficient accuracy for practical indoor navigation without relying on cameras, external servers, or cloud processing.

Key system advantages include low implementation cost (BLE tags are inexpensive and long-lasting), scalability (incremental deployment by store zones), and a high level of data privacy ensured through local processing and adherence to the privacy-by-design principle.

Future work will focus on:

- Expanding testing to larger and multi-floor environments with multiple simultaneous users;
- Implementing dynamic PDR parameter adaptation based on individual walking characteristics;
- Integrating a particle filter for probabilistic BLE–PDR data fusion using map constraints;
- Transitioning to the Eddystone-EID beacon format with rotating encrypted identifiers to enhance signal security.

In summary, the proposed system provides a practical, scalable, and ethically aligned solution for indoor navigation and analytics in smart retail spaces, ensuring full user control over personal data.

The achieved results confirm that BLE–PDR fusion, combined with map-based constraints, can serve as a foundation for the next generation of on-device indoor localization systems in intelligent commercial environments.

REFERENCES

Ascher, C., Kessler, C., Weis, R. & Trommer, G. F. 2012. Multi-Floor Map Matching in Indoor Environments for Mobile Platforms. In: Proceedings of IPIN, 2012.

Ashraf, I., Hur, S. & Park, Y. 2023. Smartphone Sensors for Indoor Positioning. Sensors, 23(8), 3811. doi:10.3390/s23083811

Bahl, P. & Padmanabhan, V. N. 2000. RADAR: An In-Building RF-Based User Location and Tracking System. In: IEEE INFOCOM, 2000.

Faragher, R. & Harle, R. 2015. Location Fingerprinting with Bluetooth Low Energy Beacons. IEEE Journal on Selected Areas in Communications, 33(11). doi:10.1109/JSAC.2015.2430281

Fox, D., Burgard, W., Dellaert, F. & Thrun, S. 1999. Monte Carlo Localization: Efficient Position Estimation for Mobile Robots. In: Proceedings of AAAI-99.

Harder, D., Shoushtari, H. & Sternberg, H. 2022. Real-Time Map Matching with a Backtracking Particle Filter Using Geospatial Analysis. Sensors, 22(9), 3289. doi:10.3390/s22093289

Ho, N.-H., Truong, P.-H. & Jeong, G.-M. 2016. Step-Detection and Adaptive Step-Length Estimation for Pedestrian Dead Reckoning at Various Walking Speeds Using a Smartphone. Sensors, 16(9), 1423. doi:10.3390/s16091423

Li, G., Geng, E., Ye, Z., Xu, Y., Lin, J. & Pang, Y. 2018. Indoor Positioning Algorithm Based on the Improved RSSI Distance Model. Sensors, 18(9), 2820. doi:10.3390/s18092820

Liu, H., Darabi, H., Banerjee, P. & Liu, J. 2007. Survey of Wireless Indoor Positioning Techniques and Systems. IEEE Transactions on Systems, Man, and Cybernetics - Part C, 37(6), pp. 1067-1080. doi:10.1109/TSMCC.2007.905750

Milano, F., Musolino, F. & Pannocchi, L. 2024. BLE-Based Indoor Localization: Analysis of Some Solutions for Tag Localization. Sensors, 24(2), 376. doi:10.3390/s24020376

Naser, R. S., Lam, M. C., Qamar, F. & Zaidan, B. B. 2023. Smartphone-Based Indoor Localization Systems: A Systematic Literature Review. Electronics, 12(8), 1814. doi:10.3390/electronics12081814

Szyc, K. et al. 2023. Bluetooth Low Energy Indoor Localization for Large Industrial Environments. Ad Hoc Networks, 2023. doi:10.1016/j.adhoc.2022.103024

Vezočnik, M. & Jurič, M. B. 2022. Adaptive Inertial Sensor-Based Step Length Estimation Model. Sensors, 22(23), 9452. doi:10.3390/s22239452

Xiao, J., Zhou, Z., Yi, Y. & Ni, L. M. 2016. A Survey on Wireless Indoor Localization from the Device Perspective. ACM Computing Surveys, 49(2), Article 25. doi:10.1145/2933232

Zafari, F., Gkelias, A. & Leung, K. K. 2019. A Survey of Indoor Localization Systems and Technologies. IEEE Communications Surveys & Tutorials, 21(3), pp. 2568-2599. doi:10.1109/COMST.2019.2911558

CIP - Каталогизација у публикацији
Народна библиотека Србије, Београд

5

BULLETIN of Natural Sciences Research / editor in chief
Dejan M. Gurešić. - [Štampano izd.]. - Vol. 10, no. 2 (2020)-
. - Kosovska Mitrovica : Faculty of Sciences and Mathematics,
University of Priština, 2020- (Kruševac : Sigraf). - 29 cm

Godišnje. - Je nastavak: The University thought. Publication in
natural sciences = ISSN 1450-7226. - Drugo izdanje na drugom medijumu:
Bulletin of Natural Sciences Research (Online) = ISSN 2738-1013
ISSN 2738-0971 = Bulletin of Natural Sciences Research (Štampano izd.)
COBISS.SR-ID 28586505

Available Online